Developments in Single-Crystal Neutron Diffraction at High Pressure

Malcolm Guthrie

A thesis submitted in fulfilment of the requirements
for the degree of Doctor of Philosophy
to the
Department of Physics and Astronomy
University of Edinburgh
2002

Declaration

This thesis has been composed by myself and it has not been submitted in any previous application for a degree. The work reported within was executed by me, unless otherwise stated.

April 2002

Acknowledgements

In the first instance, I wish to express my gratitude to Richard Nelmes who has supervised my work over the last three years. Without his guidance and support this thesis would not have been possible. Additionally, I would like to thank him for giving me the opportunity to travel so widely and to meet so many of the personalities who shape the world of high-pressure science.

I also wish to thank my second supervisor David Allan, who has always been willing to devote time to me. Dave also has the distinction of being the man who introduced me to the field of high pressure nearly five years ago.

A special thank-you must also go to John Loveday who has been unlucky enough to share an office with me for the last three years! Perhaps more than anyone, John has helped me learn how to 'do' science, and I'd like to thank him for imparting some small part of his encyclopaedic knowledge to me.

I'd also like to thank Stefan Klotz and Gerard Hamel for making their world-class expertise available to me. I especially with to thank Stefan for being "a man of principles" and for inventing the beamtime picnic! I also wish to thank our Colleagues in Washington: Dave, Russ, Jian, Zulu, Przemek, for taking so much time to help me out during my time at the Carnegie Institue. Cheers also to Eugene and Chrystele for helping to make it fun.

Closer to home, I would never have got this far without the invaluable help and friendship I've experienced at ISIS. Special thanks to Bill for helping me understand the nuts and bolts of PEARL and Duncan for providing all the technical

support I needed (and some bad jokes that I didn't!). Acknowledgement must also go to Chick, Dave Keen, Matthais, 'the vicar' and last, but by no means least, Devinder who have all helped me out enormously along the way

A mention must also go to the Edinburgh team: Thiti, Carine, Frank and Scott for their company at many conferences and during Daresbury beamtime. Also a general acknowledgement to anyone who has passed time with me sitting until the small hours at the end of a neutron beamguide.

A massive thankyou must go to my parents who have supported me throughout the last *eight years* of physics and have never once berated me for not having a proper job!

And finally, I wish to express my love and thanks to Cristina who has been there for me through the good and bad times of the last three years, and whose job it is to remind me what it's all about.

Abstract

Pressure is a powerful thermodynamic variable, capable of inducing dramatic changes in the structure and therefore the properties of matter. An accurate determination of these changes in structure provides an essential starting point for the interpretation of dynamical measurements, and a necessary foundation upon which computational ab-initio simulations are built. Diffraction studies utilising both powder and single-crystal techniques provide this important structural information and, as such, are a powerful investigative tool.

An in-depth analysis of neutron powder-diffraction data from a sample of ice VII is presented. This study involved an attempt to extract information about the detailed nature of the atomic disorder present in the water molecule, information only accessible via neutron techniques. The resulting difficulties lead to an exploration of the fundamental limits of powder-diffraction. This investigation highlighted a need to extend the maximum accessible pressure for single-crystal techniques that, for structural neutron-diffraction, is currently limited to 2.5 GPa. The majority of the work constituting this thesis was devoted to increasing this limit.

In order to realise this advance, two different techniques were developed in parallel. The first of these centred on the use of the Paris-Edinburgh (PE) cell to compress single-crystal samples. The new instrumentation, experimental methodologies and software developed by the author included modifications to both the cell

and diffractometer and are presented here. These successfully facilitated a significant increase in accessible pressure up to at least 7.2 GPa. This new capability was used in a comparative powder and single-crystal study of the structure of potassium di-hydrogen phosphate (KDP). The results of this study challenged the previously published structure. This study also gave an important opportunity to test fully the newly developed experimental methods.

The second technique to be developed by the author used a new large-volume diamond-anvil cell (DAC). This device provides optical access to the sample and thus presents the possibility of the in-situ growth of high-pressure phases. This property, combined with large apertures for the diffracted beam, gives the DAC significant advantages over the PE cell. The techniques developed to perform neutron diffraction with the cell are presented, as are those for crystal growth. It was found that the DAC is currently limited in maximum pressure by the size of available anvils. However, this was sufficient to enable an investigation of D_2-D_2O clathrate, a compound only formed under high pressure. The results of this first neutron study are discussed in comparison with the previous published structure, as determined by x-ray diffraction, which was unable to resolve the hydrogen atoms. This brought to light the possibility that the original structure was, in fact, incorrect.

Finally, these two new techniques are compared and contrasted, with a general look forward to the possibilities for new high-pressure science. These developments are assessed in light of the imminence of a new ultra-intense neutron source due to come on-line in 2006 in the USA. In addition, recent significant advances in growth techniques for artificial diamonds will also have a large effect on the design of future high-pressure cells, that will further widen the landscape that can currently be explored by single-crystal neutron diffraction.

Contents

Chapter 1

Introduction

It is true to say that many advances in experimental science follow in the wake of the development of new technology, or from the advancement of available techniques. This is perhaps especially the case in the field of high-pressure research, where the application and control of pressure has proved to be especially challenging.

One dramatic historical example of this trend is the wealth of science that burgeoned following the invention of the diamond anvil cell (DAC). For the first time, this device allowed the application of very high pressures whilst still providing access to a variety of structural and dynamical probes. The success of diamond anvil cells as tools for high-pressure diffraction is also intrinsically linked to the development of extremely bright synchrotron-radiation sources. This powerful combination has made structural measurements possible at extreme pressures of several megabars simply by reducing the volume of the sample.

It is due to the relative power of the respective sources that a dichotomy exists between neutron diffraction and x-ray diffraction. Sources of neutron radiation are intrinsically much weaker than synchrotrons and this has lead to neutron diffraction lagging behind x-ray diffraction in terms of the maximum accessible pressure. Despite this, it is still an essential probe of atomic structure, providing

both the only means by which light elements can be accurately located, and a far more accurate probe of subtle structural effects such as disorder and atomic thermal motion.

In addition to the choice of radiation, an important aspect of any diffraction experiment is whether the sample is single-crystal or poly-crystalline (powder) in nature. Techniques employing samples of the former type are the most powerful, yet they have not been the most commonly implemented for several reasons, not least a lack of appropriate sample environment equipment and corresponding experimental techniques. However, this situation is changing and, certainly in the field of x-ray diffraction, more and more high-pressure work is being performed on single-crystal samples [1]. This has arisen because the quality of modern powder diffraction is such, that its *intrinsic* limitations have become more evident. The nature of these limitations is introduced in Section 1.2, which is then followed by a more detailed exposition of the powder technique in the following Chapter 2.

This situation has highlighted a need for single-crystal neutron-diffraction techniques to be developed to higher pressures than those currently accessible. Indeed, it is only with single-crystal diffraction that some of the important benefits of neutron diffraction experiments can be exploited fully. Finally, having emphasised the importance of technology, a certain context is given to this work by a new spallation-neutron source due to come on-line in the United States in 2006. The combined improvements in source and detector technology are expected to result in an increase in effective flux of factors of 40-100 over the most powerful sources available today.

1.1 Pressure as a Thermodynamic Variable and its Use in Neutron Diffraction

The phase of bulk matter is not a constant but instead has a, sometimes complex, dependence on the experimental variables of temperature and pressure. Changes in phase can lead to dramatic changes in properties, and, therefore, any complete characterisation of a material requires exploration over a wide range of conditions. Whilst the limelight has often been ceded to the effects of temperature variation, pressure is a far more powerful variable in terms of its effect on structure.

Indeed, high pressures can induce more dramatic changes in the volume of the solid phase than is observed on warming or cooling. This can be as much as a factor of ~ 3 by 10 GPa in the case of the soft metal caesium [2]. Additionally, exotic changes in properties can arise including:

- Insulator→metal transitions. For example this is believed to have been observed in hydrogen [3], xenon [4] and oxygen [5].
- Pressure-induced amorphisation. This phenomenon has been observed in ice [6], clathrate structures [7], and in several minerals [8], notably quartz [9].
- Electronic $s \rightarrow d$ transitions. See for example [10] for a discussion of Lanthanum, Uranium and Thorium.
- Pressure-induced superconductivity. This has recently been observed in iron [11], and boron [12]
- Molecular dissociation. A dramatic recent example of this is the observation of semi-conducting, non-molecular nitrogen [13].

Additionally, pressure is a clean variable allowing large changes in bondlength without complications arising from anharmonic thermal motion. In particular, it

lends itself to systematic investigations of the effects of bondlength on material properties and transitions.

A good example of this richness of behaviour under high-pressure is given by the phase diagram of water shown in Figure 1.1 up to 4 GPa. At ambient pressure, water freezes into the hexagonal ice I_h structure at 0°C, and no further structural transition is observed from there down to absolute zero. However, under the application of even modest pressures of several tenths of a gigapascal, the true complexity of the solid phase of water begins to be revealed, and up to $\sim$ 70 GPa, twelve distinct structural phases are known to exist. At the very highest pressures, water loses its molecular character entirely as the hydrogen bond centres and ice becomes a simple oxide of hydrogen.

It is worth commenting on the pressures relevant to this thesis. Throughout this thesis, the gigapascal (GPa), as the S.I. unit of pressure, is used. Another common unit in this pressure range is the kilobar: 1 kbar = 0.1 GPa. It has already been mentioned that large sample volumes limit the maximum accessible pressures for neutron diffraction. To put this quantitatively, the maximum accessible pressure for (non-magnetic) neutron diffraction is below 30.0 GPa [15], which is a full order of magnitude below that achieved using x-ray diffraction and diamond-anvil cell technology (see for example [16],[17] and [18]).

1.2 High Pressure Diffraction Work

In many ways powder diffraction is the natural technique for high-pressure studies. Structural phase-transitions induced by pressure are often violent, and will reduce large single-crystals into fine grained powders. It is for this reason that powder diffraction has come to dominate high-pressure structural work in recent decades. Such an extended period of use has honed powder diffraction into an extremely powerful tool. These advances have been facilitated by the advent of

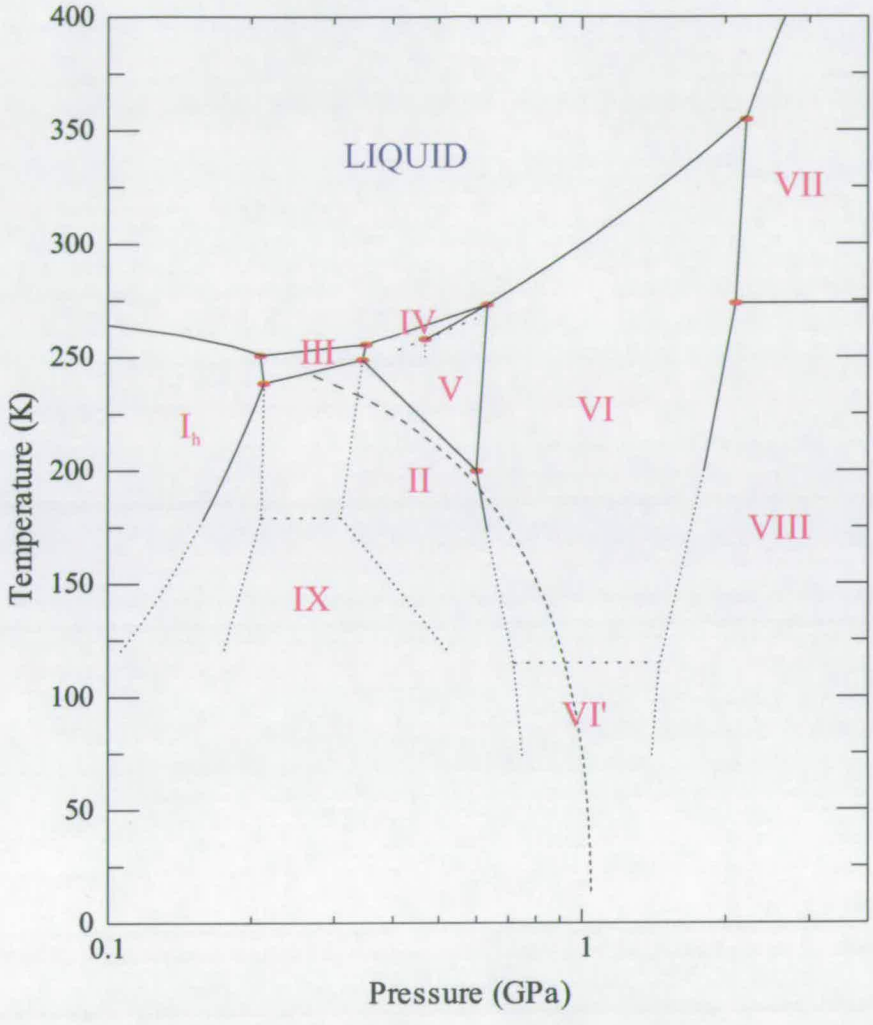

Figure 1.1. The low pressure phase diagram of H_2O ice up to 4 GPa [14]

sophisticated algorithms for refinement of the data and, of course, the remarkable increase in the available computer processor speed.

However, despite these strengths, powder diffraction has fundamental limitations. These are a direct consequence of the reduction of inherently $3d$ diffraction information - from a $3d$ structure - to a $1d$ powder pattern. This problem comes to the fore in circumstances where subtle structural effects are of interest. The measurement of effects such as atomic disorder and the determination of thermal motion depends on the accurate measurement of Bragg intensities in the region

below 0.7 Å in d-spacing. In this region, distinct Bragg peaks are very close together and become heavily overlapped. Additionally, patterns collected at high pressure are often superposed on a large background arising from the pressure cell itself. Where this background includes powder scatter from components of the cell, it exacerbates these problems.

Another difficulty arises in the solution of complex structures. Often the most taxing step in structure solution from powders is the accurate assignment of indexes to the observed reflections. For complex, low symmetry structures, there are many Bragg reflections and over-laps can render unambiguous indexing extremely difficult or even impossible. The powder pattern of ice VII shown in the following chapter (Figure 2.7) reveals the extent of the overlap even for a high-symmetry cubic structure. The situation is far worse, and indeed can become intractable, for lower symmetry structures which have a much higher number of allowed reflections.

It is for these reasons that, in the last few years, there has been a resurgence of single-crystal diffraction in x-ray studies at high-pressure [1]. Now that super-megabar pressures are routinely achievable, attention is turning more and more to the details of the structures. As the full $3d$ nature of the diffraction pattern is retained, far more accurate structural information can be determined. In addition, single-crystal diffraction has the advantage that all of the diffraction is concentrated into sharp diffraction spots, whereas in powder diffraction, for any given reflection, that scattering is spread around the full Debye-Scherrer ring. This lends the technique to measurements were incident flux, or sample volume, are fundamentally limited.

Much of the work described in this thesis was motivated by a need for a parallel development in neutron diffraction. Neutron diffraction is the most successful technique for determining the structure of hydrogen bonds, as a consequence of its unequaled ability to 'see' hydrogen atoms. In addition, because the scattering

is from the nuclei, which are pointlike, the form factor is constant and correspondingly there is no drop in intensity with decreasing d-spacing. This, in principle, allows the probing of extremely subtle atomic disorder effects but, in order to take full advantage of this particular trait of neutrons, recourse to single-crystal techniques is required.

1.3 Neutron and X-ray Radiations

Unlike modern synchrotron x-ray sources, neutron reactors or spallation sources are characterised by rather low fluxes. The impressive increase in maximum achievable pressure in structural work over the last fifteen years, has largely been achieved by minimisation of sample volumes. This illustrates an important aspect of high-pressure research following directly from the definition of pressure (P) as the force (F) per unit area (A).

$$P = \frac{F}{A}$$

As a general rule the state-of-the-art is not defined solely by the maximum achievable pressure, but by the scattering power at that pressure, which is proportional to the sample volume.

The low flux of neutron sources forces the use of sample volumes which are often a factor of 1000 larger than equivalent x-ray samples, and thus severely limit the accessible pressures. In the case of single-crystal neutron diffraction, this limitation has been considerable, and accurate structural work using the technique has been limited to 2.5 GPa. The development of high pressure single-crystal techniques is also timely: a new spallation neutron source (SNS) is planned to come online in 2006. Advances in moderator technology, detector technology and the increasing use of focusing optics for neutrons has lead to claims of up to a hundred-fold increase in effective neutron flux. It is likely that much of this increase in flux will be directly communicated to higher operating pressures, thus opening up a vast field of scientific interest. Yet, this will only be possible with

the development of new experimental techniques.

1.4 The Thesis Layout

Chapter 2: An Introduction to Crystalline Diffraction

An introduction is given to the essential theory that underpins all diffraction experiments. The discussion extends to some depth in order to provide an adequate context for the development work that comprises Chapter 4. Additionally, different experimental techniques are contrasted, with specific emphasis on the relative advantages and disadvantages of the different radiations used in diffraction work. Finally, a description of the important technique of powder diffraction is given along with an outline of its fundamental limitations.

Chapter 3: Exploring the Limits of Powder Diffraction: High Pressure Ice

An introduction to the issues surrounding the high-pressure ice phases VII, VIII and X is given with specific reference to previous structural work. The importance of determining accurately the nature of the disorder of the oxygen atom in ice VII is highlighted. A study of this structural parameter, utilising neutron powder diffraction with the Paris-Edinburgh (PE) high-pressure cell, is described. The subsequent analysis of the data rapidly concentrated on the details of the correction procedures applied prior to refinement. This highlighted several problems with routinely employed methods when applied to thermal motion studies. Despite successful identification and correction of these problematic areas, the investigation was unable to shed further light on the nature of the atomic disorder. This provided an important motivation for the main focus of this thesis: the development of single-crystal techniques.

Chapter 4: Single Crystal Time-of-Flight Diffraction With the Paris-Edinburgh Cell

The extensive development of both the PE cell and the PEARL HiPr diffractometer at ISIS to facilitate single-crystal diffraction is described. This evolution required the introduction of new experimental equipment, including a cell rotation and encoding mechanism, which is described in detail. A new detector with $2d$ resolution was installed, and a scanning methodology was developed in order to use the lower resolution powder detectors for measuring accurate single-crystal intensities. In order to extract structural information from these intensities, new calibration techniques were developed to determine the exact position of the detectors. For these new technical capabilities to be exploited, a range of software also had to be developed. This work, based on adaptation of existing crystallographic routines, is also briefly discussed. In parallel with the development of the diffractometer, the exploitation of new gasket technology to safely compress single-crystals up to pressures of > 7.0 GPa is presented.

Chapter 5: A Comparative Single-Crystal and Powder Diffraction Study of KDP up to 7 GPa

An introduction is given to the structure of potassium di-hydrogen phosphate (KDP). The importance of the geometry of the hydrogen-bond in certain phase transitions is underlined. In particular, the observation of Endo *et al.* [19] that the hydrogen bond symmetrises at a critical pressure P_c is presented. Powder neutron-diffraction data were collected to specifically investigate this interesting property. The results of this analysis revealed that the original determination of the hydrogen bondlength, which had been seen to increase with pressure, were incorrect.

Additionally, this compound was used to test the techniques outlined in Chapter 3, and high quality single-crystal data were measured up to 7.2 GPa. Despite

the presence of severe extinction, these data lent support to the powder measurements. The attempt to correct the data for the effect of extinction has highlighted the limitation of the available theoretical models of the effect, as applied to time-of-flight diffraction.

Chapter 6: Neutron Diffraction with Large-Volume Diamond-Anvil Cells

A parallel development of diamond anvil cell (DAC) techniques for neutron work is discussed here. These cells have significant advantages over PE type cells (which are highlighted), but have previously been limited by a working volume that was too small for neutron diffraction. Recent advances in the growth of artificial diamonds [20] and Moissanite [21] have made large anvils available for the first time. The use of new large volume DACs on the SXD diffractometer at ISIS is presented. In addition, these techniques were applied, for the first time, to a study of hydrogen clathrate, a compound which can only be formed at high pressure. This study suggested that the structure, previously determined by x-ray diffraction, was incorrect.

Chapter 7: Conclusions and A Look to the Future

Finally, an overview is given of the steps that have been taken towards routine neutron single-crystal diffraction at pressures of up to 10 GPa and higher is given. These conclusions suggest directions for the further development of high-pressure cells, which must utilise the advantages of both PE cell *and* DAC technology. Following this, a view of the near future is expounded with the implications of new ultra-intense neutron sources.

Chapter 2

Crystalline Diffraction at High Pressure

2.1 Introduction to Crystalline Diffraction

A large component of the work of this thesis has centred on the development of new experimental techniques and methodology. In order that the reader can appreciate the motives and method behind these developments, a reasonably in-depth introduction is given here to the under-lying theory of diffraction measurements. Whilst much of this theory is an important part of undergraduate degrees in physics, and as such is covered at length in a variety of text-books (see for example [22]), the author has found that its specific application to poly-chromatic *neutron* diffraction is less well recorded. It is thus the goal of the following section on essential diffraction theory to collate the appropriate elements of the theory, and emphasise their specific application to poly-chromatic neutron techniques.

The theoretical discussion is followed by a generalised introduction to the different types of diffraction experiment currently used in structural studies. Here, the relative merits of neutron and x-ray diffraction are juxtaposed.

A central theme throughout this thesis is the comparison of single-crystal and powder diffraction. Therefore, an introduction to powder diffraction techniques is given to clarify the contrast between the two experimental methodologies.

2.1.1 Essential Diffraction Theory

In the theory given here it is assumed that the energies involved are such that there is no momentum transfer between the incident radiation and the atoms in the sample. In this case, the diffracted beam of radiation will have the same energy as the incident beam and waves scattered from different points in space will differ only in their phase. It is convenient to define the scattering vector $\mathbf{K}$ as the difference between the final (scattered) and initial (incident) wave vectors $\mathbf{K} = \mathbf{k}_f - \mathbf{k}_i$. The phase difference between radiation scattered at the origin, and at a point $\mathbf{r}$ from the origin, can then be shown to be equal to the dot product $\mathbf{K} \cdot \mathbf{r}$.

Thus for an incident wave with amplitude A_o, the amplitude of a wave scattered at $\mathbf{r}$ is given by

$$A(\mathbf{r}) = A_o B e^{-i\mathbf{K}\cdot\mathbf{r}} \tag{2.1}$$

The additional term B is the scattering factor, a function that includes the details of the interaction between the incident radiation and the atoms of the sample. It is the precise nature of the scattering factor which determines the relative advantages and disadvantages of the different radiations used in diffraction experiments. The implications of this for the experimenter are discussed further in Section 2.2.

The expression above is extended to describe the diffracted amplitude from bulk matter by performing a summation over all of the atoms in the solid. In the special case of an ideal crystalline material, $\mathbf{r}$ can be decomposed into the sum

of a lattice vector and a basis vector giving $\mathbf{r} = \mathbf{l} + \mathbf{b}$. Substituting this into Equation 2.1 and performing the summation over all atoms in the solid (taken to be infinite in extent) gives

$$A = A_o B \sum_{h,k,l=1}^{\infty} e^{i\mathbf{K}\cdot(h\mathbf{a}+k\mathbf{b}+l\mathbf{c})} \{ \sum_{n=1}^{N} e^{i\mathbf{K}\cdot\mathbf{b}_n} \} \tag{2.2}$$

Where the integers h,k,l multiply the basis vectors $\mathbf{a}, \mathbf{b}$ and $\mathbf{c}$ to map out every point of the infinite spacial lattice. The second summation runs over all N atoms comprising the *basis* of the crystal structure.

The first exponent in this sum is called the diffraction condition: unless this is satisfied, then the entire expression is zero and there is no scattered amplitude. It depends only on the lattice (specifically it does *not* depend on the basis of atoms) and the scattering vector $\mathbf{K}$. When the diffraction condition is satisfied, it is the second exponent, called the structure factor, which then dictates the amplitude of the diffracted wave. The Equation 2.2 is readily identified as giving the Fourier transform of the crystal structure. This leads to the interpretation of a diffraction experiment as the measurement of Fourier components that, consequently, allow the reconstruction of the crystal structure by inverse Fourier transform. Thus, at it's most elemental level, it consists of:

- The determination of which particular Fourier component a diffraction peak is associated with, and
- The measurement of the intensity of that diffraction peak.

These two experimental procedures are called, respectively, indexing and structure factor extraction.

2.1.2 The Diffraction Condition and Indexing

The diffraction condition contains two components: the crystal lattice and the scattering vector **K**. Of these two, it is the latter which is the experimental variable. Throughout an experiment, **K** will be varied such that as many diffraction peaks as possible are accessed. As a vector possesses both a direction and a magnitude, this can be achieved by variation of the wavelength of the incident radiation λ, or the angle between the incident beam and the detector. The difference between these two approaches are discussed in the following Section 2.2).

Careful inspection of the form of the diffraction condition reveals that the values for **K** for which it is satisfied, also lie on the points of a lattice. As **K** has dimensions of inverse length, this lattice is called the reciprocal lattice. Its basis vectors are simply related to the corresponding basis vectors of the direct-space lattice. They are written with an asterisk to indicate their reciprocal nature, thus a general vector will be given as $\mathbf{G} = h\mathbf{a}^* + k\mathbf{b}^* + l\mathbf{c}^*$.

Following this interpretation, the diffraction condition may be rephrased $\mathbf{K} = \mathbf{G}$ where **G** is a general reciprocal lattice vector (This concept is explained further in the caption of Figure 2.1 showing the Ewald sphere construction). Furthermore, it can be shown that the scalars h, k and l correspond to the miller indices of planes of scatterers within the solid. Indeed Bragg's well known formulation of the diffraction condition begins with a consideration of specular scattering from planes of atoms within a solid. This quickly leads to the derivation of Bragg's law $\lambda = 2dsin\theta$ where λ is the wavelength of the incident radiation, d is the separation between planes and θ is the incident angle. Although the physics behind this derivation is incorrect, it is easily shown that the resulting law is mathematically equivalent to the diffraction condition described above. Thus, it is valid (and often useful) to think in terms of scattering from distinct planes, and it is for this reason that observed diffraction intensities are referred to as *reflections.*

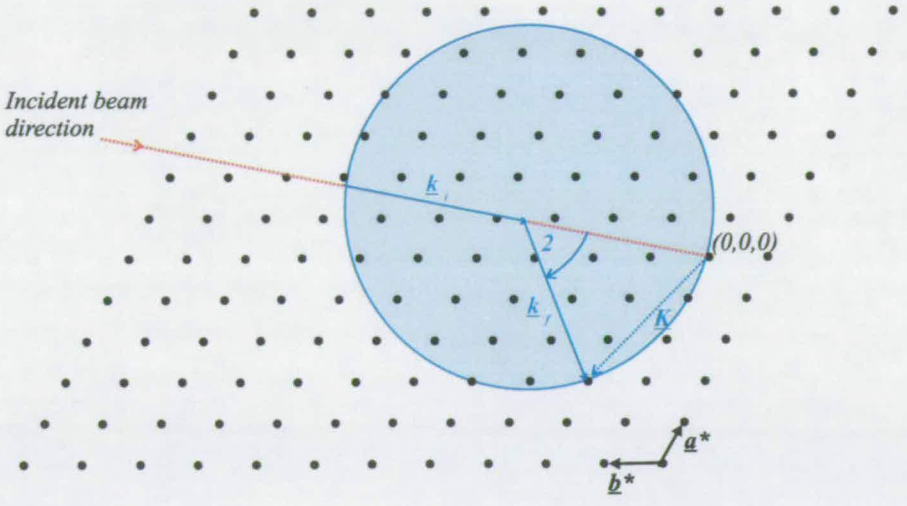

Figure 2.1. The figure shows a 2d slice through the Ewald sphere. This reciprocal-space construction reflects that, for elastic diffraction where $|k_i| = |k_f|$, the locus of all possible values of the scattering vector $\mathbf{K}$ define the surface of a sphere. From the scattering condition $\mathbf{K} = \mathbf{G}$ it follows that diffraction will occur where this sphere traverses a reciprocal-lattice point. In poly-chromatic diffraction, each wavelength will correspond to a sphere with a different radius. Therefore, if two Ewald spheres are drawn, representing the maximum and minimum wavelengths of the radiation, every lattice point contained in the volume between these two surfaces is, in principle, accessible.

The problem of indexing then requires the assignment of indices h, k and l to each of the observed reflections. Many algorithms exist to perform this task which, in the case of single-crystal diffraction, is often trivial. The task is frequently more exacting in the case of powder diffraction (see Section 2.2.2), and more sophisticated algorithms (for instance using genetic algorithm techniques [23]) are often required.

2.1.3 Structure Factor Extraction and Structure Determination

Once the diffraction pattern has been indexed, the next stage is then to measure the structure factors corresponding to each indexed reflection F^{hkl}. Here, we

immediately encounter a fundamental problem: with any detector, it is only ever possible to measure an intensity, that is to say $|F^{hkl}|^2$. The phase of the diffracted radiation is stored in the amplitude of the diffracted wave as an imaginary component of F^{hkl}. In the process of squaring this quantity, or more correctly, multiplying it by its complex conjugate, we are only left with the real component, and this information is lost. This means that in any real experiment, it is impossible simply to inverse-transform the data to recover the structure. However, if the full crystal structure is known, then the phase information can be calculated.

A full indexing of the diffraction pattern will involve the assignment of one of seven Laue classes. These classifications are then combined with 32 point groups to give 230 possible space groups. A unique space group must be assigned in order to determine fully the crystal structure. This assignment is achieved by methodically examining the observed structure factors for every accessible, indexed reflection.

The first step towards solving a crystal structure is usually to examine the data set for systematically absent reflections. The International Tables for Crystallography: Volume A [24] dictates those reflections that are forbidden for every space group. Typically, this procedure will narrow the possibilities down to a small subset of space groups. The next stage of classification is then to determine the point group. This is found by looking for different but symmetry related reflections which have equivalent intensities. Again, full listings of these are given in the International Tables. This procedure is usually sufficient to unambiguously determine the space group of the crystal structure.

Once the full symmetry of the structure is determined, the structure itself is found by refinement techniques. Here, an initial model structure is used to calculate a set of structure factors F_{calc}^{hkl} for each indexed reflection hkl. The parameters of the model are then allowed to vary until the best statistical match is found between these calculated factors (or rather their squares) and those actually observed in the experiment $|F_{obs}^{hkl}|^2$.

An important technique for establishing the 'best fit' between a given model and real data is the least-squares technique. This is appropriate where the measured data is subject experimental 'noise' that can be modeled by a simple Gaussian distribution [25]. In experiments where the data consist of counts (be they of neutrons, photons or any other quanta), this turns out to be a very good approximation [25]. Consider, initially, the measurement of a single structure factor that has the value F^{hkl} in the absence of experimental noise. As a consequence of the noise, the likelihood that a particular value F^{hkl}_{obs} is measured is given by Equation 2.3, the right hand side of which describes a Gaussian centred on F^{hkl}.

$$\text{Prob}(F^{hkl}_{obs}) \propto \exp\left[\frac{(F^{hkl} - F^{hkl}_{obs})^2}{2\sigma^2_{hkl}}\right] \tag{2.3}$$

The quantity σ_{hkl} is a measure of the severity of the experimental noise, as it determines the width of the Gaussian curve. Generally, the measurement of σ_{hkl} is an intrinsic part of the experiment, and its determination is no less important than that of F^{hkl}_{obs}.

In the real experiment, having measured F^{hkl}_{obs}, we must then infer the most likely value for the noiseless datum F^{hkl}. It follows directly from Bayes' theorem [25] that we must choose that value for F^{hkl} that maximises the likelihood of our having measured F^{hkl}_{obs} in the experiment.

In the refinement procedure we determine a set of values for F^{hkl}_{calc}, which takes the place of F^{hkl}. It follows that the refinement must proceed until the value of F^{hkl}_{calc} is found that gives the maximum value for Equation 2.3.

The probability of determining an entire data set of observed values **D**, consisting of many F^{hkl}_{obs}'s, is given by the product of the individual probabilities for each reflection, given by Equation 2.3 [25].

$$\text{Prob}(\mathbf{D}) \propto \prod_{hkl} \exp\left[\frac{(F_{calc}^{hkl} - F_{obs}^{hkl})^2}{2\sigma_{hkl}^2}\right] \tag{2.4}$$

$$= \exp\left(-\frac{\chi^2}{2}\right) \tag{2.5}$$

where

$$\chi^2 = \sum_{hkl}\left(\frac{F_{calc}^{hkl} - F_{obs}^{hkl}}{\sigma_{hkl}}\right)^2 \tag{2.6}$$

and is summed over all of the observed data *hkl*. It follows from differentiation of Equation 2.4, with respect to the set of calculated structure factors F_{calc}^{hkl}, that the maximum of the probability distribution occurs where the quantity χ^2 is a minimum. Correspondingly, the structural model that minimises χ^2 is the 'best-fit' to the measured data, because it would give the maximum likelihood of the experimenter having measured the observed data set.

The numerical value of χ^2 is one of several commonly used indices that assess the quality of a refinement. It should ideally have a value close to 1.0 as, if it is much higher than unity, then the calculated structure does not closely match the observed data. If, however, it is much lower than unity, then it suggests some problem with the estimate of uncertainties σ_{hkl}. Another common measure of the quality of a fit, used in this thesis, is the crystallographic R-factor given by Equation 2.7.

$$R = \frac{\sum_{hkl} |F_{obs}^{hkl} - F_{calc}^{hkl}|}{\sum_{hkl} F_{obs}^{hkl}} \tag{2.7}$$

The R-factor is normally multiplied by 100 and quoted as a percentage.

There is an additional caveat in assessing the quality of a refinement in crystallography, and that is that the resulting structural model must make sensible

chemical and physical sense. If, for instance, a bondlength refines as unusually short or long, it may be indicative that either structural model is incorrect, or the data are insufficient to determine the structure.

Many algorithms exist to perform structural refinements using the least squares method. In this thesis the SHELXL-97 refinements in the Crystallographic suite WinGX [26] were used for single-crystal data and GSAS [27] was used for powder refinements.

Finally, there are a few instances whereby the examination of absences and equivalences is insufficient to determine the space group precisely. In these cases refinements may be used to solve the crystal structure, as calculations using the correct space group must maximise the quality of the fit and at the same time give 'sensible' crystal structures.

Structure Factor Extraction

Before the space group assignment and structural refinement can commence, it is necessary to measure as large as possible a set of structure factors. This is undertaken in two steps: first the intensity for each Bragg peak is measured and second, this intensity is converted into a structure factor.

The intensity of a Bragg peak is typically determined by fitting some kind of idealised peakshape and then integrating. An important aspect at this stage is accurate determination of any background that may lie underneath the Bragg peak itself. This means that the experimentally-measured intensity of each Bragg peak will be subject to some uncertainty associated with the integration process δI, and some uncertainty associated with the background measurement δB. Therefore, the measured value of the intensity $I(h,k,l)$ must be quoted as

$$I(h,k,l) = I'(h,k,l) \pm (\delta I + \delta B) \tag{2.8}$$

where $I'(h,k,l)$ is its most likely value, and a measure of this likelihood is given by the sum of the terms within the brackets.

An important corollary of this is that the act of minimising the background will minimise our uncertainty in the intensity measurement. This is especially important in assessing if a reflection is absent, as it can only be said to have zero intensity within the limit of our knowledge, as determined by the experimental accuracy.

Once the intensities have been measured as accurately as possible, they must then be corrected for a variety of systematic effects arising from the physical progress of the radiation through the solid and the actual mechanics of detection. These correction terms are summarised in the Buras-Gerward equation [28] which is shown in Equation 2.9 below for polychromatic radiation

$$I(h,k,l) \propto \frac{I_o(h,k,l)L(\theta)}{\lambda^4 i_o(\lambda)\epsilon(n,\lambda)A(\lambda)E(\lambda)} \tag{2.9}$$

Throughout the work described in this thesis, no attempt is made to calculate absolute structure factors, and the constant of proportionality is taken as a universal scale factor applied to all reflections in a given run.

The various terms in Equation 2.9 (defined below) are, in general, dependent on the nature of the incident beam: specifically whether the radiation is mono-chromatic or poly-chromatic, neutron or x-ray. They also depend on the details of the diffractometer geometry and detectors used. The following functional forms are given for the case of poly-chromatic neutron radiation, both because they are the relevant forms applicable to the work of this thesis and, additionally, because the mono-chromatic x-ray case has been expounded upon at length in many publications (see for example [22], [29] or any elementary text on x-ray diffraction).

- In a polychromatic experiment, the incident flux $i_o(\lambda)$ will be a function

of wavelength. The measured intensities will be collected over a range of different energies, and, therefore, must be corrected for this variation.

- Any real detector will have some efficiency $\epsilon(n, \lambda)$ that is less than 100%. In general, this will be a function of wavelength, decreasing at higher energies where particles are less likely to interact with the detecting material. The variable n is simply a label required where more than one detector is present (e.g. in the case of a multi-element CCD array, or a pixelated scintillation counter), each of which may, in general, have different efficiencies. Typically, the relative efficiencies will vary from detector to detector in a pseudo-random manner, even if the they are made of the same material and have the same design.

- The reflectivity term λ^4 arises from the integration of the radiation over the finite divergence over which the incident beam is non-zero, i.e., the diffraction vector $\mathbf{k}$ will typically be associated with some small divergence such that $\mathbf{k} = \mathbf{k}' + \delta\mathbf{k}$. The total diffraction is integrated over the three components of the diffraction vector k_1, k_2, and k_3 giving rise to a $1/\lambda^3$ term in the monochromatic case. In the polychromatic case, the magnitude of the scattering vector $|k| = 2\pi/\lambda$ must also be integrated over, giving the additional factor of $1/\lambda$.

- The Lorentz Factor $L(\theta)$, recognizes that any data collection will take the form of a continuous scan over various values of the scattering vector. Consequently, each diffraction condition will only be satisfied for a finite time. This is best visualised in reciprocal space, where, in the case of time-of-flight diffraction, the time-varying magnitude of scattering vector is represented by a collapsing Ewald sphere moving between radii of k_{max} to k_{min} as time elapses. At very high 2θ angles the sphere collapses at a faster rate than at very low angles and therefore reflections observed at high angle will be correspondingly weakened (see Figure 2.2) as they satisfy the diffraction condition for a shorter length of time. The exact correction factor in the

time-of-flight case is $L(\theta) = \sin^2\theta$.

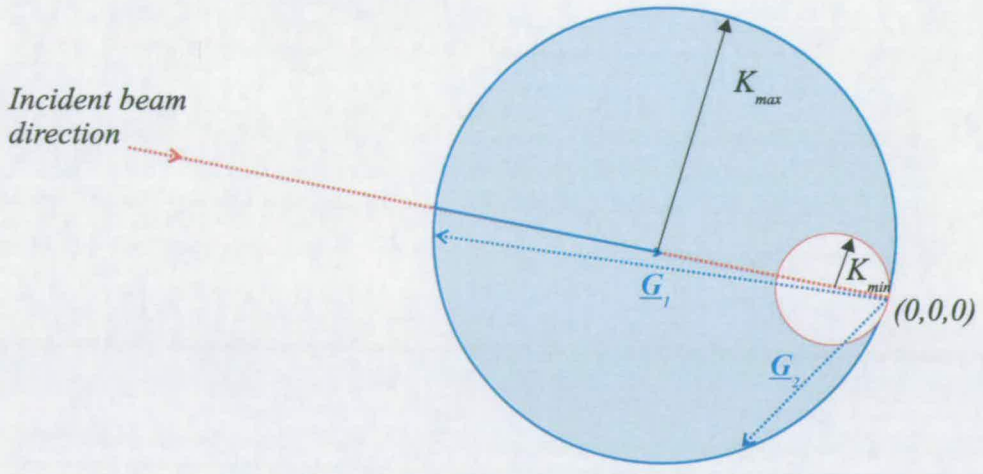

Figure 2.2. The figure shows projections of the Ewald sphere corresponding to the maximum and minimum wave-vectors. Observe that along the direction of the incident beam, a greater length of reciprocal space is traversed as the sphere collapses from k_{max} to k_{min}. Consequently, the Ewald 'front' moves the most rapidly along this direction and the scattering condition for a vector such as $\mathbf{G}_1$ (which is almost anti-parallel to the incident beam and at a correspondingly high scattering angle) is satisfied for a shorter time than that for a vector such as $\mathbf{G}_2$

- The absorption factor $A(\lambda, l)$ takes account of the weakening of the transmitted beam due to a variety of processes within the sample and any components of sample environment. It is dependent both on the nature of the radiation, the atomic constituents of the sample, and the pathlength through the sample taken by the radiation, l.

  The mathematical form of this factor is an exponential reduction of the incident intensity, I_o given by

$$I = I_o e^{-\mu(\lambda)l} \tag{2.10}$$

  The severity of the absorption effect depends on the absorption coefficient $\mu(\lambda)$ which has dimensions of inverse length and has been experimentally measured for many atomic elements and isotopes. In neutron diffraction,

the absorption coefficient has two components: real absorption μ_{real}, and absorption due to incoherent scattering events μ_{inc}.

Over the range of energies used in inelastic diffraction work, nuclear resonances are generally unimportant and μ_{real} has a simple linear form. This linear dependence has a negative slope with energy as material becomes increasingly transparent, until finally becomes zero at infinite energies. Therefore, $\mu(\lambda)$ can be taken to have the form of a straight line passing through the origin. Meanwhile incoherent scattering of the incident beam is independent of wavelength and, the corresponding coefficient μ_{inc}, is a constant. Consequently, the total absorption coefficient will have the form $\mu_{tot} = \mu_{real} + \mu_{inc} = A\lambda + B$.

- The extinction term $E(\lambda)$ describes the reduction of the transmitted beam as a result of coherent Bragg scattering. This effect is often divided into two different types both of which are illustrated in Figure 2.3. The first case, that occurs within highly perfect crystals, is called *Primary* extinction. Here, when the scattering condition is satisfied, the incident beam will be strongly scattered by the crystal, thus, weakening the transmitted beam. However, most real crystals are not perfect, and instead can be modeled as being composed of many mosaic blocks, the volume of which is much smaller than the total volume of the crystal. Within a block the crystal will be highly perfect, but the orientation of each given block relative to another will be randomly distributed about some mean value. In this case, the incident beam scattered from a given mosaic block will have to travel deep into the crystal (traversing many other mosaic blocks) until another block of identical orientation is encountered. In this case, the resulting attenuation of the beam is called *secondary* extinction. In either instance, the effect of extinction is a reduction of intensity of those Bragg reflections that scatter the most strongly. The most commonly employed model of the extinction effect is that of Zachariasen [29] which is proportional to the

structure factor squared. Extinction is a complex problem, that has been the subject of much theoretical endeavour for over fifty years [29],[30],[31]. However, during the work of this thesis, the author encountered difficulty in the application of its correction. This is discussed further in detail in Chapter 5.3.

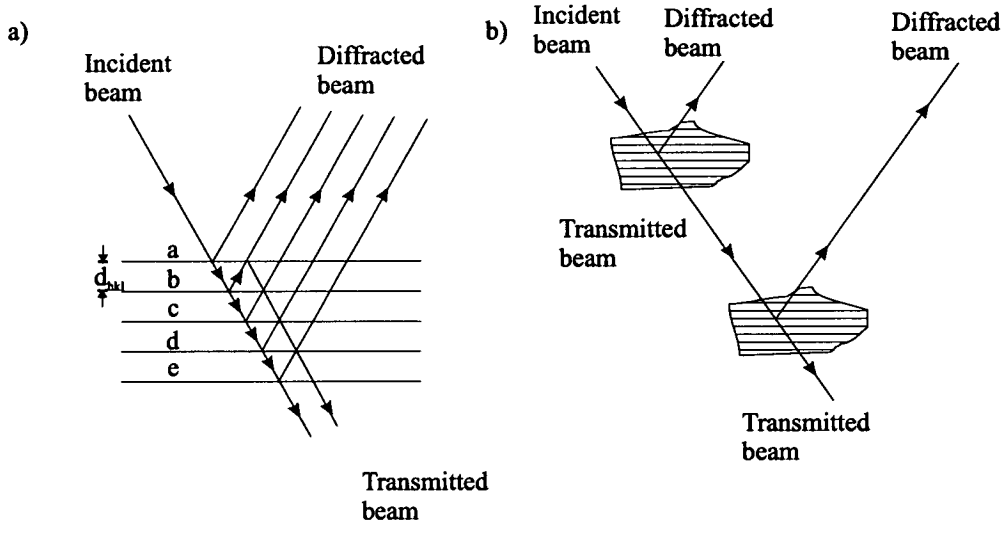

Figure 2.3. The figure on the left (a) illustrates the case of primary extinction for a highly perfect crystal. It shows the diffraction of the incident beam from successive Bragg planes. At each plane of atoms, part of the beam is reflected and part is transmitted. Now, consider the geometry of the beam reflected from plane 'b': it is also in the diffraction condition and can be reflected back off plane 'a' such that it continues in the same direction as the original incident beam. Each successive reflection introduces a phase change of $\pi/2$, therefore, radiation that has been scattered twice (or any even number of times) will interfere destructively with the transmitted beam reducing the intensity of both the transmitted and diffracted beams. On the right, Figure (b) illustrates the case of secondary extinction, where the crystal is only ideal within small 'mosaic blocks'. These regions are separated by distances much larger than their size so radiation successively scattered from the two blocks in the figure will no longer add coherently as was the case for primary extinction. The result is a reduction in the transmitted beam purely as a result of the loss of intensity due to Bragg diffractions from successive mosaic blocks.

2.2 Different Types of Diffraction Experiment

The diffraction experiments used to determine structural information can be broadly classified according to the basic technique used. In the first instance, an important distinction is the physical nature of the radiation used, as this has important consequences for the kind of measurements that can be made. High-pressure diffraction work is exclusively performed with x-ray and neutron radiations and these are juxtaposed in the following Section 2.2.1.

A second important experimental consideration is whether the incident beam of radiation used is poly-chromatic or mono-chromatic. In the first case, the radiation is composed a smooth spectrum of energies between some maximum and minimum value. Experiments of this kind are called energy-dispersive, as it is the *magnitude* of the scattering vector that is varied in order to explore reciprocal space. In the second case, a single wavelength (with some experimental divergence) is pre-selected and, therefore, the magnitude of the scattering vector is fixed. In this instance, reciprocal space is explored by varying the *angle* of the scattering vector and consequently, experiments of this type are called angle-dispersive.

Finally an important experimental realisation of angle-dispersive scattering is obtained by the use of powdered samples. Here, the angle of the incident beam is kept constant and a poly-crystalline sample is used. In an ideal sample, these crystallites are of identical size and perfectly randomised, such that all possible orientations are equally well represented. Therefore, for any given set of lattice planes, there will be an equally-sized subset of crystallites at the correct angle to satisfy the diffraction condition. Since the 70s, powder experiments have tended to dominate high-pressure diffraction. This technique is discussed in detail in Section 2.2.2 and Chapter 3 reviews the use of this technique in a high-pressure neutron-diffraction study. However, powder techniques have intrinsic limitations which are also discussed in detail in this section and the following chapter, as

they provided the motivation for much of the subsequent work of this thesis.

2.2.1 Different Radiations

There are three kinds of radiation used in the determination of atomic structure: x-ray radiation, neutron radiation and electron radiation. The last of these, used in electron diffraction, is only capable of distinguishing structure on the surface of solids (typically electrons cannot penetrate more than 100 Å below the surface) and, as such, is not relevant to the work of this thesis and is not discussed further. Of the other two, by far the more widely used is x-ray radiation. It benefits from a number of extremely powerful synchrotron sources based around the world. Neutron diffraction is used to a much lesser extent, partly because of the significantly higher cost, and partly because the sources are many orders of magnitude weaker than modern synchrotrons. There is also an issue of accessibility, with only a handful of intense neutron sources available around the world.

X-ray and neutron radiations are, of course, very different physical entities. Consequently, the physics describing their interaction with the atomic constituents of a solid is entirely different. These different characteristics lend themselves to different kinds of experiment and each radiation has relative advantages and disadvantages to consider when planning a measurement. The consequences, for diffraction experiments, are discussed in detail below.

The Interaction of X-rays With Matter

X-rays are a form of electromagnetic radiation and interact with matter via the extended electron cloud surrounding individual atoms. The negatively-charged electron cloud is forced into oscillation by the EM field and in-turn becomes the source of the secondary, scattered radiation. This has important consequences:

1. The strength of the scattered wave is proportional to the total amount of negative charge surrounding an atom. Consequently, it is extremely difficult to observe diffraction from the lighter elements and, in particular, hydrogen is almost impossible to detect with x-rays. An additional difficulty is a lack of contrast between atoms of similar atomic weights. For example, gold and lead are essentially indistinguishable to x-ray diffraction techniques.

2. The electron cloud is an extended object in space as opposed to a point. This introduces an additional component to the scattering factor, called the form factor that is a function of $\frac{\sin\theta}{\lambda}$, tending to reduce the scatter at large angles (corresponding to small d-spacings). This effect introduces a lack of resolution in the determination of structure that hinders the measurement of subtle effects such as atomic thermal-motion and multi-site disorder. An example of the functional form of the form-factor is shown in Figure 2.4.

3. Absorption effects are rather high for x-rays as their interaction with matter is relatively strong as a consequence of the long range of the electromagnetic force.

The Interaction of Neutrons With Matter

Unlike x-rays, neutrons are massive particles possessing no charge. Their interaction with other atoms is inter-nuclear via the strong nuclear force and this leads to several important characteristics of neutron-diffraction experiments.

1. The interaction that scatters neutrons from the nucleus has a rather complex dependence on the atomic number which is illustrated in Figure 2.5. In particular it should be noted that hydrogen, and other low Z atoms, have a comparatively large scattering strength in comparison with other heavier elements.

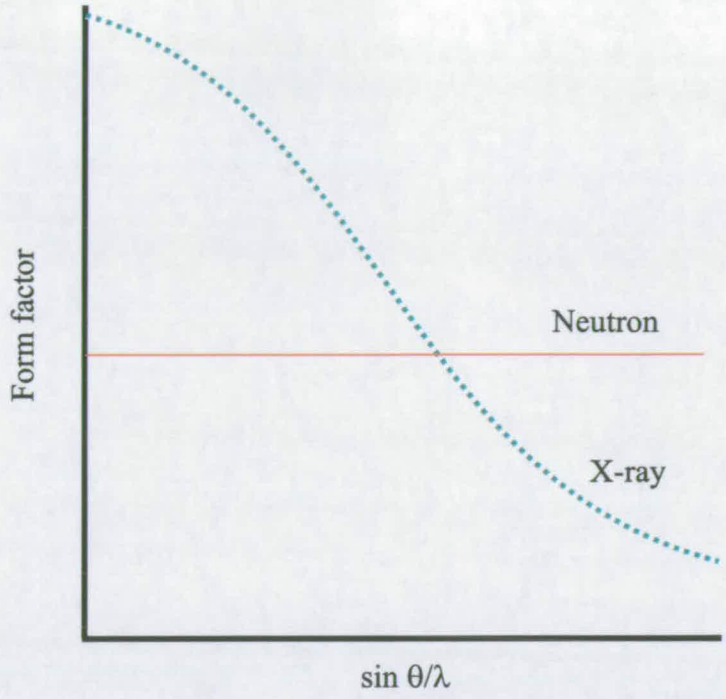

Figure 2.4. The intensity of scattered x-ray radiation is modulated by the form factor shown above. At shorter wavelengths, or larger angles, the extended electron cloud surrounding the atom appears less and less as an infinitesimal point. The effect on the scattering is a reduction in intensity from low d-spacing reflections. Conversely, the neutron-nucleus interaction is truly pointlike and, therefore, the form factor is a constant term

Unlike in x-ray diffraction, there can also be a strong isotope effect on the scattering power of the nuclei. A major contribution to this contrast between isotopes is the effect of the nuclear spin of both the incident neutrons, and the nuclei of the sample. In general, the spins of both sample and beam are completely randomised (this might not be true for extremely low sample temperatures or when working with a spin-polarised neutron beam). The distribution of spins gives rise to a range of scattering lengths for the individual nuclei, when these are averaged over the entire scattering volume of the sample they separate into two components: giving rise to both a coherent and incoherent scattering length. It is the coherent scattering that gives rise to the Bragg peaks that are measured in a diffraction experiment. Meanwhile, incoherent scattering is mostly independent of the scattering

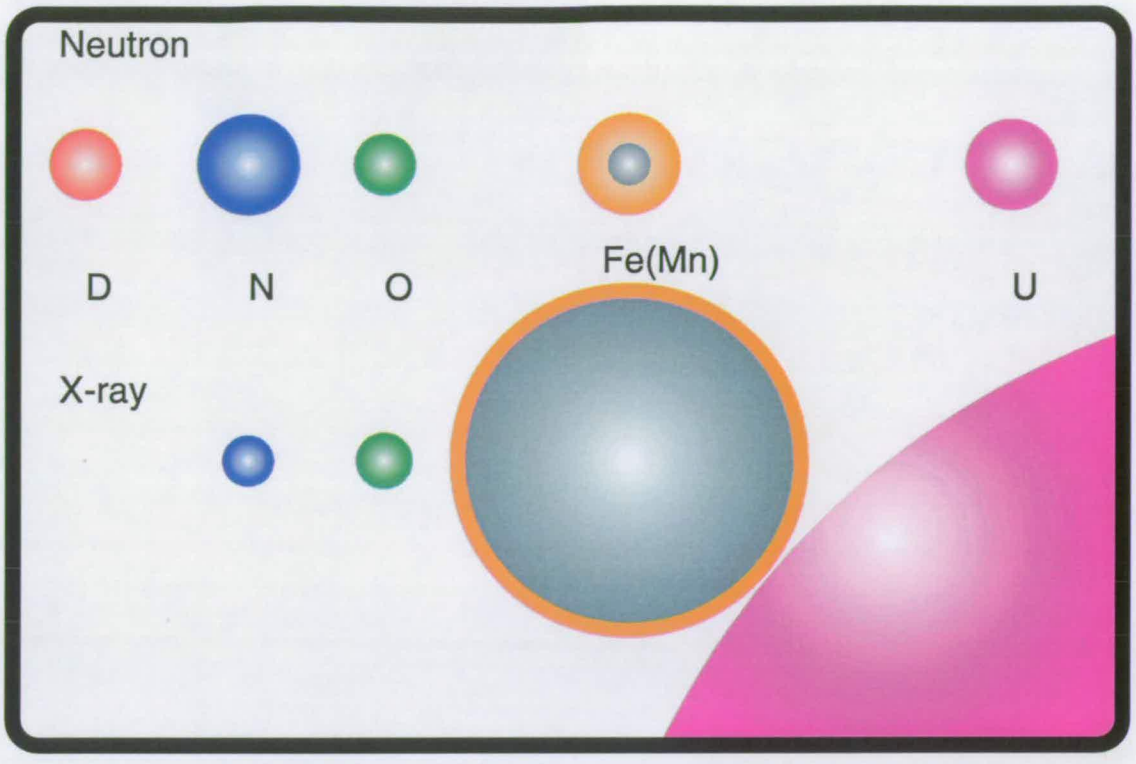

Figure 2.5. An illustration of the varying cross-sections for neutron (top) and x-ray (bottom) diffraction. In particular, notice that on this scale the deuterium D x-ray cross-section isn't visible (see the main text for a discussion of why the heavy, rather than the naturally occurring, isotope is displayed). Also highlighted is the resolution between, for instance, atoms of iron and magnesium, which are indistinguishable to x-rays.

vector $\mathbf{K}$ and gives rise to a smooth wavelength-independent background. The variation between coherent and incoherent scattering lengths between two isotopes can be dramatic.

A particular example of this, which is important for most of the work in this thesis, is the element hydrogen, the respective incoherent and coherent cross-sections are given in Table 2.1 for 2200 ms^{-1} (room temperature) neutrons [32]. It can be seen that the stable isotope has an extremely large incoherent-scattering cross-section: almost 46 times its coherent cross-section. In contrast, the second isotope, deuterium, has a low incoherent

Isotope	Coherent xs (*barns*)	Incoherent xs (*barns*)
^{1}H (hydrogen)	1.758	80.27
^{2}H (deuterium)	5.592	2.05
^{3}H (tritium)	2.890	0.14

Table 2.1. The coherent and incoherent scattering cross-sections (xs) of the three isotopes of hydrogen (for room temperature 2200 ms^{-1} neutrons) [32]. Note the high incoherent cross-section of the stable hydrogen isotope.

scattering cross-section. The consequence of this, for diffraction experiments, is that in almost all cases deuterated samples must be used. This is the case for the powder studies of the high-pressure ice phases in the following chapter, and in the clathrate studies described in Chapter 6. Some of the consequences of using a hydrogenous sample were encountered in the diffractions studies of potassium di-hydrogen phosphate described in Chapter 5.

2. As a consequence of the point-like interaction between the neutron and the atomic nucleus there is no form-factor contribution to the scattering factor. This means that, in principle, a far higher resolution can be obtained from neutron measurements making them ideal to study effects such as thermal motion and multi-site disorder. As both of these effects are extremely subtle (for example, the disorder of the oxygen atom in ice VII, that is discussed in the following Chapter is of the order of ~ 0.15 Å in size.), they require the measurement of the high frequency Fourier components that correspond to the low d-spacing reflections.

3. The neutrality of the neutron is both an advantage and a disadvantage in experiments. The lack of an electro-static interaction makes it difficult both to extract and accelerate neutrons. This is a fundamental reason for the intrinsic weakness of available neutron sources. However, the lack of interaction also results in an ability to penetrate very deeply into matter,

an attribute that comes in extremely useful when the use of bulky sample environment equipment (e.g. pressure cells or cryostats) is required.

4. There are many other advantages, such as contrast-matched scattering and magnetic scattering, that arise from the physical nature of the neutron. However these are not directly relevant, and have been discussed in detail elsewhere[1].

Experimental Sources

In addition to the different physical distinctions listed above, the choice of radiation is perhaps most strongly affected by the available experimental sources. The most striking difference between neutron sources and x-ray sources is in their relative fluxes. At the current time, the most powerful sources of x-ray radiation are synchrotrons, which can deliver up to 10^5 times the flux of the most powerful sources of neutron radiation (reactors or spallation sources). It is the weakness of the sources that is the major drawback of neutron diffraction. Especially for high-pressure work, the correspondingly large sample volumes that are required, severely limit the maximum accessible pressure.

A further advantage of x-ray sources is that small tube-sources are available allowing many experiments to be performed 'in-house'. Conversely, neutrons in sufficient quantities for diffraction work are only available from large scale facilities. Consequently, neutron work is extremely expensive.

2.2.2 Powder Diffraction

One particular and widely used experimental application of the angular-dispersive diffraction technique is powder diffraction. This is a technique whereby the sample is composed of many small crystallites, ideally of uniform size, and with an

[1] see for example the books of Squire [33] or Ardnt and Willis [34]

entirely random distribution of orientations. If this is the case, then for incident radiation of a given wavelength, some sub-set of crystallites will always satisfy the diffraction condition. For a given set of lattice planes (corresponding to a definite point on the reciprocal lattice) and a given incident wave-vector, k_i, the scattering angle 2θ is fixed, that is to say $\mathbf{k_i} \cdot \mathbf{k_f} = const.$ This gives rise to a set of concentric cones of diffracted radiation maintaining cylindrical symmetry about the incident beam. When these cones are incident on an area detector, say a phosphor based image plate or a CCD detector, they give rise to a pattern of concentric circles called Debye-Scherrer rings. A schematic of a typical experimental set-up is illustrated in Figure 2.6 for a monochromatic incident beam.

It is also possible to perform powder diffraction with polychromatic radiation. In this instance, an energy-resolved detector at any fixed position in space will see an entire powder-diffraction pattern as a function of energy. Although, of course, the wavelength at which peaks are observed will vary with angle according to Bragg's law. A specific example of the energy dispersive technique is the time-of-flight (TOF) method used in neutron diffraction. This technique, which is described in detail in Chapter 4, utilises the fact that the velocity v of a (non-relativistic) neutron is related to is energy E by the equation

$$E = \frac{m_n v^2}{2} \tag{2.11}$$

Consequently, if a pulse of poly-chromatic neutrons is produced at time T_o, the time T required for them to travel a given distance L is then given by $T = \sqrt{m_n L^2/2E}$. If a timer is set to begin at T_o, the arrival time of a neutron at a detector can be used to give a direct measure of its energy. This technique is used exclusively in the neutron work of this thesis and is discussed in an appropriate level of detail in Chapter 4. An example of the resulting TOF powder pattern is given in Figure 2.7

In the ideal powder experiment, reflections from individual crystallites should be

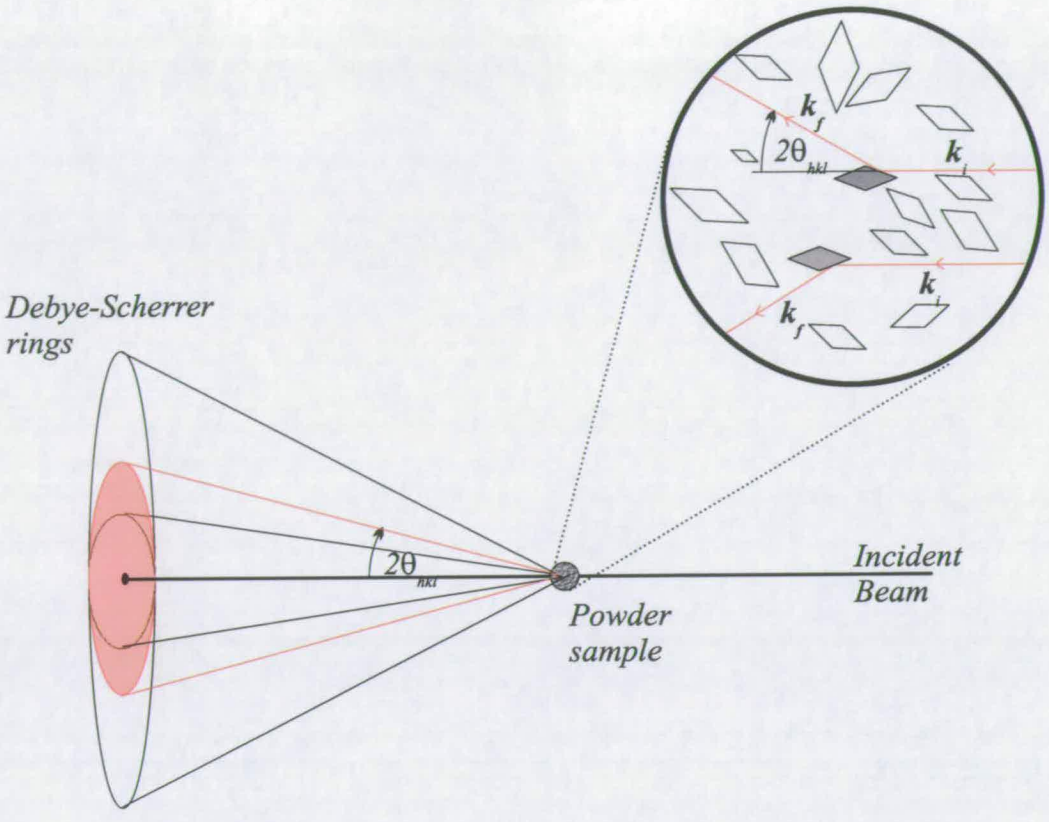

Figure 2.6. The Figure shows a schematic of a powder experiment using mono-chromatic radiation. By intercepting the diffracted cones of radiation with a plane (typically some form of detector), concentric rings are obtained with a radius directly related to the scattering angle 2θ and the distance between the sample and the plane. The insert shows how only a sub-set of crystallites with a given orientation (symmetric about the incident beam direction) satisfy the diffraction condition for a given set of lattice planes

unresolved. The pattern becomes statistical in nature, the 3d-diffraction pattern collapsed onto a single dimension (that of the angle 2θ for mono-chromatic experiments or that of some function of energy in the polychromatic case).

An inherent feature of the powder-diffraction pattern is that peaks that would be separate in space in the full three-dimensional pattern might now overlap. In any real experiment, a given Bragg peak will have some inherent width. If the mono-chromatic case is considered, this will arise from

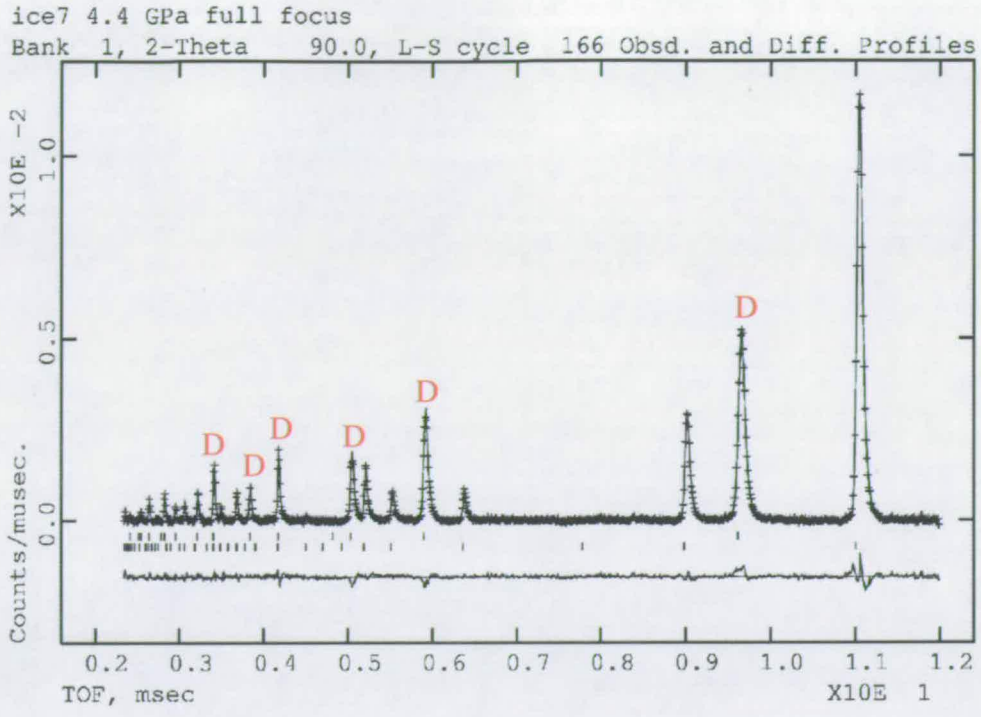

Figure 2.7. A refined fit to an ice VII powder pattern collected on the PEARL diffractometer at ISIS and displayed as a function of time-of-flight. Also present is a second diffraction pattern from the diamond anvils of the pressure cell, the strongest peaks of this phase are marked with a red 'D'. The tick marks below the peaks indicate the calculated positions of peaks indexed on the unit cell of each phase (the upper row corresponds to diamond, and the lower row to ice VII). Notice the rapidly increasing density of reflections at lower d-spacing and the corresponding overlapping of adjacent peaks.

- The divergence of the incident beam such that the actual incident wave-vector $\mathbf{k}_i$ will have some variation about its central value $\mathbf{k}_i'$. Typically, a monochromated beam will have some finite distribution of energy about the nominal value λ', such that $\lambda = \lambda' \pm \delta\lambda$. Additionally, the finite size of the source will result in some angular divergence.

- There may be divergence due to the sample itself. This can arise from deviation away from perfect crystallinity. An important aspect of this in high-pressure diffraction work is pressure induced strain broadening. This

effect becomes more pronounced at higher pressures, and presents significant difficulties in powder diffraction [35].

At low d-spacings, the density of diffraction peaks increases dramatically. This can be easily seen by considering the density of reciprocal-lattice points, between radius r and δr from the origin, as r increases. This fact, combined with the non-zero width of the Bragg peaks means that at low enough d-spacings powder peaks will begin more and more to overlap (this effect is evident in the powder pattern shown in Figure 2.7). This problem can be addressed to a certain extent by improving the resolution of the instrument. However, this does not help when peak width is dominated by sample effects and in the case when reflections that need not be symmetry related share the same d-spacing.

This means that whilst indexing a crystal structure given single-crystal data is often trivial, it can become exceedingly difficult when only a powder pattern is available. Additionally, the determination of the correct intensity for a given Bragg peak, when it is overlapped with several other peaks, can be problematic. For these reasons, it is usually the case that the crystal structure will be known prior to the powder-diffraction experiment being performed, and the data only used to refine the structural parameters as, say, a function of temperature or pressure.

Despite these seemingly serious disadvantages, modern powder-diffraction has become an extremely powerful tool, generally as a result of advances in computer technology. The most important of these advances was the development of the Rietveld refinement technique in 1967 [36], which is now almost ubiquitous in the analysis of powder data. The line through the data points in Figure 2.7 is actually a Rietveld fit (generated using the GSAS refinement software [27]).

In order to apply the Rietveld method, the observed powder pattern is digitised by sampling at a large number of points along the diffraction parameter, x (x = 2θ, time-of-flight, energy etc.). A powder-diffraction pattern is then calculated

using the available structural and experimental parameters, and a least squares technique applied to refine the best fitting structure (see Section 2.1.3). In this case, χ^2 is summed across the each bin i of the entire digitised profile [37]

$$\chi^2 = \sum_{i=1}^{N} \frac{(y_{ci} - y_i)^2}{y_i} \tag{2.12}$$

Here y_i is the observed intensity at i, y_{ci} is the calculated intensity and N is the total number of sampled points. This is a characteristic feature of Rietveld analysis - that every element of the observed powder pattern is fitted simultaneously without any prior attempt to extract individual peak intensities. It thereby intrinsically acknowledges the reduced information content of the powder pattern. It should also be noted that the measure of uncertainty σ^2_{hkl} has been replaced by the intensity y_i. This reflects the statistics of counting experiments, where the uncertainty associated with a measurement of N_i counts in bin i is proportional to $\sqrt{N_i}$ [25].

An important aspect of the definition of χ^2 given in Equation 2.12 is that the background, in addition to the Bragg intensities, is also being fitted. Correspondingly, especially in high-pressure diffraction where the backgrounds are generally high as a consequence of presence of the pressure cell, it must be treated carefully as an index for the quality of the fit. Consider the limiting case where the diffraction signal is extremely weak, a χ^2 that is approximately equal to one could be obtained by *only* fitting the background and ignoring the sample signal.

As has been mentioned previously, high-pressure diffraction has tended to have been dominated by powder experiments. This is often for the important reason that single-crystal samples have not been available either because a destructive phase transition is encountered, or simply because the experimental techniques do not exist to compress single-crystal samples to the required pressures. Powder experiments have been extremely successful. However, as experiments become more ambitious the *intrinsic* limitations of powder diffraction, as described above,

have become more apparent.

2.3 Conclusions

The purpose of this chapter has been to provide an introduction to the underlying principles of diffraction theory. This has been attempted in order to familiarise the reader with the main issues affecting the experimenters choices whilst planning a diffraction experiment. In addition, this background will clarify many of the challenges encountered in the work described in the following chapters.

Certain problems that have been introduced here will be explored in more detail in the specific manifestations in which they appear in the following description of development work in Chapter 4. In particular the correction of data for absorption and extinction effects will be seen to be non-trivial. Often these problems are best avoided by improvements in the experimental methodology employed and, where relevant, these changes will be reported in detail.

An introduction has been given to the different kinds of diffraction experiment available to the crystallographer. Specifically, the discussion has focused on the implications of the *choice* of radiation for a given type of structural measurement. This background emphasises the need to use neutron diffraction for the studies comprising this thesis.

Finally, the method of powder diffraction has been expounded at some length. Many of the limitations of the method, that were highlighted in this section, will be encountered directly in the following chapter.

Chapter 3

Exploring the Limits of Powder Diffraction: High-Pressure Ice

One of the first projects in which the author became involved as part of this thesis work was a powder diffraction study of the high-pressure phases VII and VIII of ice - using neutron radiation. In particular, it was hoped that these measurements might elucidate the nature of the disorder of the oxygen atom in ice VII. Several different models exist for this effect, and its accurate characterisation could have important consequences for our understanding of hydrogen bonding.

These experiments used the Paris-Edinburgh (PE) cell to compress samples of water ice up to pressures approaching 25 GPa. The experiments were performed on the PEARL HiPr instrument at the ISIS pulsed neutron source in Oxfordshire (the instrument is described in detail in the following chapter as is the time-of-flight technique used to collect the data[1]).

All of the neutron data used in this study were collected in the transverse mode of the instrument (see the following chapter). In this geometry, the incident beam

[1] A full description of the time-of-flight technique and the HiPr diffractometer is postponed until the following chapter 4. It is hoped that this clarifies the description of developments of the diffractometer which are given there.

travels through the front anvil of the cell to reach the sample. Whilst the resulting anvil scatter can be removed from the pattern by careful shielding, this would also remove a significant amount of the signal from the sample. Consequently, in order to maintain the signal level for very-high pressure experiments, the experimenter is forced to live with a certain amount of anvil scatter in the data. The diffraction study of ices VII and VIII was concerned specifically with determination of the atomic displacement parameters (ADP) of the oxygen atom. As such, a central goal was to probe possible limits on the accuracy of these measurements with these contaminated data. The effects of attenuation arising from the cell were also expected to correlate strongly with atomic thermal-motion, as both are described by exponential terms, and the significance of this effect was also investigated.

Despite these complications, the PE cell is the only device capable of taking powdered samples of sufficient volume for accurate study by neutron diffraction to the high pressures required. Additionally, these data still represent a 'best case scenario' for neutron work at these pressures for the following two reasons:

- ISIS is a highly intense source of neutrons (it is currently the most powerful pulsed source in the world) and deuterated ice[2] is a very strongly scattering sample. Additionally, the sintered diamond anvils used in these particular experiments have the highest level of transparency of all the available anvil materials. Therefore, the signal-to-noise ratio was one of the best obtained on PEARL for samples at such high pressure.

- The high pressure structures of ice have a high symmetry (cubic in the case of ice VII and tetragonal in the case of ice VIII). The diamond structure of the anvils also has an extremely simple (cubic) structure. The relatively small number of Bragg peaks should minimise the problems of overlapped

[2]In all the neutron studies described here, deuterated samples are used to avoid the large incoherent scattering from the naturally occurring isotope. This effect was discussed in detail in Section 2.2.1

peaks at lower d-spacings, and additionally reduce effects rising from contamination of the data by anvil scatter.

As such, these experimental studies presented an ideal opportunity to explore the limits on the quality of neutron powder-diffraction data at high pressure.

In this chapter the scientific background is given for this neutron study of the high-pressure ices, with reference to previous structural work. The significance of thermal motion measurements, as a measurement of atomic disorder, is explained. The data measured on PEARL are presented, as is an in-depth analysis of the various corrections that it is necessary to apply in order to extract accurate thermal parameters. This study revealed several factors as having a measurable effect on resulting ADPs, which had not previously been considered. This presented several changes in procedure that should be implemented in subsequent studies using the PE cell for high-pressure, neutron powder-diffraction.

However, ultimately, it was realised that a study of the detailed nature of atomic disorder of this type was probably beyond the resolution of powder data. That this was so, even for 'best case' data and with the most careful analysis, highlighted that a fundamental limit of powder diffraction had been encountered. Consequently, the study described here was one of the motivating factors for the work described in subsequent chapters in developing single-crystal techniques.

3.1 The High-Pressure Structure of Ice

The hydrogen-bonds that bind water molecules in the solid phase are highly versatile. This is evidenced by the complex phase-behaviour observed in ice: 12 distinct phases are known to exist. A glance at the phase diagram [14] (shown in Figure 3.1) reveals that much of this complexity occurs at relatively low pressures. Thus, above $\sim$ 1.9 GPa only the two phases, ices VII and VIII (the structures of which are related by an ordering transition on cooling) are observed. At higher

pressures still, the VII→VIII transition temperature drops until it reaches 0K at around 60 GPa. Above this pressure, the dominant phase VII transforms into phase X, in which the hydrogen bond becomes centred, and the molecular character of the solid is lost.

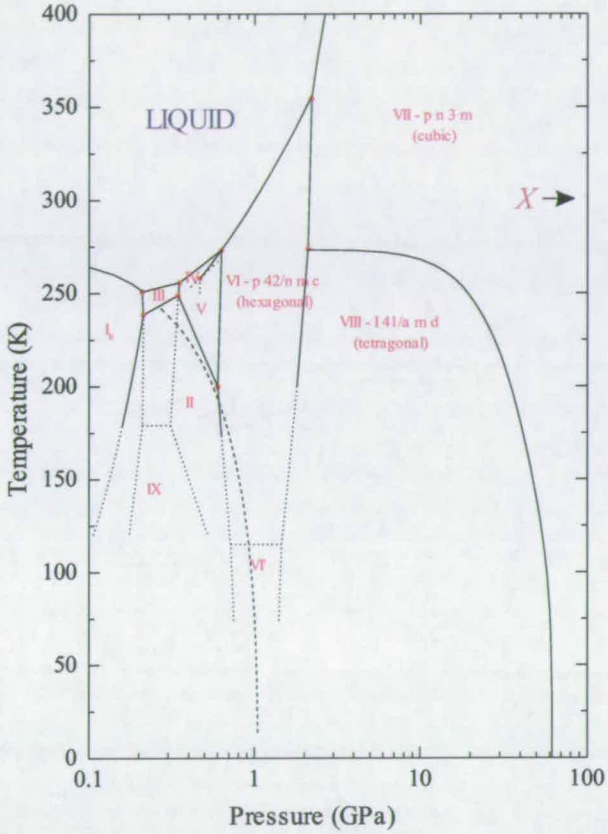

Figure 3.1. The phase diagram of H_2O ice up to 100 GPa [14] (The corresponding diagram for D_2O has a very similar general form, although actual transition pressures can deviate significantly). The onset of ice X has been reported over a range of values, here it is indicated at 60 GPa in H_2O as found by Goncharov [38] using infrared spectroscopy.

From a fundamental perspective, the structure of a 'centred-ice' has held great interest for condensed matter physicists and chemists for three decades now. Holzapfel predicted in 1972 that the application of extreme pressures would cause the hydrogen potential to symmetrise with a single minimum at the mid-point of the oxygen atoms [39]. A full characterisation of this phase would have important

consequences for the study of the hydrogen bond, and more generally would shed light on the quantum chemistry of the hydrogen atom. As such, a knowledge of its structure holds great significance in many spheres of science.

Whilst the structure of ice X has been investigated indirectly by dynamic measurements (infrared spectroscopy [40][41][38] and Raman spectroscopy [42]) and directly by x-ray diffraction [18], the only way to characterise *fully* the structure of ice X would be to perform a neutron diffraction experiment which is sensitive to the hydrogen positions. Unfortunately, the pressures involved (> 60 GPa) are far higher than those currently accessible to neutron techniques. However, phase VII is well within accessible limits, and a full characterisation of its structure provides an insight into the VII $\rightarrow$ X transition.

3.1.1 Previous Structural Work

The structures of ices VII (cubic - $\mathbf{Pn\bar{3}m}$) and VIII (tetragonal - $\mathbf{I4_1/amd}$) were first studied under their conditions of stability by Kuhs *et al.* in 1984 [43], who used powder neutron-diffraction. Both structures consist of two interpenetrating diamond-like oxygen sub-lattices. However, the protons in the VII structure are disordered, occupying 50% of four tetrahedrally arranged sites about the oxygen atom. Upon cooling into ice VIII, the protons order with the resulting tetragonal distortion of the unit cell. The molecular arrangement adopted in ice VIII gives rise to anti-ferroelectric order. Diagrams of the two structures are shown in Figure 3.2.

Kuhs *et al.* [43] reported a bondlength in ice VII (at 2.4 GPa) that was much smaller than expected: $\sim$ 0.89 Å compared to the distance they refined in ice VIII (at 2.4 GPa) of $\sim$ 0.968 (7) Å and a normal (gas phase) O-D distance of 0.98 Å [44]. The authors were unable to account for such a large discrepancy as a result of strong librations of the deuterons, and therefore proposed that the oxygen atoms must also be disordered.

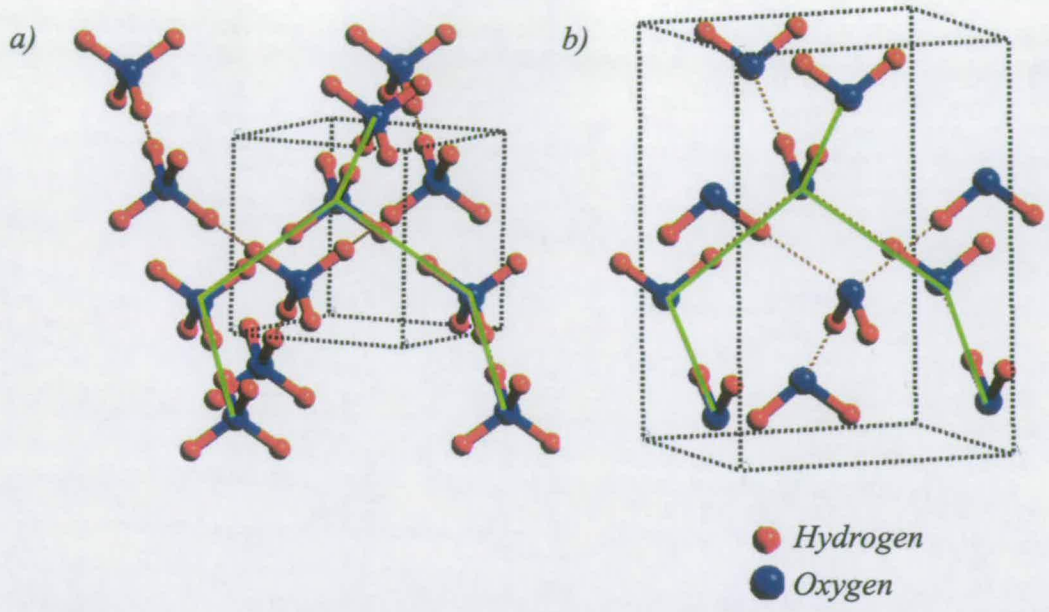

Figure 3.2. The structures of a) ice VII b) ice VIII. The respective unit cells are marked as dotted lines. Both structures are composed of two diamond-like sub-lattices, one of which is indicated by a green outline. Upon cooling from VII to VIII, the molecules on this sub-lattice order such their vertices are all pointing down. On the second sub-lattice, the molecules order in the opposite direction, resulting in the anti-ferroelectric order of the ice VIII phase.

Neutron diffraction measurements survey the bulk of a sample and also the scattering of neutrons occurs on a timescale far in excess of any molecular or atomic motion. For this reason, they give an image of the crystal structure that is averaged both temporally and spatially. Figure 3.3 illustrates one of the disorder models proposed by Kuhs *et al.* in green. In this model the oxygen atom is disordered over six sites displaced along the $\langle 100 \rangle$ directions of the unit cell. The resulting diffraction 5picture is of a single averaged site marked in red on the figure. The figure also demonstrates how the resulting *averaged* bondlength can be much shorter than the real bondlength.

The data obtained by Kuhs *et al.* had insufficient resolution to allow free refinement of the oxygen atoms probability distribution. However, by using a model that constrained the oxygen atoms to lie on position $2a$ of the space group $\mathbf{Pn\bar{3}m}$

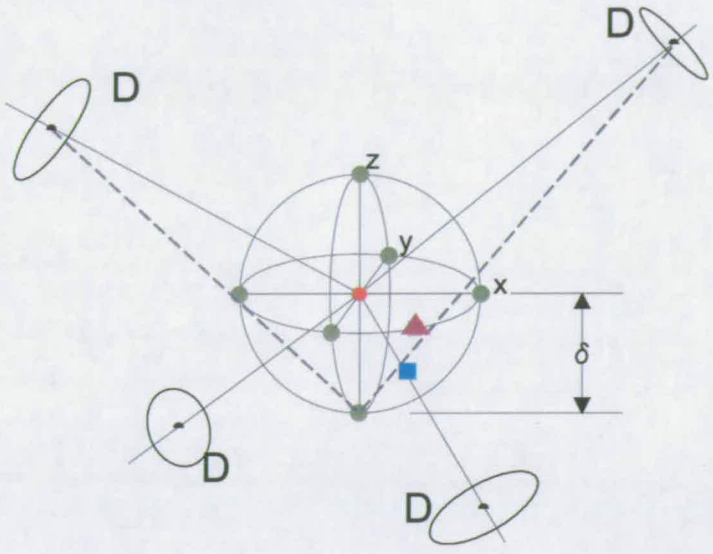

Figure 3.3. A schematic of the water molecule in ice VII demonstrating how disorder of the oxygen atom can explain a short apparent O-D bondlength [45] (note the labels x,y and z mark the directions of the unit cell axes **a**,**b** and **c** respectively). If the oxygen atom was disordered about the six-fold sites marked as green circles, a diffraction measurement would locate its *average position* at the centre of the distribution (marked as a red circle). Thus, the dotted lines indicate the real O-D bondlength whilst the solid line indicates the shorter, average bondlength that is actually measured. Also marked by a purple triangle, and a blue square are two other possible locations for a disordered oxygen atom proposed by Nelmes *et al.* [45] (They correspond to the ⟨110⟩ and ⟨111⟩ models respectively - see main text). The scale of the disorder effect is measured by the parameter δ equal to the radius of the sphere drawn through the disordered sites.

they were able to refine an anisotropic thermal parameter with gave clearly visible density bulges along the ⟨100⟩ unit cell directions. Subsequently, they applied a structural model where the water geometry was restricted to those values obtained for ice VIII at the same pressure (O-D = 0.968 Å and D-O-D = 105.6° [43]). The oxygen density was then modeled as a smooth distribution about the high-symmetry, average sites (corresponding to the central red circle in Figure 3.3) with a freely refined radius. This model refined to give a radius, δ of 0.0963 (55) Å for the oxygen sphere (this is also marked on the figure).

A short time after this, Jorgensen and Worlton [46] performed a time-of-flight

neutron diffraction experiment on ice VII. They also reported an O-D distance of 0.943(2) Å that is too short, although not quite as small as that of Kuhs *et al.* They could not improve the quality of their fit by applying Kuhs ⟨100⟩ disorder model. They also reported evidence of site disordering of the D atom, but this gave D-O-D angles of 98.2°, 100.7° and 114.0° that differ markedly from the gas phase value of 104.5°. Kuhs *et al.* had commented on disorder of the hydrogen atom, but were unable to distinguish it from anharmonic thermal motion.

The most recently published study on the disorder of the oxygen atom in ice VII was by the Edinburgh group of Nelmes *et al.* in 1998 [45]. The structure was studied up to much higher pressures (20 GPa) with the aim of clarifying the situation. The problem with all of the previous studies is that the experimental resolution was far smaller than δ, which gives the scale of the disorder effect. This was also the case for the Nelmes' study, but they attempted the different approach of studying the atomic thermal-motion obtained from free refinements as an indirect measure of the disorder. Their refinements used an isotropic thermal-parameter U_{iso}(O) to describe the oxygen atom. Meanwhile, the thermal motion of the hydrogen atom was refined as anisotropic, although symmetry restricted it to only two components: one parallel and one perpendicular to the O-D bond.

Their experimental work (using the PE cell) took advantage of a 10 K hysteresis in the VII→VIII transition temperature T_c to collect diffraction data, from both phases, under the same conditions of temperature and pressure. It was expected that any disorder would appear as an additional contribution to the thermal motion in ice VII compared to ice VIII.

The results obtained at 3.3 GPa gave:

- A clear increase in U_{iso}(O) from VII to VIII of around 0.0064(5) Å^2.
- An increase of 0.004(1)Å^2 in the component of the deuterium thermal-motion perpendicular to the O-D bond, $U_{\perp}$(D).

- No change within error in parallel component, $U_{||}(D)$.

Their interpretation was that the lack of change in $U_{||}(D)$ implied that the real thermal motion remained constant through the transition. Meanwhile the change in both $U_{iso}(O)$ and $U_{\perp}(D)$ was direct evidence of the onset of multi-site disorder in both the oxygen and the hydrogen atom at the transition. The size of the jump in $U_{iso}(O)$ was shown to correspond to $\delta = 0.135(10)$ Å by taking the radius of the (spherical) thermal ellipsoid.

In order to obtain further information about the ice VII disorder, the data were refined with the ADP parameters fixed at the values refined for the ice VIII data. In these refinements, a total of twelve disorder models were used, covering all possible combinations of four oxygen-disorder models and three hydrogen-disorder models. The models were then examined to see which gave a *molecular* geometry closest to that observed in ice VIII.

This lead the authors to state that (contrary to Kuhs *et al.*) only oxygen sites on, or within 15°, of the ⟨111⟩ directions could give plausible geometries given their determination of δ using ADP measurements. Additionally, they also investigated the hydrogen-bond geometry resulting from both the ⟨100⟩ and ⟨111⟩ models. They found marked differences in the resulting O...O hydrogen bondlengths, notably that their (preferred) ⟨111⟩ model gave rise to the presence of a mixture three possible H-bondlengths of 2.75 Å, 2.92 Å and 2.93 Å that are respectively ~ 0.1 Å shorter and ~ 0.1 Å longer than the values obtained for ice VIII. They comment on the scale of this effect: "Such changes in the H bondlength are not small; 0.1 Å is $\sim$ 20% of the total change in O...O from 2 GPa to centering [47]."

3.2 Further Investigation of Multi-site Disorder in Ice VII

After publication of their study of multi-site disorder up to 20 GPa, Nelmes and co-workers became interested in extending their study to higher pressures. This was achieved using double-toroid diamond anvils [15], and the value of $U_{iso}^{VIII}(O)$ for ice VIII was measured up to 27 GPa (both here and subsequently, the superscripts VIII and VII are used to denote parameters of either phase). The data shown in Figure 3.4 are a collation of all of the high-pressure ice work performed on the POLARIS instrument at ISIS.

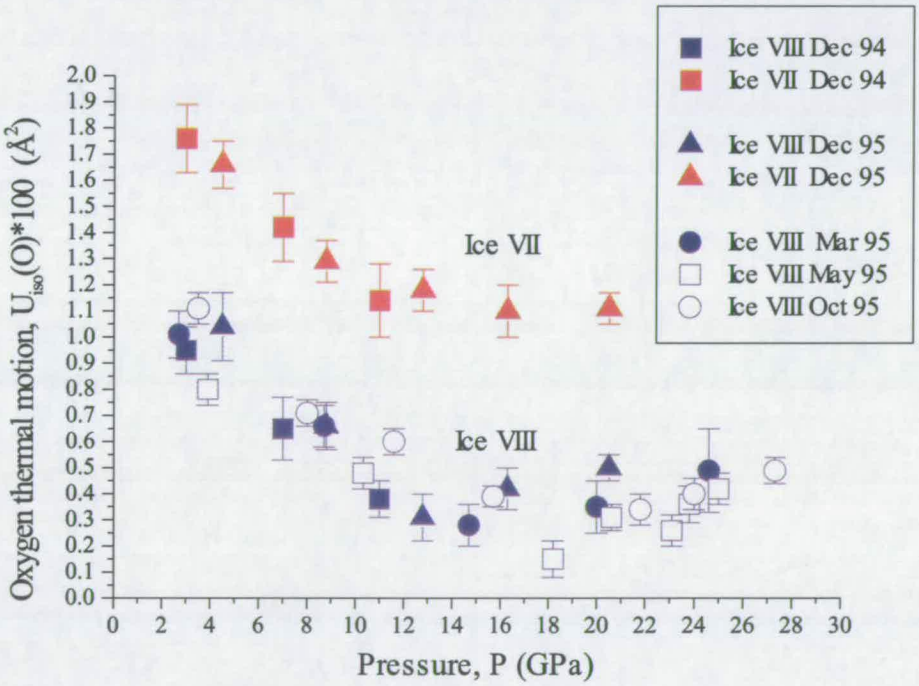

Figure 3.4. Refinements of an isotropic oxygen thermal-parameter $U_{iso}(O)$ for both ice VII and ice VIII samples on the POLARIS instrument at ISIS [48]. The ice VII values are the upper ones (shown in red) and the ice VIII values are the lower ones (shown in blue). Notice the large offset between the thermal parameter for both phases, the higher value for ice VII is taken to be an indirect measure of the oxygen disorder in this phase [45].

An intriguing aspect of these data was that, in all of the experimental runs

extended up to 20 GPa or higher, there appeared to be a minimum in the value of U_{iso}^{VIII}(O). Whilst this trend is observed in all of the experimental runs, the actual position of the minimum varies strongly in the region $\sim$ 15 to $\sim$ 20 GPa. If this corresponded to a real structural change in the nature of the disorder, it would be extremely interesting, potentially impacting on the present understanding of the VII→X transition.

The author became involved in the experimental program of the Edinburgh group in October 1998 by which time the work had been transferred from POLARIS to a purpose built high-pressure diffractometer (HiPr). Around this time, it was decided to revisit the problem of the disorder in ice VII, hopefully taking advantage of the higher flux and detector coverage available on the new instrument. Of special interest would be an attempt to remeasure U_{iso}^{VIII}(O) with the aim of unambiguously establishing if the minimum was a real effect.

Experimental Details

All experiments described here were carried out on the PEARL HiPr diffractometer at the ISIS neutron source and used the Paris-Edinburgh high-pressure cell (see Chapter 4 for more details on this and the following). Data were collected in the transverse setting where the detectors used are contained in a bank at 90° to the incident beam. A cylindrical boron nitride (BN) collimator with a 3.5 mm diameter circular cross-section reduces the size of the beam which then travels through the front anvil to reach the sample.

The anvils used were deBeers 'Syndie' sintered-diamonds, with double toroidal profiles [15]. The microstructure of the sintered diamond is poly-crystalline and this results in a strong powder pattern arising from the anvils themselves. This requires an important additional collimation system provided by 0.25 mm sheets of cadmium that are glued to the faces of the anvils. Across the spectrum of energies used, these sheets are entirely opaque and absorb radiation most of the

diffraction from the diamonds. The inner diameter of the Cd shielding used was 35 mm, this was larger than the more commonly used size of 25 mm in order to maintain the aperture for the diffracted beam as the anvils close at very high loads.

Samples of 99.5% isotopically pure D_2O from EURISO-TOP were loaded into the cell at ambient temperature as liquid samples. A sealing load of $\sim$ 5 tonnes was then applied and the cell cooled to around 200 K prior to further compression to ensure that the sample was compressed as a solid (the minimum of the water melting line is around 250 K as shown in Figure 3.1). This precaution was necessary as the anvils become porous after their first use, thus making it difficult to generate pressure with liquid samples. Loads of $\sim$ 30 tonnes were then typically applied, taking the sample to pressures 1.8-2.0 GPa and thus ensuring that the sample was in a solid phase (ice VI or VII) when re-warmed to room temperature. Taking this route to ice VII had an advantage in that it traversed several phase boundaries, and the resulting transitions combined to produce a fine, well randomised powder.

Several experimental runs were performed between December 1998 and February 1999 as summarised in Table 3.1

Pressure Determination

The equation-of-state of hydrogenous ice VII was determined by energy dispersive x-ray diffraction measurements by Hemley *et al.* in 1987 [16] at pressures up to 128 GPa. Their data were fitted with a Birch-Murnaghan function [49] with the parameters $V_o = 12.3 \pm 0.3$ cm^{3}mol^{-1}, $K_o = 23.7 \pm 0.9$ GPa and $K' = 4.15 \pm 0.07$. In 1995, Besson *et al.* [50] published the equation-of-state for ice VIII at pressures up to 10 GPa that was determined from neutron diffraction measurements. The Birch-Murnaghan parameters of for Besson's ice VIII equation of state (at 300K) are $V_o = 12.45$ cm^{3}mol^{-1}, $K_o = 20.4$ GPa and $K' = 4.7$ (the standard deviations

Date of Experiment	Ice VIII			IceVII		
	Run	P (GPa)	Integrated proton flux ($\mu Ahrs$)	Run	P (GPa)	Integrated proton flux ($\mu Ahrs$)
Dec 1998	23252	4.3	484	23247	4.3	300
	23263	8.1	632	23257	8.1	423
	23273	12.1	500	23268	12.1	966
	23287	17.1	621	23282	17.1	1194
	23296	20.4	1506	23291	20.4	760
Feb 1999	24109	3.2	601	24107	3.2	700
	24115	9.9	515			
	24124	16.0	757	24121	16.0	479
	24131	19.5	584			
	24139	22.4	728			
	24156	24.0	502	24148	24.0	204

Table 3.1. A comprehensive list of the experiments carried out on the high pressure ice phases. Each data point is labeled by a unique run number which, along with the instrument name, uniquely specifies its location in the ISIS data archive. The total number of neutrons incident on the sample is related to the integrated proton flux on the spallation target. This is given by the product of the incident proton beam current and the time for which data is collected and measured in $\mu Ahrs$ (see Section 4.1.2).

of the fit were not given), the authors also discuss the effects of temperature variation.

However, as the experiments described here reach pressures as great as 24 GPa, much higher than those reached by Besson *et al.*, it was preferable to use the ice VII equation of state to avoid any errors arising from extrapolation. Therefore, all pressures reported here were determined from refinements of room temperature ice VII powder patterns. It is assumed that the pressure change on cooling to ice VIII is small enough to not affect the results of this study. Additionally, the effect of deuteration on the equation-of-state is expected to be negligible [51].

3.2.1 Correction of Data I: Attenuation Correction and Background Subtraction

An important aspect of high-pressure powder diffraction is the effect of the (often bulky in the case of neutron diffraction) sample environment on the diffraction signal. It is necessary to attempt to correct the data for these effects prior to subsequent structural refinement. This is not a trivial problem, and it is well known that absorption-type effects can strongly correlate with thermal motion effects, as both are described by exponential factors [34].

The problem can be broken down into the two separate tasks of

- Fitting and subtracting the background
- Correcting for the attenuation of the cell on a) the incident beam and b) the scattered beam.

The attenuation correction is tackled by a first principles calculation using the program ATTEN written by Marshall [52]. The input for this calculation is the geometry of the anvil assembly, as shown in Figure 3.5, and the measured absorption coefficients for each of the materials present. The sample is idealised as a sphere occupying the sample position which is then divided into many elements. For each of these elements, the attenuation of both the incident and diffracted radiation is calculated. The attenuation experienced by the diffracted radiation is then integrated across the range of angles accessible to the detectors and, finally, this attenuation is integrated over each of the elements defining the sample position, and all angles surveyed by the detectors.

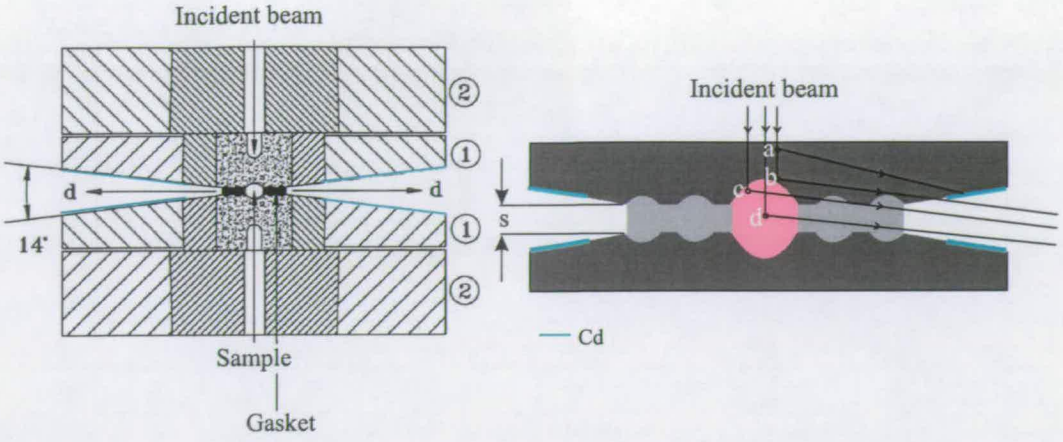

Figure 3.5. The figure on the left shows a schematic of the double toroidal anvil (1) and seat (2) assembly that applies pressure to a sample contained in a metal gasket. A more detailed description of the generation of pressure on the sample is given in Section 4.3.3 of the following chapter. The incident beam diameter is collimated down to 3.5 mm, it then travels through the aperture in the seat and then through the front anvil itself to reach the sample. The diffracted beam (d) is then measured by the transverse detector bank, which is centred at 90° to the incident beam. The detector modules subtend a solid angle of 15° in 2θ and, thus, can view the diffracted beams from the entire aperture. Marked in blue on the figure is the cadmium shielding that absorbs the powder scatter from the anvils. The figure on the right illustrates a close-up of the double toroidal anvil profile on which several beam paths have been drawn. Points 'a' and 'b' illustrate two instances of scatter from the anvil material. In the case of 'a' the diffracted beam is absorbed by the Cd shielding and doesn't reach the detectors, whilst scatter from point 'b' (which is closer to the sample position) can still escape to the detectors. Points 'c' and 'd' illustrate two instances of scatter from the sample. Notice how radiation scattered from 'c' must traverse a complex path through sample, anvil and gasket to reach the detector, whilst scatter from 'd' will experience a much less complicated attenuation effect.

In order to illustrate fully the difficulties inhibiting accurate calculation of the cell attenuation, a schematic of the PE-cell and anvils is given in Figure 3.5. Here, it is clear that the dominant effects in the calculation are:

1. Attenuation of the incident beam by the front anvil. In this case, the anvil material is sintered diamond which is a strong scatterer of neutrons. Consequently, the anvil attenuation is complicated by the presence of 'Bragg edges'. This effect is a reduction of the transmitted intensity arising from

coherent scattering from the anvils. This effect is strongly dependent on preferred orientation of the anvils and is subsequently difficult to calculate, so it is instead measured in transmission tests

2. Attenuation from the sample. In general, the absorption of neutrons by the sample is not a strong effect and can be neglected. However in some cases, for example where the sample contains protons (see Section 5.2.1) or for strongly attenuating substances, such as B_4C, this can be a strong effect and must be included.

3. Gasket attenuation. Radiation scattered from the sample position must pass through a certain amount of gasket material. The material used is Ti:Zr alloy, which does not scatter the radiation coherently and therefore introduces no Bragg-edge effects. Nevertheless, it is relatively strongly absorbing (see Appendix A) and this effect must be included in the calculation.

4. Attenuation of the diffracted beam by the anvil material. Careful examination of the geometry of Figure 3.5 reveals that the parts of the diffracted beam scattered from sample in the bottom of each anvil cup must travel though sections of anvil in order to reach the detectors.

Whilst the geometry of the anvils is well known, their separation, and the outer radius of the gasket both vary during the course of the experiment. Other important factors, which can affect the calculation and yet are impossible to determine accurately, are the packing density (when sample absorption is a significant factor) and the thickness and exact position of the Cd shielding used on the anvil face (this can be especially troublesome for very high pressure work as extrusion of the gasket can force the cadmium out of shape). Therefore, there is an element of uncertainty in the calculated attenuation function. Additionally, the present calculation is an integration across only an idealised *sample* volume and, consequently, does not accurately correct the scatter that arises from the anvils themselves.

An example of the resulting attenuation correction function, illustrating the complexity of the Bragg edges is given in Figure 3.6. The powder pattern is divided through by this in order to apply the correction.

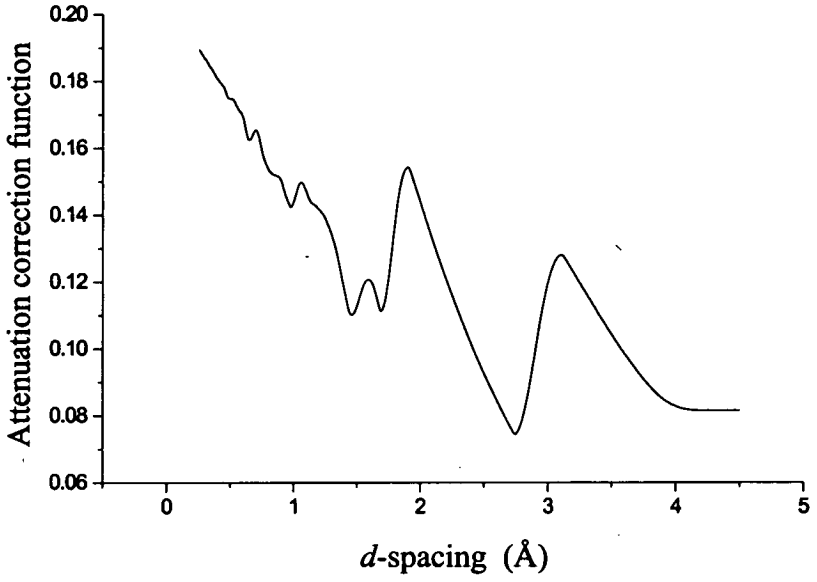

Figure 3.6. Attenuation correction for double toroid, deBeers sintered diamond anvils with 1 mm separation. This was calculated by the program ATTEN [52].

It is at this stage of the pre-refinement data processing that the problem of background subtraction is encountered. In addition to the diffraction intensity from the sample and the anvils, some background B will also be present. In the most general case, the background function is represented as the sum of two components, both of which are, in general, wavelength dependent.

$$B(\lambda) = B_o(\lambda) + B_{int}(\lambda, s) \tag{3.1}$$

The first term B_o describes background that arises from sources external to the cell, and is therefore independent of changes in the cell geometry as the sample is compressed. The second term B_{int} describes the 'internal' background that originates at the locality of the sample position, and consequently is affected by

the same attenuation effects experienced by the sample that, in turn, depend on the anvil separation s (this separation is indicated in Figure 3.5). It is important for the subsequent refinement procedure that the background is a smooth function. However, as B_{int} is also affected by the Bragg edges introduced by the front anvil, this will superimpose sharp features onto the background.

The complete measured pattern I_f can thus be represented as follows where I_{sample} is the component due to coherent scattering form the sample and I_{anv} that arising from the anvils

$$I_f(\lambda) = B_o(\lambda) + [I_{sample}(\lambda) + B_{int}(\lambda, s)]A(\lambda) + I_{anv}(\lambda)A'(\lambda) \qquad (3.2)$$

Here A is the attenuation affecting the sample (as calculated by ATTEN) and A' is the attenuation affecting the diamond that will be, in general, different from A. At present, A' is not calculated by the program ATTEN as it is likely that uncertainty in the input parameters would render the calculation susceptible to error. Instead, the approximation $A' = A$ is universally applied in powder diffraction work on the PEARL instrument. The failure of this approximation most obviously manifests itself in unphysical refined ADP parameters for the diamond phase, however, this is not thought to be a serious problem as long as the sample is not strongly absorbing (as it will be seen to be in Section 5.2.1 later). This approximation simplifies Equation 3.2 to

$$I_f(\lambda) = B_o(\lambda) + [I_{sample}(\lambda) + I_{anv}(\lambda) + B_{int}(\lambda, s)]A(\lambda) \qquad (3.3)$$

In many cases B_{int} is also negligible and the procedure used is to fit some kind of background to the focused data *prior* to attenuation correction. Typically a simple polynomial fit is applied but, a more sophisticated approach would use a pattern decomposition technique. In the latter case, the fit recognises that the data includes intensity in the form of diffraction peaks in addition to

the background[3]. This background is then subtracted and the resulting pattern corrected by division by A. Indeed, this was the method used in the analysis of previous ice diffraction data of Nelmes' [48] giving the values in Figure 3.4.

A striking feature of the ice VII data for the lowest and highest pressures shown in Figure 3.7 is a strong reduction in the background. As the external background is expected to be constant, any observed reduction is expected to be in B_{int}. Furthermore, sharp Bragg-edges are clearly visible as structure in the background of the low pressure pattern. Therefore, the observed change in background between the lowest and highest pressure is a direct observation of the reduction in B_{int} as the cell aperture closes with pressure. The magnitude of this change thus gives a lower limit on the size of B_{int} that is seen to be almost three times B_o in the lowest pressure data and, consequently, is non-negligible. Additionally, the reduction in the intensity of the sample peaks should be proportional to the reduction of B_{int}. The intensity of the largest sample peak (the [110]) at the maximum pressure is only 12.5% of that observed at the lowest pressure. It is also dramatically clear from the figures that the B_{int} component observed in the ice VIII measurement is much less than that present in phase VII (see figure caption). It can therefore be expected that, to a good approximation, B_o could be estimated using a background fitted to the highest pressure ice VIII data.

The de-coupling of the two background terms was attempted, but, on closer inspection, it became clear that the situation was complicated by an unexpected factor. It was noticed that whilst the total background at intermediate energies reduced monotonically with pressure, at the highest energies (corresponding to the lowest d-spacings), the background actually began to increase with pressure after an initial drop, and finally ended with a *higher* value than it that observed in the lowest pressure run. As has already been stated, the change in B_{int} must be proportional to the coherent diffraction signal which can be estimated by

[3]The GSAS suite of software includes an algorithm to perform the decomposition by a Lebail fit [53], this was used throughout to fit the backgrounds.

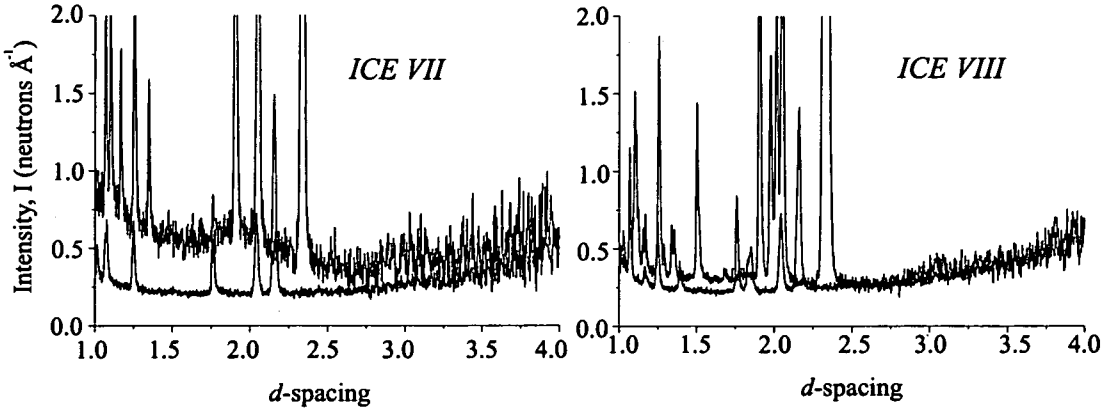

Figure 3.7. The figure on the left shows the reduction in background between the lowest and highest pressures achieved during the December 1998 ice VII measurements. The figure on the right shows the equivalent patterns for ice VIII performed on the same experimental loading. It is worth mentioning that the far larger component of the internal background in the ice VII measurement is directly attributable to diffuse scattering arising from the molecular disorder and, therefore, actually contains structural information. By de-coupling the two background components B_o and B_{int}, this information is retained in the pattern that is eventually refined. However, at present, no software is available that can attempt to fit the background as part of the refinement procedure. Consequently, it is simply fitted by the refinement background-parameters, and the implicit information that it contains is discarded.

measuring the change in area of a particular diffraction peak. This measurement was made, and revealed an almost linear decrease in intensity from the sample position with pressure. It followed that any increase in the total background must be due to some change in the external background B_o, which had been expected to be constant.

This result prompted an investigation of variation in the incident flux as an explanation. This study revealed that there *was* a time dependence of the incident flux and the effects of this are described in the following section, but, this could not account for the changes in B_o that were observed.

The most likely explanation is that this feature is an artifact, perhaps arising from failure of the vacuum of the cryostat tank (a relatively common occurrence at the time the measurements were made), which resulted in water collecting on

the exterior of the tank and the cell. Due to its high hydrogen content, even a small amount of water in the path of the direct beam could result in a significant amount of incoherent scatter which may have found its way into the detectors. Any such water would probably be shielded from the detectors by various parts of the cell and tank, and only the highest energy component would penetrate far enough to be measured.

The presence of a non-constant external background presents a difficult problem for the data analysis. Ultimately, a second set of measurements was conducted in February 1999. These data showed no evidence of a time-dependence of the external background (confirming that it was not intrinsic to the method or the sample), and the data could subsequently be corrected by the preferred method of subtraction of a background fitted by the LeBail (HP Lebail) technique [53] to the highest measured ice VIII pressure point.

It was important to quantify the effect, on the refined thermal parameter, of the different background corrections. To this end, ice VII data were corrected by subtraction of a polynomial background (A Lebail background was also refined, but was almost identical to the polynomial fit) and subtraction of a HP LeBail approximation of B_o. The resulting thermal parameters were

- $U_{iso}^{VII}(O) = 1.319(44)$ for the polynomial background
- $U_{iso}^{VII}(O) = 1.382(42)$ for a HP LeBail background

This difference is certainly significant as the postulated minimum in $U_{iso}^{VIII}(O)$ is not much bigger than a single standard deviation. This illustrates the importance of careful background subtraction for thermal motion studies, especially in cases where a significant amount of background is due to the sample.

Finally, it is clear that whilst the background of the highest pressure run gives a good approximation to B_o, the external background could be unambiguously

measured experimentally. In order to perform this measurement, a piece of shielding that completely enclosed the sample assembly would have to be built. This was not attempted by the author, but perhaps should be considered for future work.

3.2.2 Correction of Data II: Time Variation of the Incident Flux from the Methane Moderator

One possibility that was investigated as a cause for variation in B_o was that rather than being constant (as has been assumed), the incident flux might actually be a function of time. This could occur as a result of time-dependent changes in the methane moderator that acts as the effective source of radiation for the PEARL HiPr beamline (see the following chapter, Section 4.1.2 for a description of the function of moderators in neutron sources). It is a known phenomenon that radiation damage produces a build up of carbon-rich matter in the moderator, resulting in a gradual reduction of its total flux (although this effect occurs gradually over a period of many months). Additionally, as the moderator is maintained at 130K, it was possible that temperature variations might shift the flux distribution, and these might occur on a much faster timescale. Evidence for this effect should be visible in the flux measured by the beam monitor installed on the PEARL beamline upstream of the diffractometer.

The flux profile measured by the monitor $I^n_{mon}(\lambda)$ for the nth run must be corrected for the efficiency of the monitor to give the true incident flux $I^n_o(\lambda)$. Thus the detected and true fluxes are related by

$$I^n_{mon}(\lambda) = \epsilon(\lambda) I^n_o(\lambda) \tag{3.4}$$

Dividing the measured fluxes for each run by that measured in one particular reference run gives a correction function $C^n(\lambda)$. Division of the measured powder

profile by C^n results in data that would be measured if the flux were equal to the reference run. The most appropriate choice for the reference run would be that used for the vanadium correction that defines the incident flux in the focusing procedure. In practice, however, it was found that a change of moderator since the vanadium correction had been measured had resulted in changes in the aluminium Bragg edges (from the moderator casing) in the incident beam. This produced sharp features in the C^n functions, and consequently, the first ice VII run was arbitrarily used as a reference[4].

$$\frac{I^n_{mon}(\lambda)}{I^{ref}_{mon}(\lambda)} = \frac{I^n_o(\lambda)}{I^{ref}_o(\lambda)} = C^n(\lambda) \tag{3.5}$$

This was done for the all of the data collection runs using the final ice VIII run as the reference. The resulting C^n functions are shown in Figure 3.8 and show that there is some variation, most pronounced at lower energies, which in the case of run 24156 is as great as 10% at long wavelength. This was observed to have an effect on the extracted thermal motion parameters of an increase of several standard deviations, consequently, all data were corrected by dividing through by the appropriate C^n correction function. However, the changes in the incident spectrum at short wavelength are far less affected (the maximum change is 2-3%), and indeed this effect cannot account for the observed increase in external background.

[4]In principle, an additional correction term $c^o(\lambda)$ (defined exactly as before) is also required to correct for flux variation between the reference run and the vanadium calibration runs. However, this was not possible as a consequence of the change of moderator since the vanadium calibration runs had been performed

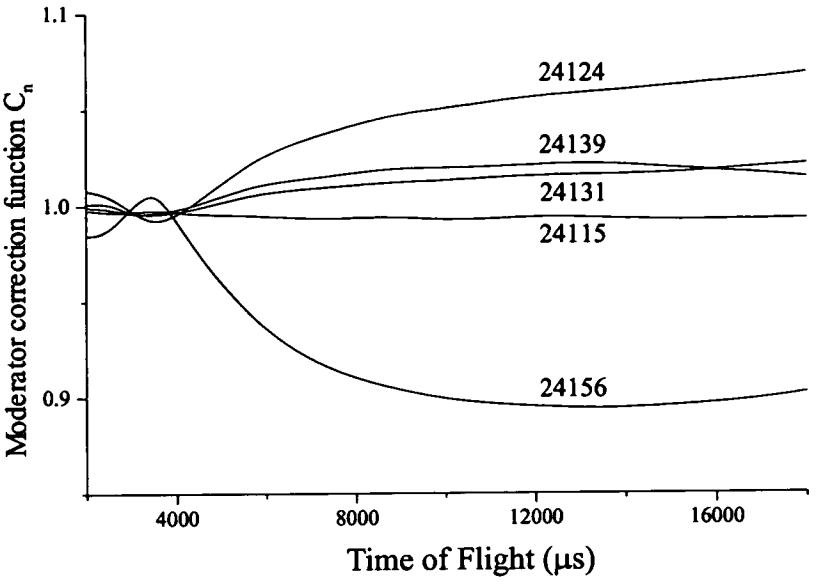

Figure 3.8. Correction functions for temporal variation in the incident flux. The reference run in this case was 24109, the run numbers for each $C_n(\lambda)$ function are included in the plot. The largest change is seen for run 24156 where the flux at long *d*-spacings is *lower* than the reference run by 10%.

3.2.3 Correction of data III: The Refined Absorption Correction and the Vanadium Correction for Incident Flux and Detector Efficiency

The attenuation correction (described above) that is applied prior to refinement includes the effect of absorption expected from the various components of the cell and sample. Consequently, subsequent refinement of absorption is only necessary if the geometry of the cell changes. This, of course, is the case: as the load increases the gasket becomes thinner and wider and, thus, the anvil separation reduces. As this is a powder diffraction experiment, it is only necessary to correct for effects that change the relative intensities of the diffraction peaks. The only such effect is that of an increased pathlength that the diffracted beams must follow through the gasket material. This pathlength can be determined as a function of load by examining the dimensions of pre-compressed gaskets (although some error must be attributed to varying packing densities of the sample between different

loadings), and a plot of is shown in Figure 3.9. As the absorption coefficient of the gasket material $\mu_{Ti:Zr}(\lambda)$ is known (by transmission measurements) it is possible to calculate the expected change in absorption as a function of load.

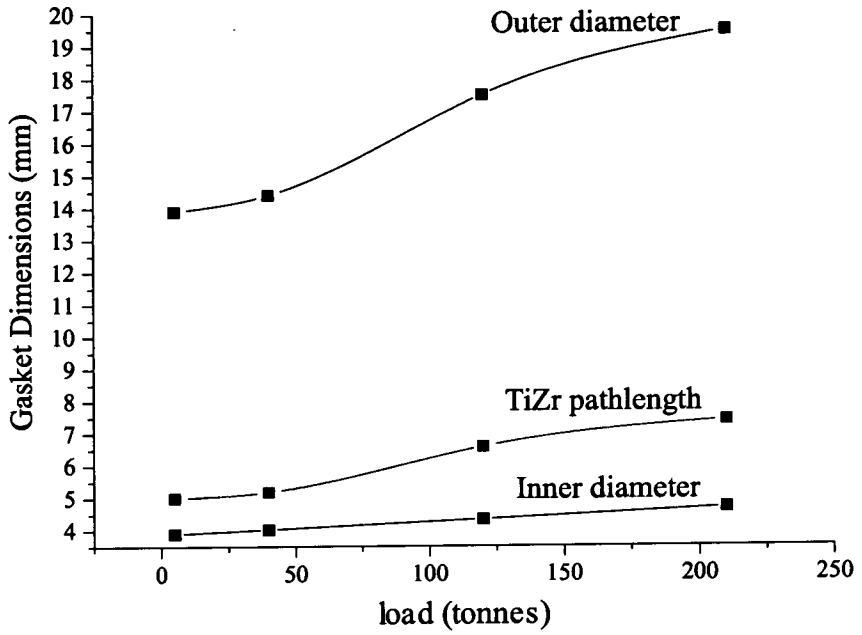

Figure 3.9. The figure shows spline fits to measured values of the inner and outer diameter of the gasket as a function of load. The resulting pathlength traversed by the diffracted beam is shown in red.

The GSAS Rietveld routine allows the refinement of a single absorption parameter. This is clearly problematic for these data, where the diamond component is known to experience a different absorption than the sample. Therefore, it was necessary to compare the refined value of absorption with the expected value to assess its validity.

The GSAS absorption correction [54] [55] is calculated according to the empirical formula

$$A_{gsas} = \exp[-T_1 A_B \lambda - T_2 A_B^2 \lambda^2] \tag{3.6}$$

where

$$T_1 = 1.7133 - 0.0368 \sin^2 \theta \quad (3.7)$$

and

$$T_2 = -0.0927 - 0.3750 \sin^2 \theta \quad (3.8)$$

By comparing this with the expected increase in absorption as the gasket deforms, it is possible to calculate a value of the absorption coefficient A_B for a given load on the cell.

In order to investigate the effect of the diamond contaminant phase on the refined absorption, selective 'focusing' of the data could be used. Focusing is a technique whereby the data measured in each of the diffractometers many detectors is combined into a single spectrum. This technique is described in detail in the following chapter (Section 4.1.4).

Two different focusing methods were employed: full-focus and mid-focus. The former sums the data measured across the complete face of the detector modules (83°-97° in 2θ), whilst the latter sums only that measured in the middle half (86.5° to 93.5° in 2θ). As a consequence of the cadmium shielding the anvil face, the diamond scatter is much reduced towards the middle of the detector and, consequently, mid-focused data have a smaller diamond component. Rietveld refinements to both mid and full focused data are given in Figure 3.10 over the page.

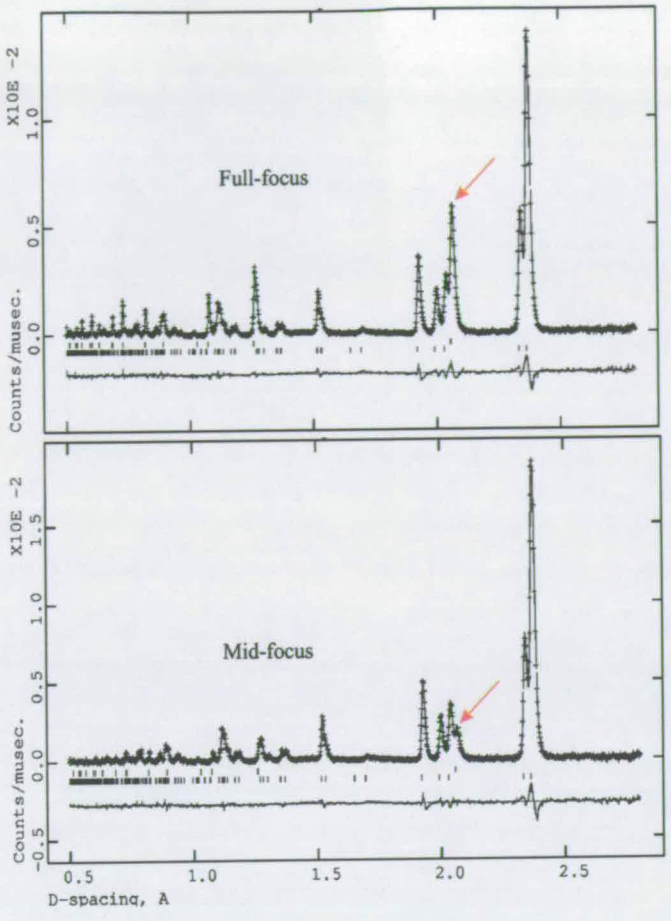

Figure 3.10. Rietveld refinements to ice VIII data, at approximately ambient pressure, illustrating the effect of full focusing (top) and mid-focusing (bottom). In both Figures, the positions of Bragg reflections are indicated by ticks underneath the powder diffraction pattern. Upper ticks indicate the diamond phase, whilst the lower ticks indicate the sample ice phase. Note the difference in size of the largest diamond peak at around 2.05 Å (indicated with the red arrow) between the two images.

The values of the refined GSAS absorption coefficients for both mid and full-focused data are shown in Figure 3.11 along with the expected values from the changes in gasket geometry. It is immediately clear that there is a large offset between the refined values for the different focuses. Also, the refinements of either types of focused data are quite different from the expected values. The large increase in the refined absorption is almost certainly an indication that it is being incorrectly fitted.

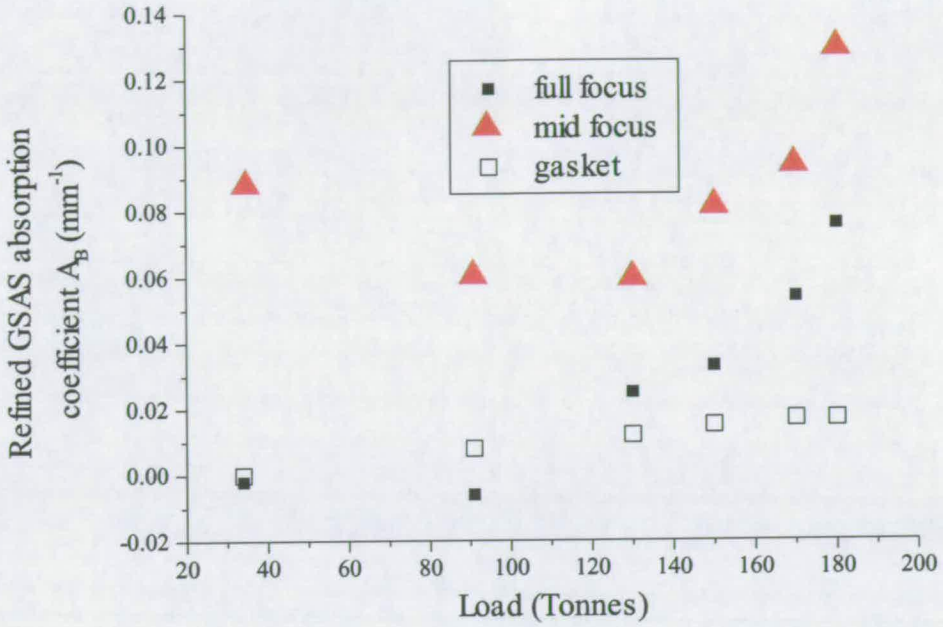

Figure 3.11. The figure shows the refined values for absorption for both mid and full-focused data as solid symbols. The hollow symbols show the values expected from the known geometrical changes in the gasket.

It was also clear that the oxygen thermal parameter was strongly correlated with the refined absorption. This was demonstrated by fixing the absorption at different values during refinements of a given data set. It was observed that the refined value of $U_{iso}(O)$ had a linear dependence on the chosen value of A_B. The refined values of the thermal parameters are shown in Figure 3.12. The previous values measured by Nelmes *et al.* [48] are also plotted for comparison.

The absolute values for $U_{iso}^{VIII}(O)$ for both data sets are offset to lower values than those of the previous study, with the mid-focused data having the lower offset. It was noted by the author that this offset could be modeled by introducing an additional constant 'dummy' component to the absorption. As the expected cell absorption is already corrected for, the effect is not a physical absorption, but must come from another source. One possibility that presented itself was a possible error in the vanadium correction that is applied as an integral part of the focusing procedure. This was not pursued by the author, and the data were

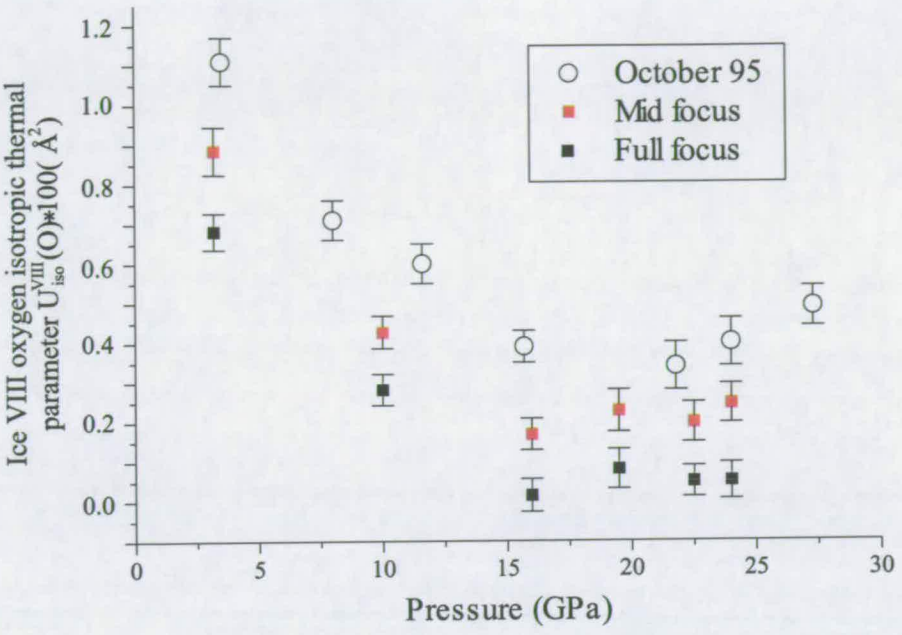

Figure 3.12. The figure shows the refined values of $U_{iso}^{VIII}(O)$ for mid and full-focused data. For comparison, data from a previous measurement of Nelmes *et al.*'s [48] is also shown

put to one side for a time.

The vanadium correction is described in detail in Chapter 4, its purpose is to correct for the wavelength distribution of the incident flux, and the energy response of the detectors. At the time of the first refinements of these data, the vanadium measurements were made using a 8mm rod of vanadium that was suspended at the centre of the instrument. A known flaw of this method was that each of the detectors which are distributed in an arc about the centre of the instrument (see the description of the instrument geometry in Section 4.1.3) viewed a vanadium spectra that had travelled through a different pathlength of vanadium. This made the necessary absorption correction applied to these data before focusing, much more complicated. The two vanadium samples are shown in Figure 3.13.

The problem was tackled by the PEARL instrument scientist who had implemented the use of a spherical vanadium target. The resulting change in the

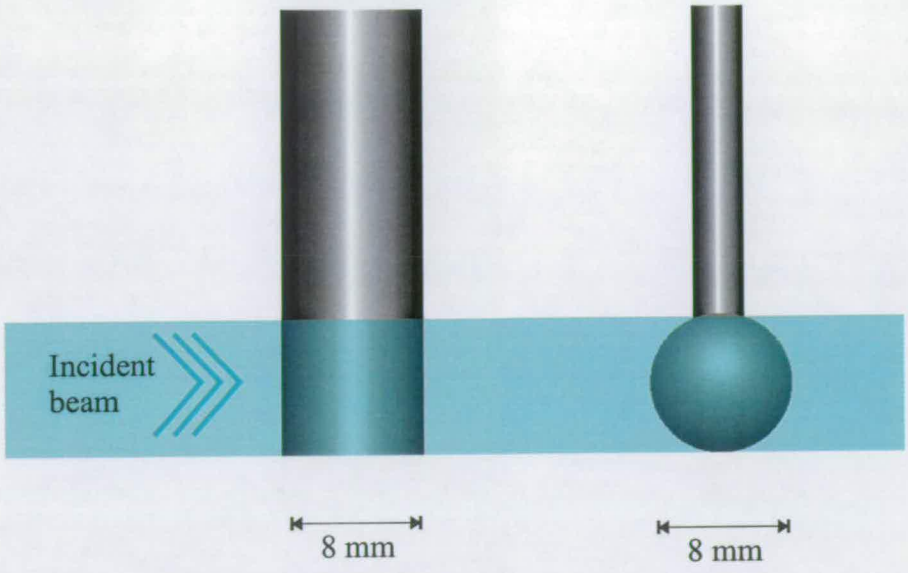

Figure 3.13. The 'rod' and 'sphere' vanadium samples shown relative to the incident beam. Whilst both have a circular cross section in the equatorial plane (that is a plane rising vertically out of the paper through the incident beam), the rod will present progressively different cross-sections as this angle changes. The sphere, on the other hand, is completely isotropic, and is the same when viewed from any direction. Consequently, the resulting attenuation is easier to calculate for the spherical sample.

profile of the vanadium correction function was dramatic, as is shown by the ratio of the rod and sphere functions given in Figure 3.14.

Upon seeing this ratio, it was immediately clear that data corrected by the older vanadium-rod function would be modified in a way that would simulate an increased absorption. This was confirmed by re-correcting the original data, using the new vanadium measurement. Subsequent refinements performed with the absorption fixed at the expected values are shown in Figure 3.15.

These refinements show that the offset observed in the original refinements can indeed be attributed to the error in the vanadium correction function. Unfortunately, when the absorption correction was permitted to refine, the mid and full-focused data again assumed offsets, with the absorption coefficients differing widely from their expected values, although they now refined to large negative

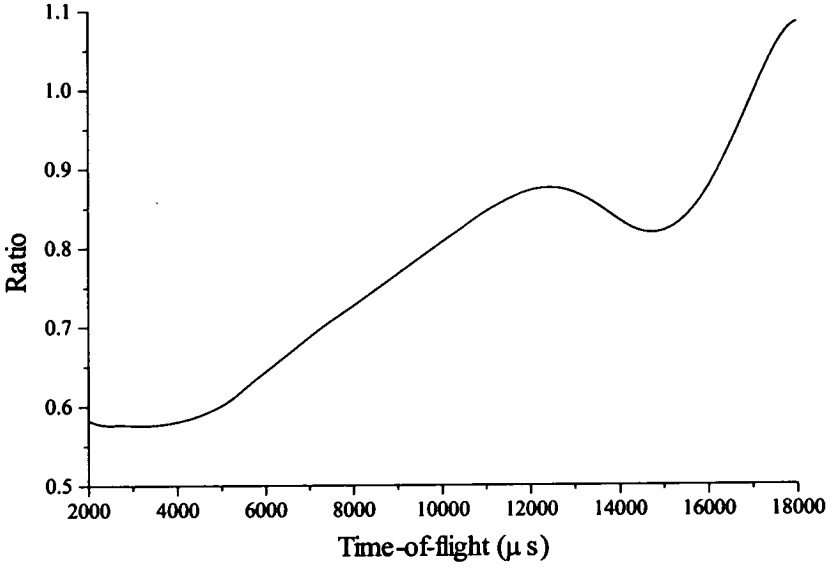

Figure 3.14. The figure shows the ratio between the old (rod) vanadium correction function and the new (sphere) correction function.

values, again the variation was much larger than could be attributed to the geometrical changes in the gasket.

It seems clear that the refinements should be carried out with the absorption fixed. This constraint causes a small increase in the χ^2 of the fit of 2-5% in the case of mid-focused data and a much larger increase of 6-19% for the full-focused data. This is strong evidence that it is the presence of diamond in the patterns that is causing the absorption correction to mis-refine.

3.2.4 Final Refinements and Results

Having investigated all of the effects described in the previous section, final refinements were carried out on the February 1999 data using both mid and full-focused data. Rietveld fits to mid-focuses of both the ice VII and ice VIII data are shown in Figures 3.16 and 3.17 respectively.

The various corrections applied to these data, as described above, are summarised here:

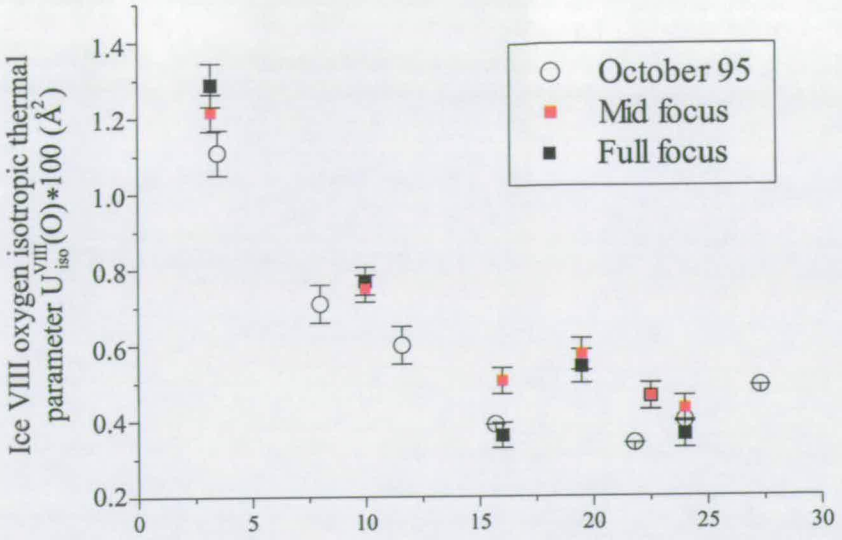

Figure 3.15. The figure shows the refined $U_{iso}^{VIII}(O)$ parameters with the new, spherical-vanadium correction applied. The offset evident in Figure 3.12 is no longer evident.

- A background fitted to the highest pressure ice VIII measurement (run 24156) was subtracted from all runs
- The effect of cell attenuation was corrected by the program ATTEN. During the refinements, the GSAS absorption parameter was *fixed* at the value calculated to reflect the changes in the gasket geometry with load
- Time variation of the incident flux was corrected by scaling to the first run (24109).
- Finally, the data were all corrected using the most recent vanadium incident flux and detector efficiency measurement, determined from the measured scatter from an 8mm diameter vanadium sphere.

All refinements contained two phases: an ice phase and a diamond phase. The Ice VII data were refined in the space group $\mathbf{Pn\bar{3}m}$ using a single-site model with the oxygen atom fixed at $(\frac{1}{4}, \frac{1}{4}, \frac{1}{4})$ (corresponding to the *average* position of the atom). Deuterium atoms were placed on 8-fold (x, x, x) sites with a 50% site occupation

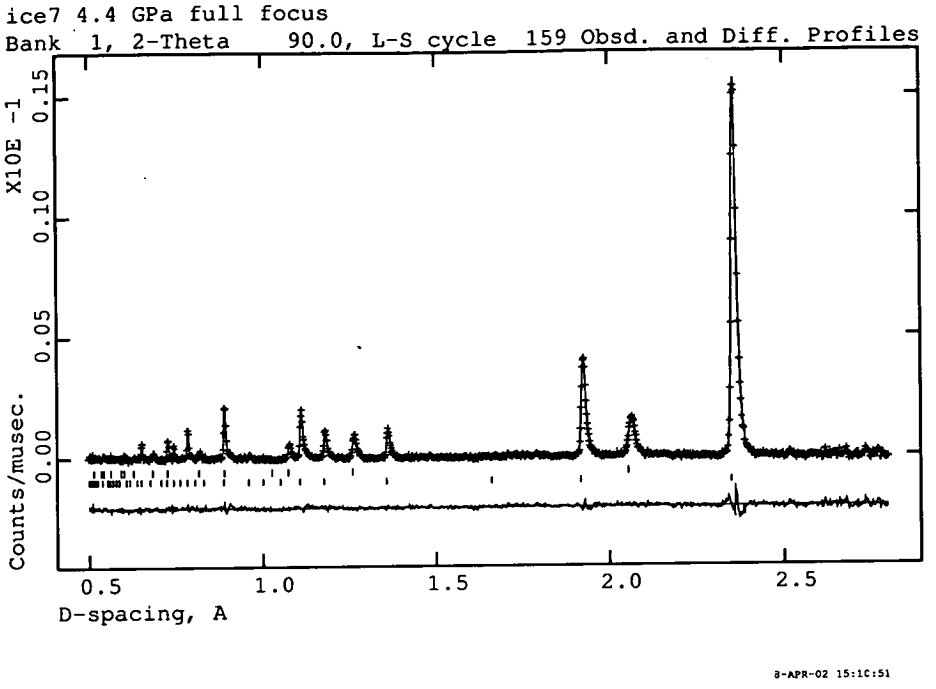

Figure 3.16. Rietveld fit of mid-focused ice VII data. The upper tick marks below the powder diffraction profile correspond to the refined positions of the diamond-anvil diffraction peaks, whilst the lower ticks correspond to the ice VII peaks. Measured data points are indicated as crosses, whilst the Rietveld fit is the solid line running through points. Below the tick marks, a difference curve is plotted showing observed minus calculated intensity.

factor reflecting their disorder. An isotropic thermal motion parameter was used to model both the real thermal motion of the oxygen atom, and its disorder, whilst anisotropic thermal motion was refined for the deuterium. Within the constraints of symmetry, the positional parameters of the atoms were allowed to vary freely.

The ice VIII refinements were performed in the space group $\mathbf{I4_1/amd}$ with the oxygen atom on 8-fold $(0, \frac{1}{4}, z)$ sites and again refined with an isotropic thermal motion parameter. The deuterium atoms were placed at 16-fold $(0, y, z)$ sites

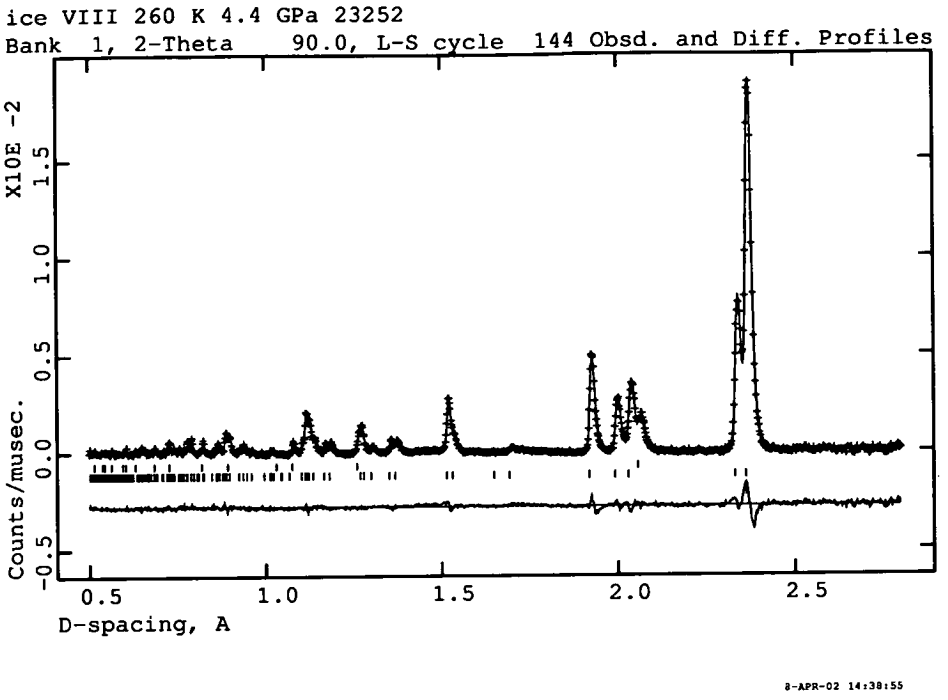

Figure 3.17. Rietveld fit of mid-focused ice VIII data. The upper tick marks below the powder diffraction profile correspond to the refined positions of the diamond anvil diffraction peaks, whilst the lower ticks correspond to the ice VII peaks. Measured data points are indicated as crosses, whilst the Rietveld fit is the solid line running through points. Below the ticks marks, a difference curve is plotted showing observed minus calculated intensity.

and the thermal motion was constrained to have components parallel and perpendicular to the O-D bondlength[5]. Again, the atomic positional parameters were allowed to vary freely.

In all cases, the lattice parameters of the ice phase and diamond phase were permitted to freely refine. The peak shapes themselves were modeled using a pseudo-Voigt function [27] that is a linear combination of a Lorentzian and Gaussian functions that is a good approximation for the time-of-flight peak shape. The

[5]This constraint was also applied by Nelmes et al. [45] and simplifies comparison with ice VII where the *symmetry* constrains the D thermal motion to be parallel and perpendicular to the O-D bond. Nelmes et al. demonstrated that this constraint did not have any significant impact on the quality of the fit.

only peak variables that were refined were the parameters σ_1 and γ_1 that govern the Gaussian width and the extent of the Lorentzian tail respectively. Any internal background that was not removed prior to refinement was fitted using a Chebychev polynomial with 8 terms during refinement.

GSAS allows the refinement of an extinction parameter that models the effect of primary extinction E_p within the grains of the powder. The presence of extinction was explored by allowing this parameter to refine, however in all but the lowest pressure ice VII data, it refined to zero. For the one data set where extinction did refine, it had a large effect on the thermal motion parameter, which refined to only 1.382 (42) $\times 10^{-2}$Å^2, when E_p was not refined. The reduction of extinction with pressure is to be expected, especially under the non-hydrostatic conditions of these loadings, as increasing strain tends to reduce the crystal quality of the powder grains.

The extracted thermal motion parameters are shown superposed on the previous, POLARIS, results in Figure 3.18, also plotted are Nelmes' values at 5 GPa.

Firstly, it is noted that the difference between mid and full-focus is within error for all but one of the measurements. However, in the 16 GPa measurement, the mid-focus refines to a larger value for both the ice VII and the ice VIII measurement. The difference is of the order of three standard deviations, which is extremely large. In all refinements, the relative amounts of each phase were independent of pressure, with sample accounting for 50(2)% of the pattern in the full-focused data and 80(2)% in the mid-focused data. Clearly, any difference between the two focusing methods is a consequence of the relative amount of diamond. Therefore, where the two give different values, the mid-focus is to be preferred.

The February 1999 data follows the same trend as the earlier measurements, with perhaps a small upwards offset in the ice VIII measurement that actually places it more in-line with Nelmes' data. Noteably, there is no evidence for the broad minimum observed in the POLARIS data. In refinements of these data,

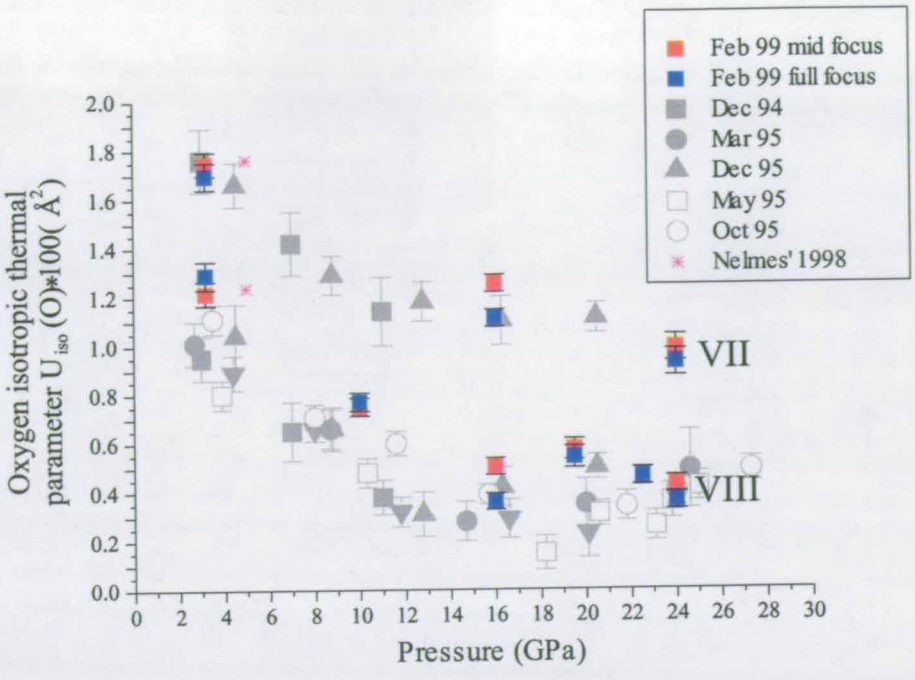

Figure 3.18. The final refined $U_{iso}^{VIII}(O)$ and $U_{iso}^{VII}(O)$ parameters shown for both mid and full refinements. For comparison, all of the earlier POLARIS data are shown in grey, and superposed in magenta are the measurements published by Nelmes at 5 GPa [45].

the absorption was permitted to vary, and the most likely explanation of the minimum is a failure of the absorption correction as the sample signal weakens at higher pressures. This would also explain the wide variation observed in the location of the minimum, which would then be expected to vary as a function of load and sample packing density rather than pressure.

3.3 Conclusions

The work described in this chapter clearly illustrated some of the difficulties inherent in measurement of thermal motion using powder techniques. The analysis of factors affecting the data suggested some changes in experimental procedure for such measurements.

In particular, the problem of accurate correction of absorption effects was encountered. Whilst it proved possible to approximate the absorbing pathlength traversed by the diffracted radiation, it would be more desirable to determine this directly, as it will vary depending on the exact packing density of the sample. Unfortunately, it appears that the contaminant scatter from the anvils prevents accurate refinement of the absorption, however, it could be determined experimentally. This could be readily achieved with the current alignment system which uses a video camera and monitor to centre the sample. With correct calibration, the image of the gasket could be used to determine its outer diameter, this method would have a sufficient level of accuracy, but might fail at the highest pressures where the optical (and neutron) aperture is very small. A second experimental tactic, which could be readily employed to simplify the absorption correction, would be to collect the data on download. In this instance the sample is immediately taken to the maximum pressure of the study, at which stage the gasket has reached its maximum level of plastic deformation. Successive, lower pressure, data points are then collected without further significant change in the geometry of the gasket.

Also highlighted, was the need for accurate calibration of the measured data for incident flux. Whilst the newer vanadium sphere measurements clearly gave more precise thermal parameters than the earlier 'rod' measurements, they take no account of time variation of the incident flux. Comparisons of the monitor spectrums of the experimental runs clearly demonstrated that such variation can be as large as 10% at long wavelengths and is consequently non-negligible. This problem is readily overcome using the monitor spectrum from a reference run, and comparing it with the monitor spectrum in the each experimental run. This should be implemented as part of the standard focusing procedure.

In conclusion, however, no new information on the disorder of the oxygen atom in ice VII was found. It had become clear that in order to directly distinguish between the $\langle 100 \rangle$ and $\langle 111 \rangle$ models, it would be necessary to exploit the higher

accuracy of single-crystal techniques. To this end, a significant development project was embarked upon, and it is this that constitutes the remaining content of this thesis.

Chapter 4

Single-Crystal Time-of-Flight Laue Diffraction With the Paris-Edinburgh Cell

4.1 Introduction

This chapter contains the first section of the authors development of single-crystal neutron diffraction techniques at high pressure. These are developments which apply to sample crystals that are pre-grown prior to loading and to the application of pressure. Furthermore, all of the work described here is based around the PEARL-HiPr diffractometer at ISIS and use of the Paris-Edinburgh cell. Developments involving in-situ growth of sample crystals at high pressure are described later in Chapter 5. Whilst, in its nature, much of the work is instrument specific to HiPr, many of the conclusions which were derived are of general use and are summarised in the concluding section of this chapter.

In order to take the following discussion to a suitable level of detail, it will be necessary to go into some depth in explaining the nature of the neutron source and the detectors used. In addition, the PE cell will be described, as its use to apply

pressure to single-crystal samples (for diffraction work), is new. It was necessary to develop specialised techniques to measure single-crystal intensities on the HiPr powder detectors and the development of the mechanics of the experiment in addition to the methodology will be discussed.

However, it is in the analysis which follows the initial 'counting of neutrons' in which much of the gritty detail resides, and suitable time will be dedicated to describing this process. The end result has been the accurate measurement of single-crystal intensities and structure factor extraction at pressures up to (but not limited to) 7.2 GPa. This has increased the pressure range available for neutron single-crystal diffraction (NSCD) by a factor of three, and in doing so makes a large sphere of new crystallography, and thence science, accessible.

The remainder of this introductory section is devoted to describing the set-up on HiPr, and the procedures in use for *powder diffraction* which existed prior to the development of single-crystal techniques.

4.1.1 The Paris-Edinburgh Cell and the PEARL Beamline

PEARL (the Pressure and Engineering Advanced Research Line) came into being in 1995 and was the home for an instrument specifically designed to perform high-pressure powder-diffraction measurements using the Paris-Edinburgh cell. Named after the two Universities collaborating in its design inception and commissioning, this recently developed high-pressure cell had demonstrated an ability to perform high quality neutron-powder diffraction at pressures a factor of ten higher than that which was previously accessible ([15] [56]).

The diffractometer, known as HiPr (High Pressure), was designed around the PE cell. This provided a large scope for optimisation of data collection. Notably, it has resulted in the use of two complimentary geometries for data collection

which, as of 1999, have been supported by a full complement of thirteen ZnS scintillator detector-modules. Whilst HiPr has been demonstrably successful in high-pressure powder diffraction prior to the work described here [57] [58] [59], no attempt had been made to use it to measure single-crystal intensities. The strong motivation for such measurements has been discussed previously, and its technical realisation comprised a major part of the work presented in this thesis.

The PE cell itself has been an important tool in many fields of high-pressure research for over a decade now. The cell has been described in detail before (see for example [56] [15] and [60]) so here only a brief introduction will be given. All of the specific developments comprising the subject matter of this thesis have involved modification of subsidiary components (eg. mechanisms to rotate the cell, and collimation specific to the HiPr diffractometer), and it is on these that the author will concentrate.

All of the different incarnations of the PE cell have the same basic design. They are comprised of a hydraulic piston-cylinder arrangement which applies a force against a platen held in place by four 'tie-rods'. The various versions of the cell have different sizes and load capacities, but all of the single-crystal developments described here used a V4 type cell, which has a maximum load capacity of 200 tonnes. A schematic of the V3 cell is shown in Figure 4.1, this is identical to the V4, apart from the lack of a rear channel through the cylinder.

The application of pressure to the sample is achieved by the arrangement of opposed anvils and seats between the piston and the platen. The anvils compress a metal gasket which communicates the pressure to the sample (see Section 4.3.3). Access to these parts is through the breech in the platen. The anvils and gaskets used in regular powder work with the PE cell have a toroidal geometry [61]. This design minimises the ratio of sample radius to gasket radius which is crucial for a cell where diffracted beams must exit through the attenuating material of the gasket. The standard anvils used at ISIS are made from tungsten-carbide but are also available in sintered diamond which although expensive is a superior

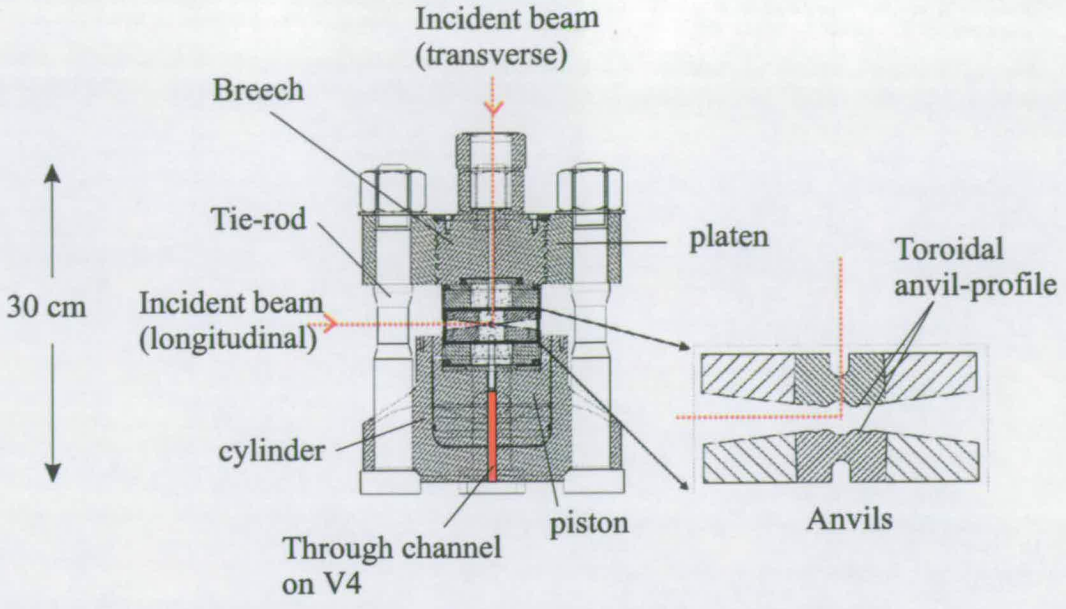

Figure 4.1. A schematic of the V3-type PE cell (note the aperture through the breech for incident radiation in the transverse mode. The V4 is identical, but has a rear channel through the piston and cylinder section as indicated by the red line. On the right of the figure is a close up of the two opposed anvils. Note the toroidal groves on the faces of the anvils.

material in terms of both its mechanical and neutron properties. The gaskets used are multi-part assemblies made from Ti:Zr alloy (see Appendix A).

An important element of the design of HiPr was the use of a tank and cradle arrangement which supports the PE cell and facilitates rotation about its axis. The purpose of the tank is to provide a vessel for containment of liquid nitrogen, which is used to cool the cell during low temperature diffraction work. However, it is also an integral part of the alignment system for the cell and consequently is used even for room temperature work. The entire tank-cradle arrangement weighs around 150kg and is lowered onto the beamline with a small crane. Once in its berth on the beamline, alignment consists of translating the cell along the incident beam direction using a camera system which is pre-aligned to a laser-centred target. This simplicity of alignment is a major benefit of TOF measurements, which allows for fixed detectors which can be surveyed accurately into place.

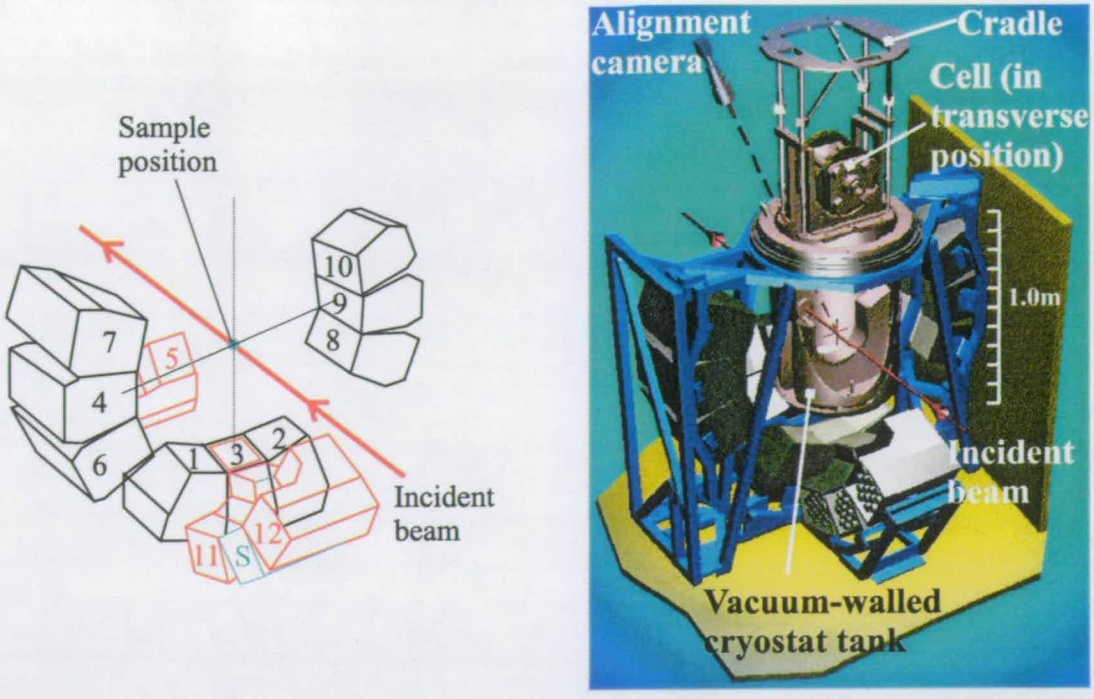

Figure 4.2. The right-hand image shows a computer generated image of the PEARL-HiPr diffractometer, the tank is mounted in its berth within the instrument, and the cradle - complete with PE cell - is being lowered into it. Note the direction of the incident radiation and the transverse and longitudinal banks of detectors (they are respectively perpendicular and parallel to the incident beam). The left hand image shows a schematic of the two detector banks - the longitudinal bank is in red, whilst the transverse bank is in black (note that detector module 3 is shared by the two banks). The numbers of each individual module are recorded with the single-crystal module indicated by an S and by a blue outline.

As the anvils have a very limited aperture of $\pm 7°$ about the cells equatorial plane, only one of the perpendicular detector banks can access the diffraction signal at any one time. For example, in the transverse mode where the cell is perpendicular to the incident beam, the accessible angle is 83° to 97° in 2θ. In this setting, the longitudinal bank (which extends from 19.5° to 161.5°) is entirely occluded (by the body of the cell itself), apart from module 3, which is perpendicularly below the sample, and is shared between the two banks.

For this reason, the entire arrangement of tank and cell must be rotated by hand between the two positions. In Figure 4.2, the cell is seen being lowered into the

transverse position. A rotation of 90° about the vertical axis brings the cell into the longitudinal setting where both incident and diffracted beams pass through the gasket. In either orientation, the cell has one more degree of freedom and this is a possible rotation about an axis coincident with the load axis and therefore coincident with the incident beam in the transverse mode and perpendicular in the longitudinal mode.

4.1.2 Time-of-Flight Laue Diffraction

The ISIS facility is one of five routinely functioning spallation neutron sources (SNS) in the world. The initial energy for neutron generation in sources of this kind comes from a particle accelerator, usually a synchrotron. At ISIS, a linear accelerator is used to accelerate H^- ions up to energies of $70MeV$ which are then injected into a synchrotron ring. At this stage, the electrons are stripped off the hydrogen ions by $0.3\mu m$ of aluminium oxide foil and the remaining protons are then accelerated up to $800MeV$. When this energy is reached, the protons are ejected from the ring by powerful 'kicker' magnets, and channeled down a vacuum path to a target composed of sheets of heavy metal which, in the case of ISIS, is tantalum. This entire process is repeated fifty times a second.

The protons colliding with the target have sufficient energy to excite the Ta nuclei, which then decay by a variety of routes. Spallation is one of the prominent decay processes that results in the ejection of some tens of neutrons per incident proton. As the number of neutrons produced is approximately proportional to the number of protons incident to the target, the latter is often used to quantify the former. The number of incident protons in a given run is given by the product of the proton beam current and the time for which data is collected. This number is conventionally given in units of microamp hours ($\mu Ahrs$), and its total is recorded for all runs in the files that contain the experimental data.

The neutrons produced by the arriving protons tend to have rather high energies

(of the order of 1 MeV) and, as with reactor sources, must be moderated to reduce their energy to a useful level. What constitutes a *useful* level depends on the particular science which is being performed and typically several different moderators are used to provide a wide range of available neutron energies.

Any given neutron entering the material of the moderator is subjected to many collisions which dramatically reduce its energy. Within a timescale (of the order of 1 μs) far shorter than the 20 ms separating the pulses from the target, the majority of neutrons will equilibriate with the moderator. This results in the production from the moderator of polychromatic pulses with a smoothly varying energy distribution which peaks at the characteristic energy of the moderator (given by its temperature). For most experimenters, the moderator can be considered the effective 'source' of the neutron radiation.

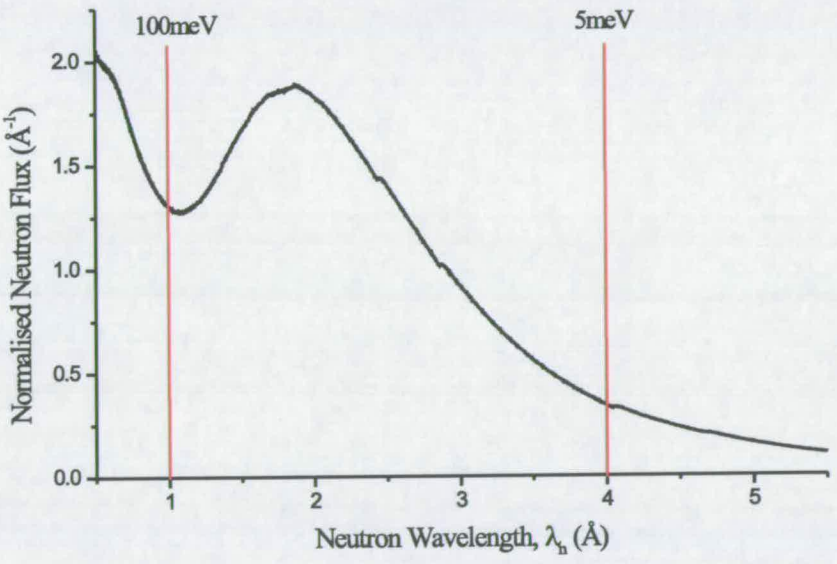

Figure 4.3. The neutron-flux profile from the ISIS 100K methane moderator as a function of wavelength. The energy E of the neutrons is related to the wavelength λ via $E_n = \frac{h^2}{2m_n\lambda^2}$ (m_n is the neutron mass) two reference energies are marked on the diagram. Note the faint presence of Bragg edges that arise from the aluminium material of the moderator containment vessel.

For diffraction studies low-energy, long-wavelength (of the order 1Å) neutrons

are appropriate. The PEARL beamline views a liquid methane moderator maintained at 100K. The flux profile of this moderator is shown in Figure 4.3. At these low energies (of the order 3-300 meV) neutrons are non-relativistic, and their energy E is related to their momentum p by $E = p^2/2m_n$. Consequently, as the neutrons travel away from the moderator they disperse themselves in space according to their energies, the more energetic overtaking the less. In the time-of-flight technique (TOF), timing electronics, which are synchronised with the pulses from the target, measure the exact arrival time of a detected neutron. As the flightpath is known, the arrival time determines the velocity and therefore the energy of an arriving neutron.

It is important to note that the physics of the moderator results in an asymmetric peakshape for TOF diffraction. This is due to the gradual (over a period of tens of μs) diffusion of neutrons from the moderator material after the initial pulse, an effect that can be described by a decaying exponential function. In the absence of this diffusion effect, the diffraction peaks are symmetric in time, having a finite width as a consequence of both the divergence of the beam, and the distribution of domains within the crystal samples. This symmetric peakshape can be accurately modeled with a Gaussian distribution, which is then convolved with the decaying exponential to give the a good model of the measured peakshape [62]. This function, often abbreviated to GEC (Gaussian-exponetial convolution), is encountered in the subsequent two chapters, as it is used to integrate single-crystal reflections.

Spallation neutron sources are naturally suited to TOF methods, but they are also possible on continuous reactor based sources (For instance the ILL research reactor in Grenoble has five TOF instruments: IN4,IN5,IN6,D7 and BRISP). This is achieved by use of a rapidly rotating 'chopper'. In essence this device is simply a disk made from neutron-opaque material placed in front of the moderator which contains a small groove through which neutrons can pass. When the chopper is rotated, the moderator is only revealed in flashes through this groove, thus,

effectively creating a pulsed source.

A given moderator may be viewed by several *beam-guides*. These tubes, leading to the different neutron instruments themselves, are evacuated to remove air absorption (which can be significant, especially if the air is humid or if the flightpath is long.). In addition to the material comprising the moderator, the properties of a beam-guide also strongly affect the characteristics of a TOF neutron instrument. By far the most significant property is the length of the beamline. Here a trade-off is made between flux (decreasing with distance from moderator in accordance with the inverse-square law) and resolution. The energy resolution increases with pathlength, as neutrons with differing energies will disperse more widely in their times-of-flight. Also, the divergence of the beam is dependent on the angular size of the moderator viewed from the sample position, and, as such, becomes narrower as the pathlength increases.

4.1.3 The PEARL-HiPr Detector Bank

The detectors on HiPr all make use of ^{6}Li-doped ZnS scintillator material. Individual neutrons interacting with the strongly absorbing ^{6}Li atoms produce alpha particles, which then interact with the ZnS generating a flash of visible light. Subsequently, this is channeled by a fibre-optic cable into a photo-multiplier tube which detects the flash, sending a digital signal to the counting electronics.

The shape of the scintillator part of the detector is designed to optimise the competition between absorption of neutrons and absorption of light. The probability of a neutron interacting with the ZnS is proportional to its pathlength through the active material. However, the probability that light generated by this interaction will escape to reach the optical fibre decreases exponentially with depth.

All of the twelve powder detector-modules on HiPr use a 'V' design as shown in cross-section in Figure 4.4. The active material of the detector is entirely enclosed

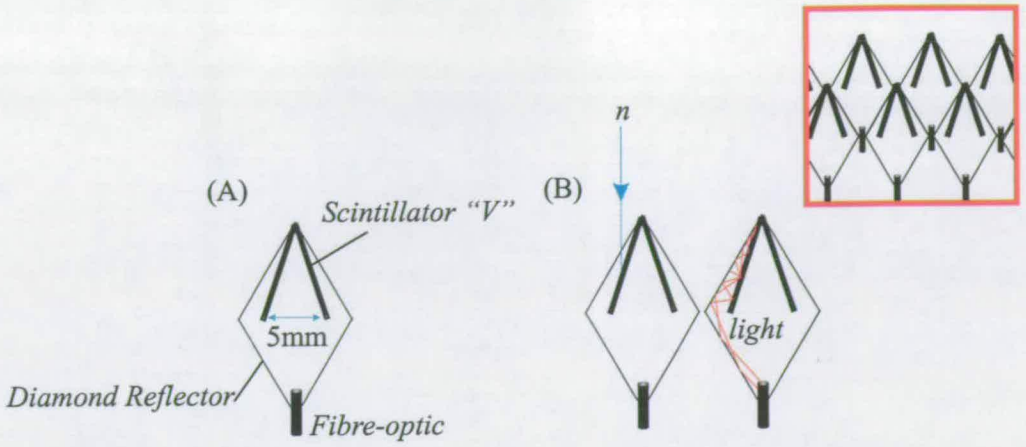

Figure 4.4. Part *A* shows a powder-detector element in cross-section contained in its diamond-shaped containment cell. Part *B* illustrates the interaction of a neutron with the scintillator 'V' and the resulting light being reflected towards the optical fibre by the cell. The insert shows how the diamond cells are stacked along rows within the modules resulting in an up-down-up arrangement of detectors.

in a diamond-shaped opaque cell. This cell ensures that only light originating from the arrival of a neutron is detected. It also has a second purpose, which is to act as a reflector which re-directs emitted light towards the optical fibre at the rear of the detector.

Each detector presents an active area of 50×5 mm^2, (with the long dimension running perpendicular to the 'V') and a complete detector module is comprised of 120 of these, which are stacked as indicated in the insert of Figure 4.4. These stacks are tilted such that the detectors all lie at a constant distance from the sample position

The rectangular area of the detectors (viewed from the sample position) results in a non-uniform spacial resolution across the face of the modules. For powder diffraction, it is most important to have a high resolution along the direction of 2θ, so that accurate d-spacings can be extracted. The detectors are arranged within the modules in a way such that this is the case.

As described previously, these powder modules are suspended around the sample position along two perpendicular arcs as shown in Figures 4.2 and 4.5. The first

Detector name	2θ angle subtended	azimuthal angle subtended	Detector Bank
TPM01	83-97°	192.5-212.5°	T
TPM02	83-97°	152.5-172.5°	T
TPM03	80.5-95.5°	172.5-192.5°	T + L
TPM04	83-97°	260-280°	T
LPM05	19.5-39.5°	172.5-187.5 °	L
TPM06	83-97°	240-260°	T
TPM07	83-97°	280-300°	T
TPM08	83-97°	100-120°	T
TPM09	83-97°	80-100°	T
TPM10	83-97°	60-80°	T
LPM11	89.5-119.5°	83-97°	L
LPM12	141.5-161.5°	83-97°	L
SXM	120.5-140.5°	83-97°	L

Table 4.1. Shows the positional parameters of all of the thirteen modules comprising the two detector banks. The azimuthal angle is defined with zero vertically up, and increasing clockwise looking along the neutron beam direction (note that the values for the modules in the transverse bank are nominal, whilst those in the longitudinal bank have been accurately determined using the single-crystal techniques described in Section 4.2.1).

of these banks, which lies at 90^o to the incident beam, is the main workhorse for powder diffraction. This *transverse* bank contains nine modules, and the signal observed in each constituent detector can be combined to give a high signal-to-noise ratio. The second *longitudinal* bank, which contains the remaining three powder modules, gives access to a wide range of 2θ values between 20° and 156°. It should be noted that one detector module is shared by both the transverse and longitudinal banks. The positions of the detectors are given in Table 4.1, along with the naming convention used (which reflects the chronological numbering scheme and the type of module).

In order to maintain the required high-resolution in the 2θ direction, two different arrangements of detector within the modules of the transverse and longitudinal bank are required. These will be referred to as transverse powder modules TPMs and longitudinal powder modules LPMs respectively. Figure 4.6 illustrates how

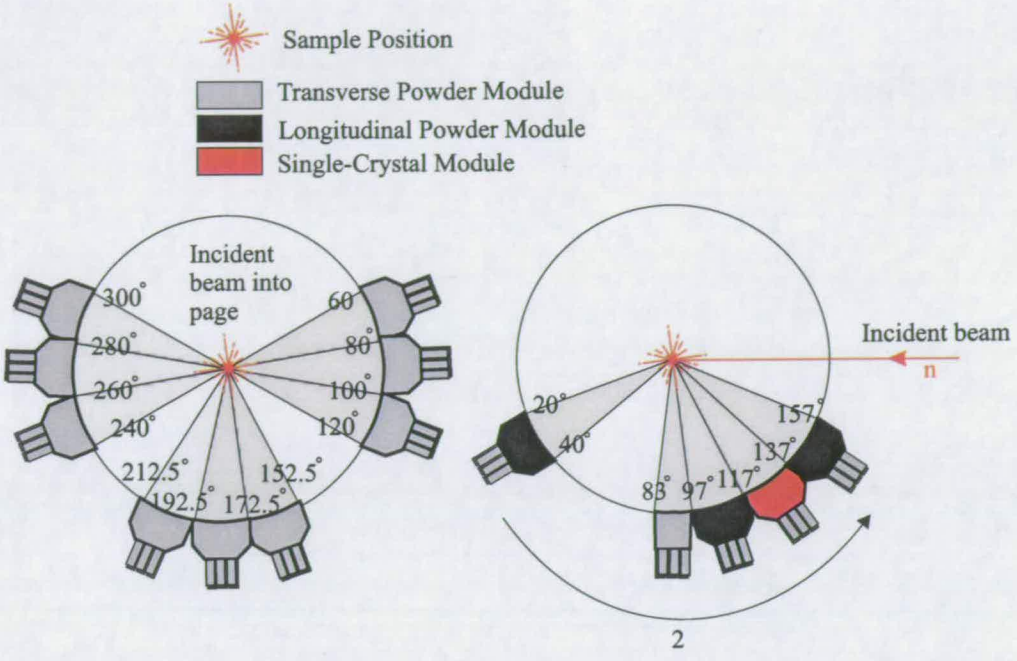

Figure 4.5. A map of both detector banks on PEARL indicating the angular position of each detector module. The figure on the left shows the transverse bank with the beam travelling into the page. The figure on the right shows the longitudinal bank with its modules distributed along the 2θ direction.

the detector elements are arranged within each module.

It is vital for the subsequent analysis of the recorded neutron data that the detector elements have an unambiguous number-scheme. On HiPr, the data analysis was complicated by the existence of three different modes of operation:

1. **The transverse mode**: Only data in the transverse detector bank are recorded.

2. **The longitudinal mode**: Only data in the longitudinal detector bank are recorded.

3. **The all mode**: Data in all detector modules are recorded.

Unfortunately, each of these modes has a different numbering scheme and throughout analysis of data care must be taken not to confuse these. Furthermore, the

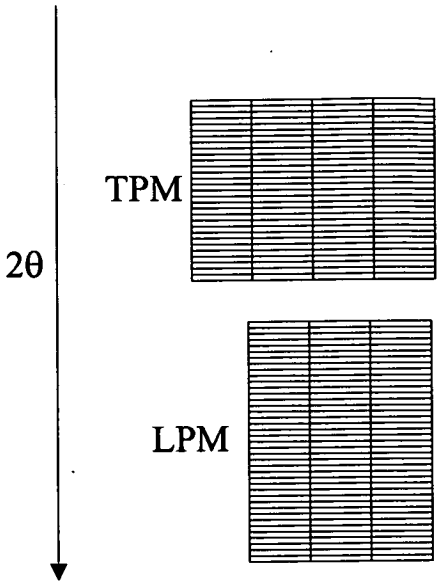

Figure 4.6. Figure shows the different arrangements of detectors comprising both the LPMs and TPMs.

numbering scheme of the detectors in the longitudinal mode was unknown, and had to be determined experimentally by the author (see Section 4.4.1).

The detector modules are suspended around an arc that has a radius of 600 mm, this results in each subtending angles of approximately 20° by 15°. The thin dimension of the modules was chosen to match the angular aperture of the standard toroidal anvils used with the PE cell: $\pm$ 7°.

Whilst these detectors banks are sufficient for powder diffraction, for single-crystal diffraction, a high resolution is also required in the direction perpendicular to 2θ. For this reason, it was necessary to install the 13^{th} detector module into the longitudinal bank of HiPr. This, so called, single-crystal module (SXM) does not use V type scintillator, but instead is comprised of a single continuous sheet of ZnS. This is then divided into 1280 square elements, each of 0.5×0.5 mm^2, by a grid of neutron-opaque material. A separate fibre-optic connects each of these elements to the photomultiplier tubes.

Such a detector operates at approximately 30% of the efficiency of the 'V'-detectors, as it presents a significantly shorter pathlength of ZnS for the incoming neutrons. However, its increased resolution is vital for determining the orientation of sample crystals. The surface area of the SXM was chosen to match that of the TPM and LPMs, and this resulted in a grid that divides the surface into 40×32 elements.

4.1.4 Calibration of Detectors for Powder Diffraction

In order to determine accurately the energy of a neutron from it's time-of-flight, it is necessary to know exactly the flight path. However, in order to only obtain d-spacings it is sufficient to determine the product $L \sin\theta$. This follows directly from Bragg's law, writing the wavelength in terms of the neutron momentum p_n, thus giving

$$2d \sin\theta = \lambda = \frac{h}{p_n} = \frac{h}{m_n v_n} = \left(\frac{h}{m_n}\right)\frac{T}{L} \tag{4.1}$$

where T is the time-of-flight and L is the flightpath.

For the full extraction of structure factors, though, it is necessary to perform wavelength dependent corrections. This is a more complicated problem, as it involves the de-coupling of L and $\sin\theta$. As each detector module on HiPr has been accurately surveyed in place, the absolute error on L can be taken to be <1 mm. Additionally, the total flightpath from moderator to detector is large (12.6124 m) and, thus, the contribution to the error in λ is at the $\pm 0.01\%$ level. The error in measuring 2θ for each element is far more significant, and this will be discussed further in Section 4.2.1.

For powder diffraction, the problem of determining the pathlength is side-stepped. This follows from the fundamental assumption of powder diffraction itself: that the intensities measured on any part of the Debye-Scherrer ring are equivalent.

This means that, as long as the *relative* intensities observed in each detector are the same, then the patterns may legitimately be merged without any loss of information[1]. This is achieved by a procedure known as *focusing* were each pattern is converted (using the $L\sin\theta$ constant) into a function of d-spacing, corrected for incident flux and detector efficiency, and then summed.

The $L\sin\theta$ constant is typically measured experimentally by placing a calibrant powder-sample with a known structure at the sample position. For this purpose, a strong scatterer with a simple structure (typically Si or Ge) is most convenient. The resulting powder diffraction pattern is then recorded in each detecting element as a function of time-of-flight. As the structure of the calibrant is known, the powder pattern can be fitted by refining the $L\sin\theta$ constant of proportionality. This is done accurately by performing a Rietveld refinement [36] on the observed pattern in each element.

In order to extract accurate structure factors, it is also necessary to calibrate the efficiency, $\epsilon(\alpha,\lambda)$ of each detector α. The denominator in the Buras-Gerward Equation 2.9, which is rewritten below in Equation 4.2, may be taken to contain an effective flux term $i_{eff} = \epsilon(\alpha,\lambda)i_o(\lambda)$, which includes both the wavelength dependence of the detector efficiencies and that of the flux emitted from the moderator.

$$I(h,k,l) \propto \frac{I_o(h,k,l)L(\theta)}{\lambda^4 i_o(\lambda)\epsilon(n,\lambda)A(\lambda)E(\lambda)} \tag{4.2}$$

An assumption used for powder-diffraction analysis on HiPr is that the wavelength dependence of the efficiency is the same for all detectors. Furthermore, the incident-flux term $i_o(\lambda)$ will also be the same for each element, as they all lie at a constant distance from the moderator (although it must be remembered that

[1]It is well known that this assumption breaks down for non-perfect powders which may suffer from preferred orientation and texture effects [35]. Indeed it was the need to investigate these kind of effects (which are especially prevalent at high-pressure) that lead to the development of the two detector geometries available on HiPr [63].

as a function of *d-spacing* this will depend on the particular 2θ of a detector). Combining these results, it is possible to separate the equation for the incident flux into wavelength-dependent and wavelength-*in*dependent parts

$$i_{eff} = \epsilon_a \epsilon(\lambda) i_o(\lambda) = \epsilon_a \epsilon i_o(\lambda) \tag{4.3}$$

The combined term $\epsilon i_o(\lambda)$ can be determined by measuring the incident flux as observed by each detecting element. The technique employed is common to all ISIS detectors and takes advantage of the nuclear properties of the element vanadium. This has a very small coherent-scattering cross-section, σ_{coh}, constituting less than 0.4% of the total scattering cross-section, σ_{tot}. Consequently, the bulk of the scattering is incoherent and thus wavelength independent and directly reflects the incident flux. As a result, the TOF spectrum measured in each element is closely related to the required function $\epsilon i_o(\lambda)$. It is only necessary to correct this for absorption and multiple-scattering effects within the vanadium calibrant itself. To simplify the absorption correction, a spherical sample is used and then a Monte-Carlo simulation [64] applied to calculate the combined correction factors. These are then applied to the flux measured in the detectors to give the correct functional form of $\epsilon i_o(\lambda)$.

As this is taken to be the same for all detectors, it can be well determined by combining all of the vanadium spectra measured in individual elements. This assumption allows a significant saving of time in the measurement of the effective flux. Of course, when the correction is subsequently applied to powder patterns measured in individual spectra, it must be converted into a function of d-spacing using the appropriate $L \sin\theta$ value for each specific detector.

Finally, the term ϵ_a is a constant unique to each element. It reflects non-wavelength dependent effects which occur *after* the scintillation event. These effects are due to factors such as the efficiency of the photo-multiplier tubes and the exact positioning of the connecting fibre-optic cable. It is possible to obtain

ϵ_α from the same vanadium measurement which gives the wavelength-dependent part of the efficiency. Again, the constant L approximation is employed, and the flux profile observed in each detecting element is integrated across a constant TOF range. The value of this integral is then taken to be proportional to ϵ_α.

4.2 Single-Crystal Measurements in the PEARL-HiPr Powder Modules

Detectors which have been primarily designed for powder diffraction are likely to present inherent difficulties for the measurement of single-crystal intensities. These difficulties had to be overcome in order to take advantage of the far larger area of active detector surface that constitutes the powder modules. All of the developmental single-crystal work was confined to the longitudinal bank, so full use could be made of the SXM whilst tackling the primary issues of data collection.

4.2.1 Calibration of Detectors for Single-Crystal Diffraction

One of the first problems which was encountered was the calibration of the detectors for single-crystal measurements. In single-crystal diffraction, the diffraction pattern is fully three dimensional, therefore, individual Bragg reflections are observed at different angles instead of an entire diffraction pattern being observed at every point in space. This means that structure factor extraction must occur individually for each reflection, and this requires the decoupling of L and $\sin\theta$. Additionally, the values of $L\sin\theta$ were not known for the SXM. This is because the individual elements are too small, and too inefficient to accurately determine a powder pattern from the calibrant sample.

In principle, the decoupling of L and $\sin\theta$ can be achieved by a complex process using a non-stationary sample. In this approach, a powder sample is used to refine $L\sin\theta$ (as in Section 4.1.4). The sample is then displaced a known amount along the incident beam direction, and the procedure repeated. From the observed variation of the refined $L\sin\theta$ and the known change resulting from the displacement of the sample, it is possible to decouple the two terms. Unfortunately, in practice this approach is impractical and prohibitively expensive in terms of the required beamtime. A more practical approach was developed using the reflections from a single-crystal sample to calibrate the position of the detectors.

The crystal structure determines the scattering vectors for each reflection for any given orientation of the crystal relative to incident beam. If both the structure *and* orientation are known, then this translates into a knowledge both of d-spacing and scattering angle, therefore giving us λ by default through the application of Bragg's law. Whilst, in principle, this provides a means to calibrate accurately the detector banks, orientating a crystal had not been attempted before on HiPr.

The techniques for determining the orientation of a crystal in a diffractometer have been described in detail elsewhere (see for example [22]). This standard approach requires the application of two matrix operators describing

1. The rotation of the basis vectors of the reciprocal lattice onto a Cartesian set fixed relative to the crystal - the *crystal* frame, **C**, a matrix conventionally called B, and

2. An operator describing the rotation of **C** onto a second Cartesian frame fixed relative to the diffractometer - the *diffractometer* frame **D**, conventionally called U.

The successive application of these two operators, UB, applied to a general reciprocal lattice vector will thus give the coordinates of that vector in the frame **D**.

In a standard single-crystal experiment, this matrix operator is used to identify the *hkl* indices of observed reflections. However, its inverse may also be used conversely to give the diffraction vector for a given reflection in the frame **D**. This is the approach which was used to calibrate the powder modules for single-crystal work.

Vital to this procedure for orienting the calibration crystal was the full two-dimensional resolution of the single-crystal module. For a known crystal structure, it is sufficient to measure the scattering vector of only two reflections in the diffractometer frame to determine fully the UB matrix. But, as even the resolution of the SXM is still fairly coarse, it was necessary to measure several reflections and then refine the UB matrix.

The procedure developed was as follows:

- The sample crystal is placed in the PE cell in the cradle arrangement with the encoding mechanism as described in Section 4.3).
- Strong reflections observed in the longitudinal bank are then indexed from their observed d-spacings and the approximate angles separating them.
- The cell is then rotated about its axis to bring these reflections one-by-one into the SXM. For each of these reflections four coordinates are determined
    1. The coordinates in pixels of the reflection on the SXM face i, j.
    2. The time-of-flight of the reflection, determined by fitting a Gaussian to the peak.
    3. The angular position of the cell about its rotation axis ω.
- This information is then used to refine the UB matrix using generalised software for multi-element detectors [70].

Several variables are required in this procedure and several assumptions are made. The most important of these is the angle γ, defined as that between the incident

beam and the vector $\mathbf{d}_{sd}$ joining the sample position and the centre of the detector. The pathlength from sample to detector is known, and it is assumed that the detector is flat and perpendicular to $\mathbf{d}_{sd}$. This allows the conversion of pixel coordinates into a vector in the diffractometer frame **D**. This information, combined with the known index of a measured reflection, and the lattice parameters, allows the angle γ to be determined from the measured TOF. If a sufficient number of reflections are measured, these assumptions can be relaxed and both the angle γ and the tilt of the SXM can be refined freely in the UB determination.

Once the UB matrix has been determined, it can be used to calibrate the positions of the powder modules. In principal, this would require tracking a single-crystal reflection of known index into each element - a very time consuming and expensive procedure. In practice, it appears sufficient to do this for only a few elements and extrapolate using the known geometry of the modules and to exploit the measured product $L \sin\theta$.

Also, it is worth noting that for the majority of single-crystal experiments there will not be any structural transition. In this situation (and given that the lattice parameters are known), the UB matrix can be determined for each pressure point. In this case, the required calibration information is determined by default for each single-crystal reflection that is measured, and, therefore, the comprehensive mapping out of the detectors is not required.

4.2.2 Single-Crystal Intensity Measurement

Intensity measurement is the single most important process in a single-crystal experiment. For any multi-detector instrument - like HiPr - it is vital that intensities are measured in an exactly equivalent fashion in each element. Where detector modules like the SXM are used, this simply means that each element must be correctly calibrated. However, the powder modules presented a particular difficulty in this respect. This was a consequence of the geometry of the

active scintillator used. As has been described in Section 4.1.3, they have a non-continuous V-type arrangement. Furthermore, each detector is handmade, and consequently there is the possibility of a rotation of the V about its vertex. This could result in the presence of a gap in-between the rows constituting the active face.

This being the case, one of the first uses of the single-crystal module was to investigate the possibility of gaps between the up-down arrangement of rows. This was achieved by measuring a single-crystal reflection in the SXM and then rotating the same reflection into the powder modules. As the SXM is constructed from a single continuous sheet of scintillator, there is no possibility that neutrons will be lost down gaps. Thus, the integrated intensity of a reflection measured here can be used as a reference against which the powder detectors can be compared.

The measurement that was performed was to locate the 400 reflection of a sample crystal[2] into the SXM and both TPM03 and LPM12 (each at lower and higher 2θ angles, respectively, than the SXM). These two powder modules are separated by a large 2θ angle, allowing wavelength-dependent effects to also be investigated. The crystal was ground by hand into a disk with radius 2.0 mm and thickness 1.0 mm, this was large enough to produce a reflection which spanned several elements in each detector. In each of these elements, the number of neutrons in the observed peak was integrated with respect to TOF by fitting with a Gaussian-exponential convolution (GEC) function (as described in Section 4.1.2).

By reducing these intensities to structure factors using the Buras-Gerward Equation 4.2, any geometric and detector-specific effects are removed. At this stage, both absorption and extinction effects were ignored.

Each integration will sample the single-crystal peak at the position of the detector, measuring its average value across the width of that particular element. The full peak can then be reconstructed by fitting these sampled intensities with some

[2]In this case, the sample crystals used were potassium di-hydrogen phosphate (KDP) and its deuterated analogue (DKDP).

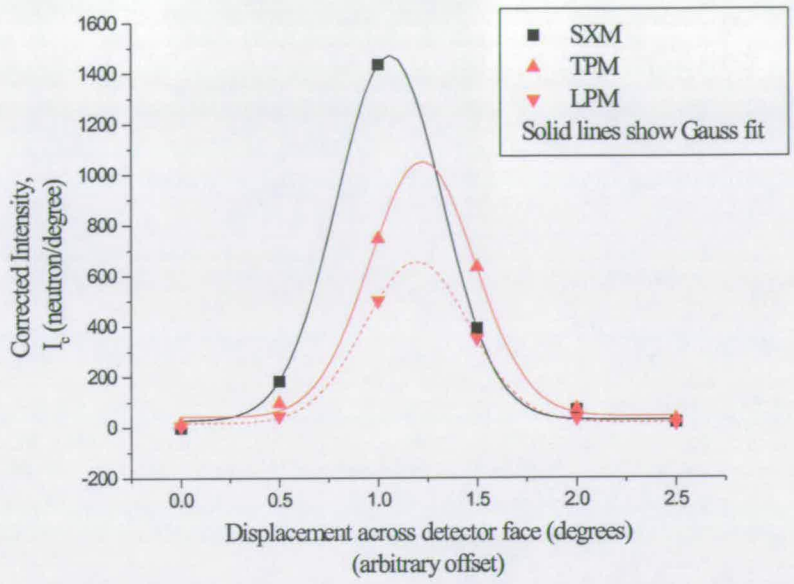

Figure 4.7. Gaussian fits to the corrected intensity of a DKDP 004 reflection measured in the SXM and - more weakly - in both TPM03 and LPM12.

peakshape. It was assumed that a simple Gaussian would provide an acceptable peakshape for the purpose. This is justified as the angular size of the reflection on the detector face is comparative with the divergence of the incident beam. If this were not the case, one would expect the peak to exhibit a flat-top. The form used was that of Equation 4.4. The same fit was performed in both of the powder modules with the peakwidth (w) constrained to be the same as that fitted in the SXM.

$$y = y_o + \frac{A}{w\sqrt{\pi/2}} e^{-\frac{(x-x_c)^2}{2w^2}} \tag{4.4}$$

In this equation, y_o is a flat background, A is the area of the Gaussian. The peak is a function of angle on detector face x (measured in degrees) and is centred on x_c.

The corrected intensities are shown in Figure 4.7 and the fitted parameters are recorded in Table 4.2. The area of the Gaussian, (A) is proportional to the square of the observed structure factor $|F_o|^2$, whilst the parameter y_o measures a simple

h k l	*parameter*	TPM03	SXM	LPM12
004	y_o (neutrons per degree)	44	29	27
	A (neutrons)	682	974	422
	w (degrees)	0.531	0.531	0.531
	λ (Å)	2.529	3.232	3.399
008	y_o (neutrons per degree)	478	30	307
	A (neutrons)	3189	3149	3249
	w (degrees)	0.519	0.519	0.519
	λ (Å)	1.264	1.616	1.700

Table 4.2. The parameters of Gauss fits to both the 004 and the 008 single-crystal reflections in two powder modules, and the single-crystal module.

linear background. It is clear that the SXM measures a significantly higher value than the powder modules. A decrease in $|F_o|^2$ with increasing 2θ (and therefore increasing λ for a given d-spacing) could be attributed extinction or absorption effects, but this cannot account for the decrease in moving from the SXM to TPM03, which is at a lower 2θ. This was initially taken to be direct evidence of gaps between the elements of the powder modules.

An advantage of TOF-Laue diffraction is that all of the reflections along a given angle in reciprocal space are observed simultaneously in the same detector element. For a high-symmetry direction such as the 00l, this means that all of the symmetry allowed harmonics can be used to examine wavelength dependent effects. For the KDP sample that was used, the 008 reflection is allowed by symmetry, so this could also be integrated.

As this reflection is being probed by shorter-wavelength (and therefore higher-energy) neutrons, effects such as absorption are much reduced. However, this can have no effect on intensity loss due to gaps in the detecting material. The results are shown in Figure 4.8, with the Gaussian fits recorded in Table 4.2. Unexpectedly, they demonstrated that the reduction in intensity observed in the powder modules for the 004 was not evident at lower wavelength. Thus, it was *not* due to gaps, but instead looked very similar to an absorption effect.

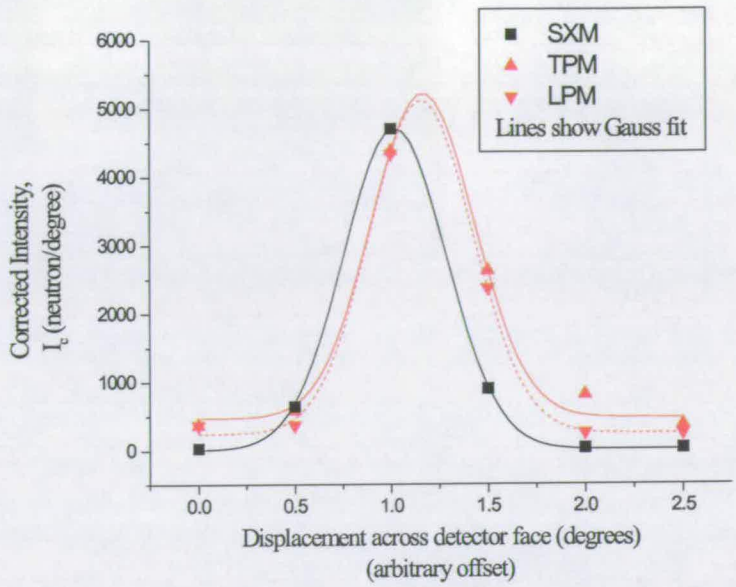

Figure 4.8. Gaussian fits to the corrected intensity of a DKDP 008 reflection measured in the SXM and in both TPM03 and LPM12. Unlike the 004 reflection (Figure 4.7), the powder modules measure a comparable intensity with the SXM.

This result was at first surprising, because there was no material between the sample crystal and the detector face that could account for such an effect. Additionally, the measured correction $\epsilon i_o(\lambda)$ should take account of the wavelength response of the element. Any explanation had to account for this, and also the fact that there was no evidence of this effect in the many powder experiments which had been performed on HiPr.

An effect that is probed by the measurement of a single-crystal reflection and *not* by a powder measurement is the possible asymmetry of the powder-detector elements. In single-crystal diffraction this is now an issue as the scattered intensity is localised in space and is potentially only viewed by one small portion of a detector element.

By consideration of the arrangement of detector elements in the powder modules a possible explanation arose. This is illustrated in Figure 4.9, which demonstrates how the misaglignments of the V about its vertex that could result in gaps might also result in overlaps of elements in the lower rows. This would lead to absorption

of the scattered beam and, thus, to variation of the wavelength dependence of the detectors response. Also, by its nature, both the gaps *and* the over-laps could be spread at random around the entire active area of the module.

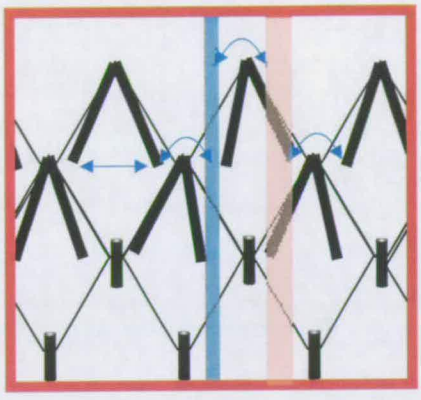

Figure 4.9. The figure shows the possible ways in which the detector 'V' elements can deviate from their ideal geometries. In particular, the blue strip illustrates how such deviations can result in gaps between adjacent detector elements. In addition, the pink strip indicates the possible resulting overlaps. Another possibility is that the V can spread out, which could also result in overlaps.

The strategy employed to explore this result in more detail was the development of a scanning technique. Here, individual single-crystal peaks are scanned across the detector face in steps.

The logic of this is clarified by consideration of the extreme case where an occluded section of an element is completely non-detecting. In each step of a scan, the visible section of the peak is sampled. Consequently, if a sufficient number of steps, of a small enough size, are taken, then the entire peak can be reconstructed from only those observations in the non-occluded part of the detector.

This required the development of motorised rotation of the cell and the capability to measure this rotation accurately. The development of these mechanisms is described in detail in Section 4.3.1. At the time when these measurements were performed, an earlier, low-resolution encoder was in use. This permitted scanning of the single-crystal peak in rather large steps of $\sim$0.25°. The scans were then

fitted with a Gaussian in the same way as has been described previously for stationary reflections (after the appropriate conversion of units: the angular step of the reflection is twice the rotation of the cell). The results for both the 004 and 008 reflections are shown in Figure 4.10. with the fitted parameters recorded in Table 4.3.

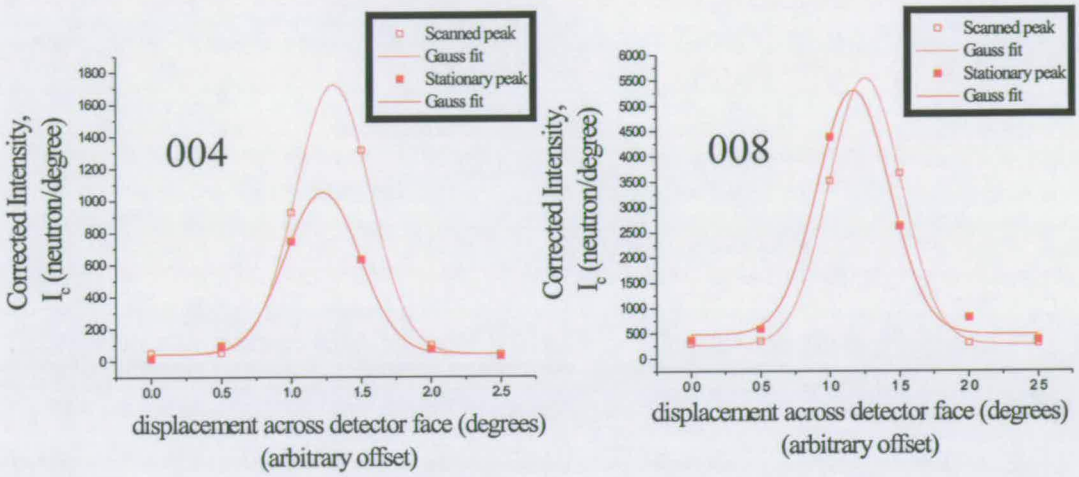

Figure 4.10. The Figure shows Gauss fits to the DKDP 004 and 008 reflection intensities measured both as stationary peaks and as a scanned ones in the TPM.

With the scan, it is immediately clear that neutrons are being measured that were in some way 'lost' in the stationary measurements. This was taken to be a direct observation of an overlap effect of the individual elements, and the scan now gave a measured $|F_o|^2$ for the 004 which agreed well with that measured in the SXM. Unfortunately, there was still some problem with the measurement of the 008 reflection which was now measured with a greater intensity than had been determined in the SXM. However, a large error in the intensity extracted from these low resolution scans is to be expected simply because the peakshape is so badly determined.

In order to improve on this situation, it was necessary to significantly increase the resolution of the encoding system used for measuring the cells position throughout a scan. The original resolution of 0.25° resulted in steps which move the reflection a distance equivalent to the detector width itself. Ideally, in order to probe

h k l	*parameter*	Stationary reflection	Scanned reflection	SXM measurement
004	y_o (neutrons per degree)	44	44	28
	A (neutrons)	682	1118	974
	w (degrees)	0.531	0.531	0.531
	λ (Å)	2.529	2.592	3.232
008	y_o (neutrons per degree)	478	276	30
	A (neutrons)	3189	3433	3056
	w (degrees)	0.519	0.519	0.519
	λ (Å)	1.264	1.264	1.616

Table 4.3. The results of Gauss fits to both the 004 and the 008 measured in both a stationary measurement in the SXM and both scanned and stationary measurements in TPM03.

asymmetries in the detectors, one requires a resolution significantly smaller than this.

It was this motivation that lead to the development of the second encoding system described in Section 4.3.1. This system allowed the determination of the position of the cell to within $\pm 0.023°$, allowing single-crystal reflections to be resolved to within $1/10^{th}$ of a pixel width. With this new capability, the measurements in the powder modules were repeated giving a direct measurement of powder-element asymmetry (Figure 4.11).

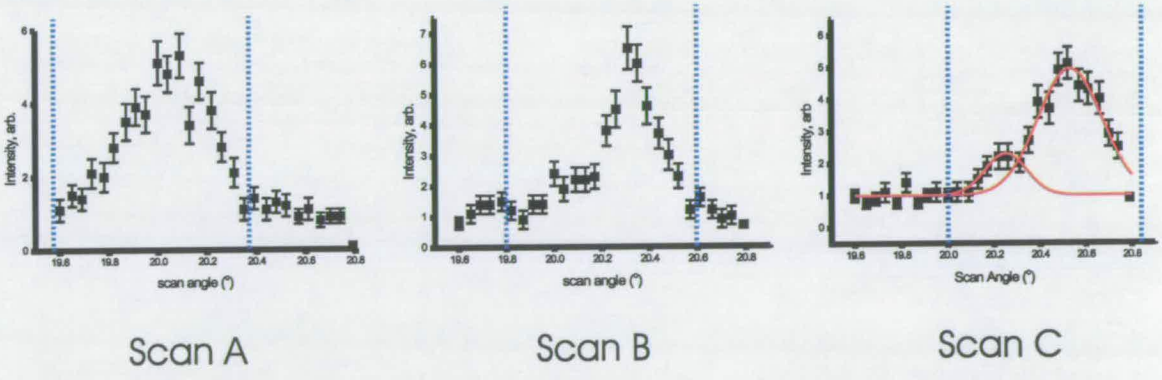

Figure 4.11. Intensity scans of the same single-crystal reflection across three *adjacent* elements in TPM03. The dotted vertical lines denote the width of the reflection.

This figure demonstrates that the response of the elements is not only asymmetric, but that this asymmetry varies in a non-systematic way from element to element. Some time had to be devoted to considering the consequences of this discovery for the use of the V-elements as viable detectors for measuring single-crystal reflections.

If a scanning technique were used to measure intensities in the powder modules, then the effect of gaps is eliminated. Any overlaps would still introduce difficulties as they will introduce a random deviation of the actual from the *average* wavelength-dependent efficiency $\epsilon i_o(\lambda)$ (measured across *all* modules), which is used to correct the data.

One possibility is to use two functions to correct for the detector wavelength response: one for the upper row and one for the lower row of detectors. These functions could easily be extracted from the original calibration data measured from the vanadium sphere. By dividing these two functions, the *average* extra absorption suffered by the lower row could be measured. This result clearly demonstrated a large reduction in efficiency (as a function of wavelength) in the lower row. However, the absorption coefficient determined from this measurement was non-linear. This may have been an indication that neutrons reaching the lower row had travelled through a range of absorbing pathlengths through the upper row. This would be expected if there was some random distribution of element tilts.

An obvious solution to this problem is to require that, during a scan, each reflection should be made to traverse at least two adjacent elements. As the rows of detectors follow an up-down arrangement, this will lead to all intensities being measured, at least once, in an upper element where there is no possibility of overlap.

Finally, there was also the chance that tilts of the element might affect its efficiency even when no overlap is present. Indeed, evidence for this is seen in Figure 4.11. The figure shows two adjacent peaks, which still show a marked asymmetry.

At least one of these must be on the upper row and therefore cannot be subject to overlap.

Again, one can consider the two efficiency factors separately. Firstly, the wavelength *independent* part of the efficiency ϵ_α might not be constant for both halves of the element. For instance, a tilt of the kind described previously would result in one side of the element presenting a smaller surface area towards the sample, which would lead to a constant reduction in efficiency. It was also possible that tilts would alter the optical pathlength from the detector surface to the fibre leading to the photo-multiplier tube.

To analyse this, a single element must be treated as two adjacent detectors. Consequently, ϵ_α (which is measured by taking the total detected flux across the entire element) will be given by the sum of two separate terms

$$\epsilon_\alpha = \epsilon_1\omega_1 + \epsilon_2\omega_2 \tag{4.5}$$

Here, the subscripts label each half of the detector (for simplicity, the function has been divided through by the incident flux integrated over time-of-flight and the long dimension of the detectors) the ϵ terms are their individual wavelength independent efficiencies and the ω terms their widths. The peakshape measured in a scan is the convolution of the reflection peakshape and the active area of the detector. As it is assumed that the asymmetry of the elements is confined to rotation of the 'V' about its vertex, it is only necessary to consider the response of the detector in this dimension (indeed, there is no way to measure in the other dimension and it is integrated over). In this dimension, each half of the detector may be represented as a top-hat function of an appropriate width and with a height equal to its efficiency.

It is a general result that the area under the convolution of two functions is equal to the product of the areas under each function taken individually [65]. Thus, if the area of the single-crystal peak is taken to be A and the total area of the

scanned peak is given by A_{tot}, then

$$A_{tot} = A\epsilon_1\omega_1 + A\epsilon_2\omega_2 = A(\epsilon_1\omega_1 + \epsilon_2\omega_2) = A\epsilon_\alpha \tag{4.6}$$

So, the intensity of the single-crystal peak is found simply by dividing the area of the scanned peak by the average efficiency, ϵ_α. It is clear, though, that the area under the scanned peak should *not* be determined by fitting with a single Gaussian, as had been attempted previously. Instead, the integrations were performed without any recourse to peak-fitting. The scan shown on the far right of Figure 4.11 demonstrates how the measured peakshape may be viewed as that measured by adjacent detectors, each possessing different efficiencies.

Now, all that remained to be explored was whether element tilts introduce a variation of the wavelength-*dependent* part of the efficiency. This was certainly conceivable, as varying the angle of the detector must change the available pathlength through the scintillator.

This kind of effect would only be detectable by performing a high-resolution scan of a reflection with several harmonics through a single top-row element. Differing wavelength-dependent efficiencies in each half of the 'V' would appear as a change of scanned peakshape for successive harmonics. This measurement was performed by scanning a DKDP 103 reflection through LPM12 , and the results are shown in Figure 4.12.

The scans have been multiplied by appropriate factors so that they can be compared on a similar scale. There is clearly a large change in peakshape in going from the 103 to the 206, but no clear change in going to the next 309 harmonic. Of the three reflections, the 103 appears to be the most symmetric, it also is slightly wider than the other two harmonics.

As a consequence of tilting, each half of the V presents a different pathlength of scintillator to the arriving neutrons. At the low energy of the 103 reflection, *both*

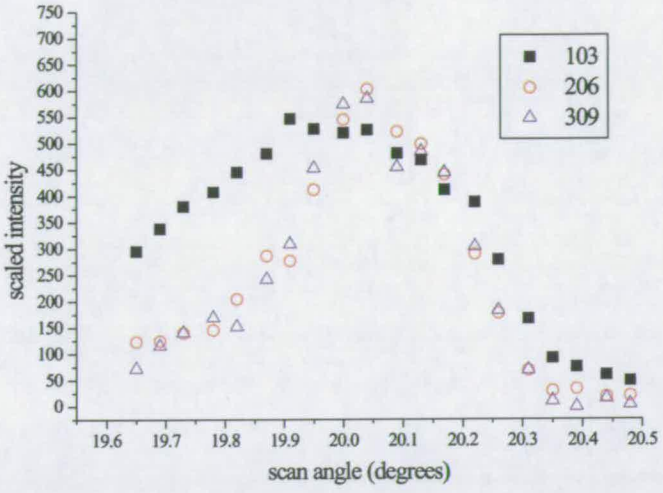

Figure 4.12. The DKDP 103 reflection and its harmonics scanned simultaneously across the same element in LPM12. Notice that, whist the peak shape changes dramatically in going from the 103 to the 206, there is no subsequent change in going to the 309.

halves of the detector are thick enough to stop most of the neutrons, therefore, the efficiency of both halves has saturated. However, at higher energies, the different characteristics of the different sides of the element become apparent.

A simplistic model of the situation can be developed. For a sheet of ZnS of uniform thickness, t at an angle δ to the vertical, the maximum pathlength is given by $l_{max} = t \sin \delta$ (see Figure 4.13). For a perfectly aligned V, the angles of each half about the vertical are $\delta_1 = \delta_2 = 18.2°$, where again the subscripts refer to either side of the detector. Therefore, a tilt of β will result in respective pathlengths of $l_1 = \sin(18.2 - \beta)$ and $l_2 = \sin(18.2 + \beta)$. If β is taken to be small ($\sim 5°$), then it can be shown that $l_1 = l - \delta l$ and $l_2 = l + \delta l$, where $\delta l = \beta \cos 18.2°$ (with β measured in radians).

The efficiencies at a given wavelength are proportional to the number of neutrons (n_a) absorbed. For a thickness of l' scintillator this is given by

$$n_a(\lambda) = I_o[1 - e^{-\mu(\lambda)l'}] \tag{4.7}$$

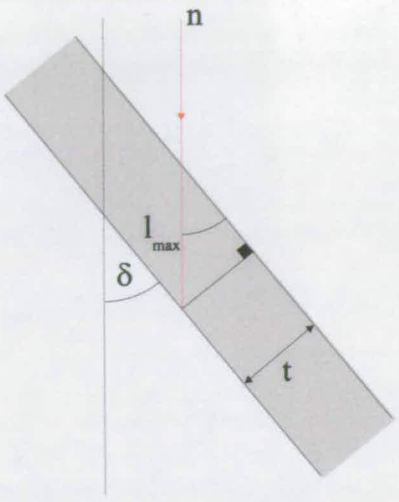

Figure 4.13. A schematic of one side of a detector V, which is at an angle δ to the vertical. If the thickness of the sheet is t, then the maximum pathlength of presented to an arriving neutron is $l_{max} = t \sin\theta$.

The result that $l_{max} = l \pm \delta l$ can be substituted into this equation. Additionally, the assumption that $\mu\delta l \ll 1$ can be safely made, for high energy neutrons, giving

$$\begin{aligned} n_a(\lambda) &= I_o[1 - e^{-\mu(\lambda)(l \pm \delta l)}] \qquad (4.8) \\ &= I_o[1 - e^{-\mu(\lambda)l} e^{\mp\mu(\lambda)\delta l)}] \\ &\simeq I_o[1 - e^{-\mu(\lambda)l}(1 \mp \mu(\lambda)\delta l)] \\ &= I_o[n_l(\lambda) \mp \mu(\lambda)\delta l] \qquad (4.9) \end{aligned}$$

In the above expression, the quantity, $n_l(\lambda)$ is the number of neutrons absorbed in one side of an un-tilted element. At this level of approximation, again the effect of the tilt cancels out. Therefore, correcting the total integrated flux measured in a detector by the average wavelength-dependent efficiency will give the correct intensity.

However, if the higher order terms $[(\mu(\lambda)\delta l)^2 + ...]$ are included (at low wavelengths

or for severe tilts), then this is no-longer the case, and the measured intensity will become successively weaker than the real intensity. Additionally, in reality, the situation is further complicated by the possible wavelength dependence of the optical coupling. As the ZnS material is highly opaque to light, the majority of detected neutrons will be those absorbed near the surface of the scintillator. For low energies there will be a greater number of neutrons absorbed at the upward facing surface. At higher energies, less neutrons are absorbed whilst traversing the thickness of the scintillator, so the number of neutrons absorbed on the upper and lower facing surfaces will become more equal. Also, in principle, tilting of the individual elements might result in a different probability for emitted light being *detected* for each of the two surfaces, but this would be a wavelength independent effect.

4.3 Technical Modifications for Single-Crystal Diffraction

In the following section, modifications to the subsidiary equipment used with the PE cell are described. Some of this work involved a significant contribution from both the ISIS technical support and colleagues at the Université Pierre et Marie Curie in Paris. Where this is the case, due acknowledgement is made.

4.3.1 Rotation of the PE cell and Encoding of its Position

By rotating a single-crystal sample it is possible to access different parts of reciprocal space, therefore, allowing access to more reflections. Whilst exploring reciprocal space, it is important to maintain an accurate knowledge of the amount by which a crystal is rotated, and in what sense. The problem is simplified in the case of the PE cell because there is only one possible rotation axis. When the tank-cradle assembly was designed, a worm-drive was installed to facilitate cell

rotation (Figure 4.14). It was desirable that this was motorised so that computer controlled data collection would be possible. It was also necessary to install a rotation measurement device to record accurately the position of the cell.

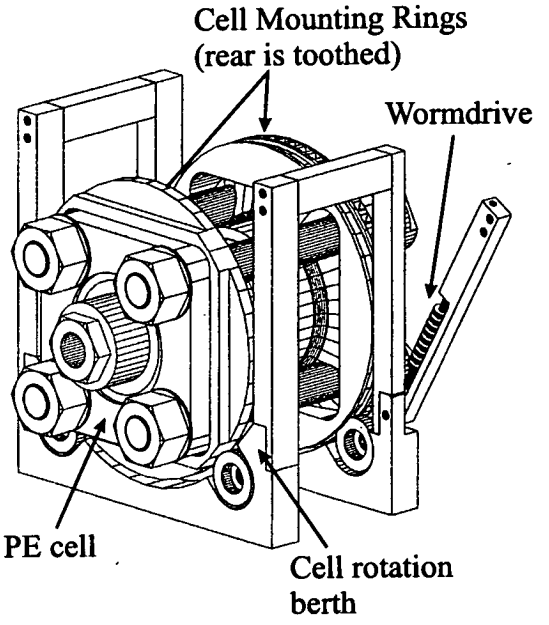

Figure 4.14. An image of the PE cell in the cradle arrangement. The worm drive is also shown.

The most important of these tasks was the measurement of the cell's position. The first attempt to solve the problem used a mechanical resolver placed on the top of the tank which was indirectly connected to a gear fixed on to the cell breech via a drive chain. This design was produced by the ISIS design office and sample-environment laboratory, and is shown in Figure 4.15. The initial motivation for using this indirect connection to the cell was a desire for the encoding system to work at the cryogenic temperatures to which the cell is subjected during low temperature diffraction measurements.

This system was built and installed, but it immediately became clear that there were fundamental problems with the design. The first of these was the backlash arising from the long-distance chain connection. The hydraulic connection to the cell restricts its rotation to $\pm 180°$, making it necessary to reverse the direction

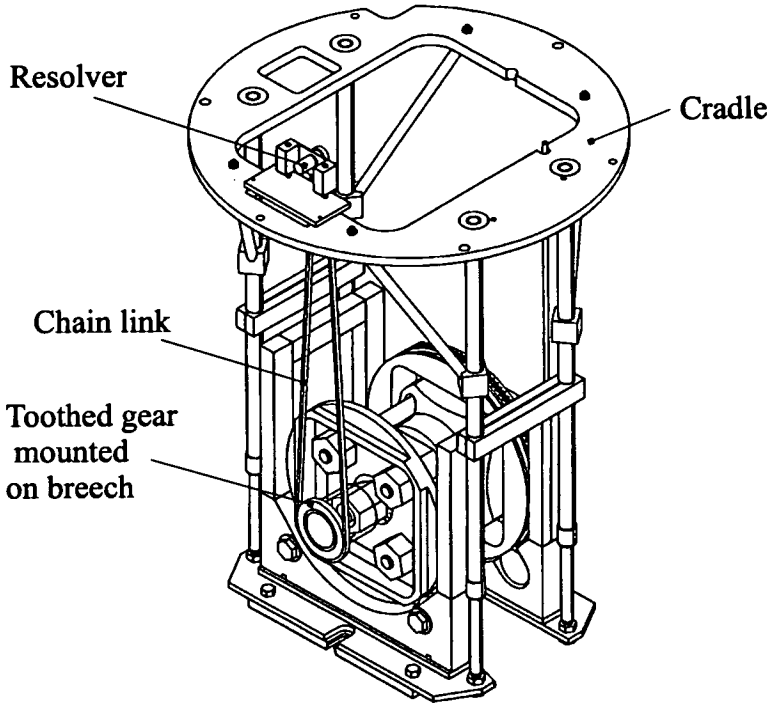

Figure 4.15. Figure shows cradle with resolver attached to cell via chain link.

of rotation of the cell during the course of an experiment. With each of these reversals, the backlash would introduce an error in the measured cell's position, and we would gradually 'lose' the cell.

A second problem was that the resolution was far too low. The mechanical resolver used had a resolution of 1024 bits which was enhanced by a 1:6 gearing ratio with the cell. These should have combined to give a maximum resolution of 0.06°, however, the connection was so loose that in practice, it was limited to $\sim 0.3°$. At this time it was becoming apparent that single-crystal data collection would require high resolution scans (see Section 4.2.2).

The combination of these two significant drawbacks led to a complete redesign of the cells encoding system. The first requirement to be relaxed was the capability of making low-temperature measurements. This acknowledged that the measurement of single-crystal intensities, and the cooling of samples, were two separate

problems, of which the former was clearly the most fundamental. Initially, the envisaged adaptation would connect a higher resolution encoder directly to the cells body - thereby negating the possibility of any backlash. One problem with this design was that an encoder would have to be coaxial with the rotation axis of the cell, and this would place it directly in the path of the incident beam when the cell was in the transverse position. Whilst hollow-core encoders are available, they presented problems for collimation and also were significantly more expensive.

This was overcome by maintaining a connection between the cell and the resolver, but using a direct meshing of commercially available, no-backlash gear wheels. With this setup, the resolver sits above the axis of the cell and is connected with 2:1 ratio of gears that give extra resolution, with no loss of accuracy due to backlash. A new optical resolver was purchased that had a resolution of 8191 bits. This resulted in both a higher precision of 0.03° *and* higher accuracy.

Both the resolver and stepper-motor drive system were connected via a CAMAC system to the instrument computer. This permitted logging of the cells position and computer control of the rotation. It was discovered that by driving the cell one pulse at a time, it could be positioned within the accuracy of the encoder. This was unexpected, because the worm-drive had not been designed to position the cell with such precision.

4.3.2 Collimation and Shielding in the Longitudinal Mode

Single-crystal data collection on HiPr was almost exclusively developed in the longitudinal mode. For powder diffraction, this orientation was less frequently used and, as a consequence, both the shielding and collimation had not been optimised. An important consideration for single-crystal work is the minimisation of background scatter (see Section 2.1.3). It was known that contaminant scattering, which was not due to the sample, was always observed in this setting,

and this had to be tracked down and eradicated.

This required the use of data visualisation software, which the author was developing for single-crystal work. Initially, these were based around command files for the pre-existing GENIE (see Section 4.4 on software) environment for visualising ISIS neutron data. The diffraction patterns observed in the detectors on HiPr are functions of three variables: the position on the detector face (two coordinates) and time-of-flight. In order to visualise this data easily, it is necessary to integrate along one of these dimensions, thus, reducing the data to a function of two variables. The most useful way to do this is to retain the TOF information and the 2θ information, meaning the data must be integrated along the direction perpendicular to increasing 2θ. Prior to integration, the data must be focused, they can then be displayed as a series of d-spacing plots at increasing values of 2θ as shown in Figure 4.16.

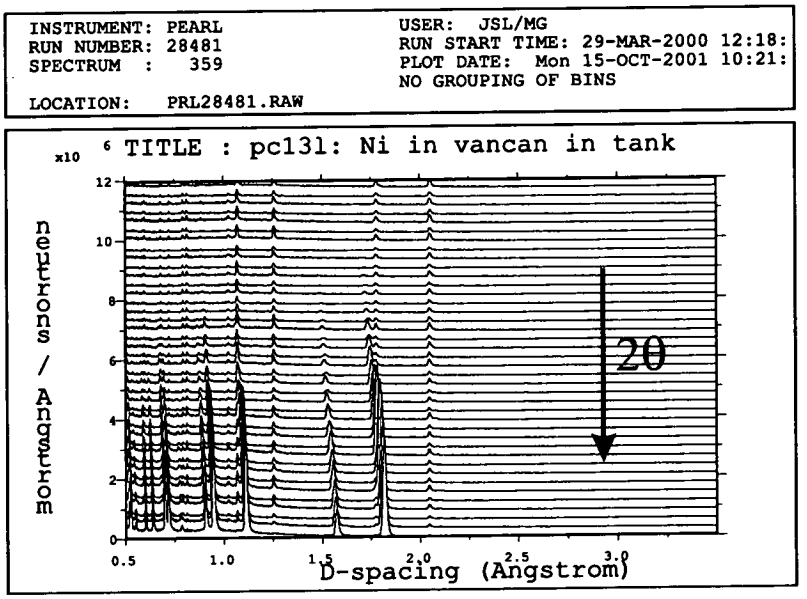

Figure 4.16. A focused multiplot of data viewed across LPM11. A powder sample of Ni was suspended at the sample position. Scatter from out-with the sample position slants obliquely across the image as the 2θ angle changes.

The multiplot shows data recorded across LPM11 for a sample of Ni that was

suspended inside an empty tank without the PE cell in place. The direction of increasing 2θ is marked on the plot. The nickel powder lines are evident as peaks running vertically down the figure at constant d-spacing. There is also a strong set of peaks running up the figure at an angle to the Ni powder lines. This is characteristic of the source of scattering lying at some distance from the instrument centre, resulting in a different set of $L\sin\theta$'s from those defined by the sample postition.

The contaminant lines continue across the end of LPM11, and continued half-way up the SXM, but were not evident in any of the other detectors. By integrating the largest of the contaminant peaks for each value of 2θ, it was possible to measure the variation of its intensity as a function of angle, and this is illustrated in Figure 4.17.

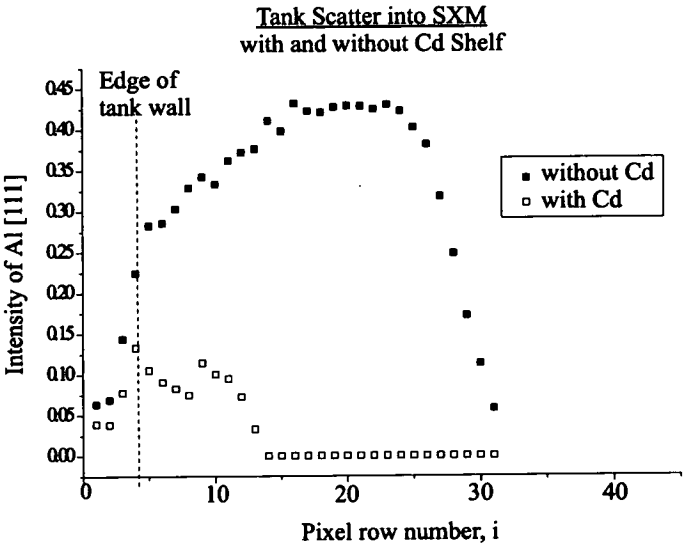

Figure 4.17. The variation of the contaminant tank scatter as a function of 2θ. The white points mark the intensity observed when a Cd shelf was extended from the top section of BC shielding on LPM12. The remaining scatter is travelling *through* the outer tank wall, the position of which, at the high 2θ end of the detector, is indicated.

The source of this anomalous scattering was clearly the tank itself. A scale drawing of the tank was made up, and onto this the positions of the longitudinal

detectors, as determined by the single-crystal calibrations, could be accurately plotted. This drawing is re-created in Figure 4.18. Marked by 'Cd' on the figure are four cadmium slats that were included in the original tank design to remove tank scatter in the longitudinal mode. It was then possible to draw ray paths on the figure and to mark on the extent of the contaminant scatter at the observed 2θ angles. From the positions of LPM11 and the SXM, it was clear that scattering from the wall of the tank was travelling through the wall itself to enter LPM11. Indeed, an increase in the intensity of the contaminant scatter is observed at the point where the detectors emerge from beneath the tank wall. The SXM is at a high enough angle that it is completely out-with the protection of the cadmium slats. It was only because of shielding on the top of LPM12 that this scatter did not fill it and the top half of the SXM.

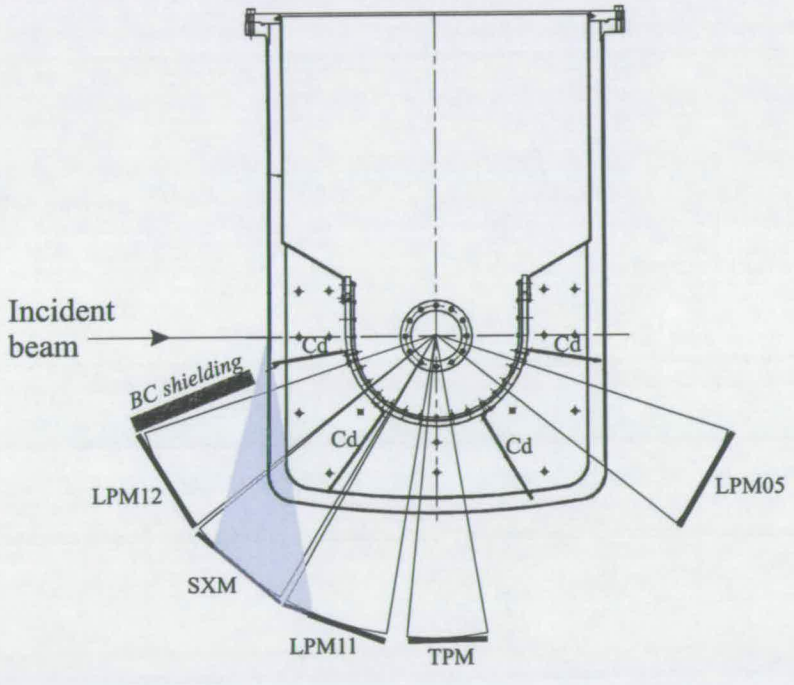

Figure 4.18. Schematic of the tank in the longitudinal position, with the detector positions marked. The shaded area corresponds to scatter from the outer wall of the tank that was not absorbed by either the cadmium slats or the BC shielding on the top of the detector.

Correcting this problem was non-trivial, because any modification had to leave

the tank usable for collecting data in the transverse setting as well. Whilst it would be straightforward to increase the external shielding to protect the top section of the SXM, this would not be able to stop radiation travelling through the wall of the tank itself. In order to achieve this, a cavity was machined into the aluminium exterior wall of the tank. This would be small enough, so that it would not affect the radiation diffracted through it in the transverse mode. Then, when used in the longitudinal mode, a slat of Cd could be inserted in the slot forming a continuous barrier protecting LPM11 and the SXM from tank scatter. This solution worked well, and was demonstrated to completely eradicate the tank scatter from the detectors.

With this gross problem corrected, attention now turned to exploring how well the beam could be collimated. Ideally, the beam of neutrons should be no larger than the sample itself, as a larger beam will only contribute to the background. The surface of the anvils were coated in 0.25 mm cadmium shielding but, as a consequence of gasket extrusion, this stopped around 5 mm short of the gasket edge, exposing a significant amount of anvil. Additionally, cadmium is known to activate in the direct neutron beam, and has a rather long half-life, so it was desirable that some other material be used for a direct-beam collimation element.

An important requirement in single-crystal diffraction is that the entire sample is illuminated by a uniform beam. Any collimator arrangement will result in a central umbra which should have the required uniform intensity, but towards its edge there will be a penumbra over which the intensity of the beam will gradually drop to zero. In order to minimise the penumbra it is important to place the collimation piece as close as possible to the sample itself. As the PE cell is rotated throughout a single-crystal experiment, it would be necessary to fix a collimator to some external piece of equipment to maintain the alignment.

The solution employed was to use a collimator mount that could freely rotate about the centring piece of the breech anvil. This mount (described in Figures 4.19 and 4.20) accurately maintained the alignment of a BN collimator piece with

the breech anvil. The collimator piece was then attached via a sprung linkage that extended vertically up to join the outer cradle. This maintained the orientation of the collimator, with respect to the incident beam, as the cell was rotated. One problem with this arrangement was that every 90° of rotation, a tie-rod would cut across the position of the cradle-collimator connection. However, the sprung mechanism would safely disengage when this occurred, after which the collimator would have to be re-aligned. Additionally, when the cell is in such a position where a tie-rod breaks the linkage, a second tie-rod will be in the path of the incident beam, so there is no reduction in the usable angular access.

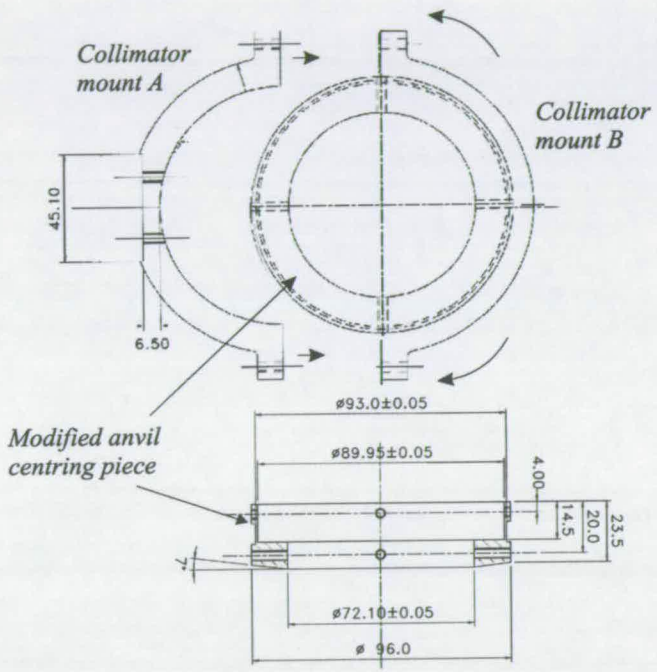

Figure 4.19. Technical drawing of the components comprising the collimator mount illustrating their assembly around a modified anvil centring piece. The positioning of these components on the anvil-seat assembly is shown in Figure 4.20 on the following page. The parts of the collimator mount A and B are attached to each other with Allen bolts where indicated and are free to rotate around the anvil centring piece

The initial collimator piece that was used was a blank BN plate, attached to a flat

surface machined in part A of the mount shown in Figure 4.19 by two countersunk screws. Activation of the collimator piece was a consideration in the design. Boron nitride has a relatively high level of activation but, correspondingly, this has an extremely short half-life, so the collimator is safe to handle after several seconds. A rectangular slot was machined into the BN that was accurately aligned with the top of the breech anvil, that is to say, the sample position.

In the first tests of the collimator, it was found that a significant amount of scatter was observed from the surface of the collimator itself. This was alleviated by the addition of cadmium shelves attached to the front and back of the collimator below where the incident beam struck (see Figure 4.20). This appeared to remove all of the surface scatter from the collimator piece. Cadmium also has the advantage of being highly malleable. Consequently, as the anvils closed, they could safely compress the inner section of cadmium, without damage. The outer (longer) Cd shelf was long enough to intercept the tie-rods in their rotation about the cells axis, and again the softness of the metal meant that no damage occurred, and the shelf could simply be re-positioned after a collision.

As is also illustrated by Figure 4.20, the collimator remains a fixed distance (of 106 mm) from the sample position. Consequently, a section of the anvil is illuminated by a small amount of the beams umbra and by a larger amount of the penumbra. This resulted in a small amount of powder scatter from the anvil, but, moving the collimator closer is complicated by the closure of the anvils at high-pressure. It was decided that this remaining powder scatter was a small enough problem to be neglected, simply contributing to the background which is subtracted during the integration procedure.

Finally, for single-crystal diffraction, it was also important to confirm the size and uniformity of the incident beam. To this end, a flat photograph was taken, a contrast enhanced negative of which is displayed in Figure 4.21. The penumbra can be clearly seen about the dark central spot of the umbra, superposed on this is the shadow of a circular collimation piece. This collimation element is part of a

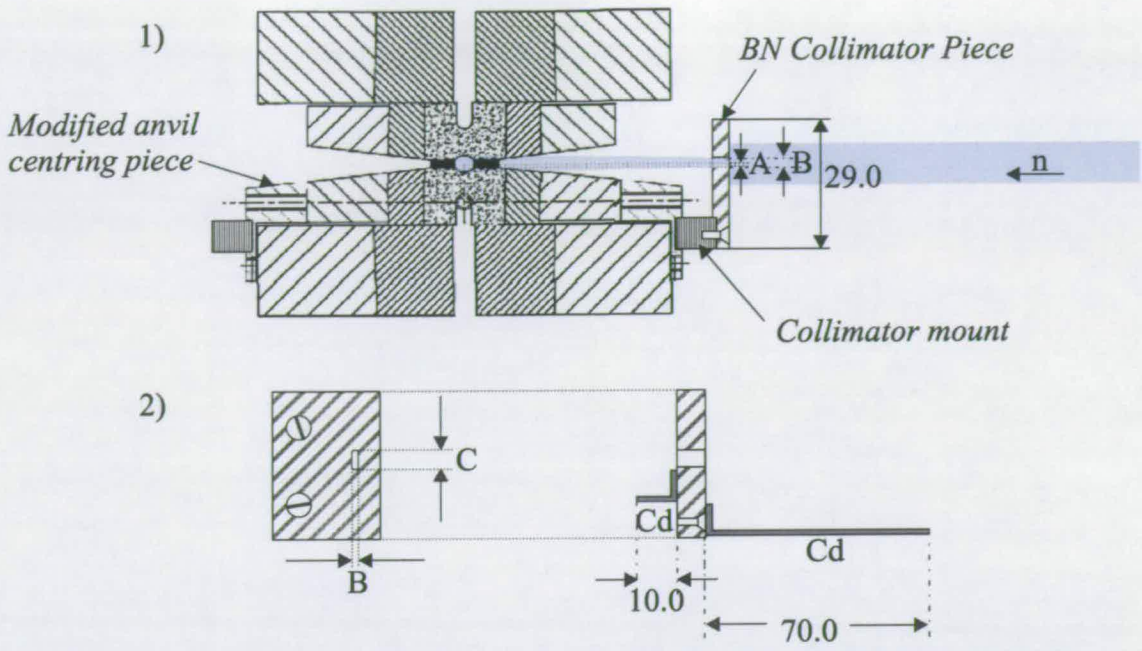

Figure 4.20. 1) The collimator assembly attached to the anvil and aligned with the incident beam 2) Schematic of the collimator from the front (left) and side (right), the additional cadmium shielding is illustrated. Dimension A is the distance from the top of the anvil to the centre of the sample ($\sim$ 0.5 mm) and dimension B is the width of the collimator. This ranged from 1 - 2 mm.

special tank used for ambient pressure measurements on HiPr, and is not present in high-pressure data collection. The central spot is 10 mm across, and it is just possible to discern that it is slightly non-uniform across its extent. This may indicate a problem with the upstream collimation elements and warrants further exploration.

The variation appears mostly across the horizontal direction. As the crystal is very thin in this direction, it is not expected that the beam asymmetry will significantly affect single-crystal measurements. One potential problem is the gradual movement of the crystal as the piston extends. This motion is of the order of 1 mm, which is quite small, but a precautionary measure would be to re-align the cell after each pressure increase.

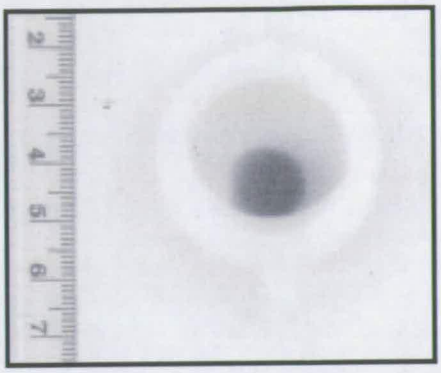

Figure 4.21. A contrast enhanced negative of the incident beam on HiPr, the scale to the left of the image is in *cm*.

4.3.3 Pressurising Single-Crystal Samples

The use of opposed-anvil pressure cells to apply very-high pressures to samples dates back to the early 60's [66] [60]. The basic method employed is the same in all types of cells. A generic diagram of a diamond anvil cell (shown in Figure 4.22) illustrates these main principles.

Two anvils made of a hard substance are forced together against a softer, metal *gasket* which contains a small void in which the sample and a *pressure transmitting medium* (PTM) is held. When a force is applied to the anvils, the pressure experienced by both the gasket and the sample increases. As this force increases further, the pressure in the gasket material becomes sufficient that plastic deformation occurs, and it begins to extrude, becoming thinner and harder. This process continues until tensile forces (maintained by friction with the anvil surface) within the gasket material balance the pressure-induced stresses causing the extrusion and equilibrium is achieved.

The PTM is a critical part of this system, as it ultimately communicates the pressure to the sample itself. It is extremely desirable to have a PTM that remains as hydrostatic as possible within the pressure range being explored. If this is not the case, then large pressure gradients can exist across the sample volume, which

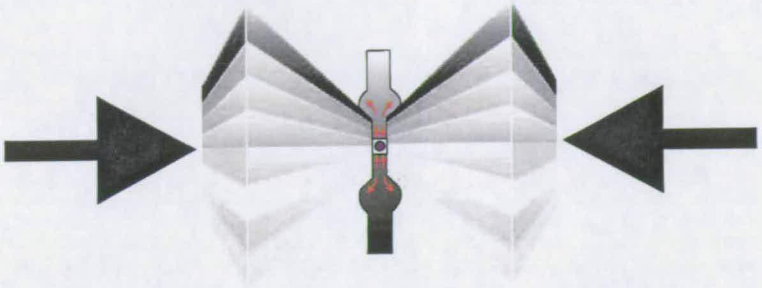

Figure 4.22. A generic example of an opposed anvil cell. The anvils are forced together as indicated by the large arrows. This increases the pressure in the gasket material, which flows until equilibrium is reached. The pressure is maintained by frictional forces and the tensile strength of the gasket material.

can distort the crystal structure and, in the case of a single-crystal sample, result in irreversible damage to the crystal.

As mentioned previously, the anvils used with the PE cell have a toroidal geometry. The toroid acts to increase the effective frictional force which contains the pressure within the gasket-sample system, and is significantly more efficient than a flat anvil. In order to reach the highest pressures in powder diffraction with the PE cell, double-toroid anvils are used which improve the pressure-load performance still further.

The use of toroidal anvils is extremely important as it minimises the amount of gasket that the incident and diffracted beam must pass through, thus minimising loss of intensity due to absorption effects. Despite this advantage, there has been a long standing problem plaguing their use: they cannot support a hydrostatic PTM. This effect has been observed empirically many times in rather dramatic fashion, the anvils routinely shattering when a pressure of around 3.5 GPa is reached [84]. Consequently, various non-hydrostatic PTMs have been used, and the resulting sample strain was tolerated as an unfortunate fact of life. The most common material in use on HiPr was fluorinert, a non-hydrogenous mixture of perfluoroinated fluids that freezes into an amorphous mixture at high pressure. Solid PTMs also used included lead and salt, but these have the disadvantage of

producing their own diffraction pattern which contaminated the signal from the sample (although this is a lesser problem for single-crystal diffraction).

In addition to the issue of which pressure medium to use, there was also the issue of which design of anvil and gasket was appropriate. All of the techniques described in the following were applied to single crystal samples of KDP and DKDP. These were interesting candidates for high pressure study (as described in the following chapter), but are extremely brittle.

Figure 4.23 illustrates all of the separate designs investigated. In all cases the crystal was destroyed as the pressure approach a rather modest 1.6 GPa. This damage could be attributed directly to non-hydrostaticity of the PTM.

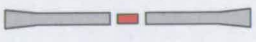

1) **Flat gasket.** This design is used with large 25 mm diameter flat anvils. It utilises a 1:3 ratio of $_{i}$ to anvil diameter. The sample void is filled with a methanol-ethanol medium. Whilst safely permitting compression of the liquid PTM to high pressure, the small maximum sample size, and large Ti:Zr radius results in a prohibitively weak diffraction signal

3) **Lead Encapsulation Gasket.** This design entirely encloses the sample crystal in Pb, which acted both as the alignment surface, and the PTM. A conical design of anvil was used that prevented tipping of the sample in order to maintain alignment. With this design, again, the KDP crystal suffered damage at ~ 1.6 GPa.

2) **Standard single toroid.** This design uses standard anvils and gaskets with the bottom anvil cup filled with lead to provide an alignment table. A fluorinert PTM was used. In addition to crystal damage at 1.6 GPa, the lead table was observed to tilt. A third problem was the observation of single-crystal diffraction peaks from the lead, which had annealed into several large crystallites

4) **Ti:Zr table Gasket.** This design is similar to gasket 3, but is composed entirely of Ti:Zr. A PTM fluid is used to fill the sample void. Again, the maximum pressure achieved was ~ 1.6 GPa.

Figure 4.23. Initial designs of gaskets used to compress single crystal samples in the PE cell. All designs were produced with the help of S. Klotz of the Université Paris 6. The conical anvils used in design (3) were developed by Klotz et al. for phonon measurements with the PE cell [67].

Finally, a breakthrough came from an independent development of techniques

to compress *liquid* samples with the toroidal anvils of the PE cell. This work, carried out by W.G. Marshall and D.J. Francis of ISIS resulted in a modified 'metal encapsulation' gasket, which they demonstrated could safely compress samples with a liquid methanol-ethanol mixture to at least 9 GPa [68]. This design is illustrated in Figure 4.24. In all cases a deuterated methanol-ethanol mixture was used to avoid the large background scatter that would arise due to incoherent scattering from the hydrogenous material[3].

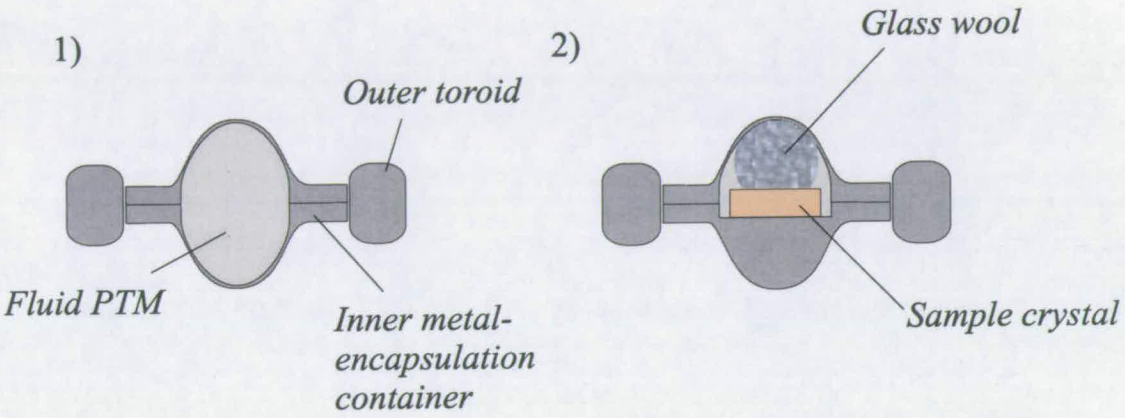

Figure 4.24. 1) The metal encapsulation system developed by Marshall and Francis [68]. The outer toroid is identical to that used with standard gaskets. The inner part is composed of two cups of Ti:Zr that entirely enclose the sample and support the stress gradient from sample to anvil. 2) Modification of the original design resulting in a flat table for single-crystal alignment.

A small modification (also shown in the figure) required for single-crystal work, was the filling of one of the gasket cups to provide a flat alignment surface. Good alignment of the samples was expected to be critical to avoid the strong attenuation of the anvil components experienced by diffracted beams travelling out of the equatorial plane. This flat surface was machined to be slightly proud (0.1 mm) of the top of the anvil, again to avoid occlusion of the incident and

[3]In fact it was observed that, over time, the PTM hydrogenated and this resulted in a significant enhancement of the background. This effect was encountered in the powder study of KDP described in Section 5.2.2. In order to minimise this problem, the PTM was stored in an air-tight container in a refrigerator, thus minimising the possibility of hydrogen exchange with moisture in the air.

diffracted beams. During loading, the sample was held in place by a small amount of petroleum jelly placed between it and the Ti:Zr flat. Additionally, a small piece of glass wool was used to keep the crystal flat against the alignment surface. The loading technique proceeded as follows:

- The PE cell was connected to the hydraulic pump and placed in a mount that maintained it in a horizontal position, with the piston anvil down.
- The outer toroid, and the flat inner-section of the gasket were placed on the bottom anvil with the sample aligned as closely as possible with the centre of the gasket.
- The lower cup was then flooded with deuterated methanol-ethanol PTM mixture.
- Meanwhile, the upper cup, with a ball of glass wool held inside, was also flooded and quickly placed on top of the lower section of gasket.
- Subsequently, as the breech was screwed into place, a continual flow of the PTM mixture was maintained over the gasket to replenish losses through evaporation.
- As soon as the breech was tightened, a sealing load of 10 tonnes was applied.

This procedure worked well, with no instances of sample damage during loading. Upon subsequent increase in pressure, the sample was observed to hold its orientation well: to within 1°. The subsequent pressure testing was also successful, and a KDP crystal was safely raised to a pressure of 7.2 GPa before being destroyed by a structural transition. The collection of diffraction data from samples at these high pressures is described in detail in the following chapter.

4.4 Software

In practice, all of the analysis described in this chapter was made possible by the development of specialised software. In some cases, this would involve the adaptation of existing programs in order to apply them to this particular case, however, this was often not possible, and specific routines had to be 'custom-made'. Rather than complete documentation, the following section constitutes a brief description of some PEARL-HiPr specific visualisation software, and the main integration software.

All software written by the author was in Fortran code in the flavour appropriate for the VMS operating system used at ISIS. Extensive use was made of various subroutines for peak fitting and searching provided by D.S. Sivia of ISIS. Additionally, visualisation subroutines made use of the PGPLOT Graphics Subroutine Library [69]. Finally, extensive use was made of software developed by A. Filhol of the ILL [70] (and implemented on the SXD instrument at ISIS) for the orientation of single-crystal samples on 4-circle diffractometers with multi-element detectors.

Appendix B contains a full listing of the software that was written to aid the work of this thesis. The FORTRAN code for these routines is included in Appendix C on the attached CD-ROM.

4.4.1 Visualisation of Single-Crystal data

A fundamental difficulty with the visualisation of single-crystal reflections on energy-resolved 2d area detectors, is that the intensities are a function of three variables and, thus, require four dimensions in order to be displayed. Typically, in order to reduce this to a three-dimensional image, one of these variables must either be discarded or integrated over. The way in which this should be done depends on which information the experimenter is concerned with at any particular

time. Consequently, this demands a certain flexibility in the software.

Visualisation techniques were required to aid in a number of tasks:

1. The rapid identification of sample peaks to determine crystal orientation.
2. 2d visualisation of reflections measured in the SXM was required to assess the overall dimensions and shape of the single-crystal peaks.
3. 2d visualisation of the entire longitudinal bank to look for occlusion arising from the tank or cell components.

The first of these tasks was most readily achieved using the GENIE software [71] developed at ISIS specifically for visualising and analysing neutron data. Focused multiplots (as described earlier in Section 4.3.2) were used to visualise a single module at a time. These facilitated manual peaksearches providing a means by which both the d-spacing, and relative angles of reflections, could be identified.

This remained a useful technique in the initial stages of development, but was subsequently replaced by an automatic peaksearch routine provided by D.S. Sivia [25]. The routines were written such that the output of the peaksearch contained the angular and time-of-flight information necessary to determine the crystal orientation. This could then be used by standardised UB refinement software [70] to determine the crystal orientation.

The second task was achieved by a simple (HiPr-specific) visualisation program called LONGDIS. This made extensive use of PGXTAL [25], a collection of FORTRAN subroutines developed by D.S. Sivia to provide high-quality 3d imaging of data via a simple FORTRAN call statements. Prior to display, LONGDIS extracts individual-element spectra from the RAW data file and integrates over a user-defined time-of-flight range. These integrated intensities can then be displayed as a 2d colour map of either the entire HiPr longitudinal detector bank, or single modules within it. Prior to display, the integrations are corrected for the

wavelength independent efficiency of the individual elements. Such a display facility was useful, not only to investigate occlusion by the cell and tank apparatus, but also to visualise time dependent changes of the detector efficiencies.

An important initial use of the software was in a definitive determination of the detector numbering scheme. As previously mentioned, this scheme is dependent on the mode of operation of the instrument and, as it turned out, the exact methodology for the numbering of the longitudinal bank was unknown. This was a consequence of the complex series of routes, both electrical and computational between the diffractometer and the instrument computer. It was essential that the exact numbering scheme was unambiguously determined.

To this end, 'L'-shaped masks of Cd were attached to the detector faces in a known orientation and a short 7 minute exposure measured. The resulting image generated by LONGDIS of the entire longitudinal bank is shown in Figure 4.25 where the shape of the Cd masks are clearly visible. By examining the apparent orientation of the masks, these images allowed the numbering schemes of the detectors to be unambiguously identified.

4.4.2 Integration of Scanned Single-Crystal Reflections

The development of the software to integrate single-crystal intensities and extract structure factors was an involved task, yet, it was essential that the procedure became automated. This arose mostly as a consequence of the scanning technique used to measure data in the powder modules. The manual integration of these peaks was extremely time consuming (taking several days to integrate the peaks from a single scan). Additionally, the procedures for extracting structure factors were rather involved and at each stage there was the possibility of an error. The development of software to perform the task reduced the errors to systematic ones in the code which could then be identified and corrected.

The coordinates required to define a scan of an individual single-crystal peak are:

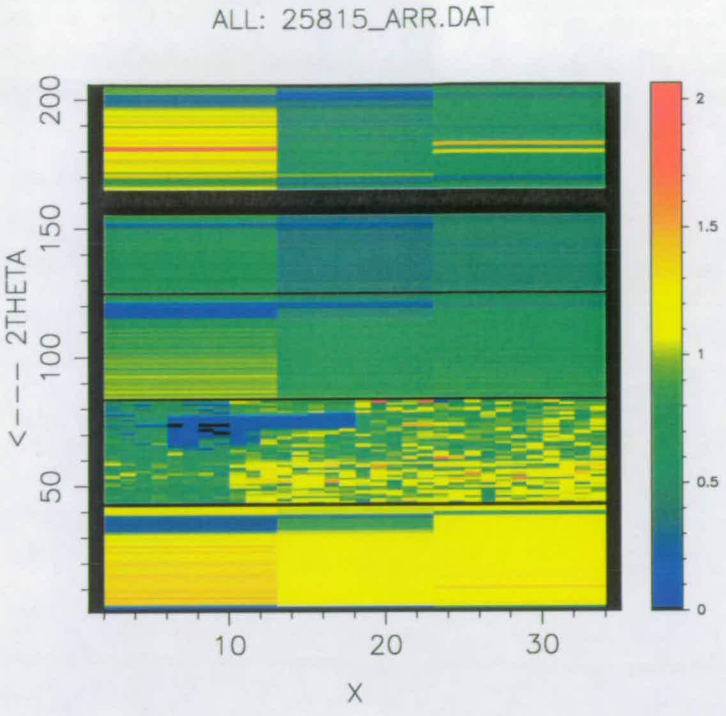

Figure 4.25. The figure shows LONGDIS output for the entire longitudinal bank. The integrated TOF data are displayed on a grid representing the detector arrangement (note the 2d resolution of the SXM)

1. The run numbers of the data collections comprising the scan.
2. The spectrum number of the element in which the peak is measured, from which the relevant geometrical and calibration information can be determined.
3. The time-of-flight of the reflection.

These coordinates are read from a data file containing the locations of the single crystal peaks. Initially, this was written by hand from direct observations of peaks, but, at later stages of development, could be generated directly from the orientation matrix of the crystal and cell orientation measured by the encoding system.

The integration process is described for an individual reflection observed in spectrum n at time-of-flight, T_n. In the early stages of development, this proceeded by

integration of the neutron counts observed in n across the entire scan. However, it was soon realised that, as during a scan the reflection crosses several elements, for a significant amount of time, spectrum n is only measuring background. Subsequently, the integrations were performed only over the runs in which the sample peak was present in element n. A safety factor was included in the scan width determination to avoid truncation of the peak.

Reflections measured in the SXM typically had a width of several elements (in the direction perpendicular to the longitudinal plane) and the capability was included to additionally integrate over this dimension. At this stage, neutron counts were normalised by the wavelength independent efficiency of the element ϵ_n.

After integration across the scan, the data are displayed as a function of TOF between $T_n \pm \delta T_n$, where δT_n is given by the user. At this stage, a subjective decision is made as to whether any peak intensity is present above background. If no peak is present, then the background is sampled and the error in this background, integrated over an estimated peakwidth, taken as the error bar on a measurement of zero intensity. If a peak is present, then it is fitted with a standard GEC function (the fitting procedure was performed by PKGEXP [25]) and the fit superposed on the display of data. For weak reflections, it was necessary to apply appropriate constraints to stabilise the fit (this situation arose when the number of points defining the peak was comparable with the number of parameters in the unconstrained fit).

The intensity is given by the area of the GEC fit, and both this, and the associated uncertainty (including the error in a linear background fit), is then corrected for the various terms in the Buras-Gerard Equation 4.2 giving squared structure factors. This is then output to file in a standard format containing the hkl index, $|F_{obs}|^2$, σ^2, wavelength and spectrum number for subsequent analysis. The details of this data analysis are described in detail in the following chapter, where they are employed in a study of the structure of KDP.

4.5 Conclusions

After a significant amount of development, both of experimental techniques and supporting software for data analysis, it is now possible to measure accurately single-crystal intensities from single-crystal samples on the HiPr diffractometer. Additionally, software has been developed to automatically perform these integrations based on peak positions predicted by an orientation matrix refined for the sample position.

In a parallel development, the capability to safely compress single-crystal samples, with an adequate volume for diffraction work, to at least 7.2 GPa has been presented. This represents almost a three-fold increase in the accessible pressure for such measurements.

The use of these techniques, for the first time, to attempt to measure accurate structural parameters at these high pressures is the subject matter of the following chapter, where the subsequent analysis and correction of the data are discussed.

Chapter 5

A Comparative Single-Crystal and Powder Diffraction Study of KDP up to 7.2 GPa

5.1 Introduction

The structure of potassium di-hydrogen phosphate (KDP) has been highly studied for many decades now. In addition to a technological importance in the optical industry, it is also interesting from a fundamental perspective, both as a ferroelectric, and as a model hydrogen-bonded solid. Any complete study of the H-bond structure requires neutron diffraction, and the first of these experiments was performed nearly fifty years ago [72].

During the 1970's attempts to explore the importance of H-bond *geometry* in KDP's paraelectric to ferroelectric phase transition at low temperature began with investigations of the isomorphs KD_2PO_4 (DKDP), CsD_2AsO_4 and RbH_2PO_4 and was extended to include the effects of pressures up to 1.65 GPa [73]. All of the structural work on KDP between 1970 and 1985 has been reviewed in detail by Nelmes [74]. In the time since this period, structural high-pressure work has

been extended up to 30 GPa and temperatures of 600°C, but only using x-ray radiation [75].

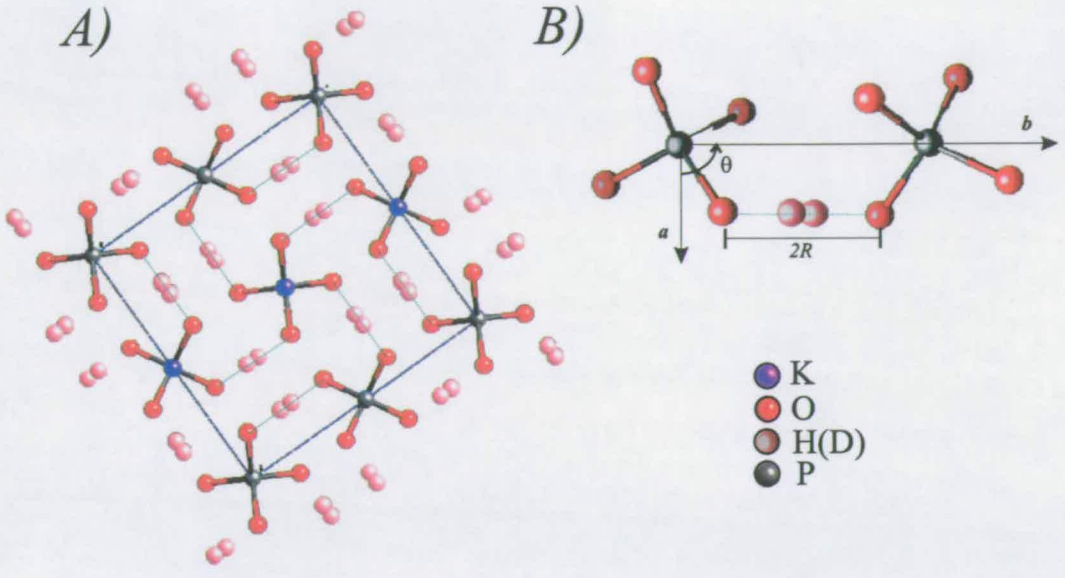

Figure 5.1. A) The KDP unit cell viewed along the (4-fold) z-axis, hydrogen bonds are indicated by dotted blue lines. B) A close-up of two hydrogen-bonded phosphate groups, again these are viewed along the z-axis. The hydrogen bondlength ($2R$) was observed to increase with pressure by Endo *et al.* [19]. This was achieved via a rotation about the z-axis measured by the angle θ.

Notably, in 1989 a single-crystal x-ray diffraction study of the ambient-temperature (tetragonal) phase was performed by Endo *et al.* at pressures up to 5.4 GPa in KDP and 6.5 GPa in DKDP [19]. Here, the authors reported a counter-intuitive elongation of the hydrogen bond (see Figure 5.1) in KDP under high pressure, beginning at a critical pressure P_c of 2.7 GPa (the same effect was observed at 4.2 GPa in DKDP). In this phase, at atmospheric pressure, the hydrogen atoms are known to be disordered over two equivalent sites between the oxygen atoms (see Section 5.1.2 later for a detailed description of the structure). Theoretical calculations had predicted that the hydrogen would exist in a single-minimum potential well for a H-bondlength of around 2.47 Å [76]. Endo *et al.* had noted that at P_c, they observed a H-bondlength of 2.45 Å and suggested that the unusual lengthening of the bond was a direct consequence of the centring of the

hydrogen atom under pressure.

The transition from a 'standard' H-bond to a centred bond is of fundamental interest and the fact that it can be induced *smoothly* by the application of pressure should permit a deep insight into the nature of the bonding. Also, the reported elongation of the bond under the application of pressure is unusual and suggests that the bond might be exhibiting some rather exotic behaviour. For these reasons, it appeared to be of significant importance to repeat the measurements using neutron radiation, which should allow the direct observation of the hydrogen-atom positions. This was done using powder diffraction techniques on the PEARL beamline.

This study also provided an opportunity to test the capabilities of the newly developed single-crystal techniques for the PEARL HiPr diffractometer (and indeed assisted in their further development). They also permit a direct comparison with the results of a powder study on the same compound and the opportunity to speculate on the advantages and limitations of single-crystal diffraction with the PE cell.

5.1.1 The Phase Behaviour of KDP

This study is concerned with the behaviour of the structure at room-temperature and at high-pressure. A complete phase diagram of KDP has been compiled and is shown in Figure 5.2. The phase behaviour at high pressure was first determined by Rapoport in 1970 [77] by differential thermal analysis, and the phase-labelling convention used in the figure (and throughout) is his. Rapoport was the first to propose the existence of the solid-solid transition from the room-temperature, ambient-pressure phase II to a new phase IV. His claim was based on the observation of phase II' and its respective phase boundaries. Extrapolation of the II'-II and II-I phase boundaries would predict a triple point at around 0.9 GPa formed with phase I. This was not, however, observed. Instead the II-II'

transition was found to disappear above 0.34 GPa and, additionally, a strong kink was observed in the II-I boundary. These observations could be consolidated by introducing the new phase IV and Rapoport plots a tentative phase boundary between it and phases II' and II.

In 1989, the single-crystal x-ray work of Endo *et al.* [19] produced structural evidence for the II-IV transition at room temperature. They performed both x-ray oscillation photography, and x-ray powder diffraction measurements to confirm that (up to their maximum pressure of 5.4 GPa) there was no evidence of a change of symmetry. Yet, their determination of both **a** and **c** lattice parameters as a function of pressure exhibited a clear kink at 2.7 GPa. This kink was accompanied by changes in the refined structural parameters and most notably, a kink in the hydrogen bondlength 2R. Further evidence of a transition followed in 1991 from the high-pressure capacitance measurements of Bao *et al.* [78]. These workers reported a sudden decrease of capacitance at 2.5 GPa at room-temperature. Finally, Kobayashi *et al.* [75] extrapolated Rapoport's II-IV phase boundary to room temperature, thus, identifying the observations of Endo *et al.* and Bao with this same phase transition.

5.1.2 The Structure of Tetragonal Phase II/IV

The transition between paraelectric-phases II and IV is second order in nature, and there is no accompanying change in the symmetry of the structure. Therefore, for both phases, the unit cell is tetragonal, with $\mathbf{I\bar{4}2d}$ symmetry, and contains 16 molecular units, two of which are shown in Figure 5.3. In the standard setting, the phosphorus atom is located at the origin, surrounded by four oxygen atoms located on tetrahedrally-distributed sites forming the phosphate groups. Each oxygen atom is related to another by hydrogen bonds that lie almost along the 2-fold axes (**a** and **b**) as indicated in the figure.

Some highly detailed work has been performed in the past on phase II using

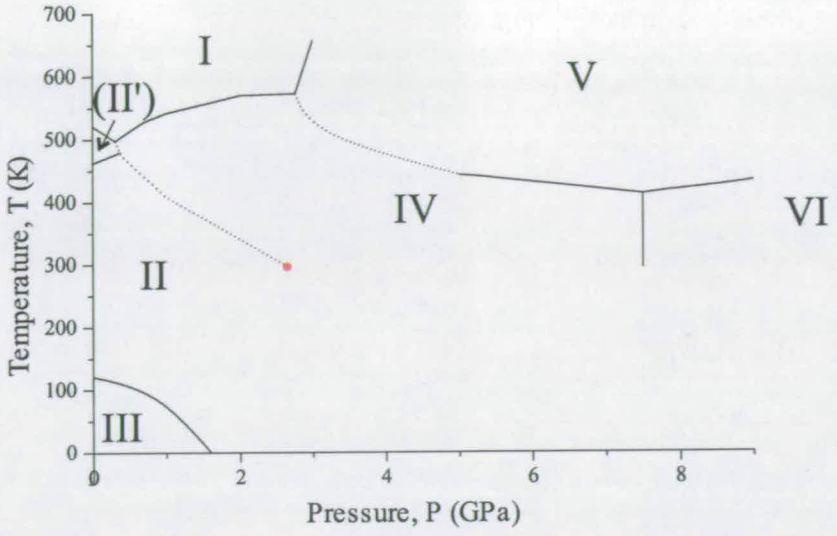

Figure 5.2. The phase diagram of KDP compiled from the data of Rapoport [77] and Kobayashi [75]. The position of Endo *et al.*'s room-temperature transition is marked by the red point.

neutron single-crystal diffraction. In this work, focused on the structural characteristics of the H-bond, Nelmes *et al.* [79] defines several useful parameters that characterise the geometry of the H-bond (these are illustrated in Figure 5.3):

- θ measuring the angular rotation of the PO_4 group about the 4-fold axis.
- 2R the O...O hydrogen bondlength.
- ϕ the angle made between the line joining H-bonded oxygen atoms and the **a-b** plane.
- ψ the angle made between the line joining the two disordered H-sites and the **a-b** plane.
- δ the separation between the two minima of the potential experienced by the hydrogen atom

The behaviour of these parameters was investigated up to 1.65 GPa (the maximum attainable pressure at the time) using single-crystal neutron diffraction and

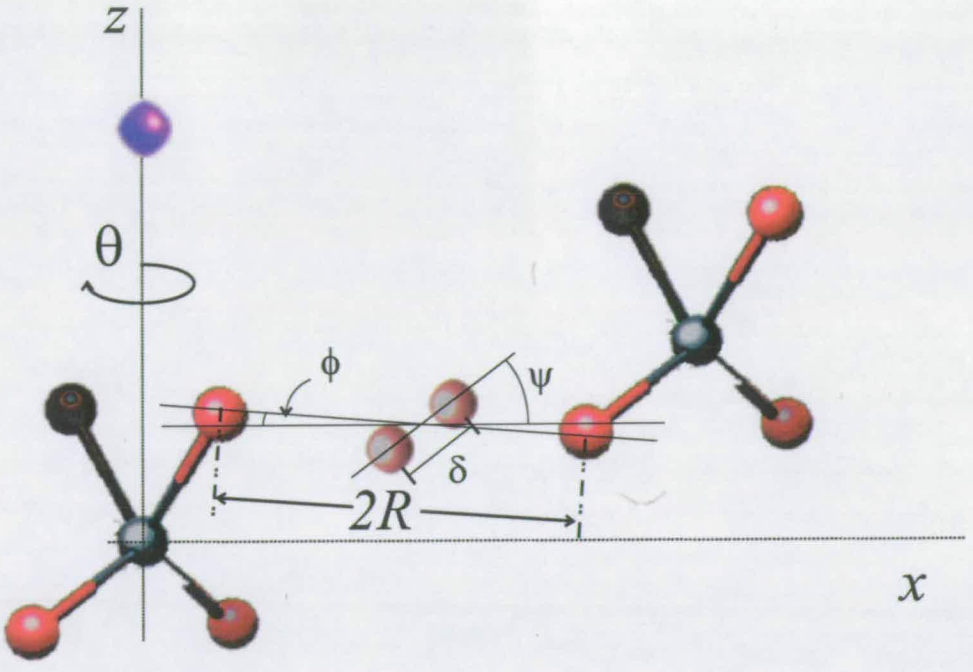

Figure 5.3. Two hydrogen-bonded phosphate groups are shown (the colour coding for the atoms is as used in Figure 5.1). Nelmes *et al.*'s parameters: θ, $2R$, δ, ψ and ϕ [79] are indicated, although the last two angles have been exaggerated for the sake of clarity (At ambient pressure, in KDP, they are $\psi = 8.8(1.4)°$ and $\phi = 0.265(19)°$ [79]). The x and z axes are parallel to unit cell vectors **a** and **c** respectively.

subsequently to higher pressures using x-ray diffraction. In 1987 a 'Users' Guide' to the crystal structures of KDP was published including this early high-pressure work [79].

5.2 A Study of The Hydrogen-bond Geometry in KDP by High-Pressure Powder-Diffraction Using Neutron Radiation

A series of high-pressure powder diffraction experiments have been carried out on KDP samples up to 5.4 GPa. The main aim of these experiments was to

investigate Endo *et al.*'s report of an elongation of the H-bondlength above 2.7 GPa using neutron radiation. These data were also required for comparison with the single-crystal measurements of KDP in the following Section 5.3.

An initial run of experiments were performed on samples of KDP and DKDP. These samples were loaded into a PE cell using single-toroid sintered diamond anvils with standard gaskets and a fluorinert PTM. However, non-hydrostaticity resulted in severe strain-induced broadening of the sample peaks. For this reason, measurements were later repeated when metal encapsulation gaskets [68] became available (see Section 4.3.3 in the previous chapter). These gaskets facilitated the use of a deuterated methanol-ethanol PTM, which remains a metastable liquid up to pressures as great as $\sim$ 10 GPa and thus provides a near hydrostatic medium up to the maximum experimental pressure here.

The dramatic increase in quality with the new PTM is clearly demonstrated in Figure 5.4, which shows a direct comparison of the effects of the two pressure transmitting media. Consequently, in the following discussion, only data measured with methanol-ethanol medium are presented. Unfortunately, time did not allow re-measurement of the DKDP data with the new encapsulated gaskets, so only the KDP measurements are presented here.

5.2.1 The Powder Patterns

As with the study of ices VII and VIII in Chapter 3, all data were collected on the PEARL-HiPr diffractometer [63], with the cell in the transverse setting, using the 90° powder bank of detectors. Rietveld structural refinements [36] were performed on the focused powder patterns using the GSAS suite of crystallographic software [27]. Prior to the refinement process, patterns were corrected for anvil attenuation (including Bragg edges), calculated by the program ATTEN [52] as described in Section 3.2.1. Incoherent scatter from the hydrogen content of KDP results in a large absorption effect and consequently, it was necessary to include this *sample*

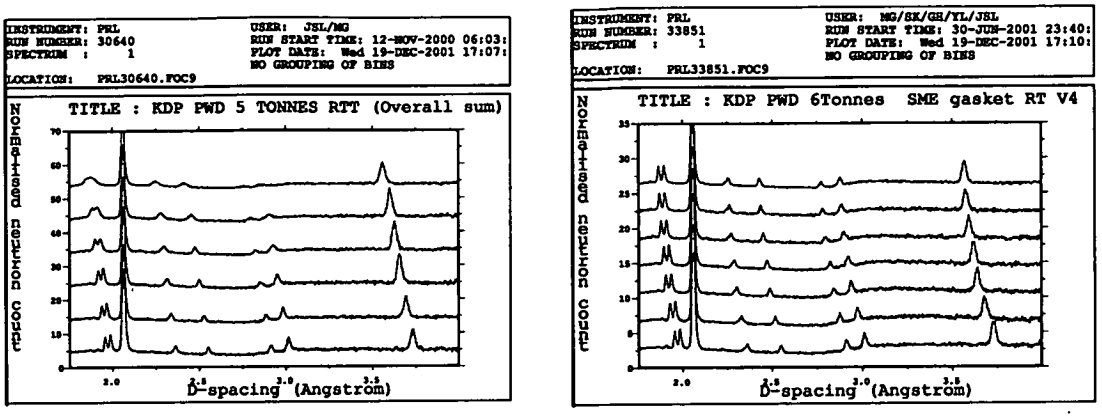

Figure 5.4. Variation of the KDP powder patterns as a function of pressure (increasing from bottom to top) for two different PTMs. The image on the left shows data measured with a fluorinert medium, whilst the image on the right shows data collected with metal encapsulation gaskets and a methanol-ethanol medium. The difference is especially pronounced for the doublet at 2 - 1.9 Å. Note that the large reflection at 2.05 Å that does not move with pressure is due to the diamond anvils.

attenuation in the calculation.

An additional effect of the incoherent scatter from the hydrogen is an extremely large internal background B_{int} (using the terminology of Section 3.2.1). This component of the background is still significant at the highest pressure point in the study. This negates the possibility of estimating B_o from the highest pressure measurement and, consequently, the function used to fit the external background in the high-pressure ice study is again used here, on the assumption that is constant in time.

A Rietveld fit obtained for a KDP powder sample, in the cell, at effectively ambient pressure is shown in Figure 5.5. Attention must be drawn to several important factors illustrated by this figure. Firstly, it is clear that the sample is a relatively weak scatterer and that the larger component of the pattern comes from the diamond-anvil scatter. It turned out that this introduced important limitations on the information that could be extracted during refinement and these are discussed further below.

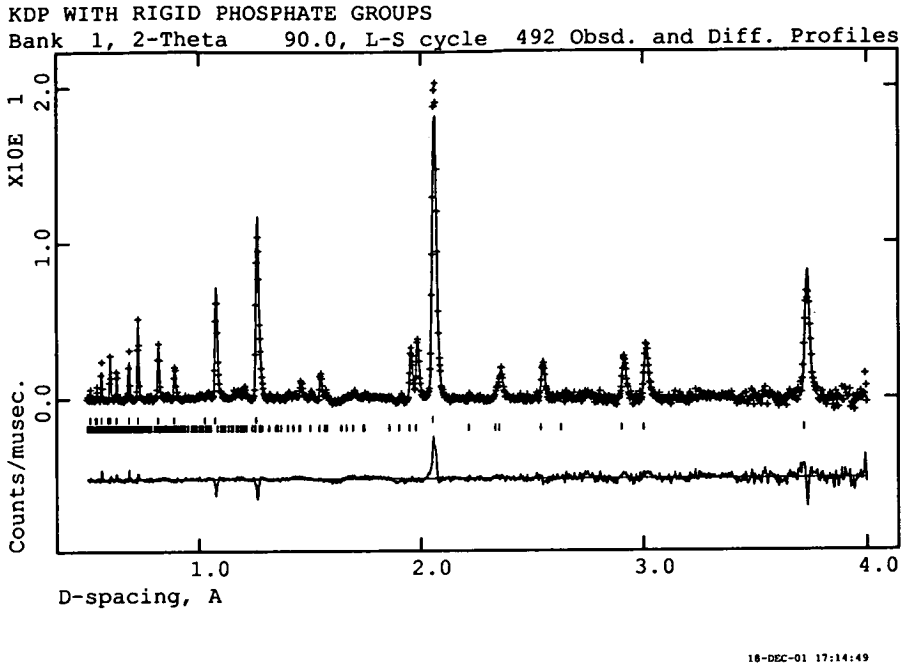

Figure 5.5. The figure shows a GSAS Rietveld refinement of a KDP powder diffraction pattern. The data points are marked with + symbols and the Rietveld fit is the line running through these. Two phases are fitted: the KDP powder sample and the diamond anvils. The respective reflection positions corresponding to these phases are marked with ticks: upper ticks correspond to the diamond phase and lower ticks to the sample phase. Below the ticks, is a difference curve showing $|F_{obs}|^2$ minus $|F_{calc}|^2$.

Secondly, from the difference curve at the bottom of Figure 5.5, it is clear that the diamond phase appears to be relatively badly fitted. This is an illustration of the failure of the attenuation calculation for the diamond phase that was highlighted in Section 3.2.1. The attempts to tackle this problem, are discussed in the following Section 5.2.2

Given the relatively low quality of the data, it was expected that no useful information could be extracted regarding the subtler aspects of the hydrogen geometry. For example, the parameters δ, ψ and ϕ would not be within the resolution of the data (for example Nelmes demonstrated that data out to a resolution of 0.5 Å was required to resolve the value of δ in KDP, which at ambient pressure is only 0.3647(28) Å in size [74]). Indeed, in all refinements, the hydrogen atom

was placed on the single site at the middle of the hydrogen bond. Despite this, it was expected that the value of 2R could be readily measured, thus giving a direct check on Endo *et al.*'s observation of the unusual expansion of the hydrogen bond. Bearing in mind the data quality, and the general observations made in Chapter 3, special care was taken during the data analysis, as described in the following section.

5.2.2 Constraints and Precautions Used During Refinement

Prior to reading the following discussion, the reader is directed to Sections 3.2.1 to 3.2.3 for a discussion of the main considerations and caveats applicable to powder refinements in the PE cell. Many of the principles discussed in these previous sections apply to the powder data measured on KDP. Additionally, as has been stated previously, KDP is an example of a *highly* absorbing sample and as such requires corresponding care throughout the refinement procedure. The implications of this for the current study and other precautions are given in detail below.

The Modelling of Atomic Thermal Motion

It was recognised that the data were insufficient to model accurately the thermal motion of the atoms. Consequently, the thermal parameters were fixed at the isotropic average of their ambient pressure values. At ambient pressure, the isotropically-averaged, in-plane thermal motion of the oxygen atom $U(\mathrm{O})$ is 1655×10^{-5} Å^2 [79]. For isotropic thermal motion, the excursions of the atom from its equilibrium position are described by a Gaussian distribution for which U is the square mean shift. Therefore, the square root of the thermal motion $\sqrt{U} = 0.1286$ Å corresponds to the radial displacement for which there is a 66% likelihood of finding the atom.

This displacement is equivalent to only 5% of 2R [79], additionally, any isotropic change in the thermal motion will not affect the measured hydrogen bondlength. This is taken as the mean separation of the oxygen atoms and, thus, cannot be changed by any *symmetric* distribution of density about it. The bondlength could be affected by anisotropic changes in the thermal motion, but it is assumed that these are negligible, and their measurement is beyond the accuracy of this study.

Fitting of the Hydrogenous Background

As a consequence of the large incoherent cross-section of the hydrogen atom, the data exhibit a very large background, upon which the Bragg peaks are superposed. Figure 5.6 shows the lowest pressure KDP data with the B_o obtained for the high-pressure ice data. The presence of strong Bragg edges in the background confirms that it originates from the sample volume. In fact, as the internal background is so large, it gives a good measurement of the attenuation that is also experienced by the sample.

Indeed, comparisons of B_{int} with the calculated attenuation correction A demonstrated that there were slight inconsistencies in the latter. Figure 5.7 shows both the highest pressure data, and the lowest pressure data plotted with the scaled A function. A consistent difference, observed in three separate data collections, was an extra component of background appearing at long d-spacings, that varied with pressure. This dependence on load is strong evidence that the effect arises from the sample position.

As has already been stated, the hydrogenous component of the sample results in a large attenuation of the incident beam. The incoherent scattering component of the absorption coefficient is around 0.17 mm^{-1}, which is extremely large, reducing the incident beam's intensity by a factor of almost 40% within the volume of the sample. Whilst most of this extra radiation appears as the considerable incoherent background, it is also likely that multiple-scattering effects will also

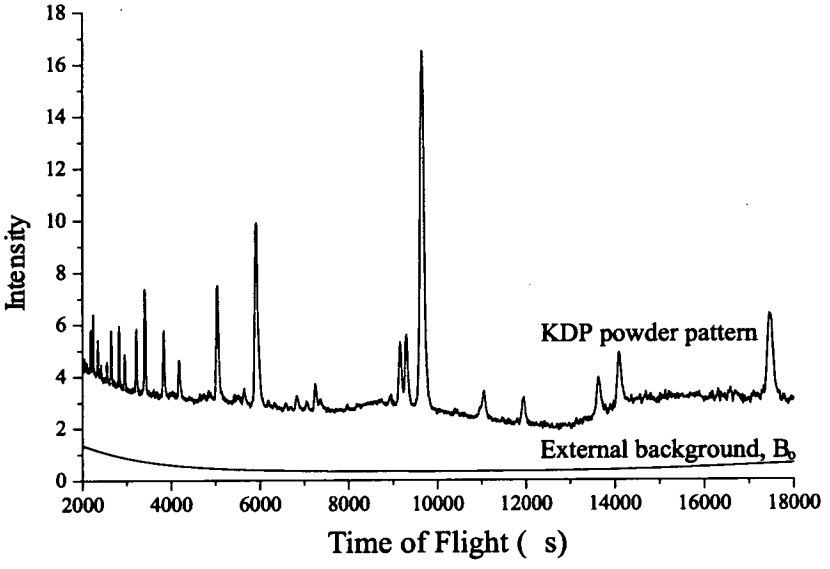

Figure 5.6. KDP data compared with the external background determined from high pressure ice measurements. The data exhibit an extremely large background due to incoherent scattering by the hydrogen atoms. The data clearly show the presence of Bragg edges as expected in an internal background B_{int} arising from a source within the sample volume.

be present. In this instance, the sample itself is acting as a secondary source of radiation, which is then re-scattered from the sample assembly, that is to say, the sample, gasket and anvils. It is likely that multiple scattering could give rise to extra components in the background.

With so many components involved, a multiple scattering effect would be extremely difficult to model, and the author merely highlights it as a possible cause of error in the Rietveld analysis. In order to assess the severity of this problem, the refinements were carried out with 8, 10 and 12 parameters describing the background. The resulting determination of the O...O hydrogen bondlength showed no measurable dependence on the number of background terms. This demonstrates that this particular structural parameter is not strongly correlated with the background determination.

Additionally, the KDP measurements were carried out on three separate samples,

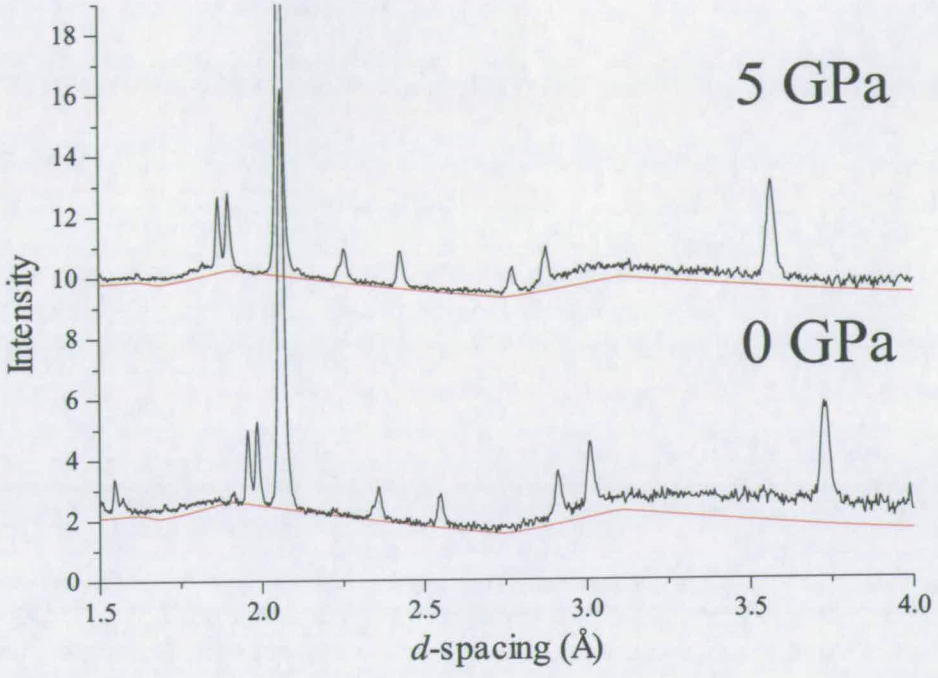

Figure 5.7. Focused diffraction patterns of KDP at 0 GPa (lower) and 5 GPa (upper). Superposed are the scaled attenuation correction functions A. Notice that at 0 GPa, above ~ 3 Å the observable background is noticeably higher than A.

the last two of which were loaded three months after the first. The data measured from the last two loadings demonstrated a large increase in the background (of almost a factor of two) which was attributed to hydrogenisation of the pressure medium over time. This substantial increase of background should exacerbate any inherent problem arising from an effect such as multiple scattering. Any variation in the hydrogen bondlengths refined from these different data sets would be a strong indication that the background was being insufficiently well modeled. This was not the case, implying that the presence of multiple scattering was not a serious problem for the analysis.

The Use of Rigid Bodies

During all refinements, the PO_4 groups were modeled as rigid bodies, thus fixing the P-O bondlength to its value at ambient pressure of 1.5403 (4) Å [79] and only permitting rotations about the phosphorus atom. This is physically reasonable as covalent bonds a extremely incompressible. Indeed, Nelmes *et al.* observed that up to 1.65 GPa, there was no change in the refined P-O bondlength within error [79] and Endo *et al.*'s higher pressure study [19] saw no change in P-O up to 2.7 GPa. Above this pressure, Endo *et al.* did observe a gradual reduction up to 5.4 GPa, however, this was rather small (of the order $\sim$ 2%) and not much larger than a single estimated standard deviation. Conversely, the effect of the groups *rotation* with pressure was known to be non-negligible and, certainly up to Endo *et al.*'s P_c, this effect acts to maintain the H-bondlength, which reduces at a much slower rate than the **a** lattice parameter.

Attenuation of the Anvil Signal

Failure of the attenuation model to correct the scatter arising from the anvils was highlighted in the ice refinements (see Section 3.2.1). As has been mentioned previously, this is expected to be especially severe where the sample is strongly absorbing. In order to assess this effect, refinements were carried out on histograms that were truncated at a different minimum d-spacings. As the number of both sample and diamond-anvil peaks increases rapidly at lower d-spacings, this leads to an increase in the amount of overlap, and, in the resulting impact of the fitted diamond peak intensities on those of the sample.

The different cut-off's that were explored were 0.5 Å, 0.6Å and 0.7Å. Again, no measurable change was observed in the refined hydrogen bondlength across the entire pressure range investigated. This was taken as evidence that this problem was also not an important one for the measurement of the H-bondlength. This is believable, as the bondlength is relatively large on the scale of the unit cell,

and consequently is sampled by the longer d-spacing reflections that correspond to the lower frequency Fourier components of the structure.

5.2.3 Results of the Powder Refinements

The results of the final refinements of the KDP data below P_c are shown in Figure 5.8, also plotted are Endo *et al.*'s single-crystal, x-ray data [19] and Nelmes *et al.*'s [79] single-crystal, neutron data for comparison.

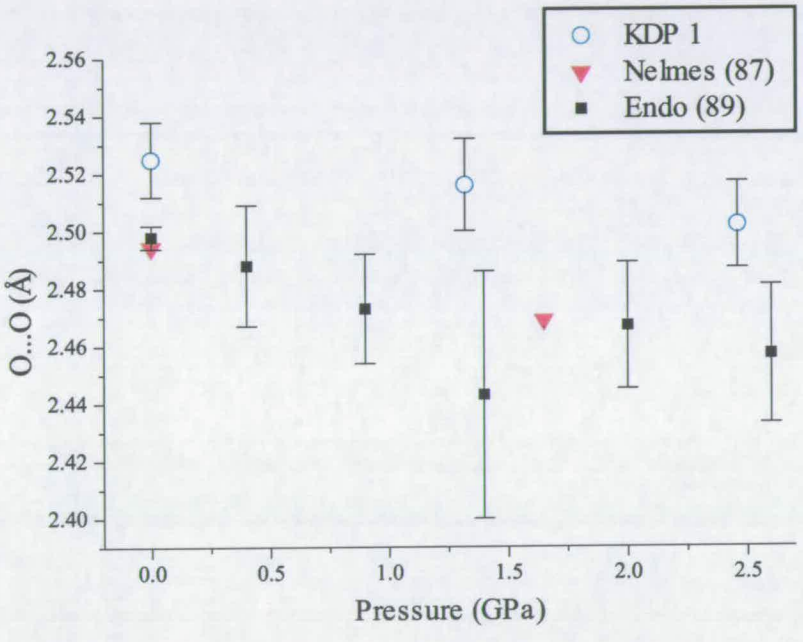

Figure 5.8. The final refinements of the author's neutron powder measurements of the hydrogen bondlength in KDP from one experimental loading. These are plotted with the measurements of Endo *et al.* [19] and Nelmes *et al.* [79] for comparison (note the greater precision of their single-crystal measurements: their estimated standard deviations at 1.6 GPa are a factor of seven smaller than the powder measurements at similar pressures and are smaller than the symbols used in this figure). The powder data measured in this study are consistently 1-2 standard deviation above both those of the previous values.

It is clear that, whilst the earlier single-crystal measurements [19] [79] agree well with each other, the current powder measurements are all offset to higher values

by ~ 0.05 Å. A similar offset was also observed in the ambient pressure measurements of the bondlength in the two subsequent measurements of the bondlengths (giving $2R = 2.518(19)$ Å and $2.525(16)$ Å compared to Nelmes' *et al.*'s value of $2.4946(6)$ Å). This is strong evidence that the offset is a systematic effect as opposed to the scatter expected as a result of experimental noise. Additionally, the ambient pressure single-crystal measurements performed by both Endo *et al.* and Nelmes *et al.* are expected to be significantly more accurate than the current powder data as they were measured in the absence of a pressure cell.

This presence of an offset could be evidence that there is some problem with the attenuation correction, a possibility that was discussed earlier in the preceding Section 5.2.2. However, such an effect is expected to change only gradually with pressure as, at these relatively low pressures, the geometry of the anvil and gasket system changes by very little and, therefore, neither does the attenuation experienced by the diffracted radiation. If this is assumed, then the overall *trend* of the data is still valid, although the absolute values must be viewed with some suspicion.

In line with this assumption, it was decided to apply a constant offset to all of the refined data points. This offset was chosen such that the ambient-pressure measurements agreed with the (more reliable) measurements of Endo *et al.* and Nelmes *et al.*

It can be seen that, with the offset, the current data agree with the previous measurements below P_c. At higher pressures, though, there is a discrepancy. The general trend of the current data is a continued decrease in hydrogen bondlength through the transition, which is borne out by all three experimental loadings.

Indeed, a best straight line though all the data points agrees well with the linear extrapolation of the previous measurements *below* P_c. There is a slight anomaly in the region of the proposed transition where there appears to be a cusp in the data. Whilst this is readily attributable to statistical fluctuations, there is a wealth of evidence (mentioned previously) that some kind of structural transition occurs

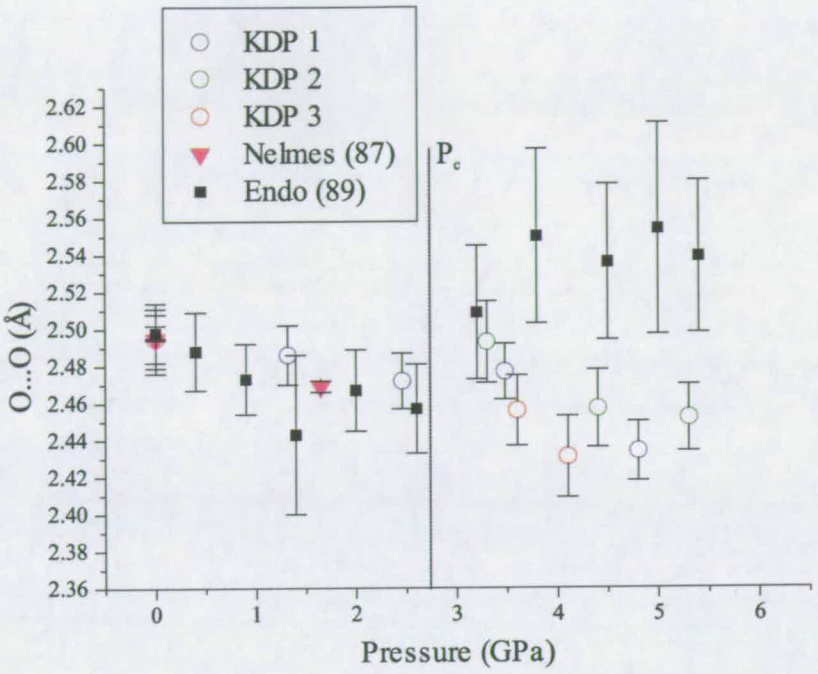

Figure 5.9. A Compilation of the author's neutron powder measurements of the hydrogen bondlength in KDP from three separate experimental loadings. As discussed in the main text, a constant offset has been applied such that the ambient pressure values agree with the measurements of Endo *et al.* [19] and Nelmes *et al.* [79], which are also plotted for comparison.

at around 2.7 GPa. It may be that this cusp is actually a real effect, however, the evidence is not strong enough to claim a definitive observation of a structural change.

In conclusion, this study has provided evidence that the high-pressure measurements of Endo *et al.* [19] were incorrect. It was a central goal of the single-crystal work described in the following section to confirm this result. Additionally, there was tantalising evidence that some kind of structural change is occurring in the region of the expected transition pressure, and it was also hoped that this could be elucidated by the greater accuracy of single-crystal measurements.

5.3 Single-Crystal Diffraction Measurements on KDP up to 7.2 GPa

The development of high-pressure, single-crystal techniques for the PEARL HiPr diffractometer was the subject matter of the previous chapter. The initial use of single-crystals of KDP and DKDP in tests of the detector geometry and of pressurisation techniques is described there. However, to demonstrate fully the technique, it was necessary to confirm that the measured intensities contained real structural information. To this end, a limited set of experiments were performed on single-crystals of KDP (only) at pressures up to 7.2 GPa. In these experiments, data were collected both with the cell stationary, with high-symmetry lines of reflections measured in the SXM, and using the stepped scans developed to take advantage of the longitudinal powder modules.

KDP provides an ideal test sample for several reasons: firstly its structure has already been well determined by neutron diffraction up to 1.65 GPa [74], and therefore a direct comparison can be made with the PEARL data up to this pressure. Secondly, the structure itself is simple, with relatively few refineable parameters. Finally, there is a certain historical resonance with this particular sample, the high-pressure characterisation of which (by *powder* diffraction) was one of the motivating factors for the development of the PE cell.

5.3.1 The Experiments

The data presented here were collected from two separate loadings of two single-crystal samples of KDP. These were both cut from the same mother crystal which had been ground into a flat plate ($\sim$ 30x20x2 mm^3) with the **a-c** plane very highly parallel to the surface of the plate ($< 0.5°$). Square 5x5 mm^2 segments cut from one end of the original plate were then glued to an aluminium rod with a 4.0 mm diameter, circular cross-section acting as a template from which the crystals

could be ground by hand into disks. The resulting cylindrical crystals were then further ground to reduce their thickness to 0.9 mm. Throughout, great care was taken to ensure that one of the original faces of the mother crystal was maintained as an alignment surface.

Both crystals were loaded in a PE cell with single-toroid, tungsten-carbide anvils and a deuterated methanol-ethanol (4:1) pressure-transmitting medium. A modified ME gasket was used with the techniques described previously in Section 4.3.3, the alignment surface of the crystal was attached to the flat part of the gasket by a very small amount of petroleum jelly. An initial load of 9-10 tonnes was immediately applied to seal the sample within the cell. The longitudinal collimator was attached, the entire cell placed in a modified cryostat tank with longitudinal shielding (see Section 4.3.2), and the cell rotation and encoding apparatus was connected. Without any further increase in load, the sample was placed into the diffractometer and illuminated with the beam. Sample reflections were clearly identified within five minutes, indicating that the crystal had survived the initial loading procedure. The cell was then rotated such that a bright, reference reflection was located into LPM3 to act as a pressure monitor.

For both loadings, the pressure was determined by comparison with Endo *et al.*'s lattice parameter measurements [19]. These data were fitted with a Birch-Murnaghan equation-of-state [49] with parameters: $V_o = 388.38(11)$ Å^3, the bulk modulus $K_o = 28.8(9)$ GPa, and its derivative $K' = 5.7(5)$ GPa. On increasing pressure, a single bright reflection in the TPM was tracked as an approximate guide to pressure. Where data were collected, the pressure was more accurately determined by measuring the d-spacings of ~ 20 reflections and refining the lattice parameters. This method allowed the determination of pressure to within 0.2 GPa.

For the first loading, the pressure was increased in gradual steps, as described in Table 5.1, up to a maximum pressure of 4.3(2) GPa ($a = 7.208(8)$ Å and $c = 6.710(7)$ Å).

Load (Tonnes)	Time at this load (minutes)	TOF (μs)	d_{400} (Å)	P (GPa)	Run No.
7	26	8977(40)	1.860(8)	0.2 (4)	35322
16	17	8856(40)	1.835(8)	1.7 (4)	35323
33	14	8708(40)	1.805(8)	4.0 (4)	35324
38	10	8670(40)	1.805(8)	4.0 (4)	35325
41	31	8640(40)	1.798(8)	4.3 (2)	35326

Table 5.1. Details of the increasing pressure steps from ambient to 4.3 GPa of the first KDP powder loading. The fourth column gives the d-spacing of the 400 reflection, which was used as a guide to pressure on increase. The last pressure point, where data were collected, was determined by refinement of the lattice parameters using the d-spacings of $\sim$ 20 reflections.

At this maximum pressure, five independent reflections with a wide angular separation were rotated into the SXM. From their positions on the detector face, the observed time-of-flights, the position of the cell w, and the lattice parameters, it was possible to refine the orientation matrix of the crystal. Data were then collected in two scans made at approximately 90° to each other. Both scans used a step size of 0.07°, each step lasting 45 minutes to 1 hour, giving a total time for each scan of the order of 9-10 hours. Additionally, the h00 and h0h lines of harmonics were given long exposures in the SXM of 1833 μAhrs and 1715 μAhrs respectively, each representing around 10 hours of neutron beamtime. Data collection in the SXM was limited to this small data set, as its detectors' limited angular coverage (combined with the high symmetry of the accessible h0l plane) meant that only one line at a time could be measured.

After these measurements, the pressure was reduced in steps, and data collected, first at 1.2(1) GPa (a = 7.370(9) Å and c = 6.882(9) Å) and then finally at 0.0(1) GPa (for this last measurement, the load was completely released from the cell). At both of these pressure points, the h00 and h0h lines of reflections were rotated in-turn into the SXM and a stationary measurements were made. The positions of the reflections in the SXM indicated no change in crystal orientation from 4.3 to 1.2 GPa, but a small change of $< 0.25°$ rotation out of the plane was observed

when the load was completely released.

Loading	Run number	Load (tonnes)	Pressure (GPa)	Run exposure, or average step exposure ($\mu Ahrs$)	Cell position ω (°)
1	35330(19)	41	4.3 (2)	160	86.91
	35352(22)	41	4.3 (2)	130	177.03
	35375	41	4.3 (2)	1833	200.28
	35376	41	4.3 (2)	1714	66.81
	35536	8	1.2 (1)	1548	200.22
	35537	8	1.2 (1)	2031	66.58
	35538	0	0.0 (1)	1529	66.58
	35540	0	0.0 (1)	1840	200.20
2	35556	50	4.5 (2)	1884	198.64
	35567	50	4.5 (2)	411	248.26
	35572(14)	71	7.2 (4)	130	198.39

Table 5.2. The table shows full details of the data collections on both loadings of KDP single crystals. In the second column, run numbers followed by a brackets indicate a scanned run, for example, "35330(19)" indicates a scan beginning on run 35330 and consisting of 19 steps (each themselves comprising an experimental run).

The second sample was taken up to 4.5(2) GPa in similar pressure steps. Again, two stationary measurements were made of the h00 and h0h lines to compare the intensities with the previous measurements. The pressure was then further increased to 7.2(4) GPa[1] and a single scan was performed. After this data collection, the pressure was further increased in steps with a bright reflection present in the TPM. At up to 81 tonnes, sharp single crystal reflections were still observed, but the subsequent measurements clearly illustrated that the peaks had begun to broaden widely in 2θ across the detector face. This broadening is consistent with the single-crystal transforming into a poly-crystalline sample, and was taken as the onset of the structural transition to KDP VI reported by Kobayashi at 7.5 GPa [75]. In the last measurement at 96 tonnes, there was no evidence of any single-crystal reflections.

[1]The highest pressure in Endo *et al.*'s data set was only 5.4 GPa, therefore an increase in the error is to be expected from the extrapolation of the equation-of-state

These experimental details are all summarised in Table 5.2. They are labeled with their experimental run numbers which are used throughout the text to refer to specific measurements. Where the data were collected as part of a scan, the notation used is the experimental run-number followed by the total number of steps comprising the scan (each constituting an experimental run) in brackets.

5.3.2 Analysis of the Data

Data Below 16.5kbar

Analysis of the data began with the ambient pressure data which could be compared directly with the known structure as determined from previous neutron studies. The measured TOF spectra of the h00 and h0h lines are given in figure 5.10. These clearly show that the data are of high quality, with strong sample peaks on a low background. In total, 14 reflections are observed out to a minimum d-spacing of just above 0.5 Å. Both lines are plotted to the same scale, and it is noticeable that the h00 line is considerably weaker than the h0h line. This effect is directly attributable to the occluding effect of the Cd shielding on the anvils face. The h00 line follows a path at a greater angle from to the scattering plane and is thus more affected. At these energies, cadmium can be assumed to be completely opaque, therefore, this effect is *only* proportional to the volume of crystal that is not occluded (See Figure 5.14 later). Consequently, the reduction in intensity is wavelength independent and can be corrected by a constant scale factor between the two lines.

With such a small number of reflections, it was clear that, certainly initially, structural refinement was not appropriate to assess the data. Instead, a far more simplistic approach was attempted, whereby structure factors were calculated using the known structure, and were then compared directly with the observed structure factors. Additionally, it would also be necessary to apply an absorption

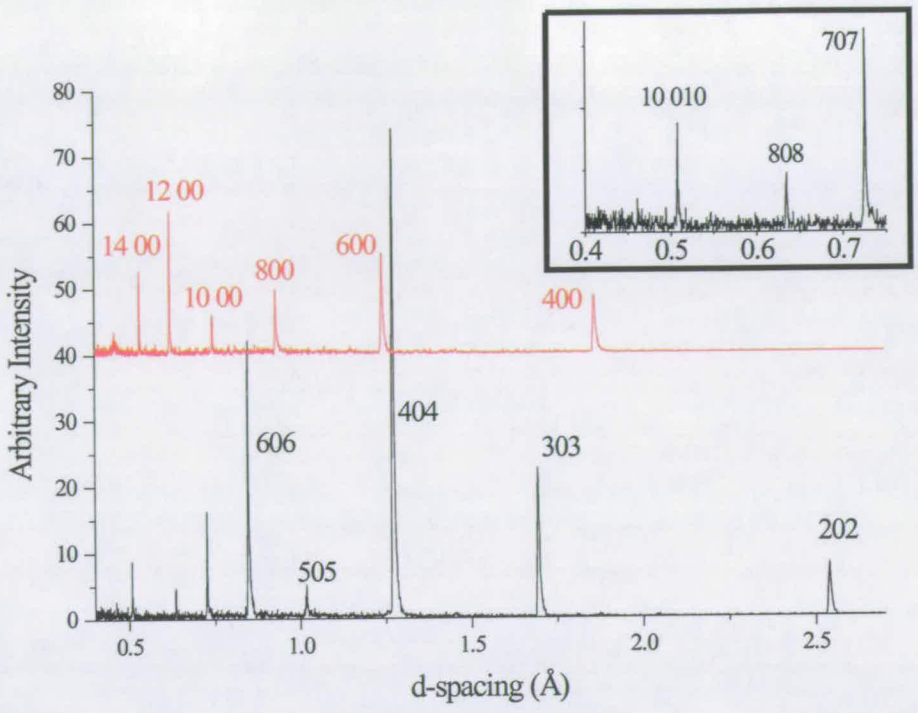

Figure 5.10. The figure shows TOF spectra measured along the h00 and h0h directions. The inset shows a close-up of the shortest d-spacing reflections on the h0h, line demonstrating the quality of the data down to almost 0.5 Å.

correction to the observed structure factors and a constant scale factor between the two lines.

Thus, ratios (r) were calculated that had the form

$$r(hkl) = \frac{|F_{obs}^{hkl}|^2 \times SF(\beta)}{A(\lambda) \times |F_{calc}^{hkl}|^2} \tag{5.1}$$

Here, SF is the wavelength-independent scale factor between the two lines and will generally be function of β, the angle out of the scattering plane.

In order to calculate the absorption correction, linear forms of the absorption coefficients $\mu(\lambda)$ were used for each absorbing component. The only relevant absorbing components are the sample itself and the Ti:Zr gasket material (see Section 4.3.2). The respective absorption coefficients listed below were *measured* for the Ti:Zr gasket material and *calculated* for KDP based on the known unit

cell contents and crystal dimensions.

$$\mu(\lambda)_{Ti:Zr} = 0.01993 + 0.01283\lambda \ \ (\mathrm{mm}^{-1}) \tag{5.2}$$

$$\mu(\lambda)_{KDP} = 0.17000 + 0.0008\lambda \ \ (\mathrm{mm}^{-1}) \tag{5.3}$$

An additional simplification applied was to use the same pathlengths through the gasket-sample system for each line of reflections. This assumption holds to first order, as there is such a small angular divergence between all of the accessible reflections. The total absorbing pathlength is the sum of the paths through the gasket and through the sample $l_{tot} = l_{Ti:Zr} + l_{KDP}$. The first of these was determined by measurement of the gasket at the end of the experiment to be 10.00(5) mm and the second is taken as the diameter of the sample: 4.0(1) mm.

Using these values, the total absorption was calculated and separated into wavelength-dependent and wavelength-independent factors as follows:

$$A = \exp[-(\mu_{Ti:Zr}(\lambda)l_{Ti:Zr} + \mu_{KDP}l_{KDP})] \tag{5.4}$$

$$= \exp[-(0.01993 + 0.01283\lambda)l_{Ti:Zr} - (0.17000 + 0.0008\lambda)l_{KDP}]$$

$$= C \times \exp[-(0.01283l_{Ti:Zr} + 0.0008l_{KDP})\lambda]$$

$$= C \times \exp[-0.137\lambda] \tag{5.5}$$

Here C = $e^{0.0199l_{Ti:Zr}+0.17000l_{KDP}}$ is the wavelength-independent component. This is the same for both reflections, and will appear as part of the overall scale factor in the comparison with the calculated structure factors.

Plots of the ratio r as a function of wavelength were used to assess the quality of the fit. Additionally, the average fractional deviation from a constant ratio (Q) was calculated as a guide to the quality of the fit. This was simply calculated as

$$Q = \frac{1}{\bar{r}N}\left[\sum_{hkl}(r_{hkl} - \bar{r})^2\right]^{\frac{1}{2}} \tag{5.6}$$

where $\bar{r}$ is the arithmetic mean of three ratio r across all hkl.

Initially, there appeared to be large discrepancies between the observed and calculated structure factors giving $Q > 66\%$. However, it was realised that these differences were consistent with the presence of a (rather large) extinction effect. This effect was modeled by using two extinction models: that of Zachariasen (Z) [80] and that of Becker and Coppens (BC) [30][31], each of which is described by a single parameter, x which is proportional to $|F_{calc}|^2\lambda^3$.

The expression used by BC (for a perfectly spherical crystal) is of the form

$$E^{-1} = y = (1 + x + \frac{A(\theta)x^2}{B(\theta)x})^{-0.5} \tag{5.7}$$

For poly-chromatic radiation x has the form

$$x \propto \frac{g|F_{calc}|^2\lambda^3}{\sin 2\theta} \tag{5.8}$$

Here, g is an extinction parameter that is related to crystal domain size in the case of primary extinction, and mosaic spread in the case of secondary extinction.

Although (as BC point out) the expression used by Z suffered from several mistakes in its derivation, its functional form is identical to that used above without the higher order term i.e. $y = (1 + x)^{-0.5}$. The expressions $A(\theta)$ and $B(\theta)$ take account of a dependence of the extinction effect on scattering angle. They are numerically calculated by BC, again for a perfect sphere, and are shown to approach zero for $\sin\theta \geq 0.9$. This is the case for both lines of reflections, which were measured at 133° in 2θ. Thus, both models would be expected to give the same result for a *spherical* sample. Nevertheless, tests were made using the

next largest angle calculated by BC, $\sin\theta = 0.8$, to gauge any possible differences between the two approaches for the cylindrical sample used.

The application of both A and E dramatically improved the fits giving Q <10% for the ambient pressure data. In order to find the optimum values of both the wavelength-dependent absorption-coefficient μ_{dep}, and the extinction parameter g, Q was calculated over a grid of values to locate its minimum and assess its width. This was performed both for Z and BC's extinction models. The inter-line scale factor (SF) giving the deepest minimum was selected as the appropriate value. The results for both the ambient pressure and 1.2 GPa data are shown in Table 5.3.

P	Z				BC			
(GPa)	A	g(scaled)	SF	Q %	A	g(scaled)	SF	Q %
0.0	0.24	2.75	1.4	9.5	0.22	2.00	1.4	10.1
1.2	0.22	5.64	1.8	17.1	0.19	3.55	1.8	19.6
0.0 *	0.24	2.60	1.4	10.1	0.21	1.90	1.4	10.8
1.2 *	0.24	1.20	1.8	7.7	0.21	0.90	1.8	6.9

Table 5.3. A tabulation of the values of the absorption coefficients A and extinction parameters g that gave the best fit as determined by the quality parameter Q. The results are shown for the two different extinction models of Zachariasen (Z) [29] and Becker and Coppens (BC) [30][31]. The value of the constant scale factor between the two measured lines of reflections SF is also given. (* The last two columns shows the results using a reduced data set with the 202,404,808,400 and 800 removed)

The first two rows of the table show results obtained when all of the data are included. It is immediately clear that the 1.2 GPa data give a much worse fit. In addition to this, the extinction is larger than at ambient pressure, and it is a general rule that the application of pressure cannot increase the amount of extinction (as it is expected to *reduce* the crystal quality). A closer inspection revealed that the large misfits were mainly due to a single badly fitted reflection in each of the two lines: the 800 and 808. Both of these reflections have extremely weak calculated structure factors (they are significantly reduced from

their ambient pressure values by the change of structure), and it is probable that ill-conditioning is strongly emphasizing any mis-fit. Additionally, those reflections that were most affected by extinction at ambient pressure (202, 404, 400) are also removed in the reduced data sets.

The third and fourth rows of the table show the results using the reduced data sets. Not only are the data better fitted, but the extinction parameter is seen to decrease with pressure as is expected.

Additionally, colour contour plots of Q as a function of both μ_{dep} and x for both the ambient pressure data and the 1.2 GPa data are shown in Figures 5.11 and 5.12. The first of these, Figure 5.11, shows the results obtained with the full set of reflections. The second, Figure 5.12, shows the results using the reduced data set. There are several features that are common to all of these images. In all cases the fit is very bad for low values of g. The fit is then seen to improve rapidly as g is increased before bottoming out into a wide valley. the breadth of this valley indicates a strong correlation between the absorption and extinction parameters.

Meanwhile, the dependence of Q on the value of μ_{dep} is much less than that on g, as the valley of the minimum tends to run parallel to this direction. The tabulated results show that the best fitting value of the μ_{dep} is significantly larger that the calculated value of 0.14 Å^{-1}, but, this value is clearly very poorly defined. Equation 5.7 obtained by BC was calculated in the absence of absorption. They also examined the effect of non-negligible absorption and found that for "...reflections significantly affected by extinction, absorption and extinction are completely correlated"[30]. The presence of cell attenuation means that this *is* the case here.

The extinction factors themselves are given in Table 5.4 (only for the BC correction) for each reflection measured at ambient pressure. It should be pointed out that these values correspond to an extremely large extinction effect. In 1988 Jauch [81] performed a comparison of different extinction models (including Z

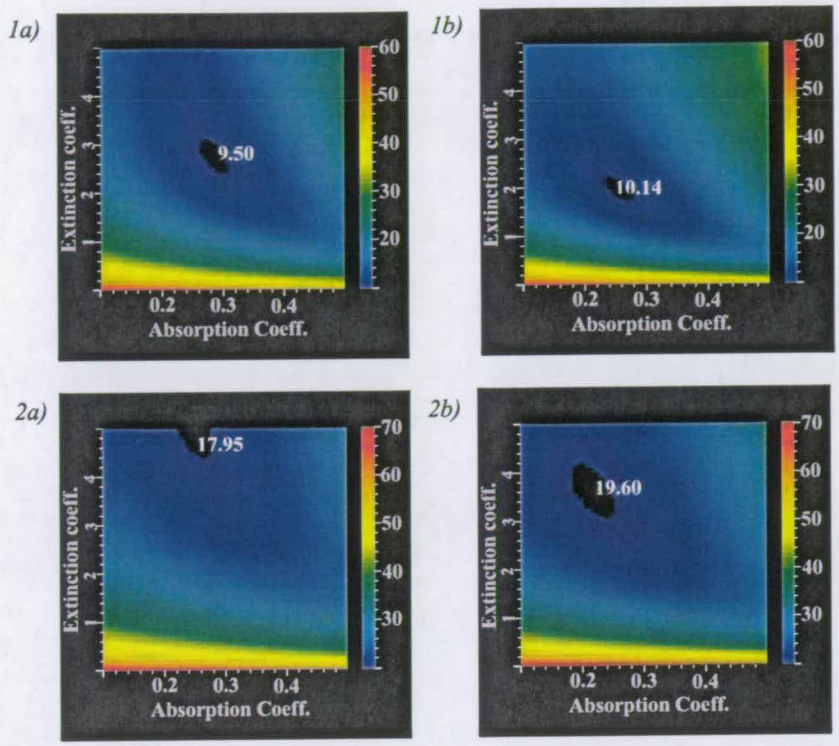

Figure 5.11. Colour contour plots of the fit Q between measured and calculated structure factors for KDP at ambient pressure (full data sets are used). Plots (1a) and (1b) are at 0 GPa for the Z and BC extinction models respectively, whilst (2a) and (2b) are for the 1.2 GPa data. The minimum value of Q is printed on the plots, note it is much shallower for the 1.2 GPa data.

and BC) for TOF single-crystal diffraction with a sample crystal of MnF_2. In this study, it was found that different cut-off values for y had a significant effect on fits of the data for all of the extinction models tested and final refinements were performed only using reflections with $y \geq 0.4$. If this requirement were applied to the current data 40% of the reflections would have to be excluded Of course, this is partly due to the reflections measured: those lying along directions of high symmetry tend to be strong reflections, and therefore are strongly affected by extinction.

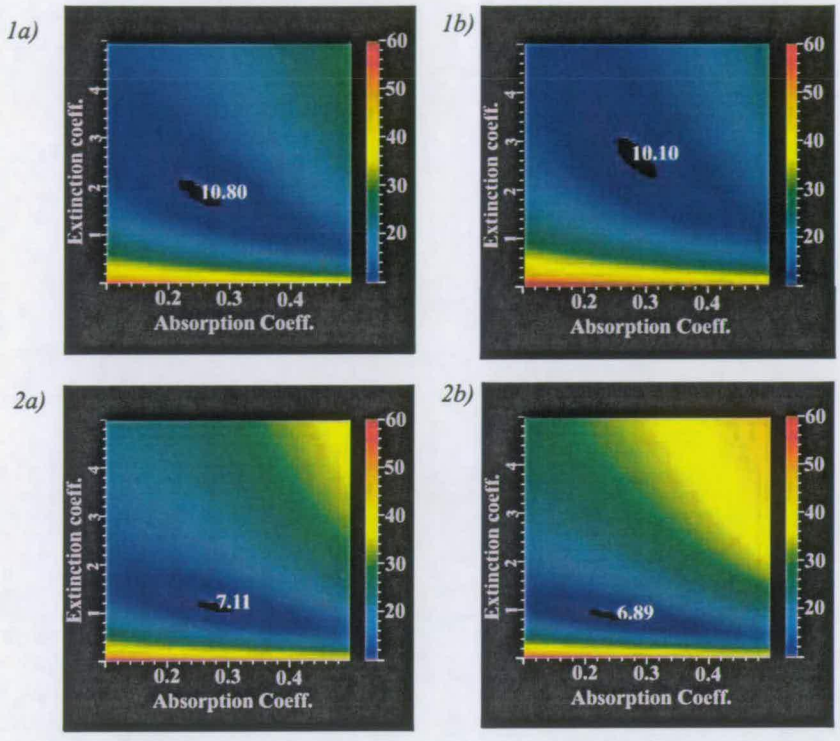

Figure 5.12. Colour contour plots of the fit Q between measured and calculated structure factors for KDP at ambient pressure (here reduced data sets were used with the 202,404,808,400 and 800 removed as discussed in the main text). Plots (1a) and (1b) are at 0 GPa for the Z and BC extinction models respectively, whilst (2a) and (2b) are for the 1.2 GPa data. The minimum value of Q is printed on the plots. The minimum value of Q is now much lower with the reduced data sets.

Higher Pressure Data: Stationary Data Collection

The analysis of the low pressure data clearly highlighted that, despite well determined intensities, the presence of severe extinction was a potential barrier to refinement of such a small data set. Despite this, it was important to attempt the refinements to establish if the higher pressure data sets contained meaningful structural information.

Unfortunately, the data are not only limited to a very small number of reflections, but these reflections only sample the structure along two well-defined directions in reciprocal space. Therefore, it was necessary to use a heavily constrained model

hkl	Full data set (0 GPa)	
	y	λ(Å)
202	0.05	4.659
303	0.14	3.111
404	0.08	2.335
505	0.88	1.867
606	0.30	1.557
707	0.70	1.333
808	0.91	1.165
10 010	0.89	0.932
400	0.15	3.568
600	0.36	2.381
800	0.65	1.787
10 00	0.79	1.427
12 00	0.45	1.190
13 00	0.67	1.020

Table 5.4. A complete listing of the value of the extinction factors y for all of the measured reflections at 0 GPa (their wavelengths λ are also given). From the definition of y in Equation 5.7 it is clear that the smaller its value the larger the extinction effect, $y = 1.0$ being equivalent to no extinction. It can be seen that many reflections are strongly affected, most notably the 202,303,404 and 400.

in the refinement process. To this end, the phosphate groups were again (as in the powder refinements) constrained to be rigid groups.

It was initially decided to use a double-site model for the hydrogen atoms. The single-crystal data extend to 0.5 Å and, thus, have a sufficient resolution (according to Nelmes *et al.* [79]) to measure the separation, δ. To this end, the hydrogen atoms were represented by a constrained 'molecule' with two, 25% occupied hydrogen atoms sites[2], each equidistant about a centre of symmetry at (x(O),0.25,0.125). The separation of the hydrogen sites was then constrained to a value derived from a linear extrapolation of Nelmes *et al.*' values for δ at 0 and 1.65 GPa (respectively 0.3647(28) Å and 0.315(11) Å) and the 'molecule' allowed to rotate as symmetry permitted.

[2]The centre of symmetry maps each hydrogen site on top of the other, thus doubling the occupancy of the individual sites giving 50% occupancy.

After the initial refinements, it became clear that this two-site model was unstable, and often did not converge, most likely because of the paucity of data. Consequently, the model was simplified further and only a single-site was used for the hydrogen atom, although an isotropic, thermal-motion parameter was permitted to refine freely. Comparisons of both models demonstrated essentially the same behaviour, and both gave almost identical R-factors.

An additional constraint was to fix the z-coordinate of the oxygen atoms. This was required as there is very little information along the c-axis in the reflections measured. Also, as the hydrogen bond lies almost perpendicular to this direction, it's length is, to a first approximation, determined by the oxygen atoms x, y coordinates.

Prior to refinement, the data were corrected for the wavelength dependent absorption with $\mu_{dep} = 0.21$ obtained in the previous section. Additionally, each line of reflections was multiplied by a constant factor scale factor as had been determined previously. No correction was applied for extinction prior to refinement. Refinements were performed using the SHELXL-97 program within the WinGX suite of crystallographic software [26].

Initially, the ambient pressure data were refined. The only variables used were:

- Rotation of the PO_4 groups about the 4-fold c-axis θ.
- An isotropic thermal parameter for the hydrogen atom $U_{iso}(H)$.
- A Z-type extinction model was used and the extinction parameter g_z was refined.

The initial refinement gave a rather bad fit with an R factor of 25.12%, and the refined value for the extinction parameter was very large (>300). However, when a constant scale factor was allowed to vary between the two lines, the fit improved dramatically.

The R-factor dropped to $\sim$ 6% and the extinction parameter correspondingly dropped to 4, but with an associated error of 6. This is reminiscent of the previous comparison of the observed and calculated structure factors: the presence of an extinction correction was required, but the exact value of the extinction was poorly determined. The other characteristic highlighted in the comparison, was that the value of the absorption was also poorly determined. Unfortunately, wavelength-dependent absorption could not be refined with the available software. Therefore, to investigate the effect of absorption, the data were corrected using different values of μ_{dep} to access the sensitivity of the fit. The results are given in Table 5.5

H model	μ_{dep} (mm^{-1})	*R*-factor	*SF*	*g*	O...O (Å) (2*R*)	P-O (Å)	U_{iso}(H) (Å^2)
2-site	0.07	-	did not converge				
	0.14	-	did not converge				
	0.21	6.7%	2.4 (3)	4 (6)	2.497 (16)	1.540 (11)	
	0.28	6.8%	2.4 (3)	2 (3)	2.494 (15)	1.540 (10)	
1-site	0.07	8.1%	1.5 (2)	415	2.500 (12)	1.541 (11)	0.077 (29)
	0.14	6.4%	1.6 (2)	296	2.505 (12)	1.541 (9)	0.070 (20)
	0.21	5.6%	2.4 (3)	4 (6)	2.504 (16)	1.541 (9)	0.050 (10)
	0.28	6.7%	2.4 (3)	2 (3)	2.504 (13)	1.541 (9)	0.045 (9)

Table 5.5. Parameters refined from SXM measurements at 0 GPa for both a 2-site and single-site model of the hydrogen atom. Four different values for the absorption coefficient, μ_{dep} were used. It can be seen that, whilst different absorptions corrections have a strong effect on the extinction parameter g, the bondlengths O...O and P-O are essentially independent of μ_{dep}.

These results clearly show a correlation between the refined extinction and the absorption correction: the extinction parameter diverging for too low an absorption correction. It is also clear that the scale factor between lines is also strongly correlated with the extinction/absorption correction. Removal of the most highly extincted reflections did not improve the fit, nor reduce the uncertainty in the value of the extinction coefficient. It is noticeable that the absolute value of the hydrogen bondlength is equal (within error) to that of Nelmes *et al.* of 2.4946 (6)

Å [79] demonstrating that the PEARL data are least consistent with accepted structure.

Refinements of the 1.2 GPa data yielded similar results. Again the single-site model was more stable and generated the results given in Table 5.6. As before, the extinction parameter was poorly determined.

μ_{dep} (mm^{-1})	*R*-factor	*SF*	*g*	O...O (Å) (2*R*)	P-O (Å)	U_{iso}(H) (Å^2)
0.07	10.5%	1.8 (4)	8 (10)	2.499 (18)	1.539 (8)	0.052 (15)
0.14	8.0%	2.2 (5)	13 (10)	2.511 (26)	1.539 (6)	0.048 (11)
0.21	5.9%	2.0 (2)	1 (1)	2.479 (11)	1.539 (6)	0.045 (8)
0.28	5.2%	2.5 (3)	0.8 (4)	2.472 (9)	1.538 (5)	0.042 (7)

Table 5.6. Parameters refined from SXM measurements at 1.2 GPa using the single-site hydrogen model. For these data, there is a stronger variation of O...O bondlength with the absorption coefficient, whilst the P-O bondlength is again independent.

Finally, the refinements of the data measured at 4.3 GPa are given in Table 5.7. These data only included stationary measurements in the SXM of the same lines of reflections as the lower pressure data sets.

μ_{dep} (mm^{-1})	*R*-factor	*SF*	*g*	O...O (Å) (2*R*)	P-O (Å)	U_{iso}(H) (Å^2)
0.17	9.7%	1.8 (4)	8 (10)	2.428 (18)	1.532 (10)	0.073 (33)
0.21	9.1%	1.0 (3)	2.2 (3)	2.422 (17)	1.534 (10)	0.072 (34)
0.25	8.1%	1.2 (4)	0.7 (8)	2.427 (15)	1.534 (10)	0.050 (22)

Table 5.7. Parameters refined from SXM measurements at 4.3 GPa with the single-site hydrogen model. This time, only the three highest absorption corrections are used, with $\mu_{dep} = 0.07$ giving an especially bad fit.

Overall, the refinements give reasonably good fits, although they are slightly worse for the 4.3 GPa data. There appears to be a certain amount of ambiguity between the scale factor, the absorption correction, and the extinction parameter. Despite this, the fitted value of the hydrogen bondlength is remarkably consistent,

as is the refined P-O bondlength. The latter agrees well with the determination of Endo *et al.* [19], but, there is a marked difference with the O...O measurement.

In fact, these single crystal results agree well with the powder refinements described in the previous Section 5.2.3 (as before, this assumes a constant offset). All of the authors measurements are shown in Figure 5.13 with the single-crystal measurements of Nelmes *et al.* [79]. The values plotted for the HiPr measurements are those for $\mu_{dep} = 0.21$ which appeared to consistently give the best fit to the data. The PEARL SXM data are, thus, not only consistent with the low pressure structure, but, also lend support to the conclusion of the powder study that the result of Endo *et al.* [19] is incorrect.

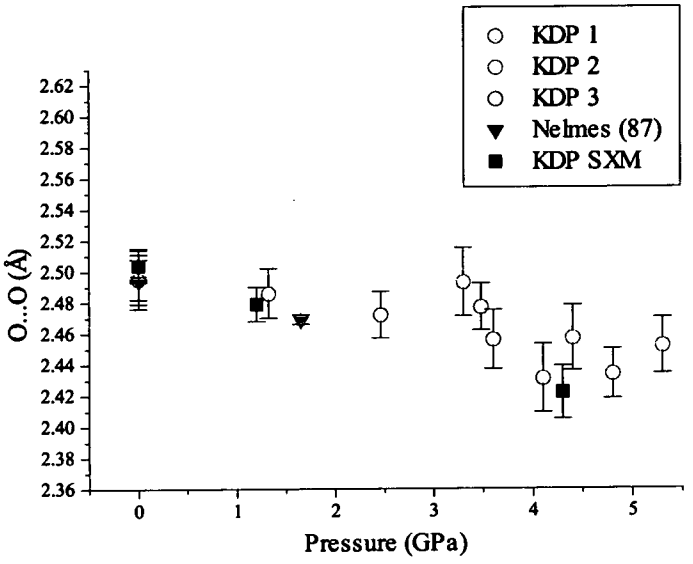

Figure 5.13. Refined values of O...O from the PEARL single-crystal measurements (corrected for absorption with $\mu_{dep} = 0.21$ as discussed in the main text). Also plotted are the single-crystal values of Nelmes *et al.* [79] and the powder data with the offset as described in Section 5.2.

Higher Pressure Data: Scanned Data Collection

It now remained to establish if the data determined from scans in the powder modules also gave meaningful results. Two scans were performed at 4.3 GPa

hkl	$\|F_{obs}\|^2$	σ^2	meth.	λ (Å)	hkl	$\|F_{obs}\|^2$	σ^2	meth.	λ (Å)
004	33.95	0.92	1	2.2877	$\bar{1}\bar{0}00$	9.87	0.91	2	1.3819
004	40.39	1.32	1	2.3006	$\bar{6}00$	29.35	1.23	1	1.6451
008	350.04	5.8	1	1.1426	$\bar{6}00$	19.96	0.48	2	2.3004
008	440.9	7.52	1	1.1499	$\bar{4}00$	11.69	0.58	1	2.4691
$\bar{3}05$	205.34	4.52	1	0.5855	$\bar{4}00$	7.29	0.37	2	3.451
$\bar{3}05$	223.95	5.49	1	0.6073	$\bar{2}00$	9.93	0.83	1	4.9337
305	22.67	1.14	1	2.24	$\bar{9}10$	21.59	2.00	1	1.0769
105	8.36	0.83	1	2.1457	$\bar{9}10$	18.91	1.69	1	1.088
105	6.62	0.66	1	2.1582	$\bar{1}\bar{0}02$	62.49	4.34	1	1.1628
107	68.19	2.87	1	1.4865	$\bar{9}12$	2.84	0.62	1	1.3001
107	72.59	2.97	1	1.4967	$\bar{8}02$	13.95	1.46	1	1.4866
208	163.05	5.51	1	1.3663	$\bar{7}01$	34.45	1.65	1	1.6077
208	190.78	4.99	1	1.3737	$\bar{6}04$	7.91	1.03	1	1.9371
2010	120.58	6.02	1	1.0709	$\bar{6}04$	8.55	1.11	1	1.9457
2010	115.46	6.4	1	1.0772	202	16.31	0.68	2	4.6774
3011	76.56	7.54	1	1.005	303	19.97	0.45	2	3.128
3011	54.42	7.46	1	1.0098	404	70.76	0.63	2	2.3415
6010	87.46	6.83	1	1.1187	505	2.29	0.38	2	1.874
$\bar{1}\bar{4}00$	68.72	2.58	2	0.9859	606	74.74	1.18	2	1.5616
$\bar{1}\bar{2}00$	267.97	8.96	1	0.8211	707	11.02	0.81	2	1.3376
$\bar{1}\bar{2}00$	112.6	2.27	2	1.1499	10010	35.15	2.4	2	0.9373
$\bar{1}\bar{0}00$	42.63	5.15	1	0.987					

Table 5.8. Complete compilation of the $|F_{obs}|^2$ measured at 4.3 GPa in both scanned collections (marked 1), and stationary collections in the SXM (marked 2).

measuring a total of 28 independent reflections were measured. These are exhaustively listed below (although those measured in overlapped elements as described in Section 4.2.2 have been excluded):

These reflections have all been corrected for a wavelength-dependent absorption effect with $\mu_{dep} = 0.21$ as before. In addition, they have been corrected for wavelength independent absorption arising from the tilt of the sample crystal. In order to achieve this, a model was developed whereby the cadmium shielding on the anvil faces was taken to be completely opaque, and to be positioned such that it absorbed all rays passing through the tungsten carbide anvil material. This has the effect that the total scattered radiation is only proportional to the volume

of sample that is un-occluded, and hence, no further wavelength dependence is introduced (the effect is only dependent of the angle out of the equatorial plane β that the scattered beam follows to the detectors). This is illustrated schematically in Figure 5.14.

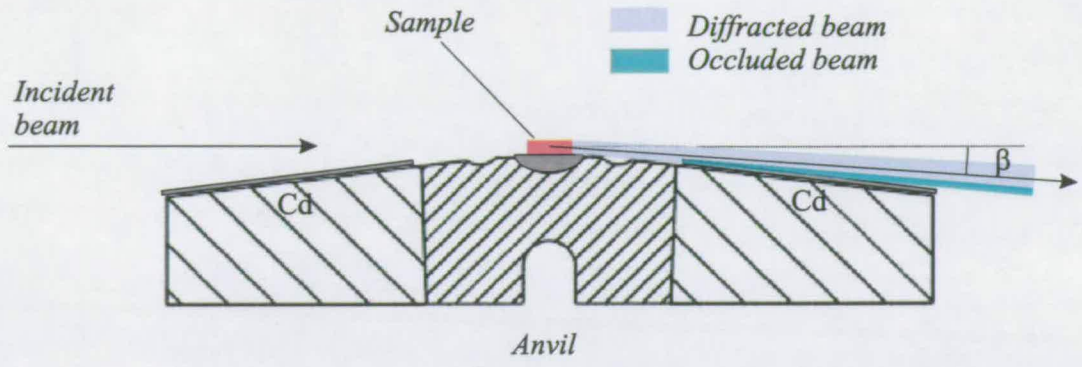

Figure 5.14. Schematic showing the occlusion of the diffracted beam by cadmium shielding, an effect that depends on the angle β, the inner diameter of the Cd, and the height of the crystal.

In order to apply this correction, the β angle of each measured reflection was determined from the orientation matrix of the crystal. The other quantities affecting the calculation are the height of the crystal, and the inner radius of the cadmium, both of which are known.

It is clear there are significant differences between different measurements of the same reflections that have been scanned through adjacent (non-overlapped) detectors. This is evidence that there *is* an extra wavelength dependence arising from tilting of the V-detector elements. In this instance, the most valid tactic is to average the two values. It must also be highlighted that the extinction observed in the stationary SXM measurements will be an even larger problem, as the data are now measured over a large range of 2θ values. This is highlighted in the measurement of the $\bar{3}05$ and the 305. As a consequence of the crystal symmetry, these two reflections are equivalent, yet, there is clearly a strong wavelength dependence beyond simple absorption (which has already been corrected for), the latter reflection measuring a factor of 10 weaker than the former.

Wavelength dependent effects are also visible in a comparison of the stationary measurement and the scanned measurement of the $\overline{h}00$ line. As this constitutes a re-determination of the same reflection, occlusion is constant. Any differences between the two is only due to wavelength dependent effects.

Perhaps unsurprisingly, given these considerations, refinements performed using this data set refined rather poorly. An R-factor of 16.7 % was achieved using the two-site model, and an almost identical value of 16.5% for the single-site model (although the latter gave a value of 7 for the extinction parameter compared with 295 for the former). The resulting hydrogen bondlength for the single-site model was 2.427 (25) Å, which agrees with the value determined from the stationary measurements of 2.422 (17) Å.

A refinement was also attempted containing only the stationary SXM data with the $\overline{h}00$ reflections from the powder scans. This gave a 9 % R-factor, which is comparable to that obtained from stationary SXM measurements alone. However, a comparison of the extinction corrected data (shown in Table 5.9) illustrates that there are still strong discrepancies between the two types of measurement. For instance the 1000 reflection measured in the scan is more than a factor of two greater than the stationary measurement. Meanwhile, the 600 reflection measures nearly 40% stronger in the *stationary* measurement.

This result is unsatisfying, as it is unclear whether the discrepancies between the stationary and scanned data collections are attributable to extinction or failure of the scanning technique. It is the opinion of the author that this work has highlighted a long standing problem with extinction corrections for TOF diffraction data. Studies such as that of Jauch *et al.* [81], have demonstrated that the current models of extinction all fail to a certain extent for strongly affected reflections. In many cases, extinction in TOF diffraction is handled simply by discarding the worst affected reflections. Whilst this approach may be adequate when large data sets have been determined, it is not ideal and, in the present

Measurement	hkl	$\lvert F_{obs}^{hkl}\rvert^2$	$F\lvert_{calc}^{hkl}\rvert^2$	$\delta(F^2)/\sigma_{hkl}^2$
scan.	1000	119.93	63.32	1.93
scan.	600	517.73	706.85	1.58
scan.	1200	3080.89	2393.95	1.39
stat.	1000	50.90	63.32	0.94
stat.	400	285.62	252.25	0.63
scan.	400	226.38	252.25	0.55
stat.	1200	2611.68	2393.95	0.49
stat.	800	0.00	0.08	0.07
scan.	800	0.00	0.08	0.07
stat.	600	712.12	706.85	0.04

Table 5.9. A comparison of the observed and calculated structure factors output by the WINGX [26] refinement software for both stationary (stat.) and scanned (scan.) reflections. The observed intensities have been corrected for the refined extinction. The parameter $\delta(F^2)/\sigma_{hkl}^2$ gives a measure of the quality of the agreement between observed and calculated structure factors, and the reflections are given in ascending quality of fit according to it.

case with an extremely limited data set, it appears to be a serious problem. Additionally, it appears that the absorption that inevitably arises from the pressure cell complicates the problem further.

Of course, these same problems will effect the 7.2 GPa data. A full listing of the intensities measured in the single scan performed at this highest pressure is given in Table 5.10. It is important to underline that the data set contains reflections that are well determined (to within a few percent) out to 0.5 Å. Regardless of the data analysis problems, this represents a step forward in single-crystal neutron diffraction at high pressure.

5.4 Discussion and Conclusions

A new powder diffraction study of KDP, combined with the newly developed single-crystal techniques, have been used to measure the hydrogen bondlength up to almost 5.5 GPa. Whilst both techniques agree well with each other (within the

hkl	$\|F_{obs}\|^2$	σ^2	meth.	λ (Å)	hkl	$\|F_{obs}\|^2$	σ^2	meth.	λ (Å)
400	42.78	0.66	3	3.2301	701	300.1	4.86	1	1.6709
400	42.53	0.71	2	3.2361	501	67.33	2.27	1	2.2164
600	151.9	1.15	3	2.1520	1002	384.91	9.04	1	1.1079
600	127.57	1.04	2	2.1568	301	140.67	3.14	1	3.1461
800	7	0.43	3	1.6168	602	1005.53	6.43	1	1.5729
800	0	0.07	2	1.6183	903	373.27	8.84	1	1.0508
1000	52.17	1.83	3	1.2908	1204	0	0.06	1	0.7806
1000	31.79	1.76	2	1.2943	1004	524.13	11.55	1	0.864
1200	612.34	4.89	3	1.0769	101	71.35	0.46	1	3.061
1200	615	4.88	2	1.0785	202	704.97	2.14	1	1.528
1400	276.09	2.55	3	0.9242	303	423.52	3.37	1	1.0182
1400	166.51	3.95	2	0.9252	404	2162.05	6.83	1	0.7668
901	139.45	6.2	1	1.3353	606	984.69	9.89	1	0.5119
901	115.31	4.67	1	1.3455					

Table 5.10. Complete compilation of the $|F_{obs}|^2$ measured at 7.2 GPa in a single scan. Reflections measured in the SXM are labeled 2 and 3 (corresponding to two adjacent detectors), and reflections measured in the powder modules are labelled 1.

experimental offset it was necessary to introduce), they disagree with the results of Endo *et al.* above P_c. They show that the bondlengh continues to decrease through the transition rather than beginning to increase. This certainly requires further investigation and, more importantly a repeat of these measurements with deuterated samples. Such samples should give better results for the powder diffraction, as the backgrounds will be reduced by a factor of six.

It is also useful to compare the behaviour of the different isotopes from a scientific perspective. The quantum mechanics of the H(D) atom are known to play an important role in the structural phase transitions in KDP [74]. This is clearly evidenced by the enormous effect on the transition pressures: DKDP transforms to phase VI 1.5 GPa higher in pressure than KDP [19]. An objective for the near future must be to develop the single crystal techniques such that the position of the H(D) atom can be determined to establish unambiguously if the hydrogen bond centres at P_c.

Despite this partial success of the single-crystal techniques, several problems have also been highlighted. Whilst intensities can be measured accurately deep into reciprocal space, the subsequent structure factor extraction was severely hampered by the presence of extinction. Not only did this prohibit free refinement of the structure at high-pressure, but it left an unresolved question mark over the intensities measured by scans in the powder detectors.

The problem of extinction is especially severe for measurements using the PE cell because the restricted aperture of the cell means that only a small volume of reciprocal space is accessible (effectively a single plane). Additionally, on PEARL, large sample volumes > 12 mm^3 are necessary to ensure a high signal level, which emphasises the extinction effect. A significant absorption effect from the gasket also correlates with extinction, adding further complication.

This problem could be tackled in one of two ways, in the first instance, by improvement of the experimental method. It is possible, if costly in terms of neutron time, to measure equivalent reflections at a range of wavelengths. Such measurements may facilitate empirical modelling of extinction, which has a strong wavelength dependence. Also it appears that if a large enough data set is determined, there will be a sufficient redundancy to discard reflections that are badly affected by extinction [81].

A second tactic, which is perhaps preferable, is for a more comprehensive theory to be developed. Whilst, Tomiyoshi *et al.* [82] have shown that the formalism developed by Becker and Coppens [30] [31] for the monochromatic case applies equally well to the poly-chromatic neutron case, it is clear that the model requires further development. This has been highlighted by the work of Jauch *et al.* [81] in TOF diffraction and, indeed, is part of the common experience of crystallographers at ISIS.

Dealing with extinction is one aspect of the general restriction of small angular openings. Another is simply that the low number of accessible reflections, which limits the potential experiments to studies of high-symmetry structures. This is

a consequence of a culture of anvil and cell design that has focused on powder measurements[3]. This does not represent an intrinsic limitation, and significant improvements could be achieved by re-design of the cell. For example, a PE-type cell is currently being developed by G. Hamel of the Université Paris VI that only has two tie-rods. This will lead to greater access to reflections within the equatorial plane. Additionally, modification of the anvils to give a larger aperture than the current 7° opening will be necessary. Not only will this permit a greater number of diffracted beams to exit, it also increases the range of angles that the incident beam can enter, thus, greatly improving the reciprocal-space access. Such developments will significantly improve the potential for single-crystal diffraction.

The following chapter contains the authors development work on an entirely different design of pressure cell. This 'panoramic' cell already has a much greater aperture than the PE cell, but is more limited in its maximum operating pressure. The various contrasting advantages and disadvantages of both cells are discussed here.

[3]The cell has also been used by S. Klotz [83] [84] for single-crystal phonon measurements, and for this also, the limited aperture has also proved problematic.

Chapter 6

Neutron Diffraction using Large-Volume Diamond-Anvil Cells

6.1 Introduction

The previous two chapters have described the development and use of the Paris-Edinburgh cell for high-pressure single-crystal measurements. A significant amount of work has also been devoted to an attempt to apply diamond-anvil cell (DAC) technology to neutron work. The DAC is extremely common in most fields of high-pressure research above 1.0 GPa, and is the only device to facilitate static measurements of structure and dynamics in the megabar region. However, a small working volume has limited the use of cells of this type for *neutron* diffraction to the relatively low pressures accessible using sapphire (Al_2O_3) anvils [85] [86]. With these sapphire anvils, accurate structural work has been achieved at 1.6 GPa and measurements of magnetic structure at higher pressures [87] of up to $\sim$ 5 GPa have been achieved using neutron-focusing optics.

DAC-type cells use anvils which are single-crystal gem-stones. In addition to

being extremely hard, the transparency of these anvils permits optical access to the sample volume. A major advantage of this, is that it facilitates the *in-situ* growth of single-crystals of high-pressure phases, by careful melting and regrowing of the sample. The ability to grow sample crystals at pressure allows structural studies of substances which are liquid or gas at ambient pressure. Additionally, most structural phase transitions are likely to damage or destroy sample crystals, and the ability to re-grow single-crystals *in-situ* permits accurate diffraction work beyond these transitions (at least to those phases existing along the melt-line).

Recent developments in growth techniques for large artificial diamonds [20] had suggested the possibility of their use in large volume DACs suitable for neutron diffraction. In addition, large single-crystals of Moissanite (hexagonal-SiC), with mechanical properties superior to those of sapphire, have also become available. A large volume cell using both diamond and Moissanite anvils has been designed by researchers at the Geophysical Laboratory of the Carnegie Institute, Washington D.C. [21]. The device is called a 'panoramic' cell, in reference to the large angular access it provides. Its use for the first time as a tool for neutron diffraction at high-pressure is the subject matter of this chapter. The candidate samples for these initial studies were the high-pressure phases of ice (VI and VII), and the clathrate structures formed from mixtures of water and hydrogen at pressures above 0.6 GPa.

The work described here reports on the initial commissioning of the panoramic cell on the SXD diffractometer at the ISIS Spallation Neutron Source. Specifically, a description is given of the first high-pressure, neutron study of a single crystal of hydrogen clathrate. The analysis of this data encountered several difficulties which are discussed with possible solutions. Despite this, reasonable evidence was obtained that the published structure of the clathrate, as determined by x-ray diffraction, may be incorrect. The validity of this conclusion and its implications are also presented.

The neutron DAC project was performed as part of a collaboration between

the Geophysical Laboratory and the University of Edinburgh. Consequently, although the author was heavily involved in the project, some of the work described is not his own. Where this is the case, it is made clear in the text.

6.1.1 The Carnegie Panoramic Diamond-Anvil Cell

Throughout this thesis, the term 'diamond anvil cell' (DAC) is used generally to cover all devices that use opposed single-crystal gemstones and a deformable metal gasket to apply pressure. As a consequence of the DACs popularity as a tool, it has been described in many publications [60]. Therefore, the description given here limits itself specifically to the Carnegie 'panoramic' DAC and its use for neutron diffraction.

Many different designs of DACs exist [88] [89] [60], but their main distinguishing feature is the use of single-crystal gem-stones as an anvil material. Whilst diamond, being the hardest of all solids, is most commonly used, other gemstones such as zirconia, sapphire and, more recently, Moissanite are also used. In fact, for large volume work, diamond anvils have been unsuitable: not only is the cost prohibitive, but flawless diamonds of sufficient size are not found in nature. Consequently large-volume cells have tended to use sapphire as a substitute. This is also an extremely hard material, and high-quality single crystals can be grown artificially to large volumes at relatively low cost.

A necessary pre-requisite for the use of the Carnegie cell in neutron diffraction was the increasing availability of large high-quality artificial diamonds. Additionally, large single-crystals of Moissanite have recently become available with greater hardness and toughness than sapphire [21].

The panoramic cell (shown in Figure 6.1)has a piston-cylinder design possessing similar elements to the PE cell, whilst being a far smaller construction with a total weight of less than 0.5 kg. The cylinder section contains three large apertures from which the cell gets its name. The load is entirely supported by the tension in

three thin webs of metal (corresponding to the tie-rods of the PE cell). These give the cell a three-fold symmetry about the load axis with apertures only slightly less than 120° wide. Parallel to the load axis, the apertures are ±32° wide, resulting in a total accessible solid angle of approximately 6.6 sr, almost a factor of thirty larger than the PE cell.

In common with all opposed-anvil cells, the force of the piston is transmitted to the backs of the anvils through seats. These must withstand relatively high loads and are made from tungsten carbide. Both front and back seats have conical apertures, these are collinear with axis of the cell and are necessary to maintain optical access and also allow 'through illumination' of the sample. Force is applied to the seats by means of six bolts, three of which have a left-handed thread. These are arranged such that two opposite-handed bolts may be tightened simultaneously thus applying the force evenly onto the piston. The force applied in this way is maintained by tension in the webs. Two adjustable dead-bolts are built into the piston section of the cell. These prevent the anvils touching and any resulting damage should the seats fail.

Pressure is communicated to the sample by the deformation of a metal gasket, as in the case of the PE cell described previously in Chapter 4. However, the geometry of the anvil faces, and hence of the gasket itself, is significantly different from that of the PE cell. At present almost all anvils used with DAC-type cells have flat faces or *culets*, the surface of which is polished to obtain a high level of parallelism with the back of the anvil. The gaskets themselves simply consist of a flat sheet of metal which has been drilled through to produce the sample void. Typically, this gasket hole is spark eroded to produce a smooth-walled cylindrical chamber of the appropriate diameter.

Flat anvils are much less efficient at maintaining pressure than anvils with toroidal grooves. The force maintaining the pressure in the sample volume comes from friction between the anvils surface and the metal of the gasket and thus requires as large an area of contact as possible. A working 'rule-of-thumb' is that the

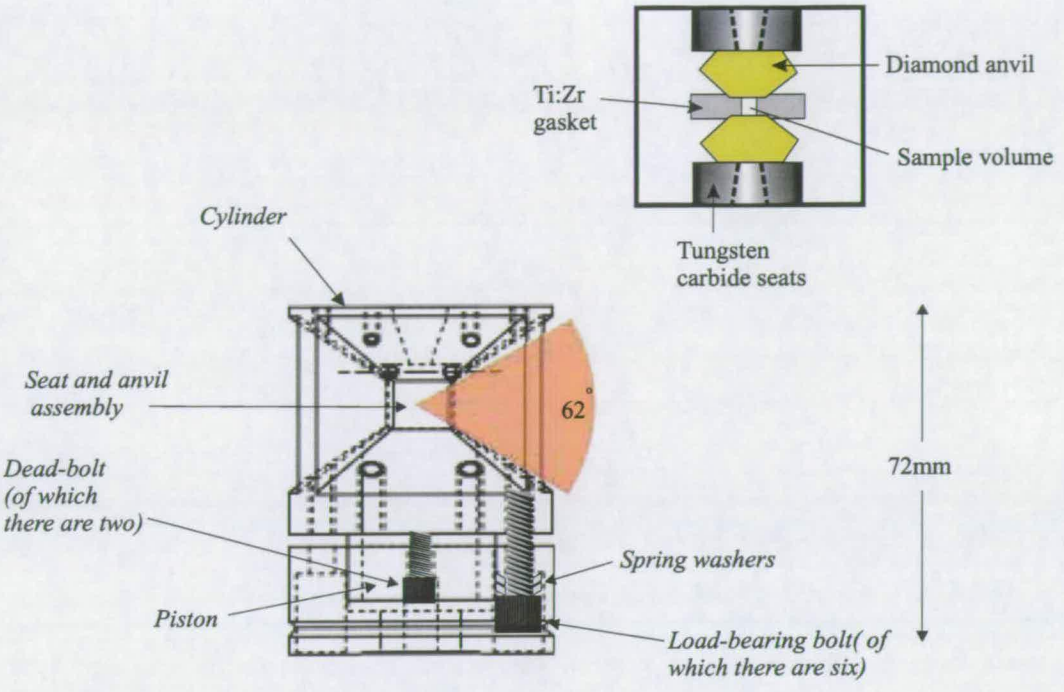

Figure 6.1. The figure shows the body of the Carnegie 'panoramic' diamond-anvil cell. Insert gives a close-up of the seat and anvil assembly, the conical apertures in the tungsten carbide seats are marked with dashed lines.

ratio of gasket-hole diameter to anvil-face diameter must be at least 1:3, this compares with a ratio of approximately 1:2 for toroidal anvils. This is a significant drawback for large volume work as, for cells of this type, the maximum size of anvil is strictly limited not only by cost, but by availability. The ratio of 1:3 can be reduced in order to maximise sample volume, but the resulting instability of the gasket limits the accessible pressures. The severity of this limitation is governed by the material properties of the metal which is used to form the gasket.

As has been described previously, both diamond anvils and Moissanite anvils were used with the panoramic cell. Anvils of both materials were available with culet diameters of 1.4 mm, 2.0 mm and 2.8 mm, each successive factor of $\sqrt{2}$ in anvil diameter giving a factor of two increase in maximum sample volume. The diamond anvils were artificially grown by CVD onto a seed crystal [20], the

presence of nitrogen impurities resulted in anvils with an olive-green colour. The Moissanite anvils are completely colourless in appearance.

6.1.2 SXD: A Dedicated Single-Crystal Diffractometer at ISIS

A major advantage of the panoramic cell is that it is small enough to be easily mounted in the SXD diffractometer at ISIS. SXD (Single Crystal Diffractometer - using the common abbreviation: x-tal) [90] was designed specifically for the measurement of single-crystal reflection intensities. Towards the end of the work described here, the diffractometer underwent a major upgrade with the number of detector modules increased from three to eleven. As the majority of the work described here was based on the original SXD-I instrument, it is this that will be described in detail here.

The SXD diffractometer is situated at the end of an 8.00 m beamline which views a deuterated-water moderator at ambient temperature. The flux profile of an ambient-temperature moderator peaks at a higher energy than the colder liquid-methane moderator viewed by PEARL. This is convenient for obtaining better statistics for shorter d-spacings reflections (corresponding to the high frequency Fourier components it is necessary measure in order to study atomic disorder and thermal motion effects [22]). The shorter flightpath compared to PEARL is also advantageous, giving an increased overall flux, which counteracts the smaller volume of the sample. The increase in divergence that occurs on shortening the pathlength is less problematic for the measurement of single-crystal reflections, which are well separated on the detector face.

The SXM installed on the HiPr diffractometer (described in Section 4.1.3) was modeled on the SXD detector modules, which were specially designed for the measurement of single-crystal intensities. The three modules that constitute the SXD detector bank are highly pixelated, each being composed of 4096 individual

Detector	2θ angle of mod. centre γ (deg)	Sample to mod. distance d_{sd} (mm)
1	120	180
2	20	150
3	-90	100

Table 6.1. Nominal positional parameters of the three detector modules on SXD. The detectors are all of equal size and, consequently, the different sample-to-detector distances result in significantly different subtended solid angles.

elements, each with an area of 3×3 mm^2, arranged in a square of 64×64 pixels. The modules are oriented such that they are symmetric about the equatorial plane of the instrument, viewing the sample position at distances ranging from 100-180 mm. The resulting detector solid angle is far larger than that on HiPr. As with the HiPr SXM, the detectors are ^{6} Li-doped ZnS sheets, the low efficiency of this kind of detector is balanced somewhat by the increased flux of the SXD beamline.

The exact positions of the detectors can be determined for each experimental run by refinements of the orientation matrix of the sample. Of the three detectors modules, two are fixed in position. The third module has a variable position in 2θ, and a variable sample-detector distance. The nominal positional parameters of the detectors are provided in Table 6.1 (although these were re-refined for each experimental run). These parameters illustrate the large coverage of scattering angle accessible on SXD. A plan-view schematic of the instrument is given in Figure 6.2

With the panoramic cell installed on SXD, it is only possible to rotate about one goniometer axis. This provides an ω rotation about the axis perpendicular to the equatorial plane of the diffractometer. The freedom of movement of the cell is less important in time-of-flight diffraction, the extra dimension of energy taking the place of an additional rotation axis.

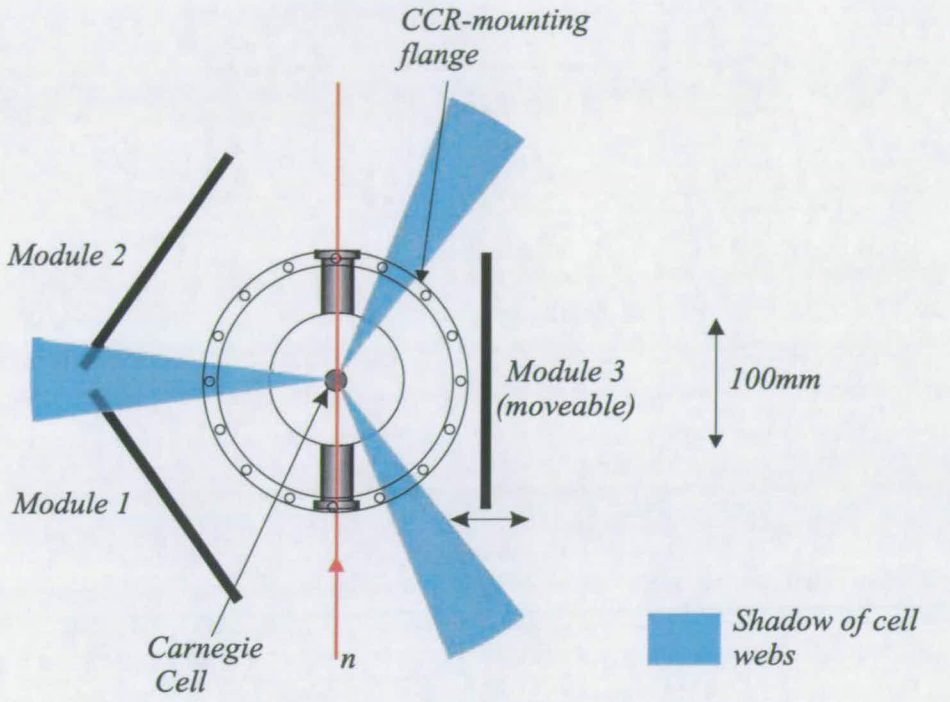

Figure 6.2. The figure shows a schematic of SXD-I as viewed from above. The ω-rotation axis of the closed cycle refrigerator (CCR), that acts as goniometer, points down into the page. Superimposed are the shadows of the Carnegie-cell webs in the standard operating geometry.

6.1.3 The Panoramic Cell on SXD

With the current alignment system, there are two potential orientations for the Carnegie cell on the SXD diffractometer. These either have the load axis of the cell parallel or perpendicular to the incident beam. In the first of these, the incident beam travels to the sample through the anvils and subsequently is diffracted through the gasket. In the second orientation, both the incident and diffracted beams travel through the gasket. By aligning the axis of the cell with the diffractometers axis, the accessible volume of reciprocal space could be maximised. This is achieved by matching the three-fold symmetry of the cell apertures with the approximate three-fold arrangement of detectors, thus minimising the occluded areas on the detector-module faces. This orientation is illustrated schematically in Figure 6.2.

The neutron beam on SXD is collimated to give an 8 mm diameter circular spot size. This was further reduced by a boron nitride (BN) collimator piece, which was designed to be brought into physical contact with the edge of the gasket. This had to be mounted directly to the body of the cell in such a way that its height could be adjusted relative to the cell, as could its angle about the axis of the cell. This was achieved using an aluminium frame mounted onto the cell itself. A cup of BN attached to the upstream end of the collimator ensured that scatter from the collimator itself did not reach the detectors (see Figure 6.3).

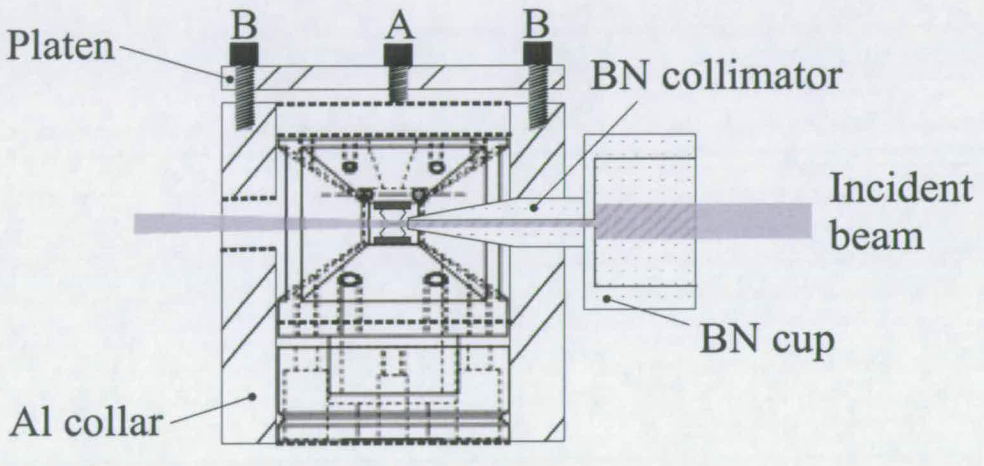

Figure 6.3. A schematic of the collimator arrangement used on SXD with the Carnegie panoramic cell. The collimator mount is comprised of two parts made of aluminium: the collar and the platen. The height of the collimator is adjusted by setting the heights of two dead-bolts (of type A) and then tightening three bolts (of type B) to move the collar. Slots are machined into the platen such that the collar can rotate around the cell by approximately 60°. The boron-nitride (BN) collimator slides through the mount and can be positioned such that it is in physical contact with the gasket. There is a hole in the collar opposite the collimator to allow the transmitted beam to exit. A cup of BN is attached to the end of the collimator facing the incident beam to absorb back scatter from the collimator itself.

The cell was attached to the base of a closed-cycle refrigerator (CCR) by a simple locking bolt. This would eventually allow the cell to be cooled to 30K but, in the initial stages of development, was simply used as a mount and rotation mechanism. A flange at the base of the CCR mates with a vacuum tank which is

built into the diffractometer. In all experimental runs, this tank was evacuated to minimise the background.

An alignment procedure was adopted that used a pointer bolted onto the flange at the base of the CCR. The height and direction of the pointer could then be aligned so that it was collinear with the incident beam. The height of the cell and its angular position could then be adjusted relative to the pointer. There are inherent inaccuracies present in this procedure, but in practice it was found to be sufficient, as the diameter of the beam is much larger than the sample size (8 mm compared to $\sim$ 1 mm). The alignment of the cell could be confirmed within five to ten minutes using the observation of diffraction peaks from the anvils themselves. The observation of scattering from both anvils gave confirmation that the beam was bathing the entire sample volume.

6.2 Sample Loading Techniques and the In-Situ Growth of Single Crystals of High-Pressure Phases

One of the motivating factors for the use of transparent anvils is the possibility of growing single-crystal samples *in-situ*. The techniques to achieve this have been in use for many years now [85] [86], and involve cycling the sample back and forth across the melt line by adjusting the variables of temperature and pressure. In this way the sample can often be annealed into a relatively small number of individual crystallites. With careful control, these can each be melted to leave only a single crystallite in contact with the melt. This is then allowed to grow at a slow rate, to minimise strain defects, until it fills the entire sample volume.

In this section, the equipment and techniques used for loading samples into the pressure cells are described. These are mostly well established techniques common

to the loading of all DAC's, and are described here for completeness. The techniques developed for growing sample crystals have aspects which are unique both to the panoramic cell and the particular samples grown for neutron-diffraction experiments and are described in some detail.

6.2.1 Preparation and Loading of Samples

The preparation of samples was carried out mainly at the Carnegie Institute in Washington and at ISIS. In order to load the cells, several pieces of essential equipment were required, these were:

- A high-quality microscope with a long working distance.
- Equipment for spark-erosion of gasket holes. This was especially useful during the initial stages of development when it was necessary to experiment with different gasket materials and dimensions.
- Ruby-fluorescence pressure measuring apparatus (see the description immediately below).
- For the loading of gas samples, a specialised high-pressure gas handling system was available in Washington.

Pressure Measurement Using Ruby Fluorescence

An important benefit of the transparency of the anvils used with the panoramic cell is that it facilitates direct pressure determination using the ruby-fluorescence technique. This technique is based on the measurement of two optical fluorescence lines that are emitted from ruby when it is illuminated by coherent light from a laser source.

The wavelengths at which these lines are observed is highly dependent on pressure. This behaviour was first calibrated by Piermarini in 1975 [91] using a linear

scale up to 30 GPa. This pressure range was subsequently extended by Mao and Bell [92] to 80 GPa who give the following formula for the pressure based on the wavelength shift $\Delta\lambda$ of the stronger of the two lines

$$P = \frac{A}{B} \times \left[\left(1 + \frac{\Delta\lambda}{\lambda_o} \right)^B - 1 \right] \tag{6.1}$$

where $A = 19.04$ Mbar, $B = 7.665$ Mbar and the wavelength at ambient pressure is $\lambda_o = 6942.8$ Å. It can be seen that (up to ~ 30 GPa) where only a small change in wavelength occurs and $\frac{\Delta\lambda}{\lambda_o} \ll 1$, the equation reduces to a linear relationship.

For the purposes of this study the effect of temperature on the shift of the fluorescence lines had to be taken into account. Heightened temperature is assumed to induce an extra shift of the peaks Δ_T which is independent of pressure. This was studied by Vos and Schouten [93] up to 127° C who found the wavelength shift of the strongest line to be given by

$$\begin{aligned} \Delta_T(\text{Å}) &= 6.591 \times 10^{-2}[T(K) - 300] \\ &\quad +7.624 \times 10^{-5} \\ &\quad \times [T(K) - 300]^2 - 1.733 \\ &\quad \times 10^{-7}[T(K) - 300]^3 \end{aligned} \tag{6.2}$$

As additional complication can arise at very high temperature (greater than several hundred degrees Celsius) where the fluorescence peaks begin to broaden strongly. However, this is not relevant to the current work in which the temperature was never higher than ~ 130°C.

Selection of Gaskets for Neutron Diffraction

Before loading could begin, it was necessary to prepare appropriate gaskets. From the perspective of a neutron-scattering experiment, the ideal gasket material would be null-scattering, thus avoiding both contaminant Bragg scattering in the diffraction pattern and also Bragg-edge effects. Bragg edges are a non-uniform reduction in transmitted-beam intensity, the losses arising from Bragg scattering of the beam as it passes through a material. As such, the effect is highly dependent on sample micro-structure and thus is extremely difficult to correct.

In order to avoid these problems, it seemed prudent to use gaskets made from Ti:Zr alloy as described in Appendix A. This material (also used to manufacture toroidal gaskets for the PE cell) was readily available and satisfied the null scattering requirements. Unfortunately, some unexpected problems became rapidly apparent with this choice. Firstly, it was discovered that upon compression to pressures exceeding $\sim$ 1.0 GPa, the gasket adhered to the surface of the anvils. This effect occurred with both diamond and Moissanite anvils, but appeared more pronounced with the latter. The adhesion was extremely strong, and any attempt to remove the gasket would also remove the top layer of anvil material. Whilst this damage was not irreparable, it was both expensive and time consuming to have the surface of the anvils re-polished.

A second problem with Ti:Zr lay with its material properties. As has been mentioned previously, the pressure within a diamond-anvil cell is maintained by friction between gasket and anvil; this is subsequently communicated to the sample by tensile forces in the gasket. It appeared that the tensile strength of Ti:Zr was insufficient to maintain both a large volume *and* high pressures given the small size of the anvils.

Finally, problems were encountered with the hydrogen gas loadings required to grow H_2-H_2O clathrate (using both H_2 and D_2). It was found that the zirconium

in the alloy reacted strongly with the gas, forming hydrides that embrittled the gasket, causing it to fail. This particular problem could be overcome by introducing a thin layer of Be:Cu around the inside of the gasket wall. This was achieved by riveting a plug of Be:Cu into a slightly enlarged hole in a Ti:Zr gasket. Subsequently, the gasket hole itself was then drilled through, leaving a protective layer of Be:Cu several tens of microns thick.

All of these large disadvantages favoured the use of a secondary gasket material. For this purpose, a variety of steels were experimented with, including: silver steel, high-tensile steel and various work-hardened steels. Out of these, the most successful was T301, a cold-worked steel that appeared to have an especially high hardness and tensile strength. The material properties of T301 were far superior to those of Ti:Zr, but iron is a relatively strong neutron-scatterer, and therefore presented significant difficulties for the diffraction experiment.

The dimensions chosen for the gaskets reflected both their material properties, the size of the anvil and nature of the experiment that the loading was intended for. For pressures less than 1.5 GPa, it was possible to use an inner-gasket diameter, which was slightly larger than half of the diameter of the culet. It was also possible to use starting gasket thickness of 0.8 to 1.2 mm. Thinner gaskets (0.5 mm) were experimented with and proved to be more stable, but could not hold sufficient volume for the neutron diffraction measurements.

Loading the Panoramic Cell

The first stage in the loading procedure is the alignment of the anvils. For all designs of diamond anvil cell, it is crucial that the faces of the two opposing anvils have a high level of parallelism relative to each other. If this is not the case, then large stresses develop at the nearest point of contact between the anvils, which can result in breakage. The quality of alignment can be determined by gently forcing the anvils into contact, and observing the appearance of Newton's

rings. This ensures that the separation between the anvils is uniform to within a few wavelengths of light. Further adjustment should be performed until only one or two rings are observed. However, in the case of the Carnegie cell such adjustment is not required, as the components of the cell are manufactured to sufficient tolerances that parallelism is guaranteed.

In addition to parallelism, the anvils must be aligned so that the culets lie directly opposite one another. The anvils are glued into place on the seats, and it is difficult to ensure accurate centring. For this reason, most DAC's also permit the adjustment of the seat position in a plane perpendicular to the axis of the cell. In the case of the Carnegie cell, this adjustment is achieved by the re-positioning of three grubs screws that clamp the seats in position. The standard method of adjustment is to fix the position of the piston anvil as close to the centre of the cell as possible. This is achieved by observation through a microscope with a graded reticule. The anvils are then pushed until they are almost in contact, using the dead-bolts to ensure that they do not actually touch. The cell can then be placed with its axis horizontal and viewed from above through a monocular microscope. By rotating the cell through 360° degrees about its axis, and viewing the anvils through each of the three apertures, it is possible to directly observe any mis-alignment. The cell is then placed vertical again, and an adjustment made to the position of the cylinder seat using the grub screws. This process is repeated until the anvils are judged to be centred, this method is accurate to within 4% of the anvils diameter.

Once the anvils have been correctly aligned, they must then be carefully cleaned. Usually, this is done with ethanol, acetone is not used as it can weaken the glue holding the anvils in place.

In a standard DAC loading, the gasket is *pre-indented* by the anvils to the desired thickness. This is an important process, where the anvils are tightened onto the blank gasket with sufficient force to deform the metal, thus leaving an indentation. This procedure has a work-hardening effect on the material of the gasket that

increases its performance. At very high pressures, pre-indentation also provides additional support for the anvils, as gasket extrusion around their tips forms a belt that acts against the tensile forces that develop perpendicular to the axis of applied load.

When using Ti:Zr gaskets a different technique of *post-indentation* had to be developed. This was necessary as a consequence of the adhesion between gasket and anvil. In this case, the hole was drilled in a blank, un-indented gasket and the sample loaded directly. The sample was then taken to pressure of around 0.9 GPa, and then *de*-compressed to $\sim$ 0.2 GPa (in the process releasing some of the sample) before pressure was again increased.

Regardless of whether the gasket had been pre-indented or not, the subsequent loading procedure was identical. Three metal supports were screwed into the base of the cylinder-section of the cell. These each contained two grub screws, which could be extended horizontally onto the outer edge of the gasket as it rested on the cylinder anvil, and hold it in place. Initially, only one grub screw from each support was extended and the gasket position could be adjusted by extending and retracting these screws. The gasket and grub-screw alignment pieces are illustrated in Figure 6.4. As extremely large gasket holes were necessary for the neutron experiments, the centring of the sample hole on the culet face was crucial. An error at this stage resulted in the gasket 'blowing-out' towards the direction where the hole is closest to the culet edge and there is correspondingly insufficient frictional force to support the sample pressure.

The procedure employed by the author for gasket alignment was to lower the piston anvil onto the gasket as it rested on the lower cylinder anvil. The weight of the piston was sufficient to hold the gasket flat against the lower anvil, whilst still allowing its position to be adjusted by means of the grub screws. The gasket was viewed through the upper piston anvil through a monocular microscope, whilst it was illuminated both from above and below. The light from above reflected from the gasket surface, clearly illuminating the edges of the upper culet. Meanwhile,

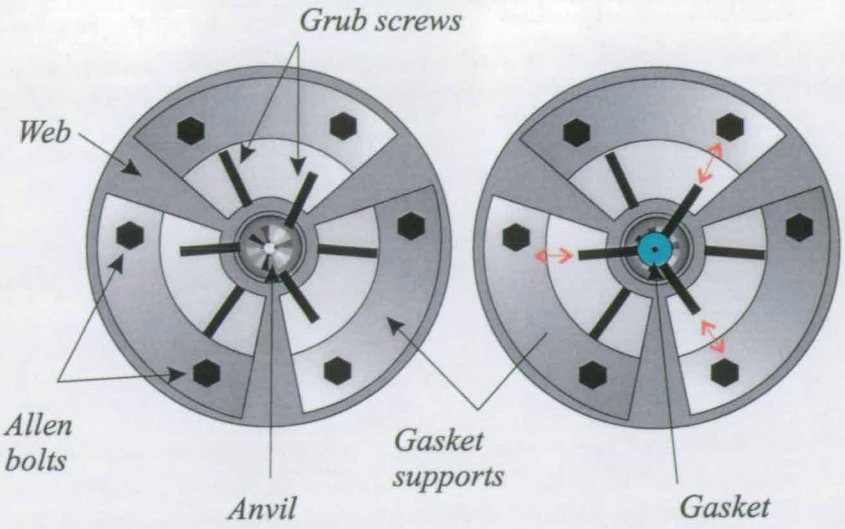

Figure 6.4. Plan view onto the cylinder part of the Carnegie panoramic cell. The three metal supports are each held in place by two Allen bolts and are separated by the cells webs. It is possible to adjust the position of all six grub screws to hold the gasket (shown in blue) firmly in place.

the light from below illuminated the gasket hole, allowing it to be aligned relative to the upper culet's edge. When this was achieved, the extra six grub screws were fastened onto the gasket fixing its position.

At this stage, the piston could be drawn out and, prior to loading, a small chip of ruby, for pressure measurement, placed in the centre of the piston anvil. The author used two different sources of ruby, one ground by hand from a large chip and the second grown in the form of tiny spheres. It was found that the spheres were much easier to locate during pressure measurement. The chips produced by grinding, were irregular in shape and often hard to distinguish from the other contents of the sample void. Typically, the ruby was placed on the anvil surface without any adhesive. Whilst this, occasionally, resulted in the ruby being lost during loading, it avoided the possibility of any reaction with the sample and an adhesive.

Water samples were loaded into the sample void using a syringe. By applying a very small pressure to the plunger, a low flow rate of water into the gasket hole

could be achieved. This ensured that the water gradually displaced the air in the sample void and minimised any bubbles that might be trapped. The gasket hole was over-filled, the resulting pool of water minimising any loss of sample that might occur through evaporation. Once the water has been loaded in this way, the piston was rapidly positioned in the cylinder. It was found that, at this stage, any remaining bubble could sometimes be displaced by repeated, gentle pumping of the piston against the water pool. Finally, the load bolts are tightened to generate a load sufficient to form a seal between anvils and gasket. At this stage, the sample is now safely loaded and the pressure can be increased further

6.2.2 Growing of Single-Crystal Samples

A specialised experimental setup was necessary during the growth of crystals. An important aspect of this setup was visualisation of the sample. It was found that connecting a CCD camera and video system to the microscope was extremely useful, making it easier to maintain observation of the sample whilst temperature and pressure were adjusted. At ISIS, a portable BETSA spectrometer permitted on-line pressure measurement, a facility that proved extremely useful. In Washington, the pressure could be measured on a Raman spectrometer, but here it was not possible to measure the pressure whilst simultaneously heating the cell and visualising the sample. By fixing the cell firmly to an optical bench, it was possible to adjust the pressure by tightening and loosening the load-bearing bolts.

A schematic of the setup used at ISIS is shown in Figure 6.5. The horizontal alignment of the cell and optical system ensured that the lens did not become too hot when the cell was heated. Indeed, in initial experiments, where a vertical set-up was used, a CCD camera was damaged by the heat convecting up from the cell. It was also sometimes useful to have the direction of viewing perpendicular to the gravitational field as the solid and liquid phases separate more clearly. However, a disadvantage of the horizontal setup was that, occasionally, the ruby could detach itself and fall out of view, inhibiting further pressure measurement.

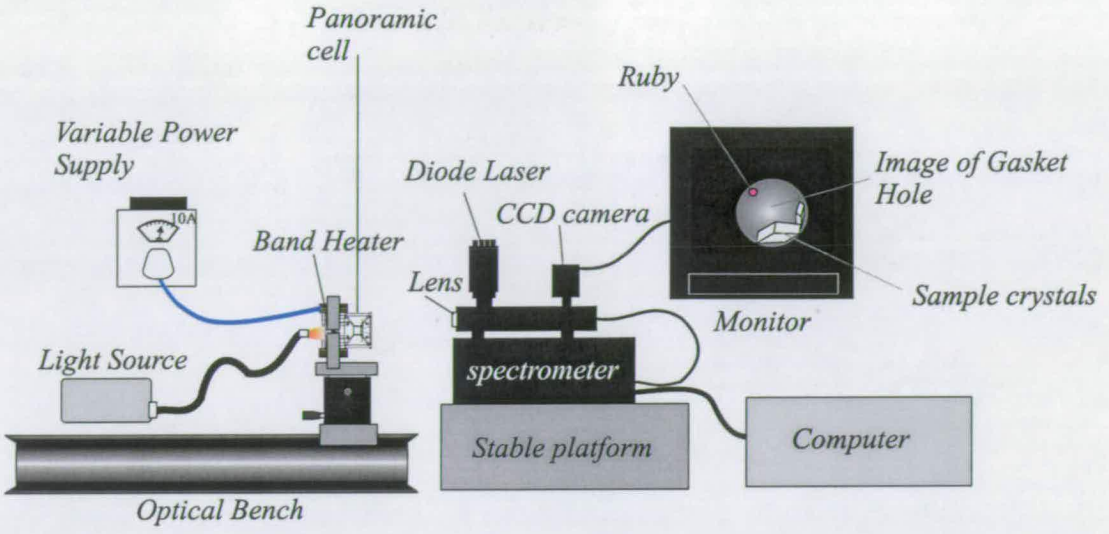

Figure 6.5. The experimental setup used at ISIS to grow single-crystal samples. The spectrometer measured the laser-induced fluorescence of a single crystal of ruby that was loaded with the sample. This set-up permitted on-line pressure measurement.

It was found that each high-pressure phase possessed unique patterns of crystal growth that were highly dependent on the crystal structure. The author was especially heavily involved in attempts to grow single-crystals of the high-pressure ice phases VI and VII. Unfortunately, these attempts were unsuccessful in producing a crystal of sufficient quality for a neutron experiment. Observations made during these endeavours suggested possible approaches which may aid future bids to grow single-crystal samples and are recorded in the following section.

6.2.3 The High Pressure Phases of Ice

At room temperature, liquid water freezes into tetragonal ice VI at 0.9 GPa. Upon further compression, there is a solid-solid phase transition to cubic phase VII at 2.2 GPa (pressures are for D_2O). Each of these phases appear to form with dramatically different micro-structures. When ice VI was formed by compression of liquid water, super-pressurising of the sample was always observed to several gigapascals above the transition pressure. When freezing occurred, the

entire sample volume solidified simultaneously. Within several minutes the ice VI would self-anneal into a relatively small number of large geometric crystallites. In contrast, the formation of ice VII, via the direct solid-solid transition from ice VI, resulted in an extremely fine grained powder. When, after the application of high temperature, this was annealed into a single crystal, its growth edges were rounded with no strong geometrical shape.

Ice VI

The initial micro-structure of ice VI, when frozen from the melt, provided an ideal starting point for crystal growth. A large change in refractive index between water and ice VI made it easy to distinguish solid from liquid and the crystals themselves were well defined polygons. The smaller crystallites could be melted either by increasing temperature or by decreasing sample pressure. With either method it was found that, once melting began, it proceeded rather rapidly, the entire sample becoming liquid in around a second or less. Once the sample became completely molten, it would then be necessary to super-cool (or super-pressurise) the liquid to re-enter the solid phase, again filling the sample volume with large crystallites.

This was most problematic when temperature was used to control crystal growth. The panoramic cell's relatively large thermal mass (compared to other DAC's [88] [89]) resulted in a time-lag between the reduction of heater power and lowering of the sample temperature. However, rapid cooling of the sample could be achieved by directing a stream of compressed air over the gasket. By making adjustments to the flow rate, the compressed air stream could be used to control crystal growth. However, in order to grow crystals which were as free as possible from defects, it is preferable for growth to proceed as slowly as possible. Generally, the compressed air was used to maintain a small seed crystal until the cell itself was sufficiently cool for it to grow without the extra cooling of the air stream. At this stage, the temperature of the cell could be gradually reduced over several

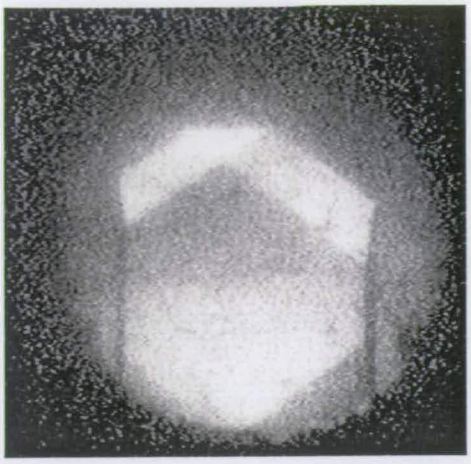

Figure 6.6. An image of an ice VI crystal growing within the gasket hole. Note the clear geometrical features of the morphology.

hours until the sample filled the entire gasket hole.

There was evidence that ice VI crystals grown in this way are extremely fragile. This was clearly demonstrated when it was attempted to stabilise the ice by increasing pressure beyond the point when the sample filled the gasket hole. Several neutron measurements revealed powder patterns that were indicative of the complete destruction of the sample crystal. Problems were also encountered when the crystal was left in equilibrium with a thin layer of liquid water. Neutron measurements on such samples revealed no diffraction signal at all. It is likely that a crystal in equilibrium might constantly be melting and re-growing and, consequently, re-orienting. This could remove the diffraction pattern as the crystal would not be stationary for long enough for diffraction spots to be measured.

The obvious solution to this problem was to stabilise the crystal by gently cooling to take it several tens of degrees Celsius below the melting temperature. This was attempted on a crystal that was grown at ambient temperature, and produced a high quality crystal from which strong diffraction was observed. However, when the crystal was re-orientated, it warmed, melted, and was lost. Subsequent efforts

involved growing the crystal at around 40 - 50 °C[1], and allowing it to cool to room temperature to stabilise. However, in these loadings, powder scatter was again observed, indicating that perhaps thermal contraction of the cell was exerting a damaging force on the sample.

Ice VII

Ice VII presented an entirely different growth morphology to ice VI. In the first instance, the difference in refractive index appeared to be much less, and it was consequently harder to distinguish between liquid water and ice (The use of polarised light and a polarising filter on the microscope also did not aid with visualisation). Additionally, the VI→VII transition produced a very fine powder that appeared, to the eye, to be indistinguishable from a featureless liquid. Upon warming at around 2.7 GPa, the ice VII powder was seen to anneal into many larger crystallites. Those crystallites on the surface of the diamond anvil appeared to be stabilised and could remain in equilibrium with the melt to several tens of degrees Celsius above the melting temperature. They would then melt extremely rapidly, and it was, therefore, difficult to perform controlled growth of a suitable seed crystal. Upon complete melting, as with ice VI, the liquid would super-cool by up to 15°C before instantaneously freezing.

It was found that, with suitable experience, it was possible to 'catch' a seed crystal and allow it to slowly grow to fill the sample void. However, problems were encountered with pressure loss in the cell, and in almost all cases, the cooled cell had dropped to below the VI→VII transition pressure. In one instance, where the pressure was increased (as with ice VI) to stabilise the crystal, a subsequent diffraction measurement again yielded a powder signal indicating that the crystal was fragile. This is at odds, however, with the experience of Loubeyre *et al.*

[1]The temperature was measured by two thermocouples placed in contact with the diamond anvils, which provide an extremely good thermal contact with the sample. Typically there was a several degree Celsius difference in temperature between the two anvils.

[18], who compressed single crystals of ice VII to megabar pressures (using gold as a "quasihydrostatic cushion"), whilst maintaining a diffraction signal. This apparent difference in behaviour may be a result of the far larger volume of the crystals that are grown in the panoramic cell.

In only one instance was a neutron diffraction signal measured from an ice VII single crystal. This was grown using a T301 steel gasket which has a higher tensile strength than Ti:Zr, and maintained the pressure more successfully. However, this crystal was too small for a feasible diffraction study: only a handful of the strongest reflections were visible, although these could be indexed on a single ice VII lattice.

6.3 Data Collection and Analysis on SXD

As has been stated previously, a major consideration for any neutron diffraction experiment is the available sample volume. The smallest volume of sample used on SXD prior to the DAC measurements was of the order of 5 mm^3 [94]. Even with the largest anvils currently available, the panoramic cell compares unfavourably with this, having a maximum volume at present of $\sim$ 1.0 mm^3. However, it was hoped that studies of strongly scattering samples with relatively high-symmetry might still be feasible. Despite this, high-pressure experiments were necessarily performed at the limit of SXD's capabilities and several difficulties were encountered as a result of this.

The first stage of an experiment involved the identification of the orientation of the sample crystal and an assessment of its quality. Once this was achieved, data collection proceeded in a systematic manner to explore as many orientations of the sample as possible within the constraints of the geometry of the cell. Significant problems were encountered with the integration of the sample peaks. Many of the peaks were extremely weak and, consequently, the automatic integration software proved unreliable. With data sets consisting of several hundred reflections,

manual integration was found to be extremely time consuming and error prone. In response to this, the author wrote software to facilitate a 'semi-automated' process which is described later in this section and in Appendix B.

6.3.1 Determination of Sample Orientation and Quality

Perhaps the largest drawback of the panoramic cell is that its small, *optical* apertures prohibit the use of x-ray radiation to characterise the sample. Ideally, prior to the neutron experiment, the orientation matrix would be determined and checks made for defects such as twinning or the presence of more than one crystal. Unfortunately, as this was not possible, it was necessary to perform the characterisation on the neutron diffractometer.

New experiments on SXD began in the following manner:

- The diffraction pattern was collected for at least two hours.
- The orientation matrices of the anvils were determined.
- Once the anvil peaks were excluded, it was attempted to index any of the remaining peaks as being from the sample and then to determine an orientation matrix. At this point, it was possible to identify if the sample was a single-crystal or poly-crystalline.
- If the sample was found to be a good single-crystal, then data collection could proceed, otherwise it was discovered that the reflections from poly-crystalline samples (each having a volume much smaller than the total) were too weak for structural characterisation, and the loading would be abandoned.

Unfortunately, at the time these experiments were conducted, the available automatic-indexing software did not have the facility of handling multi-crystal samples (i.e.

the anvils and the sample). Additionally, the peak-searching routine, used prior to auto-indexing, struggled to find weak sample peaks. Consequently, peaks were located by direct observation of the time-of-flight data (using multi-plots as described in Section 4.3.2) and indexed by hand, using their observed d-spacings and relative positions on the detector faces. Once two reflections were found that appeared to belong to the same crystal, it was then possible to fit a UB matrix. At this stage, if the orientation matrix was correct, then all of the other sample reflections could be identified, and used to refine the orientation more accurately.

In using this method, a disadvantage of the Moissanite anvils rapidly became obvious. Moissanite has a lower symmetry crystal structure ($\mathbf{P6_3mc}$) compared to diamond ($\mathbf{Fd\bar{3}m}$) and, consequently, its diffraction pattern is far more complex consisting of many peaks out to a much higher maximum d-spacing than diamond. This resulted in difficulties for the manual indexing method. Problems were also encountered when scattering gaskets were used, as weak sample reflections were extremely hard to identify amongst the ubiquitous powder peaks.

The orientation matrices of the anvils proved to be useful calibrants. Firstly, the observation of scatter from both anvils confirmed that the sample was bathed in or near the centre of the beam. They also provided an accurate measurement of the amount by which the cell was rotated in consecutive runs. Finally, as the structures of the anvils are well known, they could be used to calibrate the detector positions exactly for each run.

6.3.2 Intensity Integration and Structure Factor Extraction

The standard method for structure factor extraction on SXD proceeded in several stages:

1. A search of all the time-of-flight data to identify peaks.

2. The sample orientation matrix is used to discard all peaks not belonging to the sample.

3. Integration of each of these peaks by the addition of the spectra containing the peak centroid and its eight nearest neighbours, and subsequent fitting of the integrated peak with the convolution of a Gaussian and exponential function (GEC), as described in Section 4.1.2. This step is required because, typically, sample peaks are wider than a single element of the detector module. During the addition stage, each spectrum is corrected for the relevant wavelength-independent efficiency term (see Section 4.1.4).

4. Integrated intensities are corrected by the various other terms in the Buras Gerard Equation 4.2.

All of the peaks identified by the peak-search are stored in a USE file. In addition to the peak coordinates, these files contained a header that stored all of the geometrical information describing the instrument and detectors, and the UB matrix. A sample of this header, for one of diamond anvil USE files, is shown in Figure 6.7 along with the first four peaks generated in the peak-search.

An extract of one of the peaks identified in the USE file of Figure 6.7 is given here:

NSEQ	H	K	L	XCEL	YCEL	TIME	PKHT	IFLAG	NSPEC
	FH	FK	FL	DXCEL	DYCEL	DTIME	INTI		
2	5	-1	1	20.63	20.50	2673.16	322	0	3381
	4.99	-1.00	1.01	0.50	0.50	4.01	0		

The sequence number NSEQ = 2 labels the peak, which has been indexed on the UB stored in the USE file header. The row of real numbers (labeled FH,FK and FL): 4.99 -1.00 and 1.01 are the fitted *hkl* indices as calculated by the coordinates of the reflection and the orientation matrix. Above this are the nearest integers

to these values (labeled H,K and L): 5,-1 and 1. As the fitted *hkl* indices are very close to being integer, and the index is an allowed reflection for diamond, then this peak would be expected on the lattice described by the UB matrix and is a diamond reflection. However, for peaks NSEQ = 1 and 3 in Figure 6.7 this is not the case, and these reflections must be due either to the second diamond anvil, or the sample itself. The other terms are:

- The x and y coordinate of the reflection on the detector face in pixels (XCEL and YCEL) along with the associated uncertainties (DXCEL and D).
- The time of flight (TIME) and associated uncertainty (DTIME).
- A rough estimate of the peak intensity (PKHT). This is replaced by the integrated intensity, as determined by fitting with a GEC, to give an INT file from which the structure factors are extracted.
- The term IFLAG is set to zero for all reflections.
- Finally, the spectrum number is given in the column labeled NSPEC.

As has been mentioned before, the peak-search proved to be unreliable for samples with weak diffraction intensities. Additionally, in the case where a scattering gasket was used, the majority of peaks identified in the search were from this and not the sample. Both of these problems are consequences of the small sample size, but, a more fundamental problem with integration only proceeding on peaks identified by the peak-search is that zero intensities are not measured. The measurement that the amplitude of a given scattering vector zero within error contains valid structural information. Such information is not only useful for identification of systematic absences, but should also be included in structural refinements.

SXD specific software (based on a program written by A. Filhol for a generalised area detector [70]) was available that used the fitted UB matrix to *calculate* the

```
1    DISTMS    DISTSD      DIMX      DIMZ     NXCEL     NZCEL      IGEO
2   8000.00    158.00    192.00    192.00        64        64         1
3       RUN      TMIN      TMAX    BCKGRD    CUTOFF
4     14644    800.00  19900.00
5      XOFF      YOFF      ZOFF      TOFF
6     0.000     0.000     0.000     0.000
7      GAMM       OME       CHI       PHI
8   124.000     0.000     0.000     0.000
9    SCLERR    NUMACC (=NPEAKS/SQRT(2)) : LATFIT Parameters
10      1.0        10
11 A, B, C, ALPHA, BETA, GAMMA : Cell dimensions
12     3.5631    3.5631    3.5631        90.000    90.000    90.000
13 UB(3,3) : Orientation matrix
14    0.026931    -0.279320    -0.004602
15    0.004703     0.005076    -0.280568
16    0.279319     0.026845     0.005167
17 ABC(3,3) : Direct cell matrix
18         0.34191   -3.54619   -0.05842
19         0.05970    0.06444   -3.56203
20         3.54617    0.34082    0.06560
21  NSEQ       H         K         L      XCEL      ZCEL      TIME    PKHT  IFLAG    NSPEC
22             FH        FK        FL     DXCEL     DZCEL     DTIME    INTI
23     1        3         1         1     -3.50    -29.57   3762.72     424      0     1795
24          2.96      0.93      1.18      0.50      0.50      5.64       0
25     2        5        -1         1     20.63     20.50   2673.16     322      0     3381
26          4.99     -1.00      1.01      0.50      0.50      4.01       0
27     3        6         0         2     -0.48      1.50   2046.76     241      0     2082
28          5.83     -0.15      2.45      0.50      0.50      3.07       0
29     4        5         1         1     19.72    -23.45   2650.94     234      0     3273
30          5.01      1.01      1.00      0.50      0.50      3.98       0
```

Figure 6.7. The header of a typical SXD 'USE' file for one of the diamond anvils. This is the basic input format for all of the SXD instrument software [70]. The first eight lines are used to specify the geometry of the instrument and a general multi-element detector (a different USE file is required for each of the three SXD detector modules). The next two lines are instructions for a program (LATFIT) used to refine the crystal lattice. This is followed by 10 lines specifying the lattice and its orientation (no reference is made to the symmetry of the crystal). Finally, a list of peaks identified by the peak-search software is given, here it is truncated to show only the first four peaks.

positions of every accessible, indexed peak and generated a USE file containing *these* peaks. This was then used by the author as the starting point for integration procedure. A caveat to consider with this method it that errors in the UB matrix allow for the possibility that the calculated position of a peak might be off by as much as a pixel. This possibility had to be borne in mind during the integration, and checks made that the calculated coordinates did indeed correspond to the peak centroid.

Initially, the only available software to perform manual integration was a collection of GENIE command files, and a basic GEC fitting routine. In this procedure, the command file prompted for the spectrum number and time-of-flight of a diffraction peak. This spectrum and its eight nearest neighbours were each corrected for their wavelength-independent efficiencies (obtained from a lookup file recording the appropriate vanadium measurements) and then integrated. The combined spectrum was then displayed in the region of the input TOF and the option to integrate was given. Once integrated, the area of the peaks (and estimated standard deviation) were displayed and had to be written by hand into a new version of the USE file called with the extension INT with an identical format but storing the integrated intensities.

Several drawbacks were inherent in this method. The first of these lay in the routine used to fit the GEC function. This was a completely unconstrained fit and, consequently, was prone to fail if the peak was insufficiently defined (as many of the sample peaks were). To improve this situation, it was replaced with a more modern algorithm developed by Sivia [25], which proved to be far more robust at fitting most peaks. Additionally, these routines permitted some measure of interactivity (for example allowing the background to be fixed whilst the peak position was refined, or fixing the position whilst the peak area was refined). Whilst, strictly, each peak should be integrated in exactly the same manner for consistency, the use of such interactive fitting was necessary to obtain approximate intensities for the weakest peaks.

A second problem arose from the possibility that some of the peaks fitting the UB were actually powder peaks from the gasket. This problem was also readily corrected by a modification of the GENIE command file to display each of the nine spectra constituting the integration footprint in a multi-plot. In this way, powder lines could be identified by their presence, with equal intensity, in each of the spectra. Further modification allowed the powder peaks to be sampled in the surrounding spectra and then subtracted prior to integration.

However, by far the largest drawback of this integration method was the time involved. The integration of a single data set could take several days of continual integration. In addition, as the fitted GEC areas had to be copied by hand into the appropriate INT files (versions of a USE file containing the accurately fitted intensities, that are used for structure factor extraction) there was a significant scope for manual error. It was for this reason that the author developed new software to aid in the manual integrations. The main features of the program were:

1. Improved data visualisation.

2. The possibility of re-allocating the peak centroid position (to allow for possible error in the orientation matrix).

3. The peak location could be read directly from the USE file and the results of the integration automatically output to an INT file.

4. Selective addition of spectra within the 3×3 integration area around the peak centroid. This again represents a level of interaction that proved necessary for the integration of weak peaks that were comparable with the background summed across the entire integration area, but were clearly visible within 2-3 elements.

5. Interactive control of the GEC fitting procedure. The routine used was identical to that used in the fitting of PEARL single-crystal intensities described previously in Section 4.4.2 and in Appendix B.

6. The option of sampling the background where no peak is visible, and from this determining the estimated standard deviation on a measurement of zero intensity.

6.4 A Neutron Single-Crystal Diffraction Study of D_2-D_2O Clathrate

The techniques described above where first applied in an experimental study of the structure of D_2-D_2O clathrate. It is well documented that mixtures of water and a variety of simple-molecular fluids crystallise into clathrate structures under the application of high pressure or at low temperature [95]. These structures are composed of cages of water molecules forming a hydrogen-bonded '*host*' framework surrounding the other '*guest*' molecules. Most clathrate structures are known to fall into two distinct types, each possessing a different cage size, known respectively as structure-I and structure-II clathrate. However, both of these structures become unstable if the guest molecule is too small to fill the available volume within the cages. This is the case for both He and H_2 which both possess Van der Waal radii of less than 1.5 Å [99].

The first observation of a new clathrate formed between water and He at pressures greater than 0.28 GPa came in 1988 from Londono *et al.* [96]. The structure (space group $R\bar{3}$) was determined by neutron powder diffraction and shown to consist of a host arrangement of water molecules with the ice II structure. This framework of water molecules has channels large enough to accommodate He atoms with a stoichiometry of $He{:}6H_2O$. The difference between this channel structure and the cage structure of conventional clathrate has been highlighted by Loveday *et al.* [97] who use the term 'filled ice'. However, to avoid confusion with the previously published literature, the 'clathrate' nomenclature is retained in this thesis.

The discovery of He clathrate was followed in 1993 by the report of a new structure formed by the inclusion of H_2 molecules into H_2O under pressure by Vos *et al.* [98]. Here, x-ray diffraction measurements made on both powder and single-crystal samples determined the structure to be the same as that of He clathrate between 0.75 and 3.1 GPa, with H_2 molecules replacing the He atoms on sites

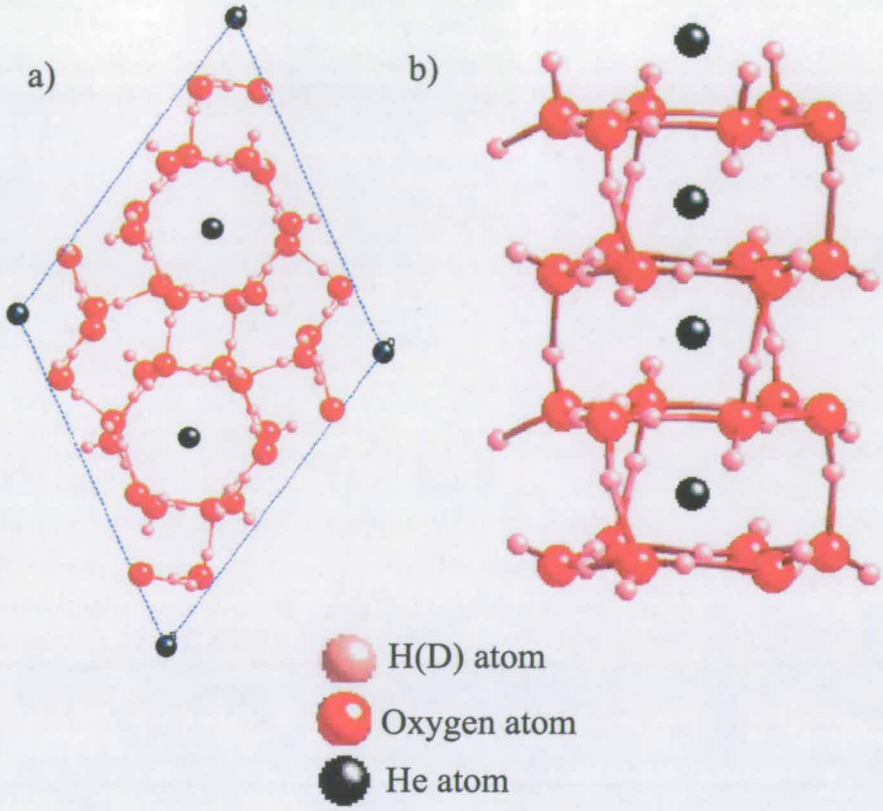

Figure 6.8. Two different perspectives on Londono's He-clathrate structure [96]. On the left (a) shows the view along the *c*-axis looking down the channels formed by six-membered rings of water molecules. The view perpendicular to this is shown in (b) where a chain of He atoms is clearly visible. This channel structure is much smaller than that of the 'cage' arrangements found in the conventional clathrate structures [97].

within the channels. Vos *et al.* also reported a new cubic structure with a 1:1 composition of H_2 and H_2O at pressures above 3.1 GPa. They labelled these two H_2 clathrate structures, respectively, as C_1 and C_2.

The structure of H_2 clathrate is of fundamental importance in the study of hydrogen bonding and H-H repulsions [98]. Unfortunately, the technique of x-ray diffraction is very insensitive to hydrogen atoms, and it is almost impossible to determine their atomic coordinates accurately. This fact motivated the present study, where neutron single-crystal diffraction, which *is* sensitive to hydrogen positions, was used to study the structure. The intention was simply to test the

new high-pressure, single-crystal techniques by attempting to measure accurately the position of the hydrogen atom within the water framework.

Unexpectedly, the data collected on SXD yielded the surprising result that the previously published structure of H_2 clathrate may have been incorrect. The observation of extra equivalents and apparent systematic absences pointed toward a possible mis-assignment of the space group by Vos *et al* [98]. Unfortunately, the complications of a complex absorption correction resulted in the degradation of the data to the point where a direct comparison with the published structure by refinement was not possible.

These difficulties were mostly a consequence of a lack of development of experimental technique, and improvements suggested by this work are discussed. The evidence that the published structure is incorrect is intriguing and warrants further study that was not possible as part of this thesis work.

As a consequence of quantum rotations of the H_2 molecule both it and He have a spherical charge distribution, and are of comparable size [99]. This size is significantly smaller than the volume of the cage and it is not immediately obvious that the cage should be able to distinguish between the two hosts. Consequently, different structures for the He and H_2 clathrates hint that there may be some additional interaction between the 'guest' hydrogen atom and the water molecules forming the host.

6.4.1 Loading Details

The author did not participate directly in the preparation of sample crystals in these experiments. Mixtures of deuterated water and deuterium gas were loaded and grown into single-crystals at the Geophysical Laboratory by J. Xu and M. Somayazulu. Whilst several loadings were attempted, only one yielded a crystal of sufficient size and quality for diffraction measurements. This crystal was loaded in the Carnegie panoramic cell using the methods described previously in Section

Run number	ω°	χ°	Run time ($\mu Ahrs$)	Collimator diameter (mm)
14644	0.0	0.0	1751	1.2
14645	244.0	0.0	2121	1.2
14646	124.5	-1.25	2609	1.2
14647	261.0	-1.25	1827	1.2
14648	137.5	-1.25	2081	1.2
14649	257.0	-1.25	2227	1.2
14650	257.0	-1.25	2250	2.0
14653	244.0	-1.25	2006	2.0

Table 6.2. Details of the data collection from the D_2-D_2O single crystal. The angle ω gives the rotational position of the cell about its axis, whilst the χ angle measures tilting of the crystal, which was apparently free to move around slightly within the cell.

6.2. The anvils used were single-crystal diamonds with 2.0 mm diameter culets, these were loaded using a 1.0 mm thick Ti:Zr gasket with a protective layer of Be:Cu around the sample volume that had a diameter of 1.1 mm. The sample crystal was grown to fill the volume, with a small amount of excess hydrogen present, giving a sample volume of almost 1 mm^3. The pressure of the sample was measured by the ruby fluorescence technique to be 1.1(1) GPa before, and 1.3(1) GPa after the diffraction measurements.

The cell was placed in the neutron diffractometer and a 1.2 mm BN collimator was put in place, but, this was replaced with a 2.0 mm collimator for the last two runs to prevent possible occlusion of the sample. The data were collected with the cell in several orientations as described in Table 6.2.

The data were indexed on the published hexagonal unit cell [98] with lattice parameters **a** = 12.902(16) Å and **c** = 6.202(19) Å. This unit cell and the orientation matrix were then used to identify the location of all accessible reflections, and integrations were performed using the software developed by the author as described above.

6.4.2 Data Analysis and Correction

Upon the initial, cursory, examination of the data during the experimental collection two unexpected observations were made. Firstly, it was noticed that reflections related to each other by the mirror plane of the $\bar{3}$m Laue class appeared to have very similar intensities. This was unexpected, as the published space group R$\bar{3}$ is a member of the lower symmetry $\bar{3}$ Laue class in which these particular reflections were inequivalent. The orientation of the crystal was such that the apparent mirror plane coincided very closely with the equatorial plane of the diffractometer. Consequently, pairs of reflections related by the $\bar{3}$m mirror plane were observed approximately equidistant from the centre of a given detector module. The scattering geometry of this situation is demonstrated in Figure 6.9.

Secondly, it was noticed that there appeared to be a systematic absence of reflections corresponding to a *c*-glide symmetry element[2] that is also *not* present in the published space group, nor indeed in any space group of the $\bar{3}$ Laue class. Although, there were two space groups in the $\bar{3}m$ Laue class that contained the *c*-glide symmetry element. Additionally it was realised that the presence of a *c*-glide implied the mirror-plane symmetry previously observed and, therefore, these two observations were consistent with each other.

These two aspects of the data had to be explored more thoroughly, for instance the observation of the apparent mirror plane could actually be attributed to twinning of the sample crystal. The *c*-glide absences had to be confirmed, and this was not possible with an integration method that began from a peak search, which by definition does not measure absent reflections! Consequently, the new integration software (described above) was developed to use existing SXD routines and the refined orientation matrix, to predict the location of every peak indexed on the published unit cell. The capability was included to measure the background

[2]The absence conditions for $r\bar{3}c$ space group are (where $i = \bar{h} - k$): $hkil$ $-h + k + l = 3n$; $h\bar{h}0l$ $h + l = 3n$ with l even; $hh2\bar{h}l$ $l = 3n$; $000l$ $l = 6n$ [24].

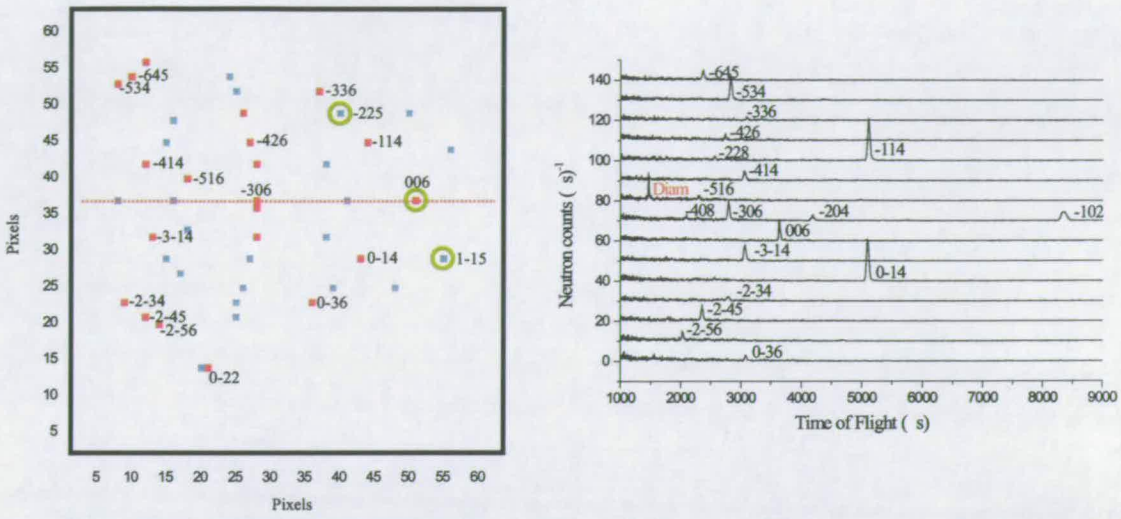

Figure 6.9. The left hand part of the Figure shows a schematic of the detector face with the locations of all the accessible reflections indexed on the C1 unit cell indicated by square symbols. Red squares indicate observed reflections, and blue squares indicate reflections where nothing was observed above background. The red-dotted line corresponds to a mirror plane symmetry in the $\bar{3}$m Laue class. Reflections circled in green correspond to reflections that are absent in the presence of c-glide symmetry. The right-hand-side of the figure shows the TOF spectra of all of the reflections measured greater than three standard deviations. The index of these reflections is also marked on the left hand figure. Note that in the TOF technique, higher harmonics of a given reflection are observed in the same spectrum (e.g. the $\bar{1}02$,$\bar{2}04$,$\bar{3}06$ etc.).

where no peak could be fitted, thus obtaining an accurate determination of the error in the observation of zero intensity.

The Accuracy of the Observed Structure Factors

The quality of these data, integrated by the new software, could be assessed by comparing the intensities of equivalent reflections. If the data have been properly corrected, equivalents should give the same structure factor, no matter where they are measured. To this end, the observed reflections were grouped into sets of equivalences according to the higher symmetry $\bar{3}m$ Laue class. It was clear that this higher symmetry was present in the data, although at this stage

it could not be determined if it was due to the structure of the clathrate or the macroscopic effect of twinning.

In many cases (although not all), the mirror-plane equivalence was observed to hold. Indeed, the agreement between mirror-plane equivalences was often better than the *expected* equivalence between repeated measurements of the same reflection (or its Friedel equivalent) in different detectors in different runs. These could differ by as much as 40-50%, so clearly additional effects that had to be considered and corrected. The possible explanations that were explored were:

- Absorption of the incident and scattered beam by components of the cell.
- The possible presence of a wavelength-independent scale factor between different runs arising from mis-alignment of the BN collimator piece.
- Extinction of the neutron beam by the sample crystal.
- Reflections from the single-crystal diamond anvils overlapping with the sample reflections.

In order that these effects could be systematically examined, lists of reflections were generated (grouped by equivalence), where each reflection was labelled by its wavelength, the run-number, and the spectrum number of the peak centroid. This information was sufficient to obtain all the geometrical information relating the neutron beam to the cell, the sample and the detectors.

The investigation began with a study of the possible effect of absorption on the incident and diffracted beam. A simple calculation demonstrated that the size of the Ti:Zr gasket was large enough to account for a 30-40% reduction of a 1Å neutron beam that passed through the full diameter of 10 mm. It immediately became clear that this effect would be highly dependent on the angle made by a diffracted beam with the plane of the gasket. That the situation was more complex still, was revealed by a close examination of photographic images of the

gasket such as that shown in Figure 6.10. Prior to taking the photographs, the cell had been downloaded and the piston pulled back, care being taken to ensure that the gasket maintained its position relative to the cylinder anvil.

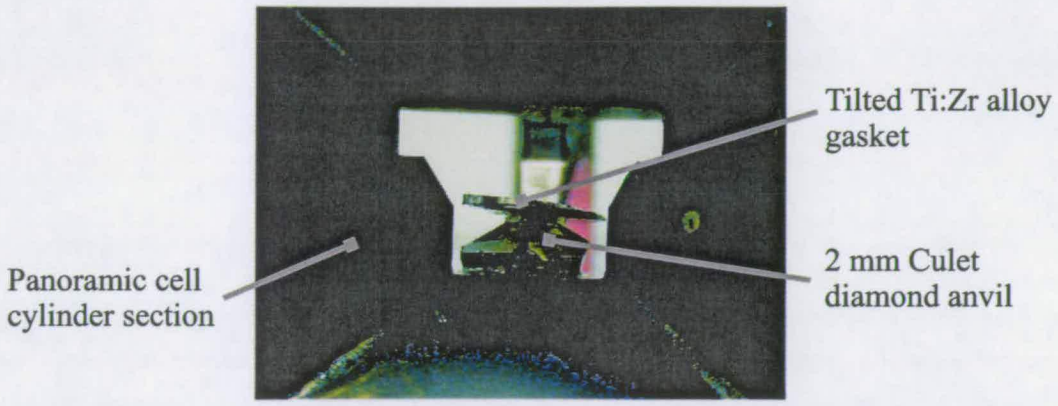

Figure 6.10. Photograph of the gasket used in the loading of the D_2-D_2O sample crystal. A clear tilt of $\sim 7°$ of the gasket is visible. Note also the thinning of the gasket to the right of the image.

The photographs clearly show a tilt of the gasket of $\sim 7°$ to the equatorial plane of the cell. Consequently, the absorbing pathlength traversed by a diffracted beam was not only a function of the angle out of the equatorial plane, but also of the angle *within* the plane. This variable absorption would also affect the incident beam, leading to potentially large differences in the intensity of equivalent reflections measured in different runs.

Clearly, for reliable intensities to be extracted, some kind of absorption correction would have to be applied. In principle, absorption of any geometry could be determined by refinements, however the author was unable to find appropriate software for energy dispersive data and, additionally, it was likely that paucity of data would make such refinements unreliable. Consequently, the approach attempted was to use a simplified model of the gasket, and calculate the expected pathlength for a given direction from sample to detector.

Two frames of reference were used to define the system:

- A diffractometer frame $\mathbf{D}$, fixed relative to the laboratory, that is described by the set of Cartesian axes $\mathbf{D}_x$, $\mathbf{D}_y$ and $\mathbf{D}_z$ with a general vector given by $\mathbf{r}_D = (x_D, y_D, z_D)$. The axes are aligned such that $\mathbf{D}_x$ and $\mathbf{D}_y$ are in the equatorial plane of the incident beam, with $\mathbf{D}_x$ anti-parallel to the incident beam. The axis $\mathbf{D}_z$ points vertically down such that a positive rotation about it corresponds to increasing the ω setting angle.

- A cell frame $\mathbf{C}$, fixed in the body of the cell and described by the set of Cartesian axes $\mathbf{C}_x$,$\mathbf{C}_y$ and $\mathbf{C}_z$ with a general vector given by $\mathbf{r}_C = (x_C, y_C, z_C)$. At $\omega = 0°$ the frames are coincident such that $\mathbf{D} \equiv \mathbf{C}$, with subsequent rotations of the cell by ω giving

$$x_C = x_D \cos\omega - y_D \sin\omega \tag{6.3}$$

$$y_C = x_D \sin\omega + y_D \cos\omega \tag{6.4}$$

$$z_C = z_D \tag{6.5}$$

The gasket was described as a rigid disk of Ti:Zr with uniform thickness t and radius r centred on the sample position. This was then allowed to tilt about that position. If the maximum tilt of the gasket out of the equatorial plane is β_m, then the tilt of the gasket β_g at any angle α about the $\mathbf{C}_z$ axis is given by

$$\beta_g(\alpha) = \beta_m \cos(\alpha - \alpha_o) \tag{6.6}$$

Where α_o is the angle at which β_m occurs. For a known gasket geometry (t and r are determined by measurement of the gasket at the end of the experiment) the model is then completely specified by the two parameters α_o and β_m.

The angles defining the diffracted beam are determined from the coordinates of the diffraction peak on the detector face and the known positions of the detectors. These are then transformed into the cell frame $\mathbf{C}$ to give the angle α of the

diffracted beam. At this stage, reflections were also removed that were occluded by the cell webs. The angle out of the equatorial plane β is the same in either frame, and can then be compared with the angle of the gasket $\beta_g(\alpha)$ in order to calculate the absorbing Ti:Zr pathlength. The geometry of this model is described in Figure 6.11.

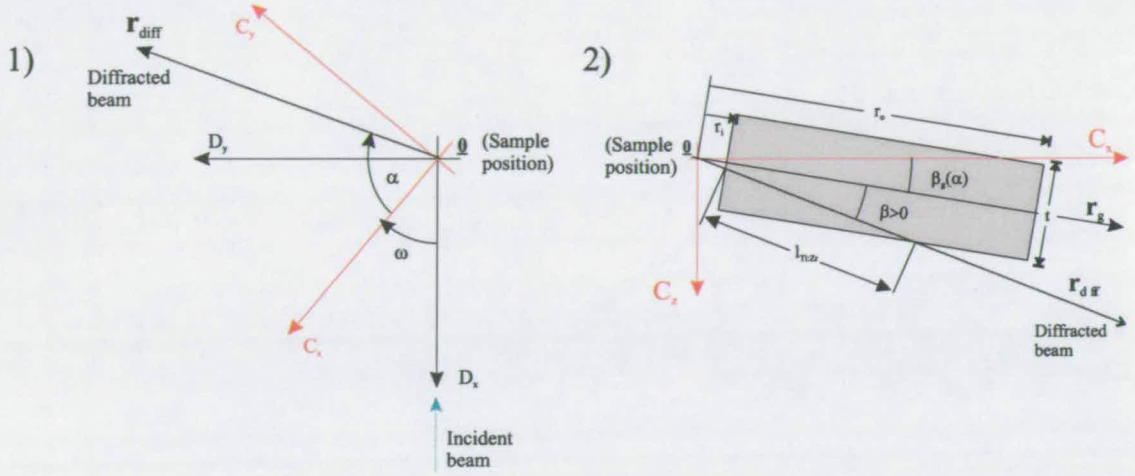

Figure 6.11. Schematic of the absorption model used. The left-hand figure (1) shows the relation between the diffractometer frame **D** and the cell frame **C** (both z-axes point vertically down into the page). Vector $\mathbf{r}_{diff}$ points along the direction of the diffracted beam, and its projection onto the equatorial plane gives the angle α when it is transformed into the cell frame. The right-hand figure (2) illustrates the section of gasket that the diffracted beam travels through. The vector $\mathbf{r}_g$ lies in the vertical plane passing through $\mathbf{r}_{diff}$ and travels through the central plane of the gasket and is thus at angle β_g to the equatorial plane as indicated. The angle of the diffracted beam out of the equatorial plane is given by β which is defined relative to $\mathbf{r}_g$ such that $\beta = 0$ when $\mathbf{r}_{diff} = \mathbf{r}_g$. The symmetry of this model means that the sign of β is unimportant, but it is defined such that it has the same sense as the axis $\mathbf{C}_z$ and, therefore, is positive in the figure.

This same calculation was also performed for the incident beam, giving the total absorbing pathlength l_{tot}. The measured intensities are then corrected by dividing through by a gasket absorption factor absorption factor A_{gas}

$$A_{gas} = \exp[-\mu_{Ti:Zr}(\lambda) \times l_{tot}] \tag{6.7}$$

where the value of $\mu_{Ti:Zr}$ is taken to be the same as that used in Equation 5.3, re-written here in Equation 6.8

$$\mu(\lambda)_{KDP} = 0.17000 + 0.0008\lambda \quad (\mathrm{mm}^{-1}) \tag{6.8}$$

The correction was performed using nominal values of $\alpha_m = 95°$ and $\beta_m = 7°$ which were determined from images of the gasket of the type given in Figure 6.10. The dimensions of the gasket were found by measurement at the end of the experiment that gave $t = 1.0$ mm, $r_o = 5.0$ and $r_i = 0.5$.

The effect of the absorption correction is shown in Table 6.3 for all of the mirror plane equivalences measured in run 14644. Again it is emphasised that, as a consequence of the geometry, these pairs of equivalences are measured at almost identical TOFs. As such, any variation is only to be attributed to varying absorption of the *diffracted* beam as a result of the gasket geometry. The values given in the table show that there is a noticeable improvement in the agreement of equivalences that is typical of that observed in all of the runs.

However, despite a good level of agreement between many pairs of reflections, there were also several cases where application of the absorption correction actually made equivalents agree *less* well. This is most likely due to the simplicity of the model applied, and the uncertainty in its parameters. Close inspection of the photograph in Figure 6.10 shows a significant amount of deviation of the gasket from a perfect disk, in particular, one edge is clearly thinner than the other and, additionally, a certain amount of curvature is evident as the gasket has bent around the anvil on application of load.

Upon further examination of the data, it was clear that the agreement between experiments measured within a given run was much closer than that between equivalents measured in different runs. In particular, the first two runs appeared to measure equivalents as too weak. This raised the possibility that there might be a scale factor between runs. As was mentioned previously, the first six data

Det. Module	hkl	uncorrected		corrected		TOF (μs)	label
		F^2_{obs}	σ^2	F^2_{obs}	σ^2		
1	612	11.3	1.7	19.3	2.9	5339	1
1	7-12	17.6	2.5	24.7	3.5	5341	
2	410	145.2	3.4	229.7	5.5	5197	2
2	5-10	159.4	3.2	229.1	4.5	5181	
2	710	15.4	2.1	23.0	3.1	3188	3
2	8-10	19.0	2.2	25.9	3.0	3183	
2	820	31.3	4.4	43.0	6.0	2598	4
2	10-20	29.2	4.3	37.5	5.6	2590	
3	-645	28.5	5.6	35.1	6.9	2368	5
3	-2-45	21.2	4.5	26.8	5.7	2350	
3	-534	17.4	2.4	21.9	3.0	2814	6
3	-2-34	15.6	2.4	20.3	3.2	2794	
3	-414	12.8	1.9	16.8	2.5	3060	7
3	-3-14	9.9	1.5	14.6	2.2	3052	
3	-114	53.4	2.4	74.0	3.3	5094	8
3	0-14	39.9	2.0	66.9	3.3	5083	

Table 6.3. Lists of equivalent reflections illustrating the effect of the tilted-gasket absorption correction.

collections where performed with a collimator that was of comparable size to the sample. Although observation of reflections from both of the diamond anvils ensured that the sample was vertically centred in the beam, there was still the possibility that the collimator was misaligned in the horizontal plane. This could result in occlusion of part of the sample and a consequent reduction in the scattering power of all reflections in that run.

Such an effect would be wavelength independent, so it would be possible to measure such scale factors by taking ratios of equivalent reflections with respect to one particular run. This was attempted by comparing ratios of equivalents across the entire data set. However, when this was attempted, the resulting ratios differed rather widely. It was possible that if extinction was present, that this might introduce a wavelength dependent effect in addition to the scale factors. In order to investigate this possibility, only data collected in the final two experimental runs was considered. As these runs used a much wider collimator, occlusion of the incident beam should not have been possible. Therefore, any discrepancy between equivalences measured in separate runs must be attributed to some additional effect.

This comparison was made resulting in six pairs of equivalences measured in both runs, these are listed in Table 6.4. In no case where an equivalent is measured as too strong does this coincide with the reflection being measured at a shorter wavelength. Therefore, extinction, which increases in proportion to the wavelength cubed (see Section 5.3.2), cannot account for the observed difference between equivalences measured in these runs. Consequently, the differences can *only* be attributed to the failure of the absorption model.

Unfortunately there are insufficient reflections that are well enough determined, and not strongly affected by the absorption effect, to accurately scale between the runs. This uncertainty in the measured structure factors strongly hindered any attempts to refine the data using the published structure. Consequently, it was impossible to conclusively determine whether the observed equivalences were

Run	h	k	l	$\|F_{obs}\|^2$	σ^2	TOF (μs)	equivalent
14650	-10	1	4	72.7	9.9	3599	1
14650	-9	-1	4	67.7	9.3	3661	
14653	-10	1	4	71.7	11.7	3086	
14653	-9	-1	4	75.8	12.8	3143	
24650	2	-5	4	41.5	9.0	2135	2
24653	-5	3	4	56.3	12.0	2213	
24653	-2	-3	4	40.9	10.9	2580	
24650	2	-4	3	30.5	5.0	2388	3
24653	-4	2	3	21.0	3.7	3305	
24653	-2	-2	3	21.3	3.8	3726	
34650	-8	3	-2	38.9	3.6	3468	4
34650	-5	-3	-2	25.8	2.5	3916	
34653	-5	-3	-2	49.4	5.2	4939	
34650	-7	1	-2	11.4	2.3	3996	5
34650	-6	-1	-2	12.3	2.4	4162	
34653	-7	1	-2	19.9	3.3	5158	
34653	-6	-1	-2	21.3	3.4	5311	
34650	-5	0	-2	11.3	2.9	4309	6
34653	-5	0	-2	17.0	3.7	5890	

Table 6.4. Comparison of equivalent reflections from the final two experimental runs

the result of twinning or not.

Observations of Absent Reflections

It was noted at the beginning of this section that there were apparent systematic absences corresponding to a *c*-glide symmetry element. Such observations of zero intensity are unaffected by the uncertainties arising from inter-run scaling and a complex absorption correction. In addition, they cannot arise as a result of twinning. In order to determine if these reflections are expected to be very weak in the published structure, a simulation was conducted. If this is not the case, and the absences correspond to strong peaks, then this would provide strong evidence that the published structure was incorrect.

The structure used in the simulation is that of He hydrate, of Londono *et al.* [96].

P (GPa)	Coord.	O1	O2	D1	D2	D3	D4	He
0.291	x	0.2216(4)	0.1893(4)	0.1513(4)	0.2235(5)	0.1076(5)	0.2370(3)	0.0
0.477		0.2195(6)	0.1896(5)	0.1517(4)	0.2248(6)	0.1089(6)	0.2380(4)	0.0
0.291	y	0.1976(4)	0.2311(3)	0.1991(3)	0.2164(3)	0.2144(5)	0.3056(4)	0.0
0.477		0.1965(6)	0.2310(4)	0.2010(4)	0.2168(4)	0.2162(6)	0.3053(4)	0.0
0.291	z	0.0477(8)	0.4801(9)	-0.0078(9)	0.1997(7)	0.4838(7)	0.5607(7)	0.297(6)
0.477		0.048(1)	0.483(1)	-0.011(1)	0.2003(8)	0.4855(9)	0.5591(8)	0.277(6)

Table 6.5. Refined fractional coordinates of He hydrate as measured by Londono *et al.* at pressures of 0.291 and 0.477 GPa [96]

The space group is $\mathbf{R\bar{3}}$, and the refined atomic coordinates at two pressures are given in Table 6.5. Deuterium was located at the site of the helium atom with a fractional occupancy of 2.0, this represents the deuterium molecule which has a spherical charge distribution due to quantum rotations [99].

The simulation was first performed with Londono *et al.*'s higher pressure, 0.477 GPa structure, and revealed that several of the unobserved reflections corresponded to calculated strong intensities. In particular, the 003 was calculated to have an extremely strong intensity, and yet appeared to be absent in the data collection. Additionally, the time-of-flight spectra containing the 003 also contains the 006, which was observed three times throughout the entire data set. This has two important consequences for accessing validity of the absences:

- It provides conclusive evidence that the absences are not attributable to some form of unaccounted-for occlusion, or accidental 'gaps' in the volume of reciprocal space surveyed.
- It provides a means by which the calculated intensities can be scaled, independently of any geometrical effects.

This final item is important because, as a diffraction experiment only attempts to determine correct *relative* intensities, they are not known on an absolute scale. Consequently, it is always necessary to multiply a data-set by some constant scaling factor. This necessity presents a problem for the current data-set, where

there is a large uncertainty in the F_{obs}'s as a result of the complex absorption correction. This leads to a corresponding uncertainty in the scaling. However, the determination of the scale factor between reflections simultaneously measured along the same direction of reciprocal space is much simpler, as all geometrical effects are removed.

The strongest observation of the 006 is given in Figure 6.12, which shows the entire recorded spectrum as a function of wavelength. In this instance the 006 is clearly visible at 1.761 Å and, consequently, the 003 reflection would be expected at 3.522 Å. A GEC function was fitted to the 006 peak giving an area of 971 (34) neutron counts. In fact, there is evidence for an *extremely* weak peak at the expected location of the 003, which was not measured during the integration procedure. Its intensity could be estimated by using a constrained GEC function which gave only 16 (5) neutron counts.

In order to scale the measured intensities of the two harmonics, it is still necessary to correct for the wavelength-dependent terms in the Buras-Gerard Equation 4.2 (BG) [28]. In particular the terms $\epsilon i_o(\lambda)$, λ^4 and $A(\lambda)$ must be corrected for. In the absence of absorption, this calculation is shown in Table 6.6

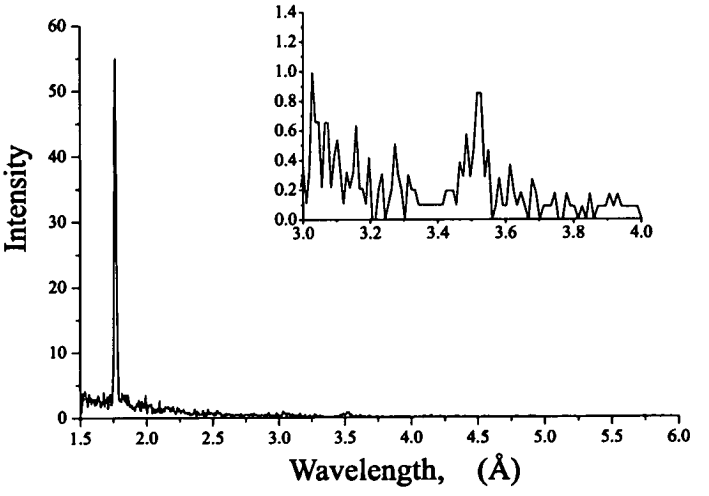

Figure 6.12. The strongest observation of the 006 reflection. Insert shows close-up of the expected location of the 003 at 3.522 Å.

hkl	Wavelength, λ (Å)	λ^4	effective flux, $\epsilon i_o(\lambda)$	BG
006	1.761 (8)	9.62 (17)	5.09 (13)	1.000
003	3.522 (16)	153.9 (2.8)	75.6 (8)	0.93 (7)

Table 6.6. Calculation of the relative Buras-Gerard correction [28] between the 003 and 006 reflections.

The simulation of Londono's 0.477 GPa structure for the 003 reflection gave a structure factor that was is 1.18 times that of the 006, multiplying this by the relative BG term in Table 6.6 gives an expected *observed* intensity of 1065(75) for the 003. Even the maximum possible absorption arising from 10 mm of Ti:Zr can only reduce this by half to which is still $> 50\%$ of that observed for the 006.

To assess how sensitive the calculated structure factors might be to pressure-induced structural changes, a simulation was also carried out using Londono's 0.291 GPa structure. The calculated intensities are 215.4 for the 006 and 99.9 for the 003 respectively. Applying the same correction factor gives an expected intensity of the 003 of 415 (29), which is significantly weaker than for the 0.477 GPa structure but is still much stronger than is observed, even with the maximum possible gasket-attenuation.

However, the fact that pressure induced structural changes can have a significant effect on the relative 006 and 003 intensities warranted further investigation. By looking at the structural parameters in Table 6.5 it is clear that the main change is in the location of the helium atom along the z-axis. By performing simulations where the hydrogen site is displaced along the z-axis by similar amounts, the dependence of the ratio of 003 over 006 could be determined and this is shown in Table 6.7.

The strength of the 003 clearly has a minimum at $z(\mathrm{H})=1/3$ where scattering from successive H_2 molecules is exactly out of phase. For this smallest possible ratio, the 003 would still be expected to have an intensity of 180(12) neutron counts. Again, this could be further reduced by a factor of 2 by gasket absorption, but

P (GPa)	H_2 fract. z-coord.	$\frac{003}{006}$
	0.36	0.32
	0.34	0.21
	0.32	0.23
0.291	0.297	0.46
0.477	0.277	1.18
	0.26	2.37

Table 6.7. Ratios of the 003 and 006 structure factors (squared) with the D_2 molecule located at a range of positions along the c-axis around those measured by Londono *et al.* for the He atom at 0.291 and 0.477 GPa [96].

this still gives an expected intensity at least a factor of 6 in excess of the observed counts.

In conclusion, the very weak measured intensity of the 003 reflection may indicate the c-glide absences are not, in fact, absent but are extremely weak. In particular, it has been demonstrated that the expected structure cannot account for the exceptional weakness of this particular reflection. This leads to the conclusion that the published structure may be incorrect, and that a new structure, possibly possessing a pseudo c-glide symmetry is required. If this is indeed the case, then the appropriate next step would be to attempt to re-determine the structure with single-crystal x-ray techniques, simply because of the far greater number of reflections that can be accessed with the available sources and pressure cells.

6.5 Conclusions

Despite the limitation of a small working volume, the first structural neutron-diffraction study at high pressure, employing diamond anvils, has been successful. The fact that, even given the significant problems with absorption corrections, strong evidence of an error in the previous (x-ray) determination of the structure of hydrogen clathrate hints at the potential power of the technique. The problem

of the absorption correction is not serious although it requires further development of gasket technology. Indeed, Ahsbahs *et al.* [85] used approximately spherical gaskets in work up to 1.6 GPa to simplify the correction.

A more important issue is the limited pressure range and limited working volume - two issues that, of course, go hand-in-hand. This also appears to be surmountable, the only limitation being the availability of large, flawless diamonds. This problem is beginning to be solved by the availability of large artificial diamonds. Such diamonds are produced by chemical vapour deposition onto seed crystals and, consequently, are not, in principle, limited in size [20]. If this is the case, then it is only a matter of time before such work can be extended in pressure - possibly into the megabar region. Of course, the problem can be approached from the other direction and a factor of ten increase in flux of neutrons, or in the efficiency of the detectors is directly communicated to a factor of ten increase in maximum accessible pressure.

The issue of working volume leads to a comparison with the PE cell. Clearly, both cells have complimentary qualities: the PE cell has a higher volume, but with a limited aperture, whilst the contrary is true for the panoramic cell. Future designs must combine the advantages of both cells in a single device. To a certain extent, this merging of the two technologies is inevitable. It is apparent that increasing the sample volume of the panoramic cell will also require greater and greater force. Even for diamonds with a 2.0 mm culet size, the 3.0 GPa pressures required for ice VII loadings require considerable exertion. This problem must be met by the use of some form of hydraulic press, perhaps similar in design to the PE cell. Additionally, many of the important problems in high-pressure science, for example solution of the structure of ice VII which motivated this work, are not possible without the *in-situ* growth of samples. This will require a move away from the opaque anvils currently used with the PE cell.

Chapter 7

Conclusions and a Look to The Future

Over the following pages, a final overview of the content of this thesis is given. In addition to summarising what has gone before, the results of this work are extrapolated, and the future developments are considered.

The first piece of work described in this thesis was a powder diffraction study of the ice phases VII and VIII. This study contained an in depth inquiry into the factors which affect powder diffraction. This lead to the determination of a variety of considerations that must be carefully observed during data collection and subsequent analysis. A notable caveat was that absorption corrections must be treated with great care in the study of thermal motion. The problems arising from two-phase patterns have also been discussed, and this area could suffer further development of the available software. For example, it would be useful if it was possible to refine different absorption corrections for different phases in a Rietveld refinement. Correct fitting of the multi-component background is also vital, and the importance of maintaining experimental control of the external background has been expounded.

The importance of this powder study, however, went beyond the improvement of

standard powder techniques. It provided the initial motivation to take the first steps towards the development of techniques to take single-crystal diffraction to higher pressures than are currently accessible.

This development work proceeded along two paths, each defined by the use of two different high-pressure cells. The more involved project focused on extending the capabilities of the PE cell, a device that had already proved itself by revolutionising neutron powder diffraction work above 10 GPa [15][56]. This work was extremely involved because it not only required the development of techniques to compress single-crystal samples to high pressures, but also involved a major adaptation of the PEARL HiPr diffractometer to perform the single-crystal measurements. A significant component of this was the need for adequate software for data visualisation and peak integration. It has been a general theme throughout the work on both PEARL and SXD that technique and hardware developments *must* be supported by adequate computational capabilities, and a substantial amount of software was written to support the work of this thesis.

Ultimately, this work resulted in the measurement of accurate Bragg intensities in the SXM, up to pressures a factor of three above those previously accessible. A significant amount of time was also devoted to facilitate measurements with the HiPr powder detectors. This resulted in a scanning method that negated inherent difficulties arising from the detector geometry. However, it was shown that these measurements may be affected by large deviations from the assumed element geometry, and this was to be tested by a single-crystal diffraction study on KDP.

This experiment was first preceded by a powder diffraction study of KDP. New metal-encapsulation gaskets were used to maintain hydrostatic conditions up to the maximum pressure achieved of ~ 5.5 GPa. The implications for the Rietveld refinement of data with a large hydrogenous background were investigated and it was shown that this did not affect the main result of the study. This result was the determination of the pressure dependence of the hydrogen bondlength O...O

at room temperature. The observed behaviour was at odds with a previous x-ray study, which had claimed a lengthening of the bond with increasing pressure. This behaviour warrants further investigation, and the need to repeat the experiment with deuterated samples was emphasised.

The powder observations were supported by the first high-pressure data collection using the newly developed single-crystal techniques. These data refined, with a constrained model of the structure, to give values that agreed extremely well with the previous studies below P_c [19] [79]. This was despite the presence of strong extinction in the data. The presence of such strong extinction was unfortunate, as it hindered a definitive assessment of the quality of data measured in the HiPr powder modules. Indeed, it has highlighted a need for a more successful theoretical model to be developed for TOF diffraction measurements. From an experimental perspective the extinction problem served to highlight the inherent difficulties presented by the limited aperture of the PE cell. This presented a clear direction for future developments of single-crystal versions of the cell. It is again emphasised that the current limitation is not intrinsic, but is simply a consequence of the device having been optimised for the entirely different requirements of powder diffraction.

Whilst the work with the PE cell was ongoing, a parallel development of techniques employing diamond anvil technology was pursued. This centred around a second cell that was small enough to be mounted on the goniometer of the SXD instrument at ISIS, a fully functional single-crystal diffractometer. The most important characteristic of this cell was that its single-crystal anvils allowed optical access to the sample - facilitating *in-situ* growth of high-pressure phases. This advantage permits studies of materials that are liquid or gaseous at ambient conditions, and also compounds, such as the gas hydrates, that are unstable at atmospheric pressure. As such, it was extremely desirable to develop the techniques to use the cell in neutron diffraction experiments.

The initial commissioning of the Carnegie panoramic cell was carried out, and

again highlighted the need for specific software. However, perhaps the greatest difficulties, from the experimental perspective, were those associated with the growth of the sample crystals. A brief description of the author's experiences in the attempt to grow ice crystals has emphasised the difficulties involved. A severe problem is an inability to assess the quality of the sample prior to the neutron beamtime. This made the process of learning to grow sample crystals an extremely time consuming task.

Despite these initial difficulties, a good quality single crystal of hydrogen clathrate was eventually grown. This was followed by a first neutron diffraction study of the structure at $\sim$ 1.2 GPa. During the course of this experiment many things were learnt about methodology. Again, the problem of absorption was encountered, resulting in subsequent difficulties in the analysis of the data. This is probably best approached by re-designing the gaskets to simplify their geometry. The need to visualise data during the experiment was also found to be vital in order to select the most appropriate cell orientations to best probe specific aspects of the structure. This was important for the clathrate study, as evidence was almost immediately noticed for unexpected symmetry elements in the data: an extra mirror plane, and possible c-glide absences. A subsequent detailed investigation that required the development of new tools for integrating the data revealed that the c-glide absence condition was actually violated, but only by extremely weak reflections. Simulations of the published structure demonstrated that the lack of strength of these reflections could not be accounted for, and suggested that this structure may be incorrect. This may have important scientific consequences: if the structure of hydrogen clathrate *is* different from that of He clathrate it may be evidence of some additional interaction between the hydrogen atom and the host water framework.

The relative advantages and disadvantages of both high-pressure cells have been discussed. In particular, the respective differences in aperture size and maximum volume are almost exactly complementary between the two cells and currently a

trade-off must be made. This has lead to the speculation that future pressure cells must draw on the capabilities of both toroidal anvil cells and diamond cells in order to extend the pressure envelope. Indeed, single-crystal 'designer' diamond [100] anvils with toroidal grooves ground onto their surface are just beginning to be used in x-ray diffraction, and these techniques could be eventually ported to large volume cells.

Clearly, much of the work presented is in its infancy, yet, it holds a great promise for the near future. This view perhaps helps to contextualise the, sometimes gritty, details that are intrinsic to the development of new techniques and underline the motivation: that these techniques will eventually give access to a new scientific landscape. Mention has also been made of the imminent arrival of new, more powerful, neutron sources and, equally importantly, increases in detector efficiency. This lends a certain timeliness to the work of this thesis.

Bibliography

[1] R. Miletich, D.R. Allan, W.F. Kuhs, *Reviews in Mineralogy and Geochemistry: High-Temperature and High-Pressure Crystal Chemistry* **41** (2000) 445 - 519.

[2] K. Takemura, S. Minomura, O. Shimomura, *Phys. Rev. Lett.* **49** No. 24 (1982) 1772 - 1775.

[3] H.K. Mao, R.J. Hemley, M. Hanfland, *Phys. Rev. Lett.* **65** (1990) 484 - 487.

[4] R. Reichlin, Y.K. Vohra, S. Martin, A.K. McMahan, K.E. Brister, M. Ross, A.L. Ruoff, *Phys. Rev. Lett.* **62** (1989) 669 - 672.

[5] S. Desgreniers, Y.K. Vohra, A.L. Ruoff, *J. Phys. Chem.* **94** (1990) 1117 - 1122.

[6] O. Mishima, L.D. Clavert, E. Whalley, *Nature* **310** (1984) 393 - 395.

[7] Y.P. Handa, J.S. Tse, D.D. Klug, E. Whalley, *J. Chem, Phys.* **94** (1991) 623 - 627.

[8] R.J. Hemley, C.T. Prewitt, K.J. Kingma, *Rev. of Min.* **29**, Mineralogical Soc America (1994).

[9] R.J. Hemley, A.P. Jephcoat, H.K. Mao, L.C. Ming, M.H. Manghnani, *Nature* **334** (1988) 52 - 54.

[10] V. Vijayakumar, *J. Phys. Chem. Sol.* **46** (1985) 17 - 20.

[11] K. Shimizu, T. Kimura, S. Furomoto, K. Takeda, K. Kontani, Y. Onuki, K. Amaya, *Nature* **412** (2001) 316 - 318.

[12] M.I. Eremets, V.V. Struzhkin, H.K. Mao, R.J. Hemley, *Science* **293** (2001) 272 - 274.

[13] M.I. Eremets, R.J. Hemley, H.K. Mao, E. Gregoryanz, *Nature* **411** (2001) 170 - 174.

[14] Philipe Pruzan, Physique des Milieux Condensés, Université Pierre et Marie Curie, Paris, *Private communication.*

[15] S. Klotz, J.M. Besson, G. Hamel, R.J. Nelmes, J.S. Loveday, W.G. Marshall, R.M. Wilson, *Appl. Phys. Lett.* **66** 14 (1995) 1735 - 1737.

[16] R.J. Hemley, A.P. Jephcoat, H.K. Mao, C.S. Zha, L.W. FInger, D.E. Cox, *Nature* **330** (1987) 737 - 740.

[17] R.J. Hemley, H.K. Mao, *International Geology Review* **43** (2001) 1 - 30.

[18] P. Loubeyre, R. LeToullec, E. Wolanin, M. Hanfland, D. Hausermann *Nature*, **397** (1999) 503 - 506.

[19] S. Endo, T. Chino, S. Tsuboi, K. Koto, *Nature* **340** (1989) 452 - 455.

[20] C-S Yan, K. Yogesh, H-K Mao, R.J. Hemley, *Proc. Nat. Acad. Sci.* In Press.

[21] Xu, J.A., & H.K. Mao, *Science* **290** (2000) 783 - 785.

[22] C. Giacovazzo, H.L. Monaco, D. Viterbo, F. Scordari, G. Gilli, G. Zanotti, M. Catti, *Fundamentals of Crystallography*, Oxford University Press (1992).

[23] B.M. Kariuki, S.A. Belmonte, M.I. McMahon, R.L. Johnston, K.D.M. Harris, R.J. Nelmes, *J. Synch. Rad.* **6** (1999) 87 - 92.

[24] T. Hahn (Editor) *International Tables For Crystallography: Volume A*, Kluwer Academic Publishers (1995).

[25] D.S. Sivia *Bayesian Analysis - A Bayesian Tutorial*, Oxford University Press (1996).

[26] SHELXL-97 A program for crystal structure refinement. G. M. Sheldrick, University of Goettingen, Germany, 1997, Release 97-2.

[27] A.C. Larsen, R.B. Von Dreele, *Los Alamos National Laboratory Report:* LAUR 86-748 (1986).

[28] B. Buras, L. Gerward, *Acta Crys.* **A31** (1975) 372 - 374.

[29] W.H. Zachariasen, *Theory of X-ray Diffraction in Crystals*, Dover Publications (1967).

[30] P. Becker, P. Coppens, *Acta Crys.* **A30** (1974) 129-147.

[31] P. Becker, P. Coppens, *Acta Crys.* **A30** (1974) 148-153.

[32] From a 'Special Feature' section of *Neutron News* **3** No. 3 (1992) 29 - 37.

[33] G.L. Squires, *Introduction to the Theory of Thermal Neutron Scattering*, Dover Publications (1996).

[34] U.W. Ardnt, B.T.M. Willis, *Single Crystal Diffractometry,* Cambridge University Press (1966).

[35] S.A. Belmonte *Ph.D. Thesis* The University of Edinburgh, (1998).

[36] H.M. Rietveld, *Acta Crys.* **22** (1967) 151 - 152.

[37] R. A. Yound (Ed.) *The Rietveld Method (IUCr Monographs on Crystallography 5)*, Oxford University Press (1995).

[38] A.F. Goncharov, V.V. Struzhkin, M.S. Somayazulu, R.J. Hemley, H.K. Mao, *Science*, **273** (1996) 218 - 220.

[39] W.B. Holzapfel, *J. Chem. Phys.* **56** (1972) 712 - 715.

[40] J. Song, H. Yamawaki, H. Fujihisa, M. Sakashita, K. Aoki, *Phys. Rev. B* **60** (1999) 12644 - 12650.

[41] A.F. Goncharov, V.V. Struzhkin, H.K. Mao, R.J. Hemley, *Phys. Rev. Lett.* **83** (1999) 1998 - 2001.

[42] P. Pruzan, J.C. Chervin, B.J. Canny, *J. Chem Phys* **99** (1993) 9842 - 9846.

[43] W.F. Kuhs, J.L. Finney, C. Vettier, D.V. Bliss, *J. Chem. Phys.* **81** (1984) 3612 - 3623.

[44] R.W. Whitworth (Editor), V.F. Pretrenko, *Physics of Ice*, Oxford University Press (1999).

[45] R.J. Nelmes, J.S. Loveday, W.G. Marshall, G. Hamel, J.M. Besson, S. Klotz, *Phys. Rev. Lett.* **81** No 13, (1998) 2719 - 2722.

[46] J.D. Jorgensen, T.G. Worlton, *J. Chem Phys.* **83** (1985) 329 - 333.

[47] P. Pruzan, *J. Mol. Struct.* **322** (1994) 279.

[48] J.S. Loveday, R.J. Nelmes, Department of Physics and Astronomy, The University of Edinburgh, Edinburgh. J.M. Besson, S. Klotz, G. Hamel, Université Pierre et Marie Curie, Paris, *Private communication.*

[49] F. birch, *Phys. Rev.* **71** (1947) 809 - 824.

[50] J.M. Besson, Ph. Pruzan, S.Klotz, G. Hamel, B. Silivi, R.J. Nelmes, J.S. Loveday, R.M. Wilson, S. Hull, *Phys. Rev. B.* **49** (1994) 12540 - 12550.

[51] R. Munro, *J. Appl. Phys.* **53** (1982) 6174.

[52] Program ATTEN: An Attenuation correction calculation for the Paris-Edinburgh Cell on the PEARL HiPr Diffractometer at ISIS, written by W. G. Marshall, ISIS Facility, Rutherford Appleton Laboratory, Chilton, Didcot, OXON, OX11 0QX.

[53] A. Lebail, H. Duroy, J.L. Fourquet, *Mat. Res. Bull.* **23** (1988) 447 - 452.

[54] A.W. Hewat, *Acta Crys.* **A35** (1979) 248.

[55] K.D. Rouse, M.J. Cooper and A. Chakera, *Acta Cryst.* **A26** (1970) 682 - 691.

[56] J.M. Besson, R.J. Nelmes, G. Hamel, J.S. Loveday, G. Weill and S. Hull, *Physica B*, **180 & 181** (1992) 907 - 910.

[57] S. Klotz, J.M. Besson, G. Hamel, R.J. Nelmes, J.S. Loveday, W.G. Marshall, *Nature* **398** (1999) 681 - 684.

[58] J.S. Loveday, R.J. Nelmes, M. Guthrie, S.A. Belmonte, D.R. Allan, D.D. Klug, J.S. Tse, Y.P. Handa, *Nature* **410** (2001) 661 - 663.

[59] J.S.Loveday, R.J. Nelmes, S. Klotz, G. Hamel, J.M. Besson, *Phys. Rev. Lett.* **85** (2000) 1024 - 1027.

[60] W.B. Holzapfel, N.S. Isaacs, (Editors) *High-pressure Techniques in Chemistry and Physics - A Practical Approach*, Oxford University Press (1997).

[61] L.G. Khvostantsev, *High Temperatures High Pressures* **16** (1984) 165 - 169.

[62] A.D. Taylor, *Rutherford Appleton Laboratory Report* RAL-84-120 (1984).

[63] *ISIS'97 Rutherford Appleton Laboratory Report*, TR-97-050 (1997).

[64] R.J. Newport, B.D. Rainford, R. Cywinski (Editors), *Neutron Scattering at a Pulsed Source*, Adam Hilger (1988). Equations given in chapter 10 for absorption and multiple scattering corrections were implemented using Monte-Carlo code (for the case of spherical and finite cylinder samples) by W.G. Marshall.

[65] D.S. Sivia, Rutherford Appleton Laboratory, Chilton, Didcot, Oxfordshire, *Private communication.*

[66] G.J. Piermarini, C.E. Weir, *J. Research NBS* **66A** (1962) 325 - 331.

[67] S. Klotz, J.M. Besson, G. Hamel, R.J. Nelmes, J.S. Loveday, W.G. Marshall, *High Pressure Research* **14** (1996) 249 - 255.

[68] W.G. Marshall, D.J. Francis, *J. Appl. Cryst.* **35** (2001) 122 - 125.

[69] PGPLOT Graphics Subroutine Library, T.J. Pearson, June 1989.

[70] RAFMD (1984) a program by A. Filhol of the Institut Laue-Langevin, Grenoble, France. This was based on an original program CODRUB by P.J. Ellis and A.W. Pryor, *Aus. A.E.C. AEEC/E Rep.191* (1968) (The version of the program used in this thesis had been further adapted from the original code for use on the SXD diffractometer by C.C. Wilson, ISIS Facility, Rutherford Appleton Laboratory, Chilton, Didcot, OXON, OX11 0QX).

[71] W.I.F. David, M.W. Johnson, K.J. Knowles, C.M. Moreton-Smith, G.D. Crosbie, E. P. Campbell, S.P. Graham, J.S. Lyall *Rutherford Internal Report* RAL-86-102 (1982).

[72] G.E. Bacon, R.S. Pease, *Proc. Roy. Soc.* **A220** (1953) 397 - 421.

[73] R.J. Nelmes, *Ferroelectrics* **24** (1980) 237 - 245.

[74] R.J. Nelmes, *Ferroelectrics* **71** (1987) 87 - 123.

[75] Y. Kobayashi, S. Endo, K.Koto, T. Kikegawa, O. Shimamura, *Phys. Rev. B* **51** No. 14 (1995) 9302 - 9305.

[76] E. Matsushita, T. Matsubara, *T. Prog. Theor. Phys.* **67** (1982) 1 - 19.

[77] E. Rapoport, *J. Chem Phys.* **53** (1970) 311 - 314.

[78] Z.X. Bao, V.H. Schmidt, F.L. Howell, *J. Appl. Phys.* **70** (1991) 6804.

[79] R.J. Nelmes, Z. Tun, W.F. Kuhs, *Ferroelectrics* **71** (1987) 125 - 141.

[80] W.H. Zachariasen, *Acta Crys.* **23**, (1967) 558 - 564.

[81] W. Jauch, A.J. Shultz, R.J. Schneider, *J. Appl. Crys.* **21** (1988) 975 - 979.

[82] S. Tomiyoshi, M. Yamada, H. Watanabe, *Acta. Crys.* **A36** (1980) 600 - 604.

[83] S. Klotz, J.M. Besson, M. Braden, K. Karch, P. Pavone, D. Strauch, W.G. Marshall, *Phys. Rev. Lett.* **79** (1997) 1313 - 1316.

[84] S. Klotz, Physique des Milieux Condensés, Université Pierre et Marie Curie, Paris, *Private communication.*

[85] H. Ahsbahs, R. Dorwarth, W.F. Kuhs, D. Londono, *High Pressure Research* **5** (1990) 807 - 809.

[86] W.F. Kuhs, H. Ahsbahs, D. Londono, J.L. Finney, *Physica B* **156** & **157** (1989) 684 - 687.

[87] D. Braithwaite, I.N. Goncharenko, J.-M. Mignot, A. Ochiai, O. Vogt, *Europhys. Lett.* **35** (1996) 121 - 126.

[88] L. Merrill, W.A. Bassett, *Rev. Sci. Inst.* **45** (1974) 290 - 294.

[89] H.K. Mao, P.M. Bell, *Carnegie Institute Year Book* **79** (1980) 409 - 411.

[90] D.A. Keen, C.C. Wilson, *RAL Technical Report* RAL-TR-96-083 (1996).

[91] G.J. Piermarini, S. Block, J.D. Barnett, R.A. Forman, *J. Appl. Phys.* **46** (1975) 2774 - 2780.

[92] H.K. Mao, P.M. Bell, *J. Geophys. Res.* **91** (1986) 4673 - 4676.

[93] W.L. Vos, J.A. Schouten, *J. Appl. Phys.* **69** (1991) 6744 - 6746.

[94] C.C. Wilson, ISIS Facility, Rutherford Appleton Laboratory, Chilton, Didcot, Oxfordshire, *Private communication.*

[95] D.W. Davidson, *Clathrate Hydrates* in *Water a Comprehensive Treatise* Ed. F. Franks, Plenum Press NY (1973) 115 - 234.

[96] D. Londono, J.L. Finney, W.F. Kuhs, *J.* Chem. Phys. **97**, (1992) 547 - 552.

[97] J.S. Loveday, R.J. Nelmes, M. Guthrie, D.D. Klug, J.S. Tse, *Phys. Rev. Lett.* **87** (2001) 215501-1 - 215501-3.

[98] Vos, W.L., Finger, L.W., Hemley, R.J., Mao, H-K, *Phys. Rev. Lett.* **71** (1993) 3150 - 3153.

[99] B.H. Bransden, C.J. Joachain *The Physics of Atoms and Molecules*, Longman (1982).

[100] J.R. Patterson, Y.K. Vohra, S.T. Weir, J. Akella, *J. Nanosci. Nanotech.* **1** (2001) 143 - 147.

Appendix A

The Neutron Properties of some Commonly Used Materials

In the design of any neutron diffraction instrument, it is important to understand how the radiation will interact with the different materials used in construction. The following list does not claim to be exaustive, but focuses on the materials relevant to this thesis. It summarises some neutron properties (for thermal and sub-thermal neutrons) and gives a basic description of the material properties

Cross-sections are all in *barns* for 2200 ms^{-1} neutrons and have been taken from the 'Special Feature' section of *Neutron News* **3** No. 3 (1992) 29 - 37. They are also available on the internet at

http://www.ncnr.nist.gov/resources/n-lengths/

Al A general purpose construction material, aluminium has the advantage of being both easy to machine and having extremely favourable neutron properties. It has a very low absorption of cross-section for neutrons ($\sigma_{abs}^{Al} = 0.231$ and $\sigma_{inc}^{Al} = 0.0082$)and for this reason it can be used, for instance, to cover the end of evacuated beam-guides and as the material from which the active

section of the methane moderator is constructed. Aluminium does have a larger coherent scattering cross-section with $\sigma_{coh}^{Al} = 1.503$ this is detectable, for example, in the Bragg edges present in the methane-moderator flux profile.

Fe Components that must bear significant loads, for example the PE cell, are composed of steel. The main constituent, iron, scatters more strongly than Al $\sigma_{coh}^{Fe} = 11.62$ and care must be taken to shield such components from the incident beam. It also has a significant absorption cross-section ($\sigma_{abs}^{Fe} = 2.56$ and $\sigma_{inc}^{Fe} = 0.4$

Cd Is an all purpose shielding material. Even a small thickness (< 0.25 mm) is effectively opaque at the neutron energies used in diffraction work. It has the advantage of being extemely malleable, and this makes it extremely useful for improvising pieces of shielding. Cadmium is unsuitable for exposure to the direct beam as its activation is long-lived. Another important drawback is that it is highly toxic, and care must be to minimise contact with it. The toxic danger is especially prevalant at temperatures above 130° C when harmful vapour can be released.

Boron Carbide and Boron Nitride Boron is also a very highly absorbing material, with an absorption cross-section of 767 *barns*. It is generally used in one of two forms, the nitride (BN) it is a white, smooth solid which is easily machined and the carbide is black and hard and is used mixed in a synthetic base. Both are useful materials as collimator of the direct beam as, whilst they strongly activate, this activity drops to almost zero within a few seconds of removal form the beam.

Ti:Zr alloy Titanium has a negative scattering length of -3.438 *barns* and Zirconium a positive length of 7.16 *barns*. When mixed in the correct proportions (approximately 2:1) these cancel out, and the material becomes completely null scattering. This gives it an important advantage as a gasket material,

in that there is no effect of Bragg edges, which are extremely difficult to model. A drawback is that the scattering is still relatively strong, and results as incoherent background scatter. Ti:Zr alloy also has a significant absorbing effect

Appendix B

Full Listing of Software

The following pages contain details of the FORTRAN software written to aid the work of this thesis. As they constitute, in total, nearly 6500 lines of code, these programs represent a significant proportion of the project. The names of each routine, along with their purpose are given. Additionally, external subroutines used are also listed along with an explanation of their use.

The source code is included on the attached CD-ROM in Appendix C.

ROUTINE	SUBROUTINE	LINES OF CODE	EXTERNAL LINKS	PURPOSE
PEARL PEAK INTEGRATION SOFTWARE				
SCAN 1.8		625	GETPRLSETUP GECSPEC INTSPEC GRAB XYGRAPH DEVINDER FNGEXP CREFOBS LMAP HEXTOINT	Main routine for integrating peaks scanned on the PEARL diffractometer. Successive versions include modifications of the peak integration (a history of the earlier versions is included in the source code).
	CREFOBS	115	LMAP TTHETCALC	Takes as input: Integrated peak intensity, associated uncertainty and spectrum number and returns a corrected structure factor with uncertainty.
	LMAP	134		Takes as input: spectrum number and returns 2 of element.
	TTHETCALC	110	PRLCOORDS	Takes as input: spectrum number and returns 2 of element and distance from sample to detector.
	PRLCOORDS	29		Takes as input spectrum number and returns coordinates (in pixels) of element for PEARL SXM.
	GETPRLSETUP	62		Reads calibrated detector positions (gamma angle and sample-detector distance) from file into common block: SETUP.
	XYGRAPH	82	PGPLOT routines	Takes as input: data set x,y, (y) and plots 2d graphs.
	XYXYGRAPH	97	PGPLOT routines	Takes as input: data set x1,y1, (y1) and data set x2,y2, (y2). Plots both on a 2d graph.

ROUTINE	SUBROUTINE	LINES OF CODE	EXTERNAL LINKS	PURPOSE
	INTSPEC	97	GRAB ISIS GET routines	Takes as input: name of raw data file, spectrum number and TOF limits. Returns integrated neutron counts and error between these limits.
	GECSPEC	102	GRAB ISIS GET routines PKGEXP	Takes as input: name of raw data file, spectrum number and TOF limits. Fits a GEC function between these limits and returns the area under the GEC and the error.
	HEXTOINT	44		Converts hex input to decimal integer.
	DEVINDER	34	PKGEXP	Call to D.S. Sivia's routine PKGEXP. Takes data set x,y, (y) and limits on x and returns the area and error of a GEC fit between these limits.
	GRAB	157	ISIS GET routines	Slightly modified version of software written by W.G. Marshall to extract neutron counts direct form ISIS raw files.
PEARL DATA VISUALISATION				
LONGDIS2		570	SUB_SUMADD2 PGPLOT routines ISIS GET routines PLOT	Takes as input: several consecutive PEARL run numbers. It then plots colour contour maps of the number of neutron counts integrated over a user defined TOF range and each run. These raw counts are corrected by the wavelength independent efficiency of each particular element. Either single modules or the entire longitudinal bank can be displayed.

ROUTINE	SUBROUTINE	LINES OF CODE	EXTERNAL LINKS	PURPOSE
	SUB_SUMADD	187	INTSPEC	Performs integration for LONGDIS2.
PRLTRAN		77		Applies different absorption and extinction corrections to integrated reflections measured on PEARL and stored in fixed format input files.
SXD PEAK VISUALISATION AND INTEGRATION SOFTWARE				
MINT1		702	GETNOR GETNOROLD GETSETUP DISQUARE SUMSQUARE GRAB COORDS COORDSII	Main visualisation and integration software for SXD data. Input is a file with the standard USE format. Output is also fixed format containing hkl indices, integrated structure factors, associated uncertainties and spectrum numbers for each reflection.
	GETNOR	36		Reads SXD wavelength independent efficiencies into common block: EFFIC.
	DISQUARE	262	PGPLOT routines GRAB	Displays grid of nine spectra (between the TOF limits of the diffraction peak) comprising the peak centroid and the surrounding eight adjacent elements. Offers the option of re-centring the peak centroid and excluding spectra. The selected spectra are then integrated into a single x,y, (y) data set which is sent to SUMSQUARE.

ROUTINE	SUBROUTINE	LINES OF CODE	EXTERNAL LINKS	PURPOSE
	SUMSQUARE	628		Integrates the selected spectra applying appropriate corrections for efficiency. Allows selective constrainment of the GEC fitting routine to permit fits of weak under-determined peaks.
	COORDSII	29		As PRLCOORDS but set up for SXD detector modules.
	GETSETUP	76		Reads calibrated detector parameters (gamma and distsd) from file.
ANGLEII		178	GETSETUP	Calculates the angle between two SXD detector elements given their spectrum numbers. Used as an aid to manual indexing.
CONE		127		Given a lattice and the hkl index of a reflection, this program searches for all reflections lying at a given angle (subject to a user defined tolerance). Used as an aid to manual indexing on SXD.
FOCPKSII		237	GETSETUP TTHETCALC	Reads in the output from the SXD peaksearch routine and converts TOF to d-spacing.
	REDSPC	26		Converts an SXD spectrum number to a 'reduced' number that begins at 1 and counts up to 4096 for each detector module.

ROUTINE	SUBROUTINE	LINES OF CODE	EXTERNAL LINKS	PURPOSE
SXDPAR		34	TTHETCALC	Given an SXD spectrum number, returns 2 and the distance from sample to detector for particular detector element.
SXMPAR		52	TTHETCALC	As SXDPAR, but works for the PEARL SXM.
	SXDTOFCONV	23	GETSETUP TTHETCALC	Given an SXD spectrum number and the TOF of a reflection, returns either its d-spacing or wavelength.
SXDVAN		254	INTSPEC	Modified from SUMADD2 to work for SXD data. Used to generate vanadium correction file for SXD.
VISEQV		209	REDSPC COORDSII PGPLOT routines	Provided graphical display of equivalents observed in SXD runs.
D2D2O GASKET ATTENUATION CORRECTION				
GASKET		251	GETSETUP BASF0 GASANG	Reads in fixed format input file pre-sorted into groups of equivalent reflections. This contains run-number, HKL indices, F_{obs}, (F_{obs}), spectrum number and wavelength. Outputs HKL indice, Fobs and (F_{obs}) - both corrected for gasket attenuation - and wavelength in a format suitable for input to the SHELX refinement software package.
	BASF0	221	GETDATA	Attempts to calculate inter-run scale factors based on the intensites of measured equivalents measured in different runs.

ROUTINE	SUBROUTINE	LINES OF CODE	EXTERNAL LINKS	PURPOSE
MISCELLANEOUS SOFTWARE FOR ANALYSING SXD DATA				
HKLSORT		177		Given the output of MAKEPLUS, a variety of HKLSORT type programs were written to arrange these data in blocks of equivalent reflections according to different Laue symmetries.
CHECKDIAM2		161		Checks each reflection in the USE file for overlap with an indexed anvil reflection.
MAKEPLUS		187		The pre-existing SXD software for converting integrated intensities to F_{obs} outputs only HKL indices F_{obs}, (F_{obs}) and wavelength. In order to attempt the gasket absorption correction, it was necessary to recover the spectrum number, TOF, run-number, and detector module number and store it in a single fixed format file. This is achieved by MAKEPLUS which reads the information from the original USE files containing the integrated intensities.

Published Work

28 December 2001

ELSEVIER

Chemical Physics Letters 350 (2001) 459–465

CHEMICAL PHYSICS LETTERS

www.elsevier.com/locate/cplett

High-pressure transitions in methane hydrate

J.S. Loveday *, R.J. Nelmes, M. Guthrie

Department of Physics and Astronomy and Centre for Science at Extreme Conditions, The University of Edinburgh, James Clerk Maxwell Building, The Kings Buildings, Mayfield Rd, Edinburgh EH9 3JZ, Midlothian, Scotland, UK

Received 8 August 2001; in final form 5 November 2001

Abstract

Three recent studies of the high-pressure transformations of methane hydrate [Chem. Phys. Lett. 325 (2000) 490; Proc. Natl. Acad. Sci. 97 (2000) 13484; Nature 410 (2001) 661] have reported apparently different behaviours. Detailed comparison of our X-ray and neutron diffraction data with those obtained in earlier work shows that there is in fact consistent behaviour on isothermal compression at room temperature with a transition from the clathrate I structure hydrate to a hexagonal hydrate with an unknown structure at ~0.9 GPa. © 2001 Published by Elsevier Science B.V.

1. Introduction

Methane hydrate is considered a model system for the study of hydrophobic hydrocarbon-water interactions [1]. It is also widely found in nature on Earth [2] and is believed to have been the dominant methane-bearing phase in the outer solar nebula during planet formation [3]. High-pressure studies probe the methane–water interaction as a function of the intermolecular distance and are a powerful probe of this interaction. Information on behaviour at high pressure is also directly relevant to the formation models of Saturn's moon Titan [3]. However, until recently the stability of methane hydrate at high pressure was poorly understood. At low pressure methane and water form the structure-I methane hydrate (SIMH) shown in Fig. 1, with methane filling two different types of cages in a framework of H-bonded water molecules. Calculations suggested that this structure would become unstable with respect to methane and water at ~1.2 GPa where the hydrate decomposition curve intersects with the water freezing curve [4]. More recent differential thermal analysis studies [5] found a triple point at ~0.6 GPa and ~315 K and stable hydrate phases up to 1.5 GPa but again considered that the hydrate would become unstable where its decomposition curve intersected the ice freezing line [5].

The first diffraction studies at high pressure have been reported recently by Hirai et al. [6,7], and appeared to show that methane hydrate decomposes progressively into water and methane over the range ~1–2 GPa. These studies found changes occurring between 0.7 and 1.0 GPa, the appearance of ice VI at 1.5 GPa, the transformation of ice VI to ice VII accompanied by the appearance of solid methane I at 2.1–2.2 GPa, and complete decomposition into ice VII and methane

* Corresponding author. Present address: Rutherford Appleton Laboratory, Didcot, Oxon OX11 0QX, UK. Fax: +44-0-1235-445720.

E-mail address: J.Loveday@ed.ac.uk (J.S. Loveday).

0009-2614/01/$ - see front matter © 2001 Published by Elsevier Science B.V.
PII: S0009-2614(01)01328-8

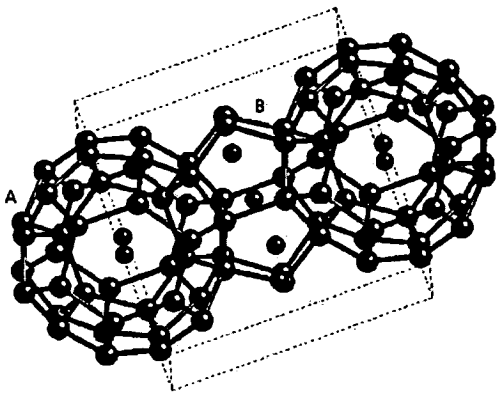

Fig. 1. Part of the structure of SIMH. The large water cages are labelled A and the small B. Methane molecules are shown within the cages.

I at 2.3 GPa. It was concluded that the non-ice phase remained SIMH at all pressures up to 2.3 GPa and the changes above 0.7 GPa were interpreted as the progressive emptying of methane from the smaller cages (see Fig. 1) producing free (liquid) methane. As said, solid methane I was not detected until the pressure reached 2.1–2.2 GPa.

More recently, two other studies have revealed significantly different behaviour. Our own neutron and X-ray studies of the compression behaviour along the room temperature isotherm have shown that methane hydrate transforms below 0.9 GPa to a new hydrate phase with a hexagonal or trigonal unit cell. Chou et al. [8] in X-ray and Raman studies reported a second cubic structure at pressures above 0.1 GPa and a transformation at 0.88 GPa and 19 °C [8, point D in Fig. 1] to a hexagonal form.

These three studies appear to show divergent behaviour. However, there are a number of inconsistencies in Hirai et al.'s interpretation. The deviation between their reported observed and calculated d-spacings for the SIMH structure is sometimes as large as 0.2 Å [6,7]. The pressure at which a diffraction signal from methane I is first seen, 2.1 GPa, is well above the known freezing pressure of methane of 1.3 GPa [1] [9–11]. And it also seems unlikely that both free ice and free methane would be produced at the same time: the Gibbs phase rule implies that coexistence of methane, ice and methane hydrate only occurs on a line in pressure, temperature and composition space, and that would have to coincide with the room temperature isotherm in the whole pressure range 0.7–2.1 GPa. Hirai et al. [6] note this and speculate that the behaviour may be the result of metastability. But, as they also state, the transitions observed are reversible which makes metastability unlikely. Furthermore the co-existence of all three phases at room temperature in the range 0.7–2.1 GPa is inconsistent with Dyadin et al.'s [5] measurements of the decomposition line.

In this Letter, we report further details of our studies [12] which show that Hirai et al.'s results are fully consistent with the existence of a new methane hydrate phase above a pressure of 0.88 GPa at 19C (for the hydrogenous from) [8].

2. Experimental

Samples of H- and D-SIMH were produced by adsorbing methane into ice at −20 °C as described by Handa [13]. Diffraction studies confirmed full occupancy of the cages. The samples were loaded at ~100 K into a Paris–Edinburgh pressure cell [14] for the neutron studies and a Merrill–Bassett diamond-anvil cell for the X-ray studies. The cells were sealed by applying pressure and warmed to room temperature. Diffraction patterns collected at 0.5 GPa confirmed the loaded samples to have the SIMH structure and full cage occupancy within an uncertainty of 5%. Neutron diffraction studies were carried out on the PEARL beamline [15] of the UK neutron facility, ISIS, at the Rutherford Appleton Laboratory, and X-ray studies were carried out using image-plate techniques [16] on station 9.1 at the UK synchrotron, SRS, at Daresbury Laboratory and on beamline ID9 of the ESRF.

3. Results

Fig. 2 shows the neutron diffraction patterns collected from deuterated (D) methane hydrate and X-ray diffraction patterns from hydrogenous

[1] Hirai et al. [6] quote a freezing pressure of 1.68 GPa for methane citing Refs. [10,11]. Neither of these studies aimed to measure the melting curve of methane. Ref. [10] discusses growth of a single crystal at a freezing point of 1.59 GPa, somewhat higher than the 293 K value of 1.3 GPa [9] which is also the value quoted and referenced in [11].

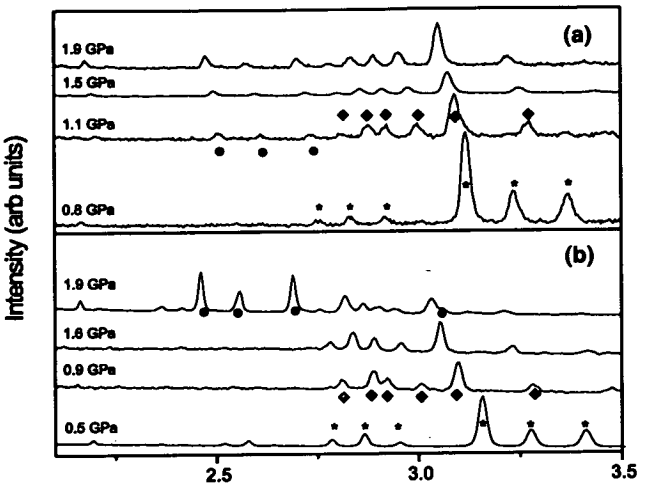

Fig. 2. Diffraction patterns of methane hydrate as a function of increasing pressure at room temperature: (a) neutron patterns collected from deuterated (D) methane hydrate; (b) X-ray patterns collected from hydrogenous (H) methane hydrate. The peaks are marked for SIMH (*), MH-II (◆) and ice VI (•).

(H) methane hydrate as a function of increasing pressure at room temperature. As noted, the initial patterns can be fitted with the established type-I clathrate SIMH structure [17]. The pattern shown at 0.9 GPa for the H-hydrate and the non-ice VI peaks in the pattern shown at 1.1 GPa for the D-hydrate can be indexed with a primitive trigonal or hexagonal unit cell ($a = 11.7911(12)$ Å, $c = 9.9210(10)$ Å and $v = 1194(3)$ Å^3 at 1.7 GPa [12]). There are significant differences in relative d-spacings as well as intensities compared with the (cubic) SIMH pattern, and it is clear that there has been a transformation to a new hydrate phase, methane hydrate II (MH-II) [12].

For both H- and D-hydrates, the transformation to MH-II is accompanied by the appearance of free water or ice indicating that MH-II is richer in methane than SIMH. Hence, rather than becoming methane poorer with increasing pressure as Hirai et al. suggested, methane hydrate becomes methane richer. In the case of the D-hydrate the transition pressure is above the freezing pressure and water released is in the form of solid ice VI (Fig. 2a), the stable ice phase at this pressure and temperature. The slightly lower transformation pressure of 0.88 GPa for the H-hydrate at room temperature means that released water will be liquid [8,18]. Surprisingly it remains liquid to well above the room-temperature freezing point of H_2O [8]: Fig. 3 presents another profile collected from hydrogenous MH-II at 1.5 GPa which contains no ice peaks but, as shown in the inset, a detectable broad diffraction feature attributable to a liquid phase. On further compression, this liquid feature disappeared and ice VI peaks appeared between 1.6 and 1.9 GPa showing that the liquid is water. Similar behaviour was observed in a second sample. On decompression, the ice VI peaks disappeared between 1.2 and 0.8 GPa – consistent with the melting line of ice VI [18]. It thus appears that the liquid observed is indeed water and that the delay in freezing on upstroke is a kinetic effect rather than a thermodynamic shift in the melting line resulting from – for example – dissolution of methane in water [2]. No evidence of free methane was observed for either the D or H hydrates.

4. Discussion

The behaviour we observe is essentially identical with that reported by Hirai et al. [6,7]. In [6] they report changes in intensity starting at 0.7

[2] The fact that melting of ice VI is observed at the correct pressure [8,18] whereas freezing is delayed suggests that residual dissolved methane is expelled from the water on freezing so that the ice VI formed is methane free.

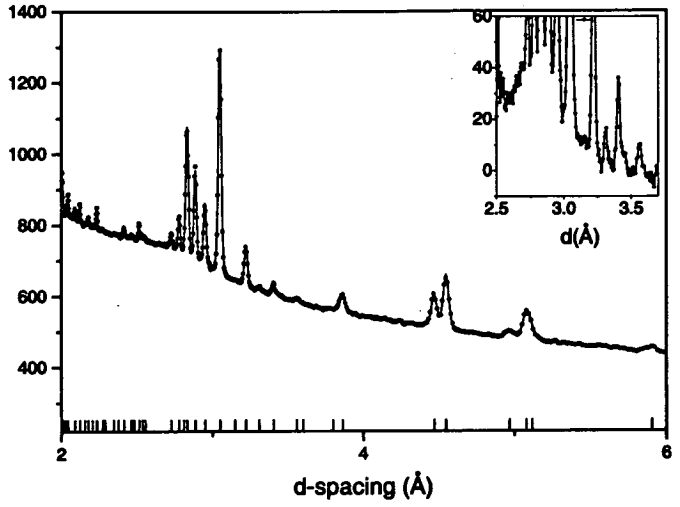

Fig. 3. The results of Rietveld least-squares profile refinement of X-ray data taken from H-hydrate at 1.5 GPa using the hexagonal MH-II unit cell described in the text. The observed data are plotted as dots and the calculated pattern as a solid line. Since the full structure of MH-II is unknown the profile refinement treated the intensity of reflections as least squares variables (the Pawley method [19]). The tick marks at the bottom of the plot denote the positions of these reflections. The inset shows the observed data in the region between 2.5° and 3.75° expanded to reveal a broad diffuse feature due to scattering from liquid water. (A linear background has been subtracted from the data in the inset.)

GPa. In fact, [6, Fig. 2] (or [7, Fig. 4]) shows a change in apparent compressibility between data points at 0.7 and 1.0 GPa. This agrees with our location of the transition from the SIMH structure in H-hydrate at a pressure between 0.5 and 0.9 GPa, and with the transition pressure of 0.88 GPa and 19 °C GPa reported by Chou et al. [8]. It should be noted here that the triple point observed at 0.66 GPa and 315 K by Dyadin et al. [5] almost certainly corresponds to the intersection of the SIMH to MH-II transition with the decomposition line. (The pressure of the SIMH to MH-II transition is thus significantly temperature dependent.) Fig. 4a shows a comparison of the peak positions at 1.5 GPa reported in [7] and our neutron data at 1.5 GPa – neutron data are used as ice VI did not appear in our X-ray data until the slightly higher pressure of 1.6–1.9 GPa (Fig. 2b). The positions of the observed d-spacings given in [7, Table 1] are marked (|) for peaks they assigned by Hirai et al. to SIMH and (▲) for peaks they assigned to ice VI. There is clearly a very good correspondence between their observed positions and our data. Fig. 4b reproduces the same data but the markers (|) now denote the *calculated* positions of the peaks listed in [7, Table 1]. The Miller indices of the SIMH peaks are shown to assist in relating the calculated positions with the observed positions shown in Fig. 4a. As can be seen, there are major discrepancies, with differences up to several peak widths in some cases. This is most striking for the (3 2 0) reflection, as marked in Fig. 4a. It is not possible to obtain any satisfactory profile refinement of the data with a mixture of ice VI and SIMH. A conclusive demonstration that MH-II is quite different from SIMH can be obtained with the ice-free pattern in Fig. 3. A best-possible Rietveld fit to these data with the SIMH structure is shown in Fig. 4c. There is clearly no fit at all, whereas the hexagonal MH-II unit cell fits very well indeed (Fig. 3). Fig. 4c also reveals that Hirai et al. mis-assigned the peak at ~3.05 Å as the ice VI (2 0 0) reflection which is close to this position (see Fig. 4b), but weak; the observed strong reflection is mostly from MH-II.

A further point of (remarkably) detailed agreement is that the results obtained by Hirai et al. are consistent with the same delayed freezing as we observe for the free water produced by the change in H-hydrate structure at ~0.9 GPa. They report the apparent change in compressibility which corresponds to the transition from SIMH to MH-II at

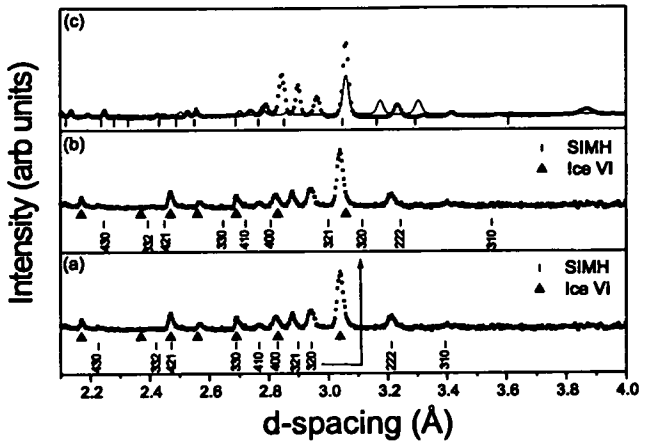

Fig. 4. (a) Neutron data collected from D-hydrate at 1.5 GPa. The symbols show the *observed* positions of reflections from SIMH (|) and ice VI (▲) taken from [7, Table 1]. (b) The same neutron data and the *calculated* positions of reflections from SIMH (|) and ice VI (▲) taken from [7, Table 1]. To establish a correspondence between these positions and the observed values shown in (a), the Miller indices for the SIMH markers are shown. (c) A Rietveld profile refinement of X-ray data at the same pressure – where ice VI is absent – using the SIMH structure.

this pressure, but do not report observing ice VI until 1.5 GPa [6,7] – close to the pressure where we observe freezing of the water. It is interesting to note that they report observing fluid in the pressure cell which they attribute to the presence of free methane [7]. It seems that this must in fact have been water. The fact that delayed freezing is observed in at least three samples, in work by two separate groups, suggests that this behaviour is intrinsic to methane hydrate, perhaps as a result of small amounts of dissolved methane in the water.

Having shown that the behaviour observed by Hirai et al. is the same as we find, the question then arises as to how it may be reconciled with the observations of Chou et al. [8]. On the basis of the lattice parameters they give it is clear that the hexagonal phase they report is MH-II. However, they also report finding a cubic hydrate whose lattice parameters are close to those expected for the type II cubic clathrate structure above 0.1 GPa [8]. Neither Hirai et al. nor we find any evidence for such a phase. However, Chou et al. have only observed this phase in samples cooled from the melt [20] whereas we and Hirai et al. compressed isothermally at RT and so this difference in behaviour appears to be a genuine dependence on P-T path. Whether the SIMH or the type II clathrate structure is the stable form of methane hydrate above ~0.1 GPa. Both we and Hirai et al. observe that on decompression at RT MH-II transforms back readily to SIMH. Hence, it is possible that for methane hydrate the type II clathrate structure is a metastable form which is kinetically favoured by formation from the melt in the same way that ices XII and IV appear to be [22].

The structure of MH-II remains an unsolved question. The lattice parameters of MH-II are close to those of the structure H clathrate [21]. However, an acceptable fit could not be obtained using this structure to either the neutron or X-ray data, producing O···O distances as low as 2.0 Å. Analysis of the pair correlation (Patterson) function of MH-II shows it to be similar to that of structure H though with some significant differences. This suggests that the structure of MH-II is not that of structure H but may be closely related to it.

5. Conclusions

The observations of the three reported studies have been shown to be consistent for isothermal compression of methane hydrate at ambient temperature. The finding of a new hydrate structure above 0.7 GPa means that the room temperature behaviour is also now consistent with the measurements of the decomposition line [5]. The

studies raise a number of interesting questions for further work. The structure of the hexagonal MH-II remains unknown. Although its lattice parameters and diffraction pattern are similar to those of the structure-H clathrate this structure does not fit the data adequately and it appears likely that MH-II has a new cage structure which may be related to structure-H [21]. The reproducible superpressing of the water produced at the SIMH to MH-II transition raises the possibility of methane partitioning between the hydrate and the water. And further work is needed to settle decisively the question as to whether the clathrate I or II structure is the stable form of methane hydrate in the range from ~0.1 to 0.88 GPa.

Acknowledgements

We thank S.A. Belmonte, D.R. Allan, D.J. Francis and M. Hanfland for assistance with experiments and Y.P. Handa and D.D. Klug for sample preparation. This work is funded by the U.K. EPSRC and supported by the U.K. CLRC through access to beamtime at ISIS and SRS, and other resources. We also acknowledge support from the British Council via a Researcher Exchange Award and from the ESRF through the award of beamtime.

Note added in proof

Since the Letter was accepted for publication, three further studies of methane hydrate transitions at room temperature have been published. (1) Single-crystal visual and Raman studies by Shimizu et al. [23], in which they observed essentially the same transition sequence as we report in [12], with a transition from SIMH to MH-II at 0.9 GPa and from MH-II to MH-III at 1.9 GPa. (2) New X-ray and Raman studies by Hirai et al. [24] in which they report observing the transition from SIMH to MH-II (structure A in their notation) at 0.8 GPa, and attribute this substantial difference in behaviour from their earlier interpretation to kinetic effects. In fact, as we have shown, their earlier results are entirely consistent with the SIMH to MH-II transition. (3) A full structure determination by us [25] of MH-III. It is a methane dihydrate in which the methane occupies voids in an ice-Ih type of water framework. This is consistent with the new Raman results of Shimizu et al.

Hirai et al. now also observe the transition to MH-III (structure C in their notation) on slow compression, as we previously found [12], but depart from us and Shimizu et al. in reporting a further intermediate form (structure B in their notation) with very similar lattice parameters to MH-III stable between 1.6 and 2.1 GPa. Their basis for identifying this apparent new form appears to be (i) a broadening of the C–H stretching mode at 1.6 GPa and (ii) a splitting of peaks in the diffraction pattern above 2.1 GPa compared with the first appearance of a new phase in their diffraction data at 1.8 GPa. The broadening of the vibron is also observed by Shimizu et al. but their single-crystal data are of better quality than those of Hirai et al. and show that the broadening increases continuously across the entire stability field of MH-II from 0.9 to 1.9 GPa. Shimizu et al. find that this can be fitted as an increasing splitting of two C–H modes which correspond to different cage environments in MH-II, as they also observe in SIMH. Our diffraction data (see patterns d,e,f,g in Fig. 1 of [12]) show the splitting of the peak at ~2.8 Å with increasing pressure apparently attributed by Hirai et al. to a transition from structure B to structure C at 2.1 GPa, but all our patterns at 2.0 GPa (1.9 GPa in the case of H-hydrate) and above can be fitted with the same MH-III structure. The pressure variation of the unit cell parameters reveals that the increasing peak splittings simply arise from anisotropic compression of the unit cell and not a further structural phase transition. There thus appears to be no evidence in either the Raman data or the diffraction data for a new phase in the range 1.6–2.1 GPa. Such a phase would also be directly inconsistent with the visual data of Shimizu et al. Small differences in reported transition pressures among these studies are within calibration errors.

Shimizu et al. and Hirai et al. both report Chou et al. [8,20] as finding a transition from SIMH to a type II clathrate, and from that to MH-II. As already noted in our Letter (above), it has been clarified by Chou et al. [20] that the type II phase

appears only in samples cooled from the liquid, and no transition between the type II phase and either SIMH or MH-II has yet been reported. Furthermore, these authors [8] find the SIMH to MH-II transition at 0.88 GPa at room temperature, contrary to the 0.6 GPa quoted by Shimizu et al. Chou et al. [20] assert that their new (type II) phase is the equilibrium from above ~100 MPa at room temperature, though they explicitly show that they do not see this phase on compression at room temperature. The new work by Shimizu et al. throws useful light on this question. Up to the transition from SIMH to MH-II, they have liquid water present, and thus hydrostatic conditions. They report observing that the SIMH single crystal 'melted and disappeared into the surrounding water and at the same time new crystals [of MH-II] grew with increasing pressure'. At the least, this strongly suggests that MH-II is an equilibrium phase. Furthermore, we have shown (as have Hirai et al. too [6,7]) that MH-II transforms readily back to SIMH at 0.9 GPa – without any significant hysteresis. These observations and the complete absence of the new type II phase in any of the several independent experiments at room temperature add up to substantial evidence that the type II form is 'not' the equilibrium phase at room temperature.

All the reported behaviour over several independent studies is thus consistent with a transition from SIMH to hexagonal MH-II at ~0.9 GPa and then from MH-II to orthorhombic MH-III at ~1.9 GPa as the equilibrium behaviour at room temperature. The possibility that the type II form found by Chou et al. [8,20] is in fact the equilibrium phase between 100 MPa and 0.9 GPa needs to be finally resolved, though this may prove difficult. At a minimum, it would be helpful and interesting to know what the type II phase transforms to under increasing pressure, and whether it can be transformed to SIMH. A complete clarification of the behaviour of methane hydrate under pressure will require solution of both the MH-II and type II crystal structures. (We note that the new study by Hirai et al. supports our present conclusion that the structure of MH-II is not the same as structure H, though it appears to be rather similar to it.)

References

[1] G. Hummer, S. Garde, A.E. Garcia, M.E. Paulaitis, L.R. Pratt, Proc. Natl. Acad. Sci 95 (1998) 1552.
[2] W.S. Holbrook, H. Hoskins, W.T. Wood, R.A. Stephen, D. Lizarralde, Science 273 (1996) 1840.
[3] J.I. Lunine, D.J. Stevenson, Icarus 70 (1987) 61.
[4] J.I. Lunine, D.J. Stevenson, Astro J. Suppl. Ser. 58 (1985) 493.
[5] Y.A. Dyadin, E.Y. Aladko, E.G. Larionov, Mendeleev Commun. 1 (1997) 34.
[6] H. Hirai, T. Kondo, M. Hasegawa, T. Yagi, Y. Yamamoto, T. Komai, K. Nagashima, M. Sakashita, H. Fujihisa, K. Aoki, J. Phys. Chem. B 104 (2000) 1429.
[7] H. Hirai, M. Hasegawa, T. Yagi, Y. Yamamoto, K. Nagashima, M. Sakashita, K. Aoki, T. Kikegawa, Chem. Phys. Lett. 325 (2000) 490.
[8] I.M. Chou, A. Sharma, R.C. Burruss, J. Shu, H.K. Mao, R.J. Hemley, A.F. Goncharov, L.A. Stern, S.H. Kirby, Proc. Natl. Acad. Sci. 97 (2000) 13484.
[9] J.D. Grace, G.C. Kennedy, J. Phys. Chem. Solids 28 (1967) 977.
[10] R.M. Hazen, H.K. Mao, L.W. Finger, P.M. Bell, Appl. Phys. Lett. 37 (1980) 288.
[11] P. Hebert, A. Polian, P. Loubeyre, R. le Toullec, Phys. Rev. B 36 (1987) 9196.
[12] J.S. Loveday, R.J. Nelmes, M. Guthrie, S.A. Belmonte, D.R. Allan, D.D. Klug, J.S. Tse, Y.P. Handa, Nature 410 (2001) 661.
[13] Y.P. Handa, J. Chem. Thermodyn. 18 (1986) 915.
[14] R.J. Nelmes, J.S. Loveday, R.M. Wilson, J.M. Besson, S. Klotz, G. Hamel, S. Hull, Trans. Am. Cryst. Assoc. 29 (1993) 19.
[15] ISIS'97 Rutherford Appleton Laboratory Report, RAL-TR-97-050, 1997.
[16] R.J. Nelmes, M.I. McMahon, J. Synchr. Rad. 1 (1994) 69.
[17] C. Gutt, B. Asmussen, W. Press, M.R. Johnson, Y.P. Handa, J.S. Tse, J. Chem. Phys. 113 (2000) 4713.
[18] C.W.F.T. Pistorius, E. Rapopart, J.C. Black, J. Chem. Phys. 46 (1969) 5509.
[19] G.S. Pawley, J. Appl. Cryst. 14 (1981) 357.
[20] I.M. Chou, A. Sharma, R.C. Burruss, R.J. Hemley, A.F. Goncharov, L.A. Stern, S.H. Kirby, J. Phys. Chem. A 105 (2001) 4664.
[21] K.A. Udachin, C.I. Ratcliffe, G.D. Enright, J.A. Ripmeester, Supramolecular Chem. 8 (1997) 173.
[22] V.F. Petrenko, R.W. Whitworth, 'Physics of Ice', Oxford University Press, Oxford, UK, 1999, p. 272.
[23] H. Shimizu, T. Kumazaki, T. Kume, S. Sasaki, J. Phys. Chem. B (2001) in press.
[24] H. Hirai, Y. Uchihara, H. Fujihisa, M. Sakashita, E. Katoh, K. Aoki, K. Nagashima, Y. Yamamoto, T. Yagi, J. Chem. Phys. 115 (2001) 7066.
[25] J.S. Loveday, R.J. Nelmes, M. Guthrie, D.D. Klug, J.S. Tse, Phys. Rev. Lett. 87 (2001) 215501.

Transition from Cage Clathrate to Filled Ice: The Structure of Methane Hydrate III

J. S. Loveday, R. J. Nelmes, and M. Guthrie

Department of Physics and Astronomy and Centre for Science at Extreme Conditions, The University of Edinburgh, Edinburgh EH9 3JZ, United Kingdom

D. D. Klug and J. S. Tse

Steacie Institute for Molecular Science, National Research Council of Canada, Ottawa K1A 0R6, Canada

(Received 22 March 2001; published 31 October 2001)

The structure of a new methane hydrate has been solved at 3 GPa from neutron and x-ray powder diffraction data. It is a dihydrate in which a 3D H-bonded network of water molecules forms channels surrounding the methane molecules. The network is closely related to that of ice-I*h* and the methane-water system appears to be the first in which a cage clathrate hydrate is transformed into an ice-related hydrate (a "filled ice").

DOI: 10.1103/PhysRevLett.87.215501 PACS numbers: 62.50.+p, 61.12.Ld

The existence of inclusion compounds involving water and hydrophobic species such as common gases and hydrocarbon molecules has long been recognized [1]. The majority of these compounds—known as clathrate hydrates—adopt one of three structures where the included guest species occupies cages formed by H-bonded networks of host water molecules [2]. These structures are believed to be stabilized by repulsive interactions between the guest and host molecules and the H-bonded host networks have no obvious relationship with known ice structures [3]. The guest-host interactions make clathrate hydrates model systems for the study of hydrophobic interactions relevant to problems in biology [4] and fundamental understanding of the water potential [5]. In addition, clathrate hydrates of gases such as methane, oxygen, carbon dioxide, and nitrogen are widely found in nature. Their behavior and properties are crucial to the understanding of processes both on Earth and in the outer solar system [6,7]. Most clathrate hydrates require at most modest pressures (of the order of a few hundred bar) to be stable. Work at higher pressures has revealed new gas hydrates in the helium- and hydrogen-water systems [8,9]. Helium hydrate and the two hydrates of hydrogen have been termed clathrates [8,9], but do not adopt any of the cage structures which are either observed or predicted for clathrate hydrates [2]. Instead they have structures related to ice-II [$(H_2O)_6 \cdot H_2$ and $(H_2O)_6 \cdot He$] [8,9] and ice-I_c ($H_2O \cdot H_2$) [8], and thus differ markedly from the three widely adopted clathrate structures—in which the guest molecules occupy distinct cages whose diameters are much larger than the channels which connect the cages together. We will refer to these latter structures as "cage clathrates." In the helium and hydrogen hydrates the guest molecules occupy channels—whose diameters do not vary markedly along their length—within a water network which is related to a known ice structure. These new clathrate hydrates might therefore be more accurately termed "filled ices."

To date there is no obvious link between the cage clathrates and filled ices: hydrogen and helium are not known to form cage clathrates and—although Raman and differential thermal analysis studies in the pressure range 0–3 GPa have revealed evidence of high-pressure transformations in argon, methane, neon, and nitrogen hydrates [10–14]—there has been no direct demonstration of new hydrate structures in any cage-clathrate-forming system [13]. Now, in methane hydrate (MH), we have found structural transformations from the low-pressure cage type-I clathrate form, MH-I [15], to two new hydrate phases, MH-II at ~1 GPa and then MH-III at ~2 GPa [16]. We show that the structure of MH-III can be viewed as a filled ice, and thus the methane-water system links the two classes of clathrate hydrates for the first time.

Samples of both hydrogenous (for x-ray studies) and fully deuterated [17] (for neutron diffraction studies) methane hydrate were produced by adsorbing methane into ice at 250 K as described by Handa [18]. Samples were loaded into a Merrill-Bassett diamond-anvil cell for the x-ray studies and a Paris-Edinburgh pressure cell [19,20] for the neutron studies at ~100 K. The cells were then sealed and warmed to room temperature. The pressure was increased from the initial sealing value of ~0.5 GPa to ~1.9 GPa. The deuterated samples transformed readily to MH-III when increased above this pressure, while in hydrogenous samples MH-III formed slowly over the course of ~12 h [16] at ~1.9 GPa. Neutron diffraction studies were carried out on the PEARL beam line of the U.K. neutron facility, ISIS, at the Rutherford Appleton Laboratory, and x-ray studies were carried out using image-plate techniques [21] on station 9.1 at the U.K. synchrotron source, SRS, at Daresbury Laboratory.

Figure 1 shows the diffraction patterns collected from samples of MH-III. Density considerations imply that MH-III has a 2:1 water-methane ratio [16]. Because the initial MH-I has a 5.75:1 water-methane ratio, these patterns are dominated by scattering from the ice VII that is formed by the 3.75 free water molecules released for every two in the MH-III. However, numerous peaks from MH-III can be identified. With the exception of the two

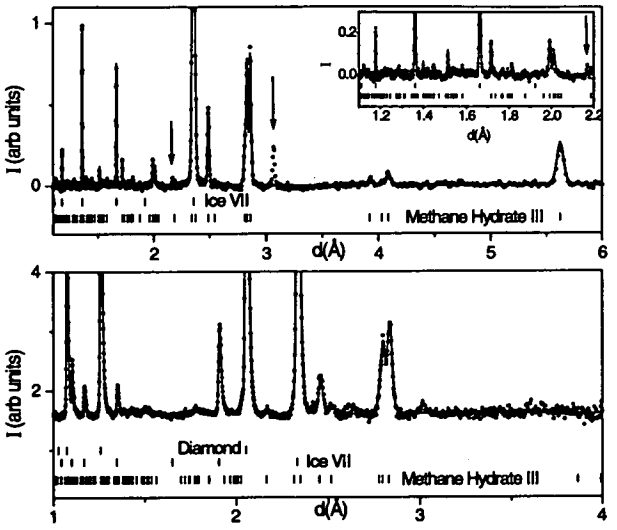

FIG. 1. Data collected from ice-VII and MH-III at 3.0 GPa and room temperature with x-rays (upper plots) and neutrons (lower plot). The inset reproduces the short d-spacing part of the x-ray pattern with an expanded scale. The observed data are shown as dots and the calculated profile as a solid line. The tick marks denote the calculated positions of the diffraction peaks from MH-III, ice-VII, and—in the case of the neutron data—scattering from the sintered-diamond anvils. The arrows in the upper plot and inset mark two additional peaks discussed in the text.

arrowed peaks in the x-ray pattern, all peaks observed can be indexed as MH-III, ice-VII, or sintered diamond from the pressure cell (in the neutron case). (The arrowed peaks do not move with pressure at the same rate as those from ice-VII or MH-III and cannot be indexed as methane [22]. They are attributed to a further minority methane hydrate phase.) The systematic reflection absences are consistent with space groups *Imcm* and *I2bm*. Density considerations require four methane molecules in the unit cell and so *I2bm* was chosen as the initial space group because it has the lowest symmetry fourfold site. Initially, the methane molecules were placed as far apart as possible on 1/4, 0, 0 sites. The oxygen atoms were then found from Fourier difference maps. Further refinements could be made stable only by fixing the oxygen atoms at $x = 1/4$. This implies that the symmetry of the heavy-atom structure is *Imcm*.

Each oxygen atom has four neighboring oxygen atoms at a plausible distance to be hydrogen bonds, ~2.8 Å, and space group *Imcm* implies that these hydrogen bonds be disordered—four half-occupied H(D) sites around each oxygen atom. However, a stable fit to the neutron data could not be obtained using a proton-disordered structure and so a number of possible proton-ordered structures were explored. Only one maintains the b-c mirror planes of the heavy-atom structure. This arrangement, in space group *Pmcn*, has two nonequivalent water molecules. The atoms of one type of molecule all lie in the b-c mirror plane so that, for example, oxygen atom 1 in Fig. 2(a) donates H bonds to atoms 1′ and 6. The second type of molecule has its H atoms related by reflection in the b-c mirror plane, such as oxygen atom 2 which donates H bonds to atoms 1 and 3. Fits using this structure were stable for both the neutron and x-ray data, and showed a marginal improvement of the fit to the neutron data but no improvement of the fit to the x-ray data. Thus the evidence for a proton-ordered structure is marginal but it cannot at present be ruled out. Full resolution of the question of proton ordering is likely to require neutron data from a sample composed solely of MH-III, if a way can be found to make such a sample. (As explained, MH-III samples made by compressing MH-I unavoidably contain a large amount of free ice.) However, the state of proton ordering does not significantly alter the structure and the conclusions to be drawn. The final refinements [23] shown in Fig. 1 and the distances in Table I were obtained using a proton-disordered structure in space group *Imcm*. Also included were four H(D) atoms placed on the C site with a large thermal motion to approximate the scattering from the presumed rotationally disordered methane molecules. As can be seen, the quality of the fits is good and the interatomic distances (Table I) are plausible.

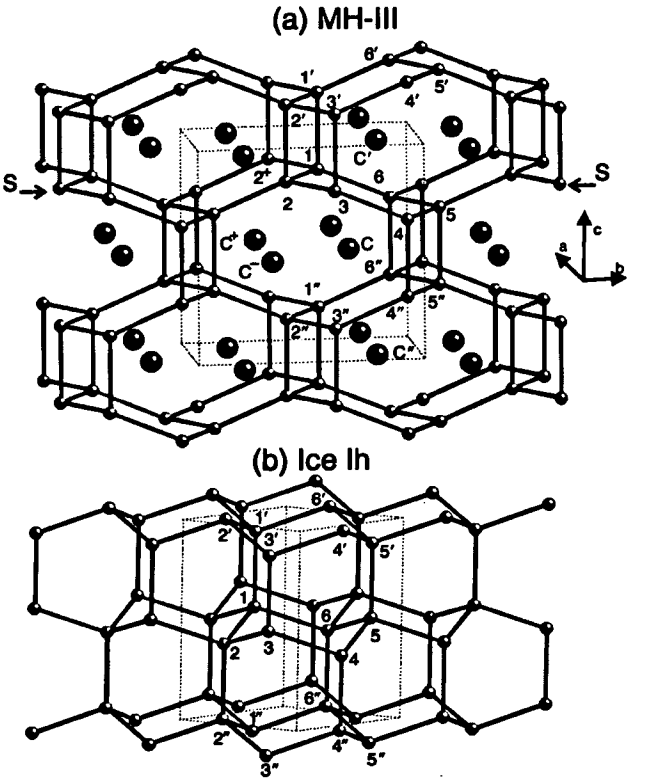

FIG. 2. The structure of (a) MH-III and (b) ice-Ih viewed perpendicular to their c axes. The smaller spheres are O atoms of the water network and the lines denote H bonds. The larger spheres in (a) are the methane molecules. MH-III is viewed approximately along its a axis and ice-Ih is viewed approximately along a [110] direction. A given symbol with single, double, or no prime denotes atoms related by translation along the c axis; superscripts + and − in (a) mark related atoms displaced along $\pm a$.

TABLE I. Selected bond lengths in MH-III at 3.0 GPa.

From	To	Length Å
C	C′, C″	4.053(6)
C	C^+, C^-	3.852(21)
O1	O1′	2.811(10)
O1	O6	2.807(14)
O1	O2, $O2^+$	2.783(9)
C	O4, O6, O4″, O6″	3.297(10)
C	O2, O2″	3.359(13)
C	O5, O5″	3.544(4)
C	O1, O3, O1″, O3″	3.552(4)

The heavy-atom structure of MH-III is remarkably similar to that of ice-I*h* when viewed along the *c* axes (Fig. 3). The H-bonded water network is composed of puckered *a*-*b* sheets of edge-sharing six-membered rings of water molecules—such as *S* in Fig. 2—which are cross linked along *c*. The rings form hexagonal channels running along the *c* axis, and the methane molecules sit between the *a*-*b* sheets close to the axis of these channels. At first glance the structures look significantly different when viewed perpendicular to *c* (Fig. 2). However, closer inspection of the rings (for example, those labeled 1, 2, 3, 4, 5, and 6 in both structures) reveals that the difference is relatively small and principally concerns the H bonds formed along the *c* axis by oxygen atoms 2 and 5. In ice-I*h* they H bond to oxygens 2″ and 5′. In MH-III, they bond in the opposite directions along *c* to oxygens 2′ and 5″, while the general topology of all the other H bonds remains the same in the two structures. The reversal of these H-bond directions (see (+) and (−) in Fig. 3) means that in MH-III the frequency along the *a* axis of interlinking *c* axis H bonds is roughly doubled relative to the frequency in the corresponding direction in ice-I*h* and the frequency along the *b* axis is halved. As a result, instead of the three intersecting channels at 60° intervals perpendicular to *c* found in ice-I*h*, MH-III has only one channel perpendicular to *c* which is directed along the *a* axis. The channels are much larger than those of ice-I*h* because of the halving of the interlink frequency along *b*—there is no bond between oxygens 5 and 5′, for example; these channels are equivalent to two adjacent ice-I*h* channels. We can thus regard the H-bond network of MH-III as a distortion of the ice-I*h* network, where one set of channels perpendicular to *c* is expanded to accommodate the methane molecules within the structure.

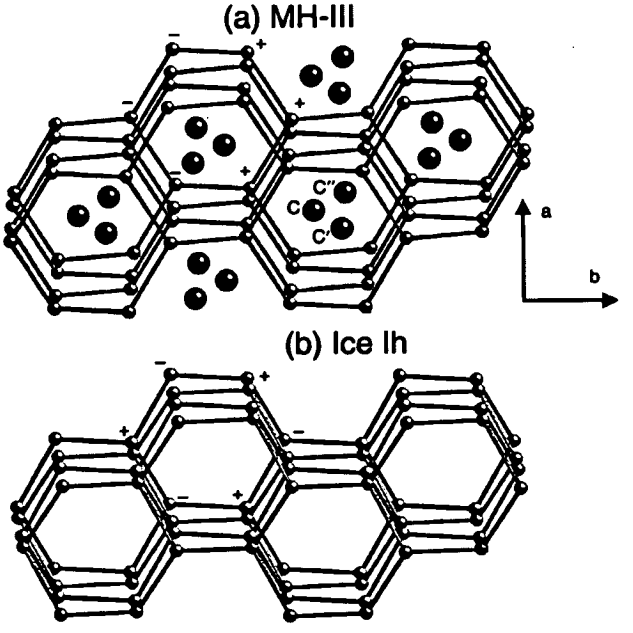

FIG. 3. The structure of (a) MH-III and (b) ice-I*h* viewed parallel to the their *c* axes. The (+) and (−) symbols show the sense of *c*-axis H bonds from the puckered sheet labeled *S* in Fig. 2.

The need for this expansion is made clear by an examination of the interatomic distances. Each methane is twelvefold coordinated and the shortest C···O distances in MH-III are the six at ~3.3 Å in Table I. By comparison, if methane could occupy sites in the channels of ice-I*h* then the corresponding distances would be only ~2.9 Å even at ambient pressure [24]. To relieve this implausibly short distance within the ice-I*h* topology would require an implausibly large (>10%) increase in some H bond lengths. In MH-III, the doubling in size of the *a*-axis channels (see above) and the increase of ~0.4 Å in the maximum width of the channels along *c* (from 5 to 5′) allow closer packing of the methane molecules by displacement along *b* towards the center of the *a* axis channels. They are then offset from the centers of the channels running along *c*, giving the zigzag arrangement of methane positions—for example, from C′ to C to C″—visible in Fig. 3(a). This displacement lengthens the shortest C···O contacts and reduces the shortest C···C distance. Given that the latter (from C to C′) is close to the value found in methane I at the same pressure [22], it appears likely that the balance between O···C and C···C repulsions determines the location of the methanes. It should be noted here that the O···C distances are much shorter than in the low-pressure structure-I methane hydrate (by ~0.5 Å). Furthermore, if there is a C-H bond directed along the short C···O contacts then the H···O distances would fall well within the upper limit for weak C-H···O hydrogen bonds [25].

The distortion of the ice-I*h* water network to achieve reasonable C···O distances involves very little change in the H-bond *lengths* (only 1% longer than in ice-I*h*) but instead involves distortion of the O-O-O *angles*. The angles in ice-I*h* (109°) are close to the ideal tetrahedral value [3], whereas in MH-III they range between 90° and 120°. While these differ considerably from the ideal value they are consistent with the range of values found in the high-pressure phases of ice—for example, ice-II exhibits a very similar range of angles [3]. This tendency to respond to perturbation by a change of the angles rather than of the O···O distances appears to be the general response of water networks. Densification up to 2 GPa through the various phases of ice is also achieved largely by distortion of

O-O-O angles [3]. However, in MH-III, the distortion of the angles from ideal tetrahedral values produces a water network which is 15% *less* dense than ice-I*h* at atmospheric pressure [24]. Nevertheless, the overall density of MH-III is within ~1.0% of the mean density of a 2:1 mixture of ice-VII and methane-I at 3.0 GPa [22,26]. Since both ice-VII and methane-I have densely packed structures—methane-I is close packed [22] and ice-VII undergoes no coordination changes up to at least 150 GPa [27]—it appears that MH-III is also densely packed and may be stable over a pressure range much wider than the current observed range of ~10 GPa [16].

The C···O contact distances reveal that the methane-water repulsions in MH-III are quite strong. Whereas the long C···O distances of ~3.8 Å found in MH-I lie close to the minimum in the methane-water potential as shown in Fig. 1 of Ref. [28], the C···O distances of ~3.3 Å in MH-III lie well into the repulsive part, with a repulsive interaction energy of the order of ~1 kJ mol^{-1} [28] at 3.0 GPa. MH-III thus provides experimental access to a completely unexplored regime of the methane-water interaction [5] and will prove to be a valuable system for studies of dynamics and modeling to improve knowledge of this part of the potential. The repulsive interaction increases strongly with pressure and is more than doubled at 11 GPa (the highest pressure reached in this study), where the C···O distances are reduced to ~3.1 Å. It is clearly now of great interest to explore this system to much higher pressures, both to probe deeper into the repulsive region and to establish the ultimate stability limit of the MH-III structure.

In spite of the relatively large distortions of its water network, MH-III has key structural features in common with the filled-ice gas hydrates [8,9]. Like these structures, MH-III in no sense has cages, and instead the guest molecules sit in channels within the water network with relatively short ~3.3 Å water-guest distances. MH-III can thus be regarded as a filled ice. It is the first to be found with an ice-I*h*-related water network, and the first example of a transformation from a cage clathrate to a filled ice. Many other cage clathrates have been shown to have phase transitions in the 1–2 GPa range [10–14] and it is probable that these transitions also signal a change from cage structures to channel or filled ice structures. It is likely that this type of transformation provides a route by which stable gas hydrates can exist at pressures above 10 GPa [16]. However, existing evidence suggests that the structures are not the same in detail as methane hydrate and these differences are likely to be determined by the repulsive part of the gas-water potentials now being opened up to study.

We thank S. A. Belmonte, D. R. Allan, and D. J. Francis for assistance with experiments and Y. P. Handa for sample preparation. This work is funded by the U.K. EPSRC and supported by the U.K. CLRC through access to beam time at ISIS and SRS, and other resources. We also acknowledge support from the British Council.

[1] H. Davy, Philos. Trans. R. Soc. London **101**, 1 (1811).
[2] G. A. Jeffery, Compr. Supramol. Chem. **8**, 788 (1984).
[3] V. F. Petrenko and R. W. Whitworth, *Physics of Ice* (Oxford University Press, Oxford, 1999), Chap. 11, pp. 252–283.
[4] G. Hummer, S. Garde, A. E. Garcia, M. E. Paulaitis, and L. R. Pratt, Proc. Natl. Acad. Sci. U.S.A. **95**, 1552 (1998).
[5] K. Lum, D. Chandler, and J. D. Weeks, J. Phys. Chem. B **103**, 4570 (1999).
[6] W. S. Holbrook, H. Hoskins, W. T. Wood, R. A. Stephen, and D. Lizarralde, Science **273**, 1840 (1996).
[7] J. I. Lunine and D. J. Stevenson, Icarus **70**, 61 (1987).
[8] W. L. Vos, L. W. Finger, R. J. Hemley, and H. K. Mao, Phys. Rev. Lett. **71**, 3150 (1993).
[9] D. Londono, J. L. Finney, and W. F. Kuhs, J. Chem. Phys. **97**, 547 (1992).
[10] Y. A. Dyadin, E. G. Larionov, D. S. Mirinski, T. V. Mikina, and L. I. Starostina, Mendeleev Commun. **7**, 32 (1997).
[11] Y. A. Dyadin, E. Y. Aladko, and E. G. Larionov, Mendeleev Commun. **7**, 34 (1997).
[12] Y. A. Dyadin, E. G. Larionov, A. Y. Manakov, F. V. Zhurko E. Y. Aladko, T. V. Mikina, and V. Y. Komarov, Mendeleev Commun. **9**, 209 (1999).
[13] M. G. E. van Hinsberg, M. I. M. Scheerboom, and J. A. Schouten, J. Chem. Phys. **99**, 752 (1993).
[14] H. T. Lotz and J. A. Schouten, J. Chem. Phys. **111**, 10242 (1999).
[15] C. Gutt, B. Asmussen, W. Press, M. R. Johnson, Y. P. Handa, and J. S. Tse, J. Chem. Phys. **113**, 4713 (2000).
[16] J. S. Loveday, R. J. Nelmes, M. Guthrie, S. A. Belmonte, D. R. Allan, D. D. Klug, J. S. Tse, and Y. P. Handa, Nature (London) **410**, 661 (2001).
[17] Deuteration eliminates the high background given by incoherent neutron scattering from hydrogen atoms.
[18] Y. P. Handa, J. Chem. Thermodyn. **18**, 915 (1986).
[19] J. M. Besson, R. J. Nelmes, G. Hamel, J. S. Loveday, G. Weill, and S. Hull, Physica (Amsterdam) **180B–181B**, 90 (1992).
[20] R. J. Nelmes, J. S. Loveday, R. M. Wilson, J. M. Besson, S. Klotz, G. Hamel, and S. Hull, Trans. Am. Crystallogr. Assoc. **29**, 19 (1993).
[21] R. J. Nelmes and M. I. McMahon, J. Synchrotron. Radiat. **1**, 69 (1994).
[22] R. M. Hazen, H. K. Mao, L. W. Finger, and P. M. Bell, Appl. Phys. Lett. **37**, 289 (1980).
[23] The refined values of the variable structural parameters at 3.0(1) GPa, were $a = 4.7458(5)$ Å, $b = 8.0644(9)$ Å, $c = 7.8453(7)$ Å, $y(\mathrm{C}) = -0.1857(15)$, $U_{\mathrm{iso}}(\mathrm{C}) = 2.9(10) \times 10^{-2}$ Å^2, $y(\mathrm{O}) = 0.4100(10)$, $z(\mathrm{O}) = 0.1792(6)$, $U_{\mathrm{iso}}(\mathrm{O}) = 1.0(4) \times 10^{-2}$ Å^2. $x(\mathrm{C}) = 1/4$, $z(\mathrm{C}) = 0$, and $x(\mathrm{O}) = 1/4$. (There is a $0, 1/4, 0$ shift of origin compared with the $1/4, 0, 0$ *I*2*bm* sites mentioned in the text.)
[24] V. F. Petrenko and R. W. Whitworth, *Physics of Ice* (Ref. [3]), Chap. 2, pp. 10–35.
[25] G. A. Jeffrey, *An Introduction to Hydrogen Bonding* (Oxford University Press, Oxford, 1997).
[26] R. J. Hemley, A. P. Jephcoat, H. K. Mao, C. S. Zha, L. W. Finger, and D. E. Cox, Nature (London) **330**, 737 (1987).
[27] P. Loubeyre, R. LeToullec, E. Wolanin, M. Hanfland, and D. Hausermann, Nature (London) **397**, 503 (1999).
[28] J. S. Tse, M. Klein, and I. McDonald, J. Phys. Chem. **87**, 4198 (1983).

Stable methane hydrate above 2 GPa and the source of Titan's atmospheric methane

J. S. Loveday*, R. J. Nelmes*, M. Guthrie*, S. A. Belmonte*, D. R. Allan*, D. D. Klug†, J. S. Tse† & Y. P. Handa†

* *Department of Physics and Astronomy, University of Edinburgh, Mayfield Road, Edinburgh EH9 3JZ, UK*
† *Steacie Institute for Molecular Sciences, National Research Council of Canada, Ottawa, Ontario, Canada K1A 0R6*

Methane hydrate is thought to have been the dominant methane-containing phase in the nebula from which Saturn, Uranus, Neptune and their major moons formed[1]. It accordingly plays an important role in formation models of Titan, Saturn's largest moon. Current understanding[1,2] assumes that methane hydrate dissociates into ice and free methane in the pressure range 1–2 GPa (10–20 kbar), consistent with some theoretical[3] and experimental[4,5] studies. But such pressure-induced dissociation would have led to the early loss of methane from Titan's interior to its atmosphere, where it would rapidly have been destroyed by photochemical processes[6,7]. This is difficult to reconcile with the observed presence of significant amounts of methane in Titan's present atmosphere. Here we report neutron and synchrotron X-ray diffraction studies that determine the thermodynamic behaviour of methane hydrate at pressures up to 10 GPa. We find structural transitions at about 1 and 2 GPa to new hydrate phases which remain stable to at least 10 GPa. This implies that the methane in the primordial core of Titan remained in stable hydrate phases throughout differentiation, eventually forming a layer of methane clathrate approximately 100 km thick within the ice mantle. This layer is a plausible source for the continuing replenishment of Titan's atmospheric methane.

The low-pressure structure of methane hydrate is composed of water cages surrounding methane molecules which stabilize the cages through van der Waals forces—in the 'clathrate I' type of structure[8]. This is referred to as structure-I methane hydrate, or SIMH, and has an ideal composition of 5.75 water molecules to each methane molecule. The stability of clathrate hydrates as a function of pressure has been explored[3] using calculations based on the van der Waals–Platteeuw model[9,10]. These models are general and predict that the clathrate structure becomes unstable with respect to ice and the guest species at the intersection of the decomposition curve with the ice freezing line, because of the greater changes in entropy and volume in forming crystalline clathrate from ice instead of liquid water. In the case of SIMH this is estimated to occur at about 1.2 GPa (ref. 3).

Recent synchrotron X-ray diffraction studies[4,5] have shown a change in structure above 1 GPa, interpreted as the progressive emptying of the smaller cage sites in SIMH—thus liberating free methane—up to 2.2 GPa, where dissociation to ice VII and methane I occurs. This suggests that the expected dissociation occurs as a gradual process over ~1 GPa. However, the fit of this model[4,5] to the observed data is poor. Hirai *et al.*[4] also noted that their finding of three-phase coexistence at room temperature was thermodynamically inconsistent with measurements of the decomposition curve[11], which identified a triple point at about 0.6 GPa and 320 K, and they speculated that this inconsistency was evidence of metastability. We have now carried out a detailed neutron diffraction study of the behaviour in the range up to 10 GPa on fully deuterated (D-) methane clathrate, and have made comparative synchrotron X-ray studies of H-methane hydrate.

Figure 1a shows neutron diffraction patterns obtained from the D-hydrate on increasing pressure. Up to 0.8 GPa (profile a), the diffraction pattern was that of SIMH. At 1.1 GPa (profile b), the three strongest peaks of ice VI appeared between 2.5 and 2.75 Å (marked by filled circles), and the formation of a new methane hydrate phase (methane hydrate II, MH-II) was indicated by the six peaks marked by diamonds. On further compression, MH-II underwent a transformation at 2.0 GPa (profile d) to methane hydrate III (MH-III), indicated by the appearance of the peaks marked by squares, with an accompanying increase in height of the ice VI peaks which shows MH-III to be richer in methane than MH-II. At 2.2 GPa the ice VI progressively transformed to ice VII (profiles f and g). MH-III remained stable to 10 GPa without further phase transformation. To mimic the pressure–temperature (P–T) path followed by the primordial core during Titan's accretion[1], samples were also compressed to approximately 3 GPa at 130 K and then warmed to room temperature. The sample was found to amorphize on compression and then transform on warming to MH-III and ice VII as can be seen in Fig. 1c.

The observation of new hydrate structures appears to conflict with the behaviour described by refs 4 and 5, and so X-ray data were collected to explore the behaviour of H-hydrate. The sequence of changes was found to be the same as in the D-hydrate up to

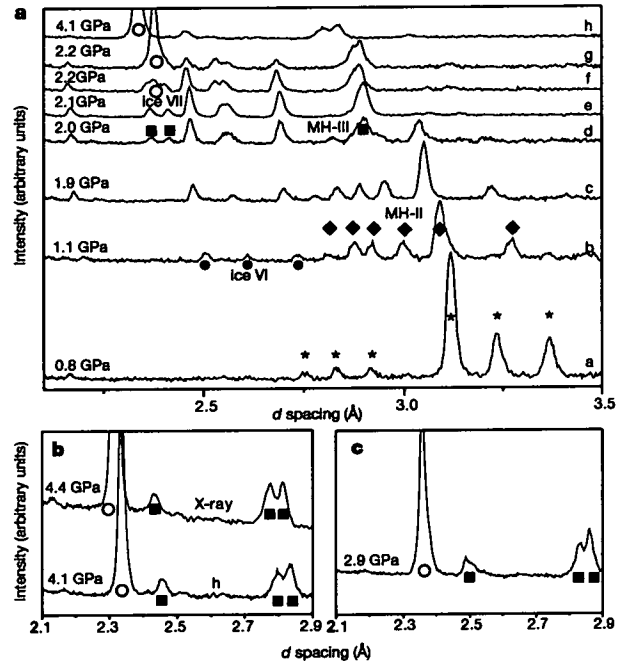

Figure 1 Diffraction patterns showing the three phases of methane hydrate. Peaks are marked for SIMH (asterisks), MH-II (diamonds), ice VI (filled circles), MH-III (squares) and ice VII (open circles). **a**, The neutron diffraction patterns of deuterated methane hydrate on increasing pressure at room temperature. **b**, A comparison of X-ray data collected from H-methane hydrate at 4.4 GPa with neutron data collected from D-hydrate at 4.1 GPa (profile h in **a**). **c**, A neutron diffraction pattern collected from D-methane hydrate at about 3 GPa after being compressed at around 130 K and warmed to room temperature. The samples of H- and D-SIMH were produced by adsorbing methane into ice at −20 °C as described elsewhere[21] and loaded at about 100 K into a Paris–Edinburgh pressure cell[22] for the neutron studies and a Merrill–Bassett diamond-anvil cell for the X-ray studies. The cells were sealed by applying pressure and warmed to room temperature. Fits to diffraction data confirmed full occupancy of the SIMH cage sites. Neutron diffraction studies were carried out on the PEARL beamline[23] of the UK neutron facility, ISIS, at the Rutherford Appleton Laboratory, and X-ray studies were carried out using image-plate techniques[24] on station 9.1 at the UK synchrotron, SRS, at Daresbury Laboratory and beamline ID9 of the European Synchrotron Radiation Facility. Pressures were determined from the known compressibilities of SIMH, ice VI and ice VII in the case of the neutron experiments and using the ruby fluorescence method in the X-ray case.

1.9 GPa—except that MH-II formed at the slightly lower pressure of about 0.9 GPa where water is still liquid[12] and this water supercompressed so that ice VI only appeared above 1.6 GPa. (This supercompressing of water was also observed in refs 4 and 5, and appears to be a reproducible kinetic effect.) Different behaviours were observed above 1.9 GPa, depending on the rate of compression. A sample taken up in pressure 'normally', in steps of some 0.2–0.5 GPa every 1–2 h, transformed as predicted into ice VII and methane I. But the results with the D-hydrate suggested the probable influence of kinetics, and so we held another sample at 1.9 GPa for 12 h. This transformed into a mixture of ice VI and MH-III. At 2.2 GPa the ice VI transformed to ice VII, and at 4.4 GPa this sample gave the pattern shown in Fig. 1b, marked X-ray (profile h of the D-hydrate at a similar pressure is shown for comparison). As for the D-hydrate, hydrogenous MH-III was found to be stable indefinitely up to at least 10 GPa, and samples compressed to approximately 3 GPa at 130 K were found to be MH-III and ice VII when warmed to room temperature.

This behaviour is fully consistent with earlier work. The tabulated *d* spacings from the pattern interpreted as low-occupancy SIMH and ice VI at 1.5 GPa in ref. 5 match the MH-II and ice VI peak positions found in our data, and the (cubic) SIMH structure gives a very poor fit with differences in observed and calculated peak positions as large as 0.2 Å. The transition was found below 1 GPa with solid ice VI not appearing until a significantly higher pressure (1.5 GPa in refs 4 and 5). And no solid methane appeared until the MH-II phase starts to transform to ice and methane[4,5], as we also observe for the normal rate of increase of pressure. The transition to MH-II is also consistent with the decomposition curve determined in ref. 11 and it is very probable that the "second hydrate" proposed[11] above 0.6 GPa was in fact MH-II.

In addition to the three MH-III peaks marked in Fig. 1b, 13 other peaks from MH-III were clearly visible in the X-ray data. From these it was possible to solve the structure as body-centred orthorhombic with unit-cell dimensions $a = 4.7458(5)$ Å, $b = 8.0644(9)$ Å, $c = 7.8453(7)$ Å and $v = 300.26(3)$ Å^3 at 3.0(1) GPa. The structure has eight water molecules and four methane molecules in the unit cell, consistent with the composition estimated from the relative peak heights of ice VI and SIMH. The details of this structure solution will be published elsewhere. A Murnaghan fit to the volume as a function of pressure, as shown in Fig. 2, gives an ambient-pressure bulk modulus $B_0 = 15.2(5)$ GPa with a rate of change with pressure $B' = 4$. These results and those for SIMH place constraints on the density of MH-II. On the basis of peak heights, the molecular composition is estimated to be 3.5 water : 1 methane and the patterns can be indexed with a hexagonal unit cell with $a = 11.7911(12)$ Å, $c = 9.9210(10)$ Å and $v = 1194(3)$ Å^3 at 1.7(1) GPa. The volume of the whole sample must decrease with pressure and MH-II must then contain between 28 water molecules with a water : methane ratio of 3 : 1 and 39 water molecules with a ratio of 4 : 1. The values plotted in Fig. 2 are for 34 water molecules and a 3.5 : 1 ratio. This composition is close to the mean value and is also the composition of the hexagonal structure-H (sH) clathrate[13] which has an axial ratio close to that of MH-II. However, although MH-II and sH also have similar pair correlation functions, a fit to the sH structure gave implausible nearest-neighbour oxygen to oxygen distances. We conclude that MH-II does not have the hexagonal clathrate structure but may be closely related to it. (After this work was completed another study observed the same hexagonal phase and concluded on the basis of the *c/a* ratio that it has the sH structure[14]. We have rechecked our analysis and have not altered our conclusion.)

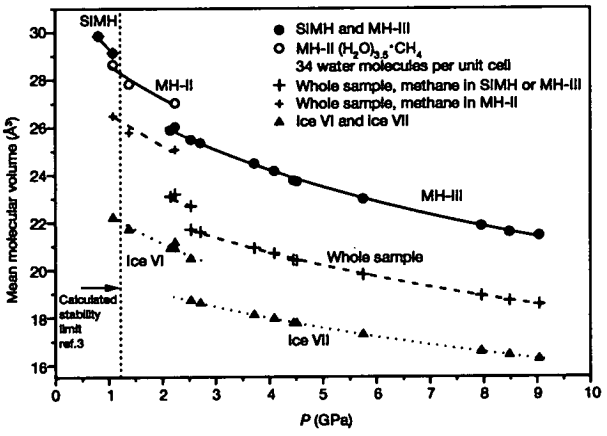

Figure 2 The compression of methane hydrate. The pressure dependence of the mean molecular volume for the three methane-hydrate phases (circles), ices VI and VII (triangles), and the whole sample (crosses)—which is a water–methane mixture corresponding to the 5.75:1 ratio of the initial SIMH—showing that the compression of the overall sample is largely achieved by the transfer of water from methane hydrate phases to the relatively dense ice phases. The values for the whole sample were obtained by placing all the methane and the appropriate amount of water (5.75 water molecules per methane for SIMH, 3.5 water molecules per methane for MH-II, and 2 water molecules per methane for MH-III) in the relevant methane hydrate phase, and the remaining water in the relevant ice phase. The values for MH-II were calculated for the middle of the range of possible values as described in the text. The solid line through the MH-III data is the best-fitting Murnaghan equation of state. All the other lines are guides to the eye.

These high-pressure structures of methane hydrate have probable relevance to gas hydrates in general. High-pressure transitions have been reported in the hydrates of neon[15], argon[16,17] and nitrogen[18] and the dissociation curves of neon and argon hydrates[15,16] show similarities to that of methane hydrate[11]. However, none of the differential thermal analysis and light-scattering studies reported until now conclusively indicates the existence of new hydrate structures, as against a change in guest occupancy or in state of ordering[18]. Given the similarities in the dissociation curves, and the fact that nitrogen and argon have similar radii to methane, it is possible that at least argon and nitrogen hydrates also adopt the MH-II structure and that the second transition reported in argon hydrate[17] may be to the MH-III structure.

The discovery that methane hydrates remain stable up to 10 GPa has important consequences for the modelling of Titan. Established models[1,2,19] suggest that at the end of accretion Titan had a primordial core made up of a mixture of (1) rock, (2) ammonia monohydrate, and (3) methane clathrate that had been dissociated into ice and free methane by the core pressures of 2–6 GPa, all surrounded by a thick rocky 'carapace'. Outside the carapace was a layer of high-pressure ices capped by an ammonia-water ocean, with an outermost surface layer of ice Ih. It is believed that melting in the core through radiogenic heating would have caused eventual rupture of the carapace, leading to core overturn, and gravitational differentiation in which the (low-density) free methane would rise quite rapidly to the surface and form part of Titan's early atmosphere[1,2]. There is a long-standing debate[6,7] on how the atmospheric methane is replenished, as photochemical processes are expected to destroy the methane too rapidly for the current atmosphere to be a remnant of a primordial methane-rich atmosphere[6,7]. Possible proposed sources include the presence of pools of liquid methane on the surface[6,7], and a near-surface regolith formed by the interaction of atmospheric or other free methane with surface ice[20]. These depend on an extensive escape of free methane following differentiation, which would require passage of most of the methane through the ammonia–water ocean. Models vary significantly in the predicted nature and thickness of this ocean, depending on assumptions about the composition of the primordial ices, thermal evolution, and so on; the most recent work concludes that the ocean thickness must be too great for methane to traverse without re-enclathration[2].

Our results change the basis of this debate by showing that all or

most of the core methane will remain within the satellite after differentiation, irrespective of the thickness (or existence[19]) of the ocean. First, we show that the material originally accreted into the primordial core as SIMH will be a mixture of ice and MH-III under the P–T conditions at the end of accretion. As we have also established that the SIMH to MH-II and MH-II to MH-III transitions are both readily reversible, gravitational differentiation after core overturn will return all the core methane to SIMH as the methane-containing component rises above the final core and passes through the layer of ice phases at the bottom of the mantle (which are denser, as Fig. 2 shows). The outcome will be a layer of SIMH some 100 km thick either just below or just above the ammonia–water ocean—the ocean's density is not well enough known to determine which. In either case, this large amount of SIMH will be stable to the base of the surface ice layer (where the pressure is estimated to be 0.1 GPa (ref. 2)).

These results imply that it is unlikely that Titan has surface pools of methane. Instead, the SIMH layer provides a possible long-term source of atmospheric methane through convective processes such as cryovulcanism[1,2,20]. The presence of an approximately 100 km thick SIMH layer will also have an impact on the modelling of thermal and rheological processes[2]. Furthermore, the incorporation into the SIMH layer of a substantial amount of water that was previously believed to be free will increase the ammonia content of the ammonia–water ocean and hence increase its thickness. □

Received 27 June 2000; accepted 26 January 2001.

1. Lunine, J. I. & Stevenson, D. J. Clathrate and ammonia hydrates at high-pressure—application to the origin of methane on Titan. *Icarus* 70, 61–77 (1987).
2. Grasset, O., Sotin, C. & Deschamps, F. On the internal structure and dynamics of Titan. *Planet. Space Sci.* 48, 617–636 (2000).
3. Lunine, J. I. & Stevenson, D J. Thermodynamics of clathrate hydrate at low and high pressures with application to the outer solar system. *Astrophys. J. Suppl. Ser.* 58, 493–531 (1985).
4. Hirai, H. *et al.* Methane hydrate behaviour under high pressure. *J. Phys. Chem. B* 104, 1429–1433 (2000).
5. Hirai, H. *et al.* Methane hydrate, amoeba or a sponge made of water molecules. *Chem. Phys. Lett.* 325, 490–498 (2000).
6. Lorenz, R. D. The weather on Titan. *Science* 290, 467–468 (2000).
7. Lunine, J. I. Does Titan have an ocean? A review of current understanding of Titan's surface. *Rev. Geophys.* 31, 133–149 (1993).
8. Gutt, C. *et al.* The structure of deuterated methane hydrate. *J. Chem. Phys.* 113, 4713–4721 (2000).
9. van der Waals, J. H. Statistical mechanics of clathrate compounds. *Trans. Faraday Soc.* 52, 184 (1956).
10. van der Waals, J. H. & Platteeuw, J. C. Clathrate solutions. *Adv. Chem. Phys.* 2, 1 (1959).
11. Dyadin, Y. A., Aladko, E. Y. & Larionov, E. G. Decomposition of methane hydrates up to 15 kbar. *Mendeleev Commun.* 7, 34–35 (1997).
12. Pistorius, C. W., Pistorius, M. C., Blakey, J. P. & Adimiraal, L. J. Melting curve of ice VII to 200 kbar. *J. Chem. Phys.* 38, 600 (1963).
13. Udachin, K. A., Ratcliffe, C. I., Enright, G. D. & Ripmeester, J. A. Structure H Hydrate: a single crystal diffraction study of 2,2 dimethylpentane.5(Xe,H_2S).34H_2O. *Supramol. Chem.* 8, 173–176 (1997).
14. Chou, I. M. *et al.* Transformations in methane hydrates. *Proc. Natl Acad. Sci.* 97, 13484–13487 (2000).
15. Dyadin, Y. A. *et al.* Clathrate hydrates of hydrogen and neon. *Mendeleev Commun.* 5, 209–210 (1999).
16. Dyadin, Y. A., Larionov, E. G., Mirinski, D. S., Mikina, T. V. & Starostina, L. I. Clathrate formation in the Ar-H_2O system under pressures up to 15,000 bar. *Mendeleev Commun.* 7, 32–34 (1997).
17. Lotz, H. T. & Schouten, J. A. Clathrate hydrates in the system H_2O-Ar at pressures and temperatures up to 30 kbar and 140 °C. *J. Chem. Phys.* 111, 10242–10247 (1999).
18. van Hinsberg, M. G. E., Scheerboom, M. I. M. & Schouten, J. A. The vibrational spectra of N_2 in clathrate-hydrates: A new high-pressure phase transition. *J. Chem. Phys.* 99, 752–754 (1993).
19. Grasset, O. & Sotin, C. The cooling rate of a liquid shell in Titan's interior. *Icarus* 123, 101–112 (1996).
20. Stevenson, D. J. in *Proceedings of Symposium on Titan* 29–33 (European Space Agency Special Publication SP-338, Toulouse, 1992).
21. Handa, Y. P. Compositions, enthalpies of dissociation, and heat-capacities in the range 85K–270K for clathrate hydrates of methane, ethane, and propane, and enthalpy of dissociation of isobutane hydrate, as determined by a heat-flow calorimeter. *J. Chem. Therm.* 18, 915–921 (1986).
22. Nelmes, R. J. *et al.* Structure studies at high pressure using neutron powder diffraction. *Trans. Am. Cryst. Ass.* 29, 19–27 (1993).
23. *PEARL—Pressure and Engineering Research Line* 28–29 ISIS'97 Rutherford Appleton Laboratory Report RAL-TR-97-050 (RAL, Didcot, 1997).
24. Nelmes, R. J. & McMahon, M. I. High-pressure powder diffraction on synchrotron sources. *J. Synch. Rad.* 1, 69–73 (1994).

Acknowledgements

We thank D. J. Francis, T. Bovornratanaraks and M. Hanfland for assistance with experiments, and O. Grasset and D. J. Stevenson for helpful discussions of their work. Our work is funded by a research grant from the EPSRC, and supported by CCLRC through access to beamtime and other resources.

Correspondence and requests for materials should be addressed to J. S. L.. (e-mail: J.Loveday@ed.ac.uk).

A thermodynamic connection to the fragility of glass-forming liquids

L.-M. Martinez & C. A. Angell

Department of Chemistry and Biochemistry, Arizona State University, Tempe, Arizona 85287-1604, USA

Although liquids normally crystallize on cooling, there are members of all liquid types (including molecular, ionic and metallic) that supercool and then solidify at their glass transition temperature, T_g. This continuous solidification process exhibits great diversity within each class of liquid—both in the steepness of the viscosity–temperature profile, and in the rate at which the excess entropy of the liquid over the crystalline phase changes as T_g is approached. However, the source of the diversity is unknown. The viscosity and associated relaxation time behaviour have been classified between 'strong' and 'fragile' extremes, using T_g as a scaling parameter[1], but attempts to correlate such kinetic properties with the thermodynamic behaviour have been controversial[2,3]. Here we show that the kinetic fragility can be correlated with a scaled quantity representing excess entropy, using data over the entire fragility range and embracing liquids of all classes. The excess entropy used in our correlation contains both configurational and vibration-related contributions. In order to reconcile our correlation with existing theory and simulations, we propose that variations in the fragility of liquids originate in differences between their vibrational heat capacities, harmonic and anharmonic, which we interpret in terms of an energy landscape. The differences evidently relate to behaviour of low-energy modes near and below the boson peak.

The understanding of fluidity and diffusion in viscous liquids is in a state of flux. Formerly considered as a problem in energy-barrier crossing—and hence strictly kinetic in nature—it is now being suggested by molecular-dynamics (MD) studies that liquid diffusion is a process dominated by thermodynamic factors. Nearly three years ago, Sastry *et al.*[4] presented an 'inherent structures' analysis of MD data on a binary Lennard–Jones liquid (BMLJ), showing that two key dynamic features could be related to the static structure through the potential-energy hypersurface features that the liquid explores with highest probability at different temperatures. These were the onset of 'super-Arrhenius' behaviour, and the location of the mode-coupling theory critical temperature T_c (obtained by power-law fitting of the diffusivity versus temperature relation). An implication that the landscape excitation profile would provide a measure of liquid fragility that was basically thermodynamic was quantified by Speedy, who derived[5] an expression for thermodynamic fragility in which the excess entropy 'frozen in' at the kinetic glass transition plays an important scaling role.

This implication was also followed up by Ito *et al.*[2], who recast Kauzmann's normalized entropy data in a T_g-scaled form that has the same appearance as the common kinetic fragility plot. Their plot also assigns a key scaling role to the excess entropy frozen in at T_g. They observed, qualitatively, that the ordering of liquids was the same in both kinetic and thermodynamic manifestations. This notion was however immediately contested by Ngai *et al.*[3,6]. These authors suggested, from an analysis of the dielectric relaxation times and entropies of nine molecular liquids[3], that the correlation was unreliable at best and, in the case of polymeric liquids[6], was not applicable. Here we provide data on a much wider set, which includes all the cases of ref. 3, in order to clarify this problem. Clarification is demanded because, if kinetic fragility is indeed dominated by thermodynamics in the 'normal' case, then a significant simplification of the whole fragility phenomenon

High Pressure Research, 2000, Vol. 17, pp. 149–155
Reprints available directly from the publisher
Photocopying permitted by license only

NEUTRON DIFFRACTION STUDIES OF HYDROGEN-BONDED ICES AT HIGH PRESSURE

J. S. LOVEDAY[a,*], G. HAMEL[b], R. J. NELMES[a], S. KLOTZ[b], M. GUTHRIE[a] and J. M. BESSON[b]

[a]*Department of Physics and Astronomy, The University of Edinburgh, Edinburgh, EH9 3JZ;*
[b]*Université P et M Curie, 4 Place Jussieu, Paris, France*

(Received 1 October 1999)

The development of the Paris–Edinburgh cell has extended the pressure range for neutron diffraction by a full order of magnitude to 30 GPa. This advance has provided a wealth of new information on the high-pressure behaviour of ices such as water–ice, ammonia, methane and hydrogen sulphide. We have now put in place technique developments to permit loading of water–gas mixtures into the Paris–Edinburgh cell.

Keywords: Neutron diffraction; Ices

1. INTRODUCTION

The high-pressure behaviour of simple molecular systems provides fundamental insight into the density dependence of interatomic interactions. The ices (H_2O, NH_3, CH_4, H_2S) are a very important group of such simple systems because they allow exploration of the H-bond interaction – an interaction important to problems ranging from the behaviour of the Earth's mantle to the function of biological molecules – over a range of bond strengths and geometries. And the

*Address for correspondence: ISIS Facility, Rutherford Appleton Laboratory, Chilton, OXON OX11 0QX, United Kingdom. Fax: 44 1235 445720, e-mail: J.Loveday@ed.ac.uk

properties of these ices at high pressure underpin models of ice-containing planets and satellites like Uranus and Neptune, and Titan, Ganymede and Triton. There has been a recent surge of new interest in the study of ices at high pressure. Light-scattering studies have provided the first definitive evidence of the H-bond centring transition in ice [1–3] – a longstanding goal for high-pressure science; X-ray studies have found evidence of further transitions in ice at megabar pressures [4]; work on hydrogen sulphide has revealed that this ice becomes metallic [5]; and studies of methane have revealed complex time-dependence in the transition sequence above 5 GPa. In parallel, developments in *ab-initio* modelling techniques have provided unprecedented accuracy in calculations of these systems [6, 7] leading to predictions of protonic conduction in both ammonia and ice at high P and T [8].

One of the developments which has contributed to this heightened level of interest has been the access to accurate structural information in the range 3–30 GPa which has been made possible by the development of the Paris–Edinburgh neutron diffraction cell [9, 10]. The opposed-anvil design of this cell has significant advantages for studies of ices over other large volume apparatus in that it is relatively easy to load liquid and gaseous samples. In this short review, we summarise the results obtained to date – with a comprehensive bibliography – and present details of a newly developed technique for sample loading. This has enabled us to extend our work to studies of mixtures but also has potential advantages in other areas.

2. HIGH PRESSURE STRUCTURES OF ICES

Our initial studies were of ice itself. Measurements of the O–D bondlength in ice VIII [11] – stable above 2 GPa – revealed that the rate of increase of O–D with pressure to 10 GPa was at least five times smaller than previously predicted on the basis of light-scattering and X-ray studies [12]. This indicates that the change in interatomic potentials is very different from previous expectation, a view which has since been confirmed by Hartree-Fock calculations [13, 14]. More recent work has extended the pressure range from the initial limit of 10 GPa to 22 GPa using sintered diamond anvils [15], and revealed that O–D remains essentially constant [16] up to at least one third

of the H-bond centring pressure [1]. Careful attention to the corrections for attenuation by the pressure cell [17] has allowed accurate refinement of thermal (atomic displacement) parameters at high pressure. Comparisons of the thermal motion in ices VII and VIII provided the first direct evidence of multi-site disorder of both oxygen and deuterium atoms in ice VII [18]. From the magnitude of the displacements, it was possible to show that to obtain a plausible molecular geometry the displacements and the local structure of ice VII have to be significantly different from, and more complex than, previously accepted models. Studies to 20 GPa reveal that the magnitude of the disorder displacements are *P*-independent up to this pressure and so may persist up to H-bond centring [18]. The low mass (for a large volume cell) of the Paris–Edinburgh cell allows relatively easy work at low temperatures [19]. Studies of ice VIII at ~90 K in the 0–2 GPa range have revealed the existence of an isosymmetric phase transition at pressures below the stability range of ice VIII [20]. Other work at ~90 K has revealed that ice VI transforms at ~5 GPa into ice VII rather than ice VIII and that this ice VII can be recovered to ambient pressure [21].

Loading techniques have also been developed for high boiling- point gases [22]. Studies of ammonia provided the first determination of the structure of ammonia-IV showing that it was orientationally ordered rather than disordered as was previously thought on the basis of X-ray studies, and revealing a complex H-bond arrangement [23]. Studies of D_2S have identified the transition from phases II to I′ for the first time and have shown that it involves increased ordering of the deuterium atom arrangement which in both phases is consistent with the idea that the molecules are rotating about a single axis [24]. The structural changes at the transition show that this transition signals the onset of significant H-bonding [25]. And studies of methane phase IV have revealed that this important phase has a unit-cell volume of ~1000 $Å^3$ and a complex structure [26].

3. LOADING TECHNIQUES FOR MIXTURES

The behaviour at high pressure of water–gas mixtures such as the clathrate hydrates and the ammonia hydrates is emerging as being of high importance. These systems access phenomena which cannot be

explored in single component systems (for example mixed H-bonds and hydrophobic repulsions) and their high-pressure behaviour is also directly relevant to problems in Earth and planetary science. Work with such mixtures adds further complexity to the loading process because the composition is added as a variable and because these mixtures are generally not stable under ambient conditions. The procedures developed for the work summarised in Section 2 do not allow us to mix liquids and gases while retaining control over the composition. To overcome this problem, we have now developed techniques to allow samples to be loaded into the anvils of the Paris–Edinburgh cell at low temperatures where the mixtures are stable or metastable.

The new technique is based on first loading samples into the anvils separate from the pressure cell, and then inserting the anvil assembly into the cell to apply pressure. The principles of a simple assembly for this purpose are shown schematically in Figure 1. Two (opposed) anvils are cooled in liquid nitrogen and the sample is then placed into the gasket on top of one anvil. For the best results, the sample is loaded as a liquid cooled to its stability region – as is the case of the ammonia hydrates which can be stabilised by cooling to ~200K. This liquid then freezes into the sample space at 77 K. However, materials like methane hydrate which must be loaded as metastable solids at

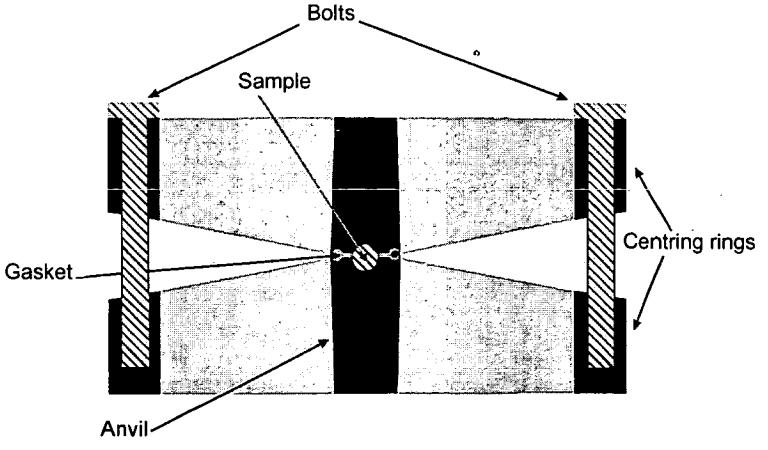

FIGURE 1 A schematic cross section of the simple assembly used to load mixtures into the Paris–Edinburgh cell.

77 K have also been successfully compressed. Once the sample space is filled, the second anvil is put in place, located by guide pins, and the whole assembly is held together by means of bolts which connect the centring rings surrounding the anvils (Fig. 1). The temperature during this process is maintained at 77 K by the nitrogen bath. The assembly is then transferred rapidly while still cold to the Paris–Edinburgh cell and a small load of ~5 tonnes applied to seal the sample.

These procedures use the relatively large, 200-tonne, Paris–Edinburgh cell to apply and maintain the small load needed for sealing. We are now in the process of developing a clamp to overcome this limitation (Fig. 2). The principal differences from the setup shown in Figure 1 are the inclusion of tungsten carbide seats to support the anvils and much stronger bolts to hold the assembly together. In the current design, a force of ~5 tonnes can be applied to the anvils using a separate small press and locked in by tightening the bolts. The assembly can thus be loaded and sealed without the need for a Paris–Edinburgh cell. A further larger-capacity clamp has been built to extend the maximum sealing force to 20 tonnes. A clamp offers the obvious advantage that samples can be loaded into it and stored prior to inserting it in the Paris–Edinburgh cell but its small size also has

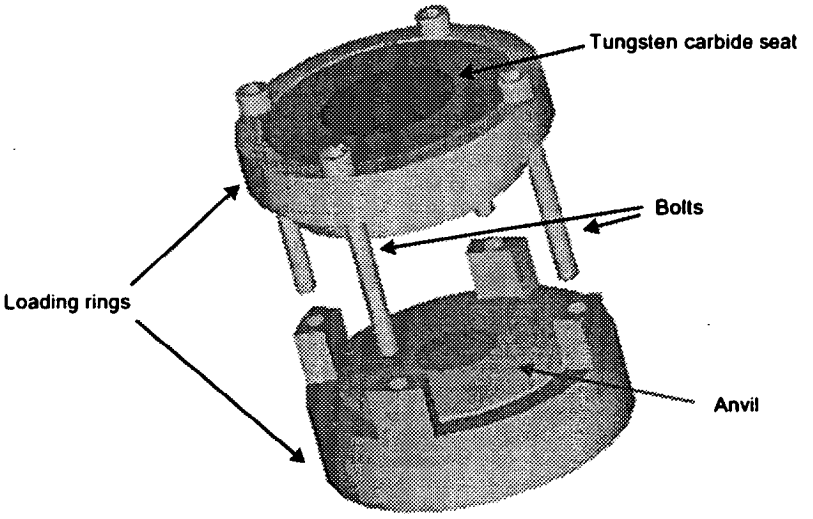

FIGURE 2 An exploded view of the 5 tonnes loading clamp described in the text.

other advantages. It allows loading to be carried out in the controlled atmosphere of a glove box, making it possible to load highly air-sensitive samples, and the small size will also greatly simplify the loading of gases. The clamp will be both much quicker to cool than the whole Paris–Edinburgh cell and easier to manipulate.

The prototype device in Figure 1 has already allowed the first neutron diffraction studies of mixtures above ~ 0.5 GPa. Studies of ammonia monohydrate have revealed the existence of five new phases up to ~ 6 GPa [27] including the first example of a hydrogen bonded molecular alloy [28]. Studies of ammonia-dihydrate have shown that, like water–ice, this material undergoes pressure-amorphisation [27] and we have successfully carried out explorations of the stability limits of methane hydrate.

4. CONCLUSIONS

The impact of the development of the Paris–Edinburgh cell has always been greatly enhanced by its flexibility for sample loading and parallel development of new techniques for sample loading. The loading rings and clamps described here have already opened up a new area of work in the high-pressure behaviour of mixtures which promises to be very fertile and will further extend the range of samples which can be studied.

Acknowledgments

We acknowledge D. J. Francis for assistance during these experiments. This work is funded by the U.K. Engineering and Physical Sciences Research Council through research grants and by the Central Laboratory of the Research Councils through access to beamtime at the ISIS Facility and other support.

References

[1] Goncharov, A. F., Struzhkin, V. V., Somayazulu, M. S., Hemley, R. J. and Mao, H. K. (1996). *Science*, **273**, 218–220.
[2] Song, M., Yamawaki, H., Fujihisa, H., Sakashita, M. and Aoki, K. (1999). *Phys. Rev. B*, **60**, 12644–12650.

[3] Goncharov, A. F., Struzhkin, V. V., Mao, H. K. and Hemley, R. J. (1999). *Phys. Rev. Lett.*, **83**, 1998–2001.
[4] Loubeyre, P., LeToullec, R., Wolanin, E., Hanfland, M. and Häusermann, D. (1999). *Nature*, **397**, 503–506.
[5] Sakashita, M., Yamawaki, H., Fujihisa, H., Aoki, K., Sasaki, S. and Shimizu, H. (1997). *Phys. Rev. Lett.*, **79**, 1082–1085.
[6] Bernasconi, M., Silvestrelli, P. L. and Parrinello, M. (1998). *Phys. Rev. Lett.*, **81**, 1235–1238.
[7] Benoit, M., Marx, D. and Parrinello, M. (1998). *Nature*, **392**(6673), 258–261.
[8] Cavazzoni, C., Chiarotti, G. L., Scandolo, S., Tosatti, E., Bernasconi, M. and Parrinello, M. (1999). *Science*, **283**, 44–46.
[9] Besson, J. M., Nelmes, R. J., Hamel, G., Loveday, J. S., Weill, G. and Hull, S. (1992). *Physica B*, **180 + 181**, 907–910.
[10] Nelmes, R. J., Loveday, J. S., Wilson, R. M., Besson, J. M., Klotz, S., Hamel, G. and Hull, S. (1993). *Trans. Am. Cryst. Ass.*, **29**, 19.
[11] Nelmes, R. J., Loveday, J. S., Wilson, R. M., Besson, J. M., Pruzan, P., Klotz, S., Hamel, G. and Hull, S. (1993). *Phys. Rev. Lett.*, **71**, 1192–1195.
[12] Klug, D. D. and Whalley, E. (1984). *J. Chem. Phys.*, **81**, 1220–1228.
[13] Ojamae, L., Hermansson, K., Dovesi, R., Roetti, C. and Saunders, V. R. (1994). *J. Chem. Phys.*, **100**, 2128–2138.
[14] Besson, J. M., Pruzan, P., Klotz, S., Hamel, G., Silvi, B., Nelmes, R. J., Loveday, J. S., Wilson, R. M. and Hull, S. (1994). *Phys. Rev. B*, **49**, 12540–50.
[15] Klotz, S., Besson, J. M., Hamel, G., Nelmes, R. J., Loveday, J. S., Marshall, W. G. and Wilson, R. M. (1995). *Appl. Phys. Lett.*, **66**, 1735–1737.
[16] Nelmes, R. J., Loveday, J. S., Marshall, W. G., Besson, J. M., Klotz, S. and Hamel, G. (1998). *Rev. High Pressure Science and Technology*, **7**, 1138–1140.
[17] Wilson, R. M., Loveday, J. S., Nelmes, R. J., Klotz, S. and Marshall, W. G. (1995). *Nucl. Inst. Meth. A*, **354**, 145–148.
[18] Nelmes, R. J., Loveday, J. S., Marshall, W. G., Hamel, G., Besson, J. M. and Klotz, S. (1998). *Phys. Rev. Lett.*, **81**, 2719–2722.
[19] Klotz, S., Besson, J. M., Hamel, G., Nelmes, R. J., Loveday, J. S. and Marshall, W. G. (1996). *High Press. Research*, **14**, 249–255.
[20] Besson, J. M., Klotz, S., Hamel, G., Marshall, W. G., Nelmes, R. J. and Loveday, J. S. (1997). *Phys. Rev. Lett.*, **78**, 3141–3144.
[21] Klotz, S., Besson, J. M., Hamel, G., Nelmes, R. J., Loveday, J. S. and Marshall, W. G. (1999). *Nature*, **398**, 681–684.
[22] Klotz, S., Gauthier, M., Besson, J. M., Hamel, G., Nelmes, R. J., Loveday, J. S., Wilson, R. M. and Marshall, W. G. (1995). *Appl. Phys. Lett.*, **67**, 1188–1190.
[23] Loveday, J. S., Nelmes, R. J., Marshall, W. G., Besson, J. M., Klotz, S. and Hamel, G. (1996). *Phys. Rev. Lett.*, **76**, 74–77.
[24] Loveday, J. S., Nelmes, R. J., Marshall, W. G., Besson, J. M., Klotz, S. and Hamel, G. (1998). *Rev. High Pressure Science and Technology*, **7**, 1121–1123.
[25] Loveday, J. S., Nelmes, R. J., Klotz, S., Hamel, G. and Besson, J. M., *Phys. Rev. Lett.*, in press.
[26] Loveday, J. S., Nelmes, R. J., Marshall, W. G., Besson, J. M., Klotz, S. and Hamel, G. (1998). *Physica B*, **241**, 240–246.
[27] Loveday, J. S. and Nelmes, R. J. (2000). *Rev. High Pressure Science and Technology*, **8**, in press.
[28] Loveday, J. S. and Nelmes, R. J. (1999). *Phys. Rev. Lett.*, **83**, 4329–4332.